Measurement of atmospheric antiproton spectrum

大和, 一洋

(Degree)
博士（理学）
(Date of Degree)
2004-03-31
(Date of Publication)
2009-05-26
(Resource Type)
doctoral thesis
(Report Number)
甲3106
(URL)
https://hdl.handle.net/20.500.14094/D1003106

Measurement of Atmospheric Antiproton Spectrum

Kazuhiro Yamato

March, 2004

Abstract

The energy spectrum of atmospheric antiprotons has been measured in the range 0.2 to 3.3 GeV. The measurement was carried out at balloon altitude with the atmospheric depth of 4.5 to 26 g/cm^2, and at the ground level, about 1000 g/cm^2 by BESS detector. The antiprotons were identified by the mass measurement based on the precise measurements of rigidity, time-of-flight, and energy loss. Overwhelming e^-/μ^- backgrounds were eliminated with a threshold-type aerogel Čerenkov counter. Our balloon observation was made at Ft. Sumner, New Mexico U.S. and no primaries below cut off rigidity of 4.2GV were allowed to get into the atmosphere. Then we detected pure atmospheric anti-protons for the first time in the energy region below this magnetic cut off.

Using this spectrum, we evaluated the accuracy of antiproton production model. The production model based calculation made by Stephens seems to be consistent with our result at the small atmospheric depth. At deep atmospheric depth, the model calculation made by Huang which does not include tertiary production gives better agreement than that of Stephens model at deep atmosphere. This implies that tertiary production is small.

Contents

Chapter 1

Introduction

1.1 Cosmic-Ray Antiprotons

The origin of cosmic-ray antiprotons ($\overline{p}$'s) has attracted much attention since their observation was first reported by Golden *et al.* [1, 2]. The major part of cosmic-ray antiprotons is believed to be secondary particles produced by interactions of high energy cosmic-ray particles with interstellar matter in our Galaxy. The secondary antiprotons offer a unique probe [3] to study cosmic-ray propagation and solar modulation [4, 5]. As other possible sources of cosmic-ray antiprotons, one can conceive novel processes, such as annihilation of neutralino dark matter [6, 7] or evaporation of primordial black holes [8, 9].

1.2 Importance of atmospheric antiprotons

1.2.1 Background of cosmic-ray antiprotons

Antiprotons coming from the Galaxy give us the interesting information as described in the previous section. Thecrefore, the cosmic-ray antiproton measurements were carried out actively in 1990s by BESS [10, 11], IMAX [12], CAPRICE [13], MASS [14] and also other instruments. These observations were carried out at an altitude of about 37 km using large balloons (a few tens of million cubic feet), where the typical residual atmospheric depth is about 5 g/cm^2. The reason for the observation at the high altitude is, of course, to avoid the background of the atmospheric antiprotons produced in the residual atmosphere. The expected atmospheric antiprotons at a typical balloon altitude are about 1/3 of the galactic antiprotons.

In the BESS experiment, the atmospheric antiprotons have been estimated in the following way. The calculation of Mitsui [15] was used as a reference value of expected atmospheric antiproton flux at 5 g/cm^2. The systematic uncertainties of the expectation was taken by the maximum difference of three independent calculations (Mitsui [15], Stephens [16], Pfeifer [17]). Figure 1.1 shows the results of these calculations and the relative differences. In these calculations, Pfeifer *et. al.* and Stephens originally adopted higher proton flux observed by Webber *et. al.* [18], which is higher than the observed and widely recently accepted BESS-98, and AMS results [19, 20] by about a factor 1.2

at energies relevant to antiproton production. The calculation of Mitsui was based on a proton flux measurement by BESS [19]. Thus, we plotted atmospheric antiproton flux in the Figure 1.1 after normalized by this factor.

These independent three calculations give similar values around the peak at 2 GeV. This seems to indicate that the accuracy of these calculations are high enough, since these independently results derived almost agree with each other. However, we need to check the accuracy of the results by an experimental observation.

1.2.2 The characteristics of the antiprotons

Both the secondary galactic antiprotons and atmospheric antiprotons are produced by the hadronic interactions. Thus, the cross-section of antiproton production in nuclear collisions is the most important to estimate the flux of galactic antiproton as well as atmospheric antiprotons. Unfortunately, the accuracy of antiproton production cross section were measured by using the accelerator is not good enough. Therefore, Stephens scaled of $p+p$ cross section as $p+A$ cross section [21]. In the calculation of Huang, a new parametrization was developed from existing experimental data [26]. In the calculation of Pfifer *et. al.*, they used the Monte Carlo code of DTUNUC for the nucleus-nucleus interaction [17]. A direct measurement of atmospheric antiproton allows us to study which model gives the correct spectrum.

In addition to the production, survival feature of antiprotons in the atmosphere is not clear. The reaction cross section $\overline{p}$ + Air has not been measured by the accelerator experiment. Therefore we need to scale the existing data. We usually use the carbon data because the atomic weight of Carbon is nearly the same as that of Nitrogen and Oxygen which are the elements of the air. But, strictly speaking, they are not the same elements. Moreover the existing experimental cross section of $\overline{p}+C$ has an error of $5 \sim 50$ % [22, 23, 24]. The type, energy and direction of the produced secondary particles have no been measured exactly.

Recently, very interesting observation and the calculation were published in this respect. One is antiproton observation at the mountain altitude by BESS spectrometer [27]. The results is shown in Figure 1.2 by the filled square. The result of calculation shown in dot-dash line in the same figure [26]. Below 1 GeV, the result is different from the expected flux of an earlier work of Stephens [16] shown in dash line. The difference of these calculations is due to the different treatment of tertiary production of antiprotons. Here, the tertiary production means the antiproton produced by the inelastic interaction between the antiproton and the nucleon, i.e. $\overline{p} + N \rightarrow \overline{p}^* + X$. The energy of tertiary antiproton is assumed to be smaller than the energy of the incident antiproton. Huang does not include this tertiary production in his calculation. The shape of the observed flux seems to agree with the Huang's flux, although this statement relies on the statistically poor data at low energy region.

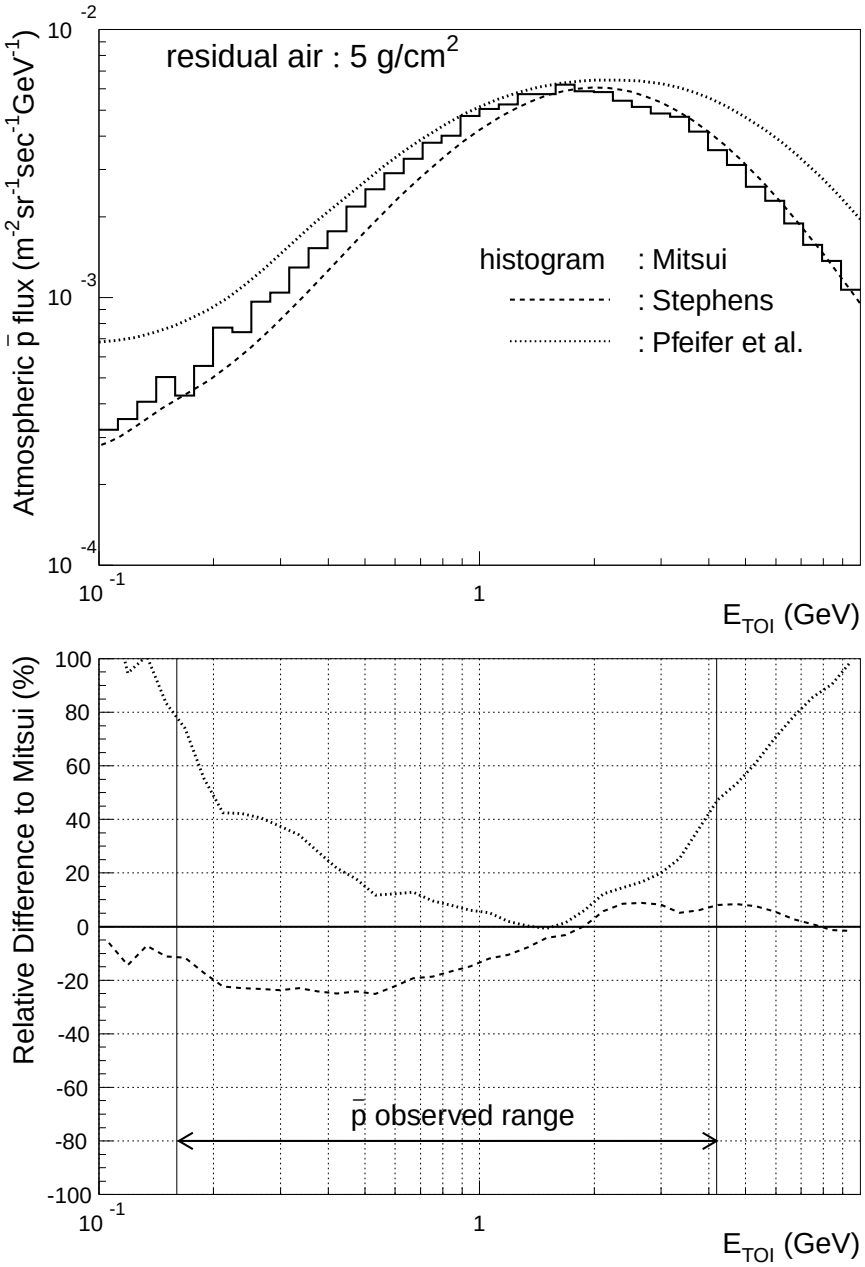

Figure 1.1: The calculated estimation of atmospheric antiproton flux in BESS 97-2000. Top figure shows the three independent calculations of atmospheric secondary antiprotons at a residual air of 5 g/cm^2 by Mitsui [15] (histogram), Stephens [16] (dashed curve), and Pfeifer *et. al.* [17] (dotted curve). Bottom figure shows the relative difference between Stephens or Pfeifer *et. al.* and Mitusi, i.e., (Stephens-Mitsui)/Mitusi or (Pfeifer-Mitsui)/Mitsui.

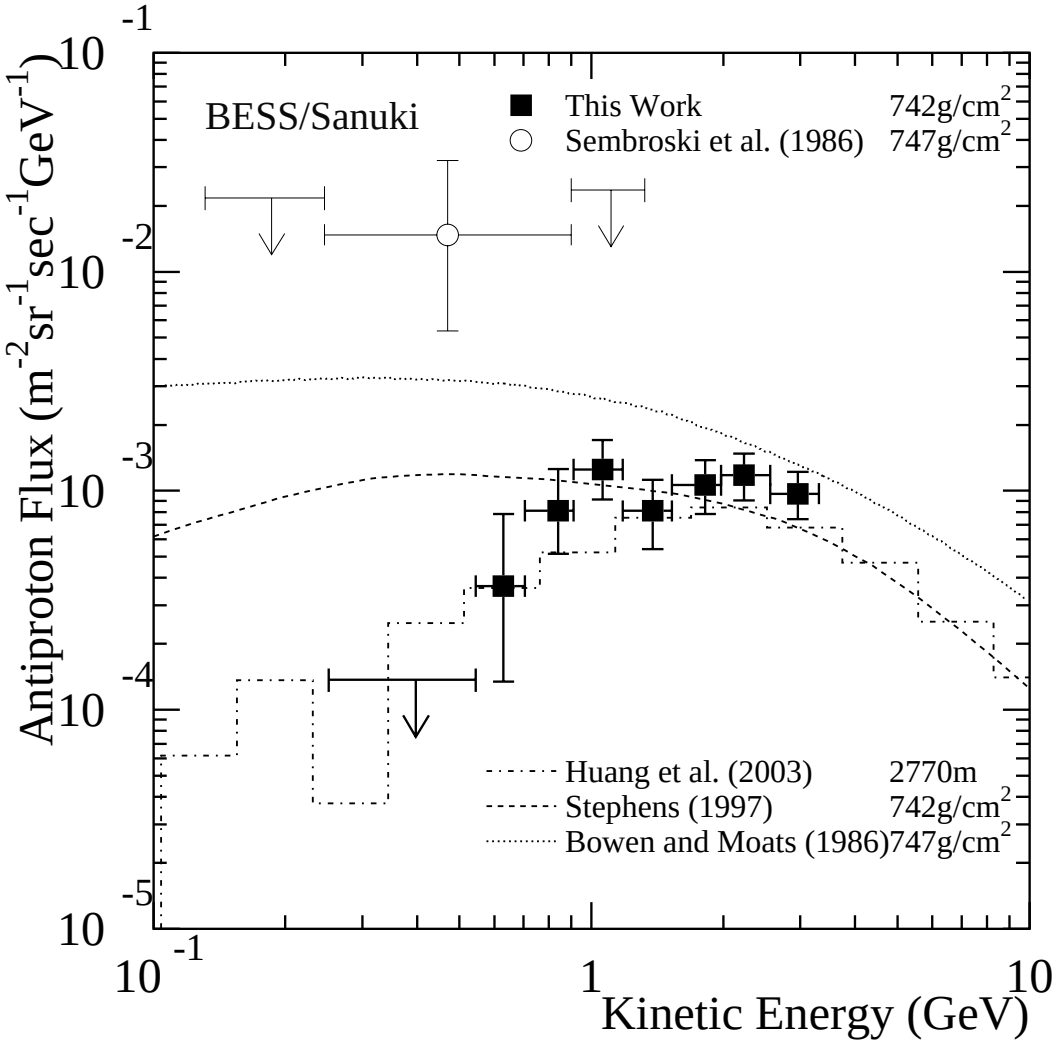

Figure 1.2: The measured atmospheric antiproton flux (filled square) at the mountain altitude [27], and the independent calculations of Stephens (dashed curve) and Huang (dot-dashed curve). The two calculations are good match above 2 GeV. However the difference is clear at the low energy.

1.3 Significance of the analysis of Antiproton Fluxes at any different altitudes

In this thesis, we present the two observations at balloon altitude and at ground level. One was carried out at atmospheric depth of 4 to 26 g/cm^2 in Ft. Sumner, New Mexico, U.S. in 2001. The other was observed in Tsukuba, Japan in 1997 at ground level in Tsukuba, Japan (about 1000 g/cm^2).

From the results of these calculations, the atmospheric antiproton flux increases up to the atmospheric depth of about 100 g/cm^2. Above this altitude, including a typical balloon altitude, antiproton production is major process, because hadronic interaction process of produced antiprotons is very small. Therefore, to confirm the production of antiprotons, an observation at small atmospheric depth using the balloon is better.

While, an observation at the large atmospheric depth is suitable to investigate the interaction model between antiproton and the nuclei. Because interaction mean free path is above 100 g/cm^2, primary cosmic rays interact many times before arriving at the mountain altitude or ground level. Thus the specific feature of each interaction model is amplified by many interaction collisions.

Thus, we studied these subject as following schemes in this thesis. We explain about experimental apparatus and conditions in Chapter 2 and 3 respectively. The procedure of identification of antiproton candidates are described in Chapter 4. To calculate the atmospheric antiproton flux, we estimate various efficiencies, and then show the observed flux in Chapter 5. In the chapter 6, we compare the observed flux with some theoretical calculations.

Chapter 2

Experimental apparatus

2.1 Detector Layout

2.1.1 Detector Configuration

In this thesis, we analyzed the data collected in three experiments. The two experiments were performed in spring and autumn of 1997 on the ground. The another one was performed in summer of 2001. Hereafter we denote **'Exp-12'** for the spring of 1997 experiment, **'Exp-16'** for the autumn of 1997, and **'Exp-34'** for the flight experiment in 2001.

The detector components were arranged concentrically as shown in Figure 2.1 and 2.2. The basic configuration of two detectors is very similar and most of the components were used in common in each experiment. A particle traversing the apparatus passed through, from outside to inside, a plastic scintillator hodoscope (TOF), two layers of outer drift chambers (ODC) (Exp-34 only), a superconducting solenoid (MAG), two layers of inner drift chambers (IDC) before entering a central jet type drift chamber (JET), An aerogel Čerenkov counter (ACC) was placed between the upper TOF hodoscope and the cryostat. In addition, between the lower TOF and the lower ODC, a lead plate and Scintillation fiber hodoscopes (Scifi) were installed for Exp-34. All these detector components were contained in a pressure vessel.

Solenoidal magnets covering a detector system have often been disfavored in previous cosmic ray experiments [28, 29, 30, 31, 32] because of the unavoidable material in the particle passage. However, a thin superconducting solenoid developed at KEK [33, 34, 35, 36] enabled us to adopt this horizontally cylindrical configuration.

The cylindrical configuration, usually used in the high energy collider experiments, has many advantages in the cosmic ray application too. The strong and uniform magnetic field was generated in a large volume inside the solenoid where a large acceptance tracking system was installed. Therefor good momentum resolution was easily obtained while keeping the whole detector size compact. The detector had a wide-open geometry, and the JET could fully "visualize" the incoming tracks or any interactions inside the apparatus. Inelastic interactions accompanied by several secondary tracks can easily be identified (see Figure 2.3). A probability of charge mis-identification due to large angle scattering was

negligibly small.

The uniform magnetic field strength over the large tracking volume assured nearly constant geometrical acceptance for wide energy ranges. the acceptance changed only a few percent from the lowest detectable energy ($\sim$200 MeV) up to $>$ 100 GeV. The detector performance changes little for various hit positions and incident angles too. These characteristics were essentially important for reliable determination of the absolute flux of the cosmic radiation.

We use hereafter a cylindrical coordinate system; r, ϕ and z, and a Cartesian coordinate; x, y and z, where y and z being the vertical axis and the axis of the solenoid, respectively.

2.1.2 Particle Identification

Particle identification in the BESS experiment is basically performed by mass reconstruction according to the relation, $m = ZeR\sqrt{1/\beta^2 - 1}$. The rigidity, momentum per charge ($R \equiv pc/Ze$), is precisely measured by reconstructed particle trajectory. The velocity, β, is derived from the path length and the time-of-flight between the upper and the lower layers of the TOF. The energy deposit in the TOF provides the magnitude of the charge, Z, and additional information on the velocity according to the relation, $\mathrm{d}E/\mathrm{d}x \approx (Ze/\beta)^2 f(\beta)$. The sign of charge is determined by the deflection and the particle direction, up-going or down-going, determined by the TOF. The mass is finally calculated from these measurements.

The separation of muons and electrons from protons is performed by ACC. Protons of energies below Čerenkov threshold are distinguished from the muon and electrons.

2.1.3 Requirements for Balloon

For BESS-2001 the apparatus is to be launched by a balloon, the performance of the detector should sometimes be compromised with the requirements specific to the balloon experiment. Weight and power are the primary issues. Since the lifting capacity of the balloon is limited, heavier weight on board results in a lower altitude to be reached and thicker residual air above the apparatus. The more power requires more batteries, otherwise the flight time becomes short. Most of the electronics on board, including all the CAMAC (Computer Automated Measurement And Control) modules [37], are specially designed for this experiments. The functions of each module is carefully selected and minimized in order to simplify the circuits and to reduce their power consumption while keeping the signal processing speed as possible. Low power consumption also benefits the temperature control of the payload. The local temperature near certain power consuming components increases in the daytime and might reach to the maximum tolerable level. The optimization of heat insulation and ventilation to stabilize the temperature inside the vessel becomes a difficult task for high power dissipation.

Stray magnetic field is another issue. Since a magnet return yoke is too heavy to be loaded in the payload, a dipole magnetic field is maintained around the detector. Any detector components sensitive to the magnetic field should be properly treated. Detailed

descriptions are given in the relevant sections.

As a balloon payload, the apparatus should be robust enough to withstand the impacts of launching, parachute opening and landing. It was estimated that a 10 G acceleration is applied to the detector. The support structure of each detector component was designed so that the 10 G acceleration would not cause fatal damage. As for the suspension system of the superconductor, we have performed mechanical analysis and have confirmed that the operating magnet did not quench during the 10 G impact test.

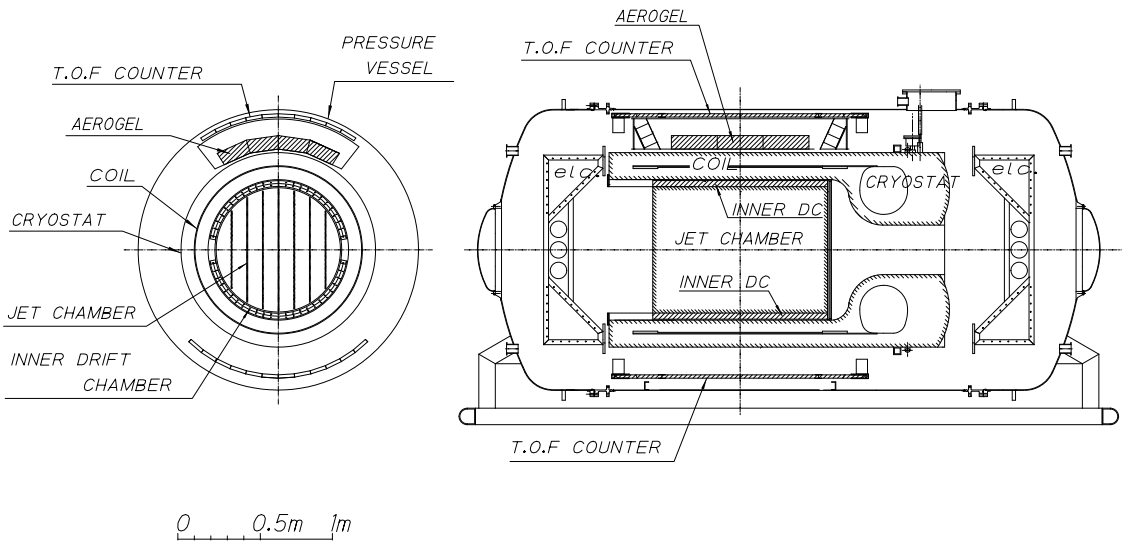

Figure 2.1: Cross section of the BESS detector for Exp-12 and Exp-16.

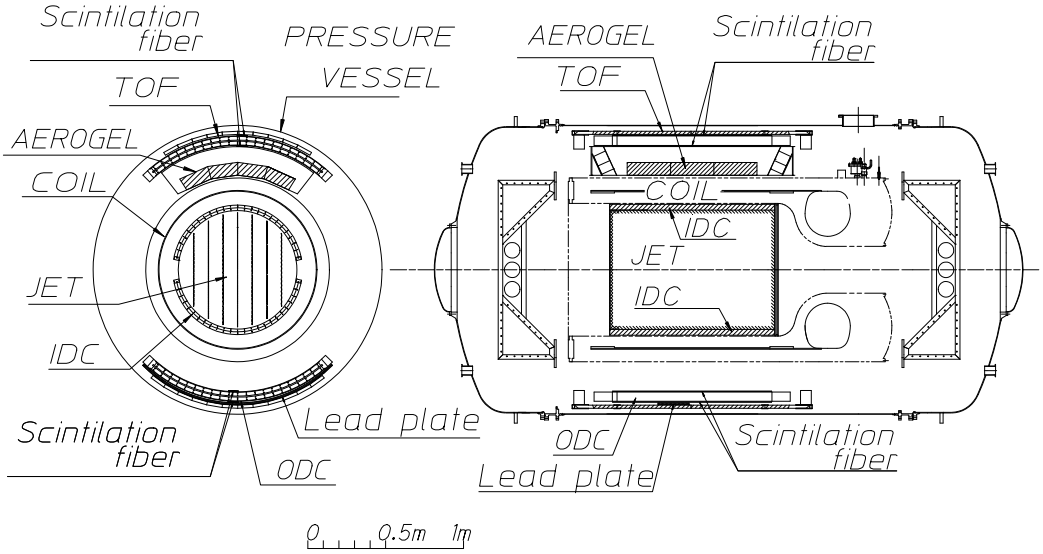

Figure 2.2: Cross section of the BESS detector for Exp-34.

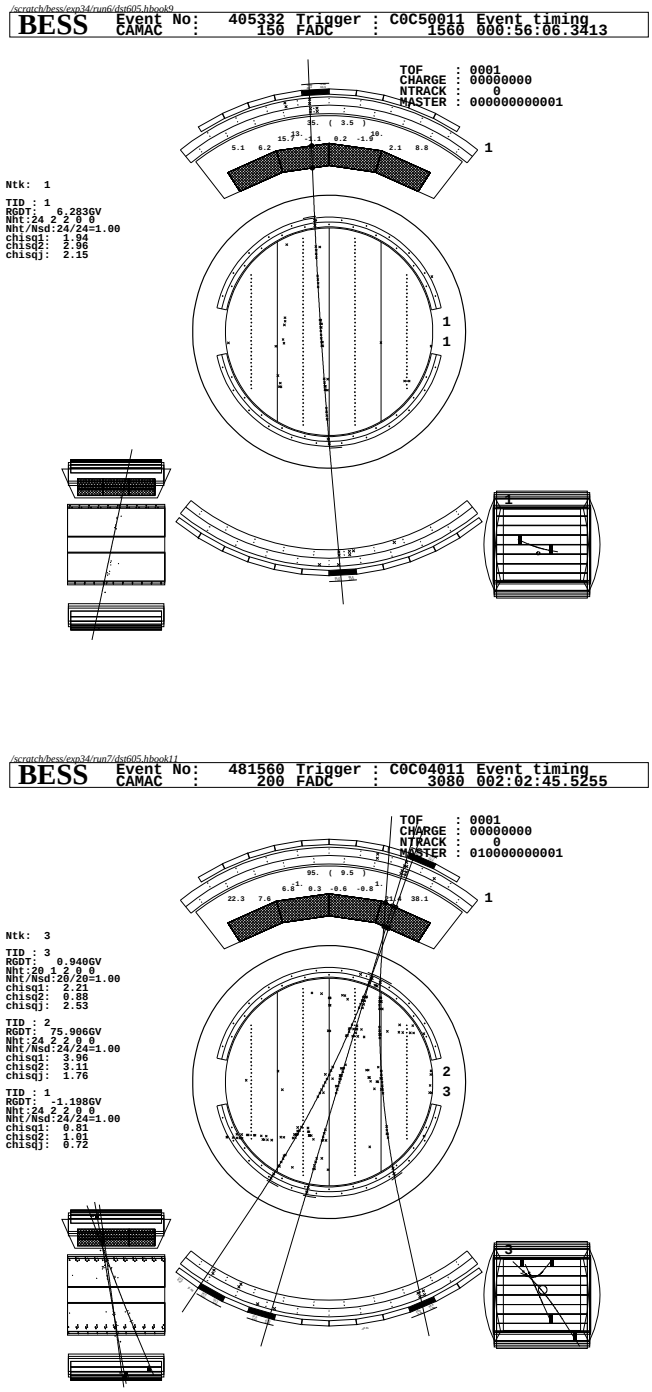

Figure 2.3: Examples of event display: a typical single-track event (top) and three-track event showing the interaction at the coil (bottom).

2.2 Superconducting Solenoid

The superconducting solenoid magnet is the central core component of the magnetic rigidity spectrometer. The magnet was specially designed to provide uniform magnetic field in a large solid-angle acceptance with minimizing incoming particle interaction with the magnet wall material [33, 34].

The superconducting coil was wound with aluminum-stabilized NbTi/Cu superconductor in four layers in the central area and in eight layers in both axial ends for better field uniformity. Figure 2.4 shows the cross section of the solenoid. A central magnetic field of 1.2 Tesla was generated with a field of uniformity of 12 % in the central trackers (JET/IDC) with a wall transparency of 0.2 radiation length [35].

The coil was indirectly cooled by thermal conduction through pure-aluminum strips and the outer support cylinder linked to a liquid helium reservoir located in one end of the solenoid coil. This configuration realized advantages of the minimum wall material in the detector acceptance and also an intrinsic safety protection against a magnet quench with suppressing sudden pressure rising in the reservoir.

The solenoid coil was successfully tested up to a central magnetic field of 1.2 Tesla and was operated at 1 Tesla in the scientific balloon flights [36]. Major parameters of the solenoid magnet are summarized in Table 2.1, and the flux line and the field strength contour are shown in Figure 2.5.

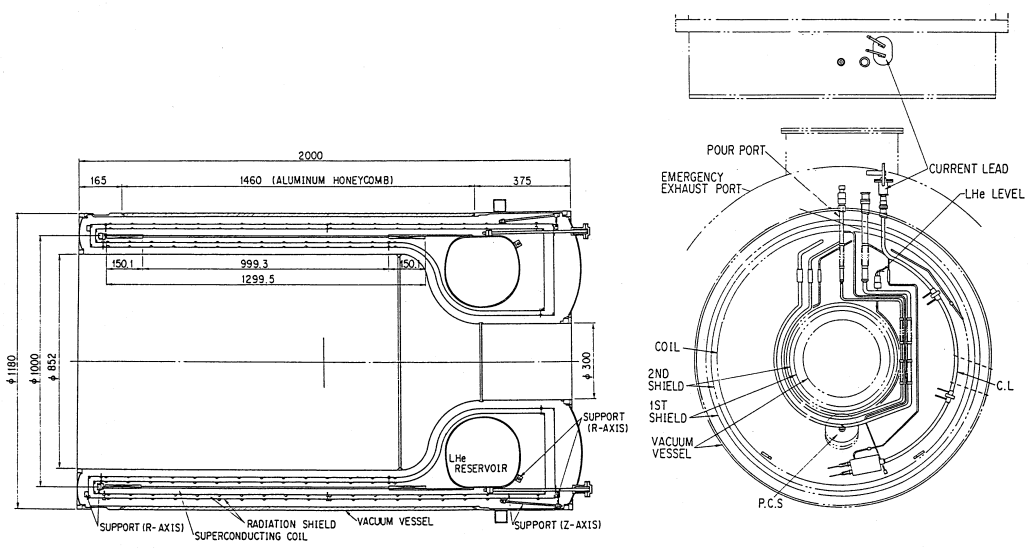

Figure 2.4: Cross section of the superconducting solenoid.

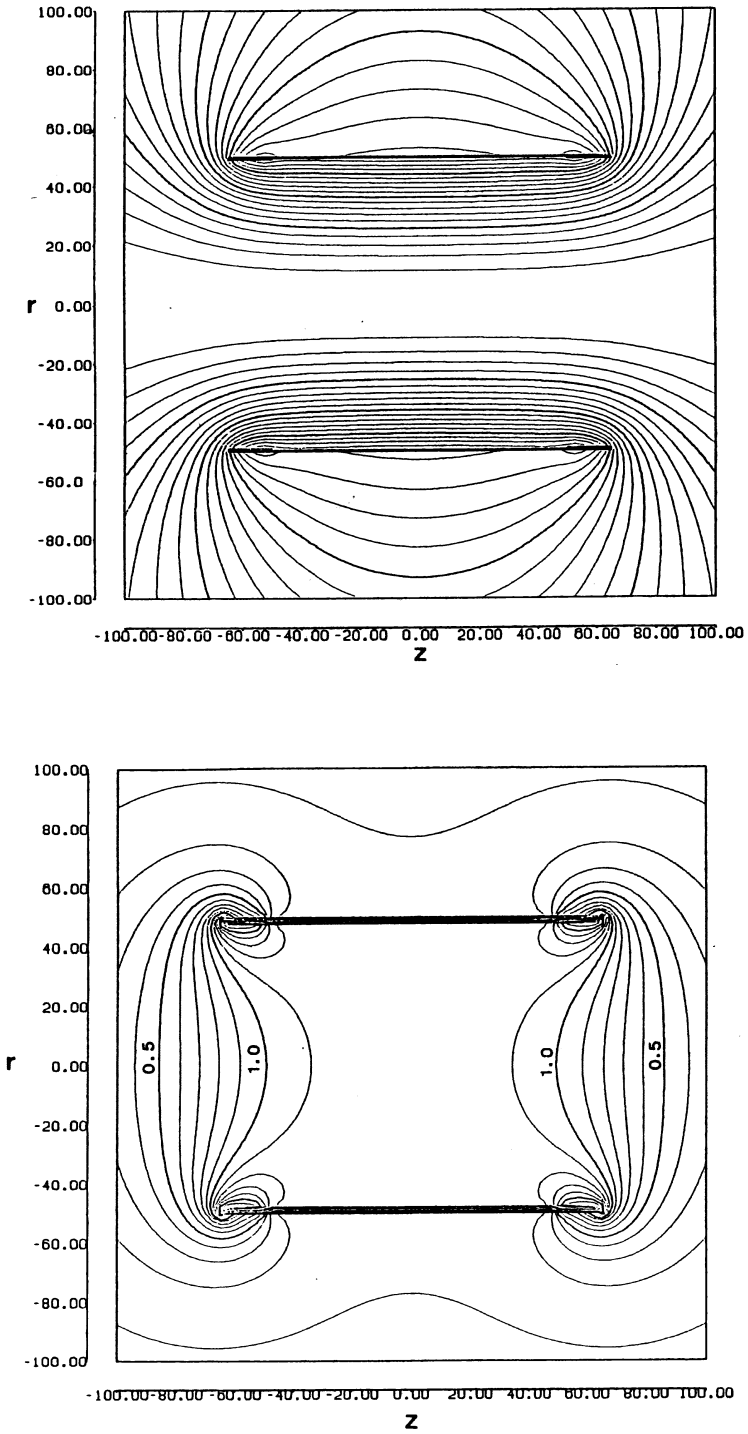

Figure 2.5: Flux line (top) and field strength contour (bottom) of the superconducting solenoid.

Table 2.1: Main parameters of the superconducting solenoidal magnet (MAG).

Dimensions	
Coil diameter	1.0 m
length	1.3 m
coil thickness (center)	5.2 mm
(end notch)	10.4 mm
Cryostat diameter	1.18 m
length	2.0 m
Useful aperture diameter	0.85 m
length	1.0 m
Central field	1.0 T (1.2 T*)
Current	430 A (520 A*)
Stored energy	815kJ
Wall thickness	0.22 X_0 per wall
	4.7 g/cm^2 per wall
Total weight	430 kg
Conductor	Nb/Ti/Cu
Stabilizer	Pure Al (99.999%)

* Tested

2.3 Tracking

2.3.1 JET Chamber

The JET chamber was located inside the warm bore (0.85 m in diameter and 1.34 m in length) of the solenoidal magnet, providing a particle trajectory in $r - \phi$ plane by drift time measurement and in z direction by charge division read-out.

A schematic view of the JET is shown in Figure 2.6, and its parameters are summarized in Table **??**. The sensitive volume of the JET is a cylinder of 1 m in length and 754 mm in diameter. The chamber is subdivided into four sections in vertical by cathode planes in which gold-plated aluminum wires of 200 μm in diameter are stretched at 6.7 mm interval. At the center of each section, there is a signal wire plane in which sense wires (gold-plated tungsten-rhenium alloy, 20 μm in diameter) are equally spaced at 13.4 mm intervals alternated with potential wires (gold-plated aluminum, 200 μm in diameter). Each of the two central (side) sections contains 52 (32) sense wire. In order to resolve left-right ambiguity, the sense wires are staggered by $\pm 500\mu$m from the center plane defined by the potential wires. The maximum drift distance of one section is 95 mm.

The high voltages of the potential and cathode wires are -2.85 kV and -10.80 kV, respectively. The sense wires are kept at ground level. The electric field strength in the drift region is about 0.85 kV/cm, which corresponds to the maximum drift time of 12.3

μs using a gas mixture described below.

Every wire is positioned and fixed by a feed-through, which is stuck in a hole drilled through the end plate. The feed-through has a Derlin bush for positioning, a brass lead for soldering and a Derlin sleeve for electrical insulation. The inner diameter of the bush is 270 μm for potential/cathode wires and 80 μm for sense wires enabling us to achieve a positioning precision better than 50 μm. The wire tensions are adjusted to be half their elastic limits to allow for deformation of the chamber due to temperature variation and acceleration impact.

In order to reduce weight and material, the wall of the cylinder was constructed with a honeycomb plate. It was made of 6 mm thick Aramid core with skins of 125 μm thick copper plated Kapton sheets. The field shaping strips with various widths depending on the azimuth were etched on the inner surface of the cylinder. Resistors connect the neighboring strips with proper resistance to form a uniform drift field.

The end plates were made of 20 mm thick aluminum, rigid enough to support a total wire tension of 1.53 kN. From the weight consideration, may pits of 15 mm depth were scooped out in the end plates. The pits are used to house preamplifier boards. Inside the end plates, G10 boards with copper-etched field shaping patterns were glued to complete the field cage.

The total weight of the JET chamber is about 80 kg. The average material passed by a penetrating particle is 0.48 g/cm^2 including two chamber walls and wires.

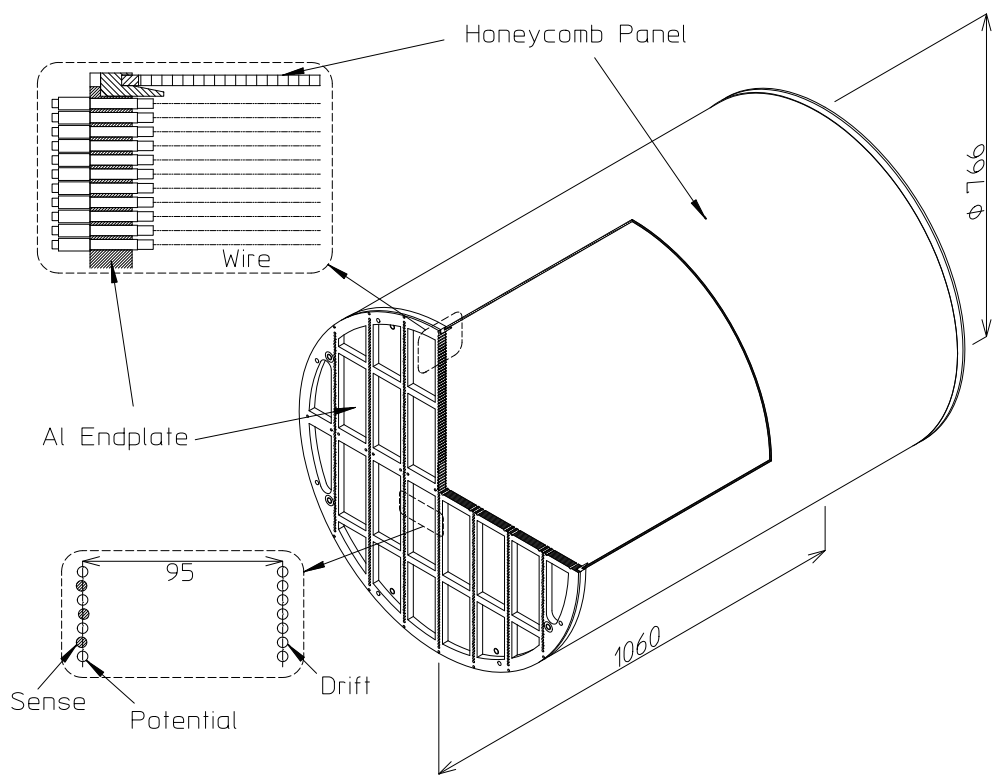

Figure 2.6: Schematic view of the JET chambers.

Table 2.2: Parameters of tracking chambers.

JET	
Shape and Size	Cylindrical, 766 mm$\phi\times$ 1066 mm
Sense wires	W/Re (Au plated), 20 μmϕ, 176 wires
Tension	0.392 N
Wire spacing	13.4 mm
Cathode wires	Al (Au plated), 200 μmϕ, 196 wires
Tension	2.94 N
Wire spacing	6.7 mm
Maximum drift length	95 mm
Spatial resolution	175 μm (x), 2.0 cm (z)
Maximum Detectable Rigidity	220 GV
IDC	
Shape and Size	Arc-shaped, R=384-420 mm,
	$\lvert\phi\rvert < 82.0°$, L = 1060 mm
Sense wire	W/Re (Au plated), 20 μmϕ, 11/12 wires
Tension	0.392 N
Wire spacing	13.0°
Potential wires	Al (Au plated), 200 μmϕ
Tension	3.43 N
Spatial resolution	220 μm (ϕ), 470 μm (z)

2.3.2 Inner Drift Chambers

The IDCs, located just inside the cryostat, provide track hit positions in the z-direction with high precision through diamond-shaped vernier strip readout as well as in the azimuthal direction through drift time measurement. Their cell structure in the azimuthal direction is also used by the second-level trigger for track-pattern recognition making a quick determination of the angular deflection and the sign of charge of incident particles.

The IDCs are arc-shaped drift chambers with identical double layer structure except for their dimensions. A schematic view of them is shown in Figure 2.7 and main parameters are summarized in Table 2.2.

Each chamber is composed of four Aramid-core honeycomb panels with G10-plastic end and side plates. The skins of the honeycomb panels, copper-plated Kaptons sheets, electrically isolate the two layers. The sensitive volume of each layer is 12 mm thick and is divided into cells by alternately stretched sense and potential wires. The wires are fixed by the same feed-throughs as used in the JET at an interval of 6.50° in azimuth for the IDC, corresponding to a half-cell size of about 50 mm. The wire position in one layer is shifted by a half-cell pitch with respect to the other layer. By adopting this double layer configuration, the left-right ambiguity can be automatically resolved and quick hit cell information is available by making a coincidence of the two overlapping cells.

Field shaping strips of 1.5 mm in width are etched on the inner surface of the copper-

plated Kapton sheet at a 3 mm interval. The strip pattern on opposite side of the IDC layer is slightly shifted so that the direction of the electric field is tilted by 5.5° with respect tot the drift (azimuthal) direction in order to compensate for the Lorentz angle arising from the magnetic field of 1 Tesla.

Vernier-cathode-strip pairs of 7.5 mm width are etched on both sides of the sense wires. As shown in Figure 2.8, each pair consists of a diamond-shaped inner strip and an outer strip with complementary shape. A cycle length of the pattern is 100 mm for the IDC. The strip patterns on opposite sides are shifted by a quarter pitch along the z-direction to give a precise hit coordinate. There are four strips in total associated to a single sense wire, which are read out separately.

In order to set a potential of vernier strips at ground level, the high voltage applied to the sense wires is +2.68 kV and the high voltage to the potential wires is -4.06 kV for the IDC. The average electric field in the drift region is 0.8 kV/cm.

Since the chamber structure is fragile against over-/under-pressure, a 0.5 mm thick aluminum plate is glued to the outer surface of the chamber for mechanical reinforcement.

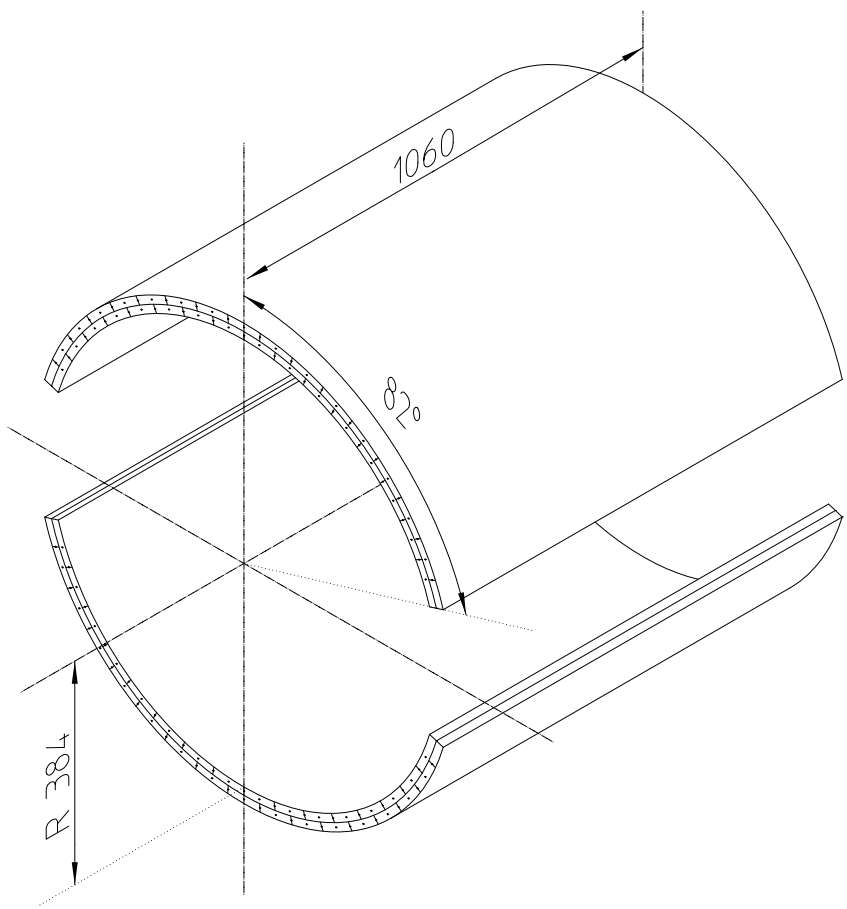

Figure 2.7: Schematic view of IDC.

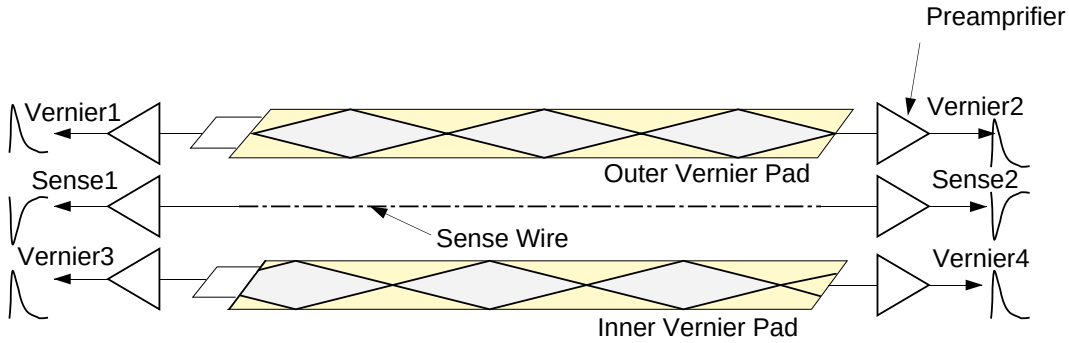

Figure 2.8: Read-out scheme for IDC signal.

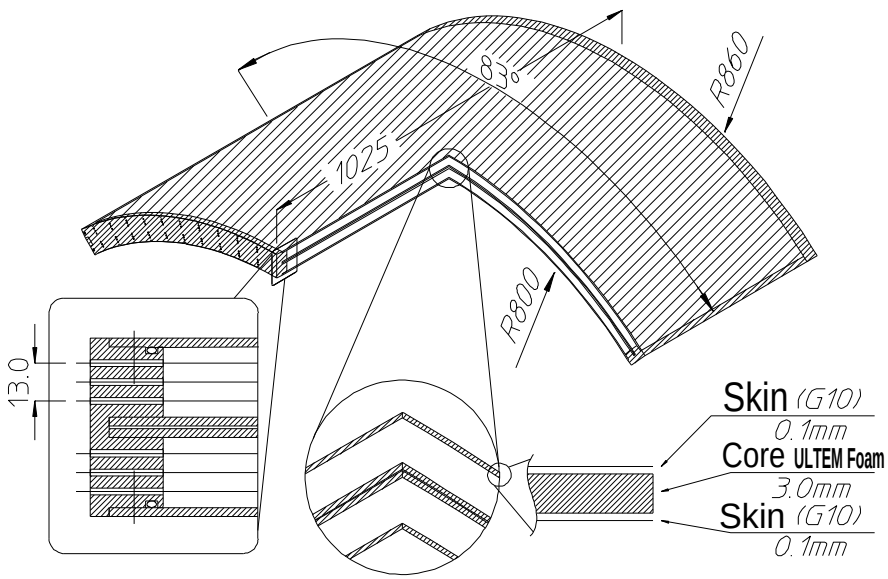

Figure 2.9: Schematic view of ODC.

2.3.3 Outer Drift Chambers and Scintillation Fiber

The ODCs were cell-type arc-shaped drift chamber as same as IDCs and installed between TOF and the solenoid. Each ODC consists of two layers in a radial direction. In each layer, two sense wires are stretched at the center of each cell. One ODC provided four hit points along the track. Spatial resolution of each hits is 150 μm in the $r - \phi$ direction.

In order to carry out real-time calibration of the ODCs during flight, a scintillation fiber detector covers outer and inner surface of one cell of the ODC.

Using these ODCs and scintillation fibers track length became almost doubled from JET/IDC's track length, and we can measure more higher energy particle. But in this analysis, we did not use these ODCs.

2.3.4 Chamber Gas

The JET, the IDCs and the ODCs are filled with the same gas mixture of CO_2 90 % and Ar 10 %, called "slow gas". The drift velocity at 1 atm and with an electric field of 1 kV/cm is about 8.1 mm/mus. Owing to its slow drift velocity and small longitudinal diffusion of drift electrons, good spatial resolution and good double-track separation can be achieved by using reasonably low power and moderate speed readout electronics, at the expense of delicate control of high voltages and pressure of the gas.

The pressure vessel is also filled with the same chamber gas. Thus any chamber suffering a small leak would still be operational during flight. The valves at the inputs and the outputs of the chambers are closed just before launching, and the chambers are operated without gas circulation during a one-day flight.

2.3.5 High Voltages

High voltage power supplies are compact DC-DC converter modules. The high voltages are applied to the chambers through low-pass filters. The output voltage is adjusted by an external resistor and switched on/off by a command issued from the ground station. The ramping profile of the output voltage is internally controlled so that it takes fifty seconds before reaching the nominal value. The output voltage and current are monitored by the monitor system. A small iron cylinder inside the module shields magnetic components.

2.3.6 Readout Electronics

- **Preamplifiers**

  The signals from the sense wires of all the chambers and the vernier strips of the IDC are fed to the same type of preamplifiers (Fujitsu MB43458), which can cope with both polarities, negative signals from the wires and positive signals from strips. The preamplifier chip is monolithic IC with four equivalent amplifier circuits with a gain of 7 mV/μA and 96 Ω input impedance [38]. Typical pulse height of the preamplifier output is 10 mV while the noise level remains below 0.2 mV.

  The preamplifier boards for JET have four or three amplifier chips (16 or 12 channels/board). They are individually buried in pit of the aluminum end plates covered with aluminum plates for noise shielding. Because of the high power consumption of the digitizing electronics, all the wires of the JET could not be read out. The number of channels was compromised considering a required momentum resolution and the total power consumption. In each of the two central (side) sections, 24 (16) sense wires out of 52 (32) are read out. And the signals of 16 (8) sense wires out of 24 (16) are read at both ends for charge division. Up to 24 points in $r - \phi$ and in z are sampled for an incident charged particle penetrating the central region of the JET.

  The preamplifier boards for the IDCs have a single chip. They are attached to the end plates of the chambers and are housed in copper shield cage. The IDCs are read out from a single end of each sense wire and four strips.

- **FADC**

  The output of preamplifiers of the JET wires and the IDC vernier strips were fed to flash analog-to-digital converter (FADC) modules. The FADC module has 16 input channels. 23 modules (368 channels in total) were housed in two EUROCARD industry standard crates. The 128 channels were used for JET Chamber readout, the 176 channels for IDC vernier strips and the remaining 64 channels for ODC readout.

  The FADC system was developed to meet the requirements of this experiment, low power consumption and fast data compression [39]. The input signal to the FADC module is further amplified by main-amplifier with a gain of 10 (40) for the JET (IDC). It is digitized by a FADC (HITACHI HA19211BMP) with 8-bit resolution at a rate of 28.5 Msps for a duration of 18 μs (512 samples in total). A digital comparator then compares the digitized data with a preset value and only data above the threshold are written in a FIFO memory. This zero suppression process is executed synchronously with the digitization on each FADC channel without costing any extra time. Then a data compressor module in the FADC crate further compresses a sequence of the non-zero data train into a small number of useful information; the channel number, the total charge of the pulse, the timing of the signal arrival, the pulse width and the first two raw data of the pulse. Thus the data volume was reduced by a factor of 3 in average. For a typical single track event, the data compression process took less than 200 μs.

- **Amplifier/Discriminator**

  The sense wire signals from the IDCs are further amplified and discriminated by amplifier/discriminator (A/D) modules. The discriminated sense wire signals from the A/D modules are used to issue a second level trigger. A detailed discussion on the trigger process is made in Section **??**.

2.3.7 Performance

The transverse and total rigidity of a particle is determined by fitting the three-dimensional hit positions measured by the drift chambers. Energy loss in the chamber gas is also measured using the charge information of the JET. To obtain hit positions in $r - \phi$ plane, the drift velocity was calibrated using the obtained data. Although the drift length is approximately proportional to the drift time, some nonlinear effects exist due to distortion of the electric field. This no-linearity was corrected by fitting the x-t relation with a third-order polynomial function.

- **Position Measurement**

  The JET and the IDCs determine the rigidity of a track. First, good hits, defined as hits with enough charge and pulse width, are selected. They are connected to form a candidate trajectory. The transverse rigidity, R_T, is then calculated by applying a circular fitting to those hits associated to the track. This procedure is iterated adding new hits close to the track and dropping deviant hits. The resultant R_T

is hen corrected for the non-uniformity of the magnetic field. From a Monte Carlo simulation for various trajectories in the exactly calculated magnetic field, correction factors to the rigidities were derived as a function of track position, inclination, and rigidity. The correction factors reproduce the original rigidities within a typical accuracy of ± 0.2 % for tracks within a fiducial volume, the central sections plus the inner half of the side sections of the JET.

To determine the total rigidity, R, we obtain a dip angle, θ_{dip}, which is defined as an angle between the total rigidity vector and $r-\phi$ plane. A sinusoidal fitting in $r-z$ plane is applied to the selected hits in the JET and the IDCs iteratively, as in the $r-\phi$ fitting, to eliminate irrelevant hits. All possible combinations of IDC hits are examined, since the IDCs provide only the z-positions within a vernier strip pattern cycle of 100 mm. The resultant θ_{dip} is the one obtained from the combination which gives the minimum χ^2 value. The total rigidity R are derived from R_T and θ_{dip} as $R = R_T/\cos\theta_{dip}$.

Based on the residual distributions shown in Figure 2.12, the overall spatial resolutions of the JET and the IDCs in $r-\phi$ plane are respectively estimated to be 175 μm and 187 μm. Figure 2.11 of the spatial resolution.

The errors of the rigidity measurement were estimated for each track in the $r-\phi$ fitting process. Figure **??** shows the estimated errors of $1/R_T$. The open dashed and shaded histograms correspond to proton samples with trajectory satisfying $N_{expect} \geq 16$, $N_{expect} \geq 20$, and $N_{expect \geq 24}$, respectively. Note that requirement of the larger N_{expect} means requirement of the longer track. Both histograms have a clear peak around $\Delta(1/R_T) \sim 0.0045$, which indicates the maximum detectable rigidity (MDR) is about 220 GV in this BESS detector.

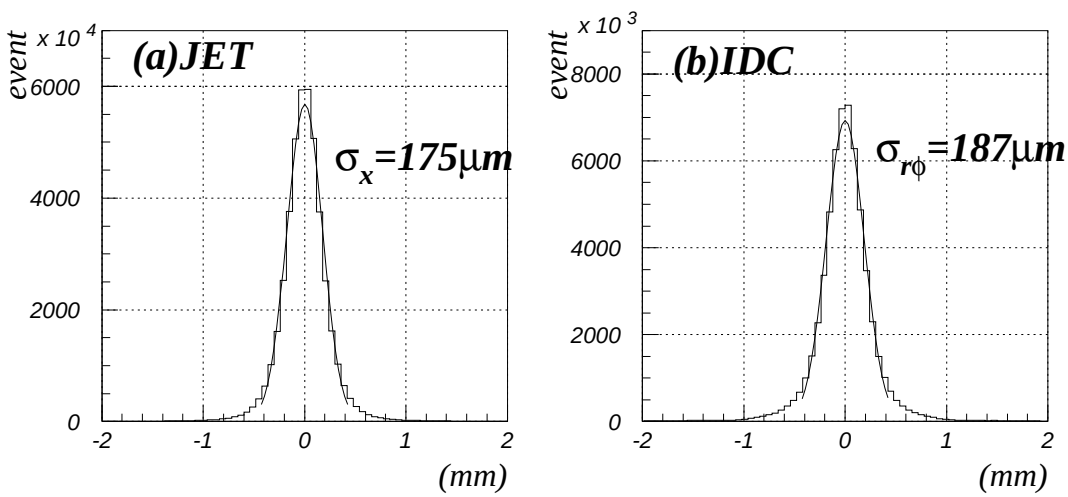

Figure 2.10: Fitting residuals for JET and IDC in r-ϕ plane

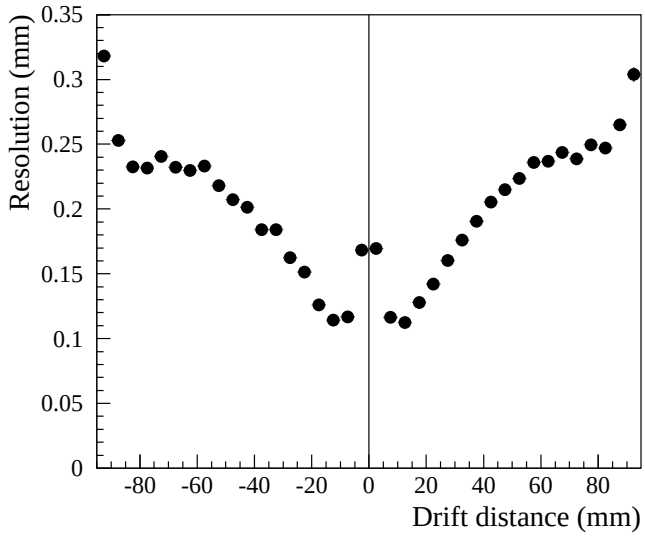

Figure 2.11: JET chamber r-ϕ resolution as a function of the drift distance.

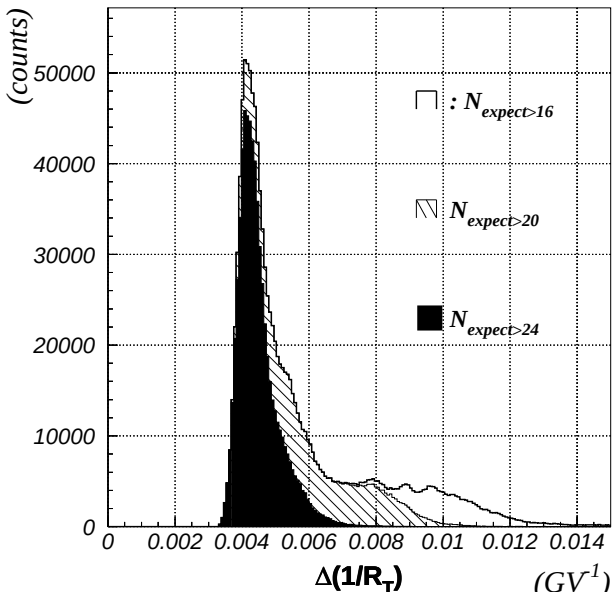

Figure 2.12: Distribution of error in inverse of transverse rigidity in the flight. Open, dashed, and hatched histograms represent $N_{expect} \geq 16$, $N_{expect} \geq 20$, and $N_{expect} = 24$, respectively.

- **z-Position Measurement**

  The z-coordinate of a hit position is obtained by using the charge division of the JET, and the vernier strip readout for the IDCs.

  First we roughly determine hit positions along the sense wires of the JET by the charge division method. The z-coordinate of a hit position is derived from the charges read out at both ends of the hit wire (Q_a and Q_b). Hit position (z) is given by

$$\frac{z}{L} = \frac{(R+r)\,Q_b - rQ_a}{R\,(Q_a + Q_b)}$$

  where L and R are the length and the resistivity of the sense wire and r is the input impedance of the preamplifier. We obtained the z-position resolutions of 11.6 mm for single-charged particles (Figure 2.13), by the JET, which are precise enough to identify the particular vernier strip cycle of the IDCs hit by a track.

  After the coarse determination of the z-coordinate, we use the vernier strips of the IDCs to get the z-coordinate precisely. The hit position along the z-axis is measured using the signal charges induced on the associated vernier-strip pairs. We define a normalized charge ratio, ε, for a pair of vernier-strips, A and B.

$$\varepsilon_{I(O)} = \frac{Q_{AI(O)} - Q_{BI(O)}}{Q_{AI(O)} + Q_{BI(O)}}$$

  where $Q_{AI(O)}$ and $Q_{BI(O)}$ denote the charges induced on A and B of the inner vernier-pad pair (outer vernier-pad pair). The ε parameters are linearly related to the z-axis position of the avalanche point. Figure 2.14 shows a scatter plot of ε_I vs ε_O for the IDC vernier strips. A circuit along the round-square locus corresponds to a vernier-strip pattern cycle of 100 mm along the z-axis. We can deriver the z-coordinate of a hit position by comparing a measured ε pair with the numerically calculated values. The deviations of the measured ε values from the calculated line are translated to the z-position resolution, giving the resolution of 422 μm by the IDC vernier strips as shown in Figure 2.13. The performance of the tracking system is summarized in Table 2.2.

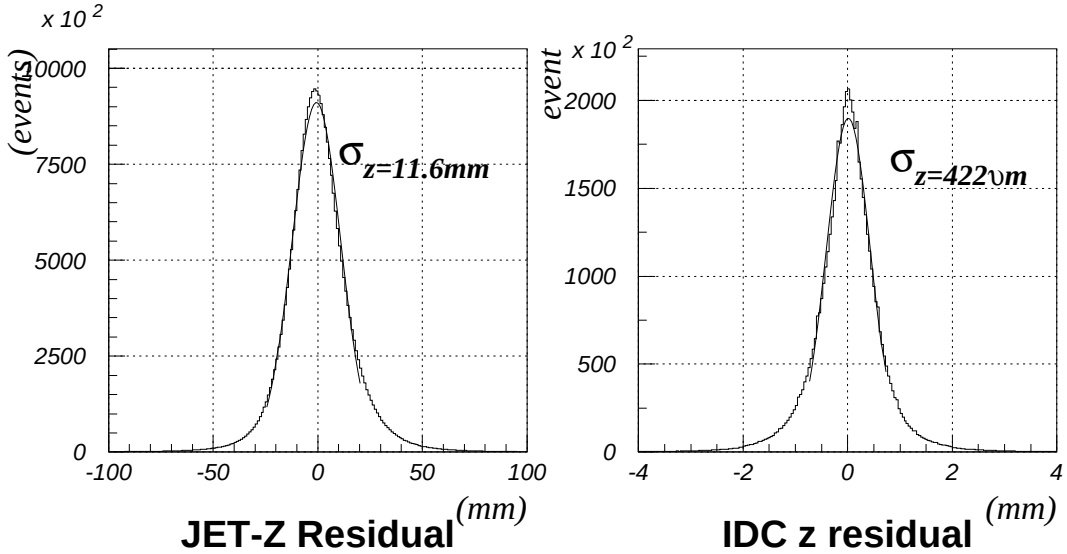

Figure 2.13: Residual distribution of the IDC along the z-coordinate.

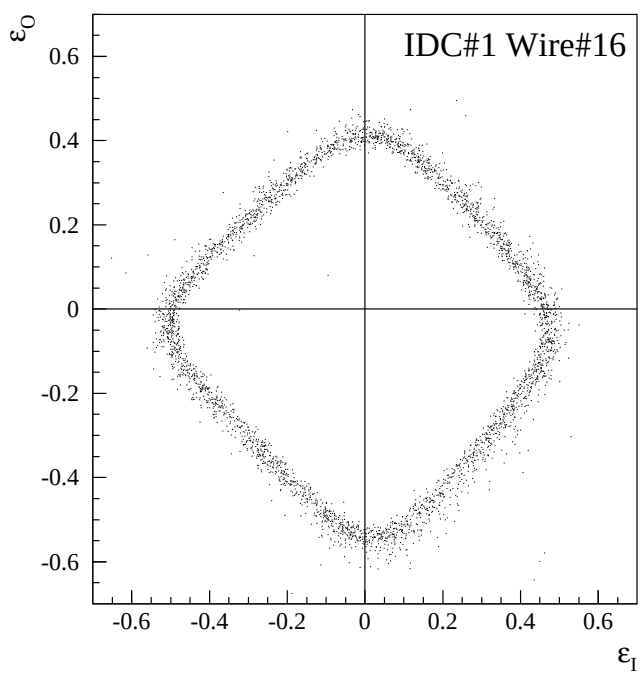

Figure 2.14: Scatter plot of the ε parameter of the inner (ε_I) and outer (ε_O) pad.

2.4 Time-of-Flight

2.4.1 TOF Hodoscopes

The TOF hodoscopes consist of ten upper- and twelve lower- plastic scintillation counter paddles (950 × 100 × 20 mm, BICRON BC-404). A light-guide (Figure 2.15) made of UV-transparent acryl plate (Mitsubishi Rayon) is affixed to the scintillator with optical epoxy (BICRON BC-600), connecting each end of a counter to a 2.5 inch Fine-Mesh magnetic field resistant photomultiplier tube (PMT), i.e., a Hamamatsu R6504S assembly type. To minimize the loss of photo-electrons in the PMT caused by the magnetic field, PMTs are placed tangential to the acryl plate such that the angle between their axis and magnetic field lines is less than 16°. Ends with attached light-guide are fit into circular holes in an aluminum plate, and four springs (Figure 2.15) are used to prevent separation from a light-guide. A 1 mm thick silicon pad (Shin-Etsu OF113) lies between the light-guide and PMT to minimize shock and vibration during shipping, launching, and parachute landing. Connection points on both sides of the pad are coated with optical grease (Shin-Etsu optseal, refractive index $n = 1.47$).

To determine the most suitable light-guide shape regarding timing resolution and effective [39, 41] nubmer of photoelectrons (N_{pe}), we inverstingated various fish-tail-shaped light-guides using a simulation code (GUIDE7 [42]) in conjunction with cosmic-ray and beam test data, which ultimately allowed us to optimize the angle and shape of the planes. Briefly, after selecting three shapes based on simulation results and cosmic-ray data, the best was determined using the results of beam tests.

The 2.5 inch Fine-Mesh PMT has the bialkali (Sb-Rb-Cs, Sb-K-Cs) photocathode of which the effective diameter is typically 52 mm resulting to 2.01 times as large compared to that of the corresponding 2 inch. one used in the '95 flight. It exhibits a wide sensitivity for wavelengths ranging from 300 to 650 nm, while also well matching the scintillator light spectrum which has its maximum emission at 480nm. The Fine-Mesh PMT has 19 dynodes situated about 0.8 mm apart. Electrons are accelerated by parallel electric fields between the dynodes; hence allowing the device to be used in a magnetic field if the direction of the magnetic field is parallel to the PMTs longitudinal axis. The signal from the anode provides timing information and that of the 19th dynode is used as a first-level trigger. Signals from 13th and 18th dynodes are used to obtain the energy loss ($\mathrm{d}E/\mathrm{d}x$) of incident particles. The signal from the former dynode is used for highly charged particles.

2.4.2 Electronics and Signal Processing

The output signals from the counters were used for three different purposes; timing measurement, charge measurement and first-level trigger generation. To avoid the interference in the electronics with each other, three signals extracted from the anode, 18th and 19th dynodes were utilized for the above purpose, respectively.

The anode signals were used to issue STOP pulses for timing measurements, because they have the highest pulses suitable for the discrimination. The leading-edge type discriminator was implemented in a 16 channel single-width CAMAC module developed for this experiment, being composed of ECL comparators and differential drivers for output

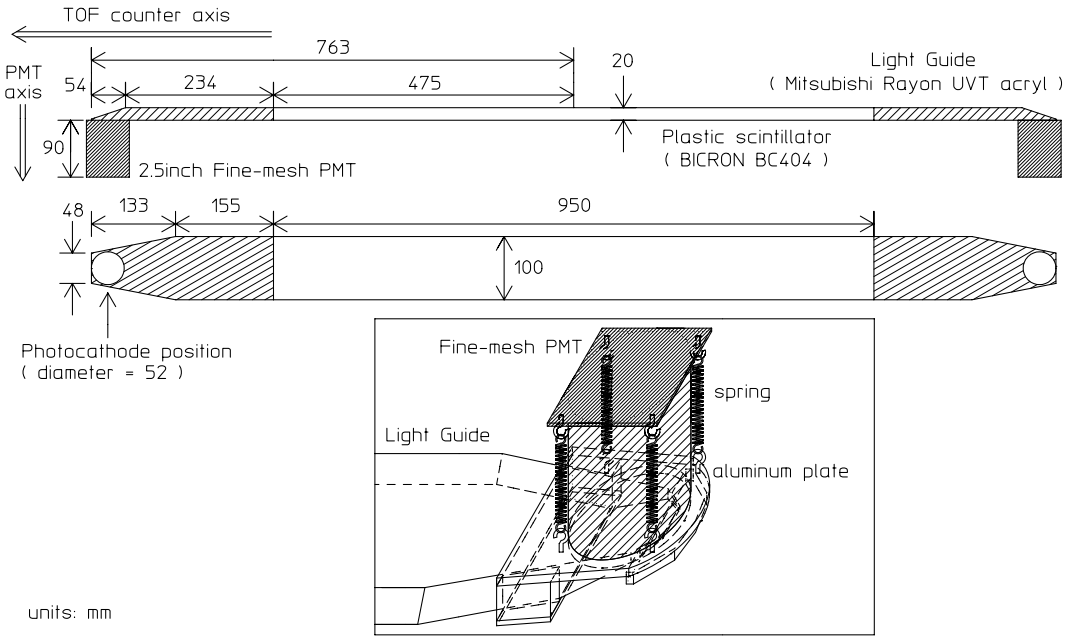

Figure 2.15: Overview of a TOF counter.

STOP pulses. Threshold levels were set to 15 mV, that are about 1/60 compared to the anode pulse-heights of minimum ionizing particles (MIPs). Pulses from the discriminators are fed into CAMAC TDC module [43], which has 12 bit resolution with the conversion gain of 25 ps/count.

Every 18th dynode signal is distributed, after converted its polarity by a pulse-transformer (with a low permeability material core) and delayed by a air-core delay-line, to the CAMAC ADC module [44] for charge measurement during a common gate of 250 ns.

The 19th dynode signals were used to generate the first-level trigger, from which START pulse was issued for digitization. Concerning the trigger process, details are discussed in Section **??**.

2.4.3 Principle of timing measurement

We discuss here on the crossing time of a particle and time-of-flight, i.e., its difference between upper and lower layers of TOF counters of the BESS spectrometer including the details of their deriving processes. In the following discussion, we assign the numbers 1 and 2 to the test counter PMTs.

PMT signals have the time jitter associated with pulse heights, so called 'time-walk' effect [45, 46]. Therefor the measured TDC time must be corrected for the time-walk effect (the time-walk correction). The time-walk corrected timing for PMT i, t_{ic} is expressed as,

$$t_{ic} = t_i - W_i/\sqrt{q_i} \tag{2.1}$$

where t_i, q_i and W_i are respectively the measured TDC time, the measured charge of the PMT signal, and a correction parameter fitted from data.

Using the time-walk corrected timings for each PMT, we then define the crossing time based on the hit position and the timing information. The hit position of the counter is defined using z coordinate along the counter's longitudinal direction as shown in Figure 2.16 where the counter center is defined as $z = 0$. The crossing time of a particle in this paper is the timing based on the reference timing, T_{ref} which is subtracted as the offset timing and determined by the TDC common start. We define the crossing time for PMT1,2 of a counter, $T_1(z)$ and $T_2(z)$ to be

$$T_1(z) = t_{1c} - (L/2 - z)/V_{eff} - T_{ref} \tag{2.2}$$

$$T_2(z) = t_{2c} - (L/2 - z)/V_{eff} - T_{ref} \tag{2.3}$$

where t_{1c}, t_{2c}, and T_{ref} are respectively the time-walk corrected timings, reference timings; while z is the hit position of the counter, L the length of the counter including light-guides, and V_{eff} the effective velocity of light in the scintillator. The measured rms of $T_1(z)$ and $T_2(z)$ are denoted as σ_1, σ_2, respectively. We use $1/\sigma_1^2$ and $1/\sigma_2^2$ as the weight of the combination of $T_1(z)$ and $T_2(z)$, respectively, for crossing time measurements.

We then construct the weighted average [**?**] of crossing time measurements, $T_{w.a.}(z)$ as follows:

$$T_{w.a} \equiv \frac{T_1(z)/\sigma_1^2 + T_2(z)/\sigma_2^2}{1/\sigma_1^2 + 1/\sigma_2^2} \tag{2.4}$$

For upper and lower TOF counters of the BESS spectrometer, the crossing times are calculated as combined timing of two PMTs of a TOF counter by using Eq.(2.4) together with z-position. The TOF of the BESS spectrometer obtained from the data for TOF counter PMTs, T_{tof}, is expressed as,

$$T_{tof} = T_L - T_U \tag{2.5}$$

where T_U and T_L are weighted averages (Eq.(2.4)) of the upper and lower layers of TOF counters, respectively.

2.4.4 Performance of TOF System

TOF data were analyzed with incident angle correction of the ADC counts using scintillator path length, time-walk correction, and correction of timing z-dependence. Figure **??**(a) shows the TOF resolutions (ΔT) during the flight. TOF counters have a time resolution of 84.1 ps. The ΔT is the difference between the TOFobtained from the data of TOF PMTs, T_{tof} (Eq.(2.5)), and the TOF expected from the tracking information, T_{trk}, i.e.,

$$\Delta T = T_{tof} - T_{trk} \tag{2.6}$$

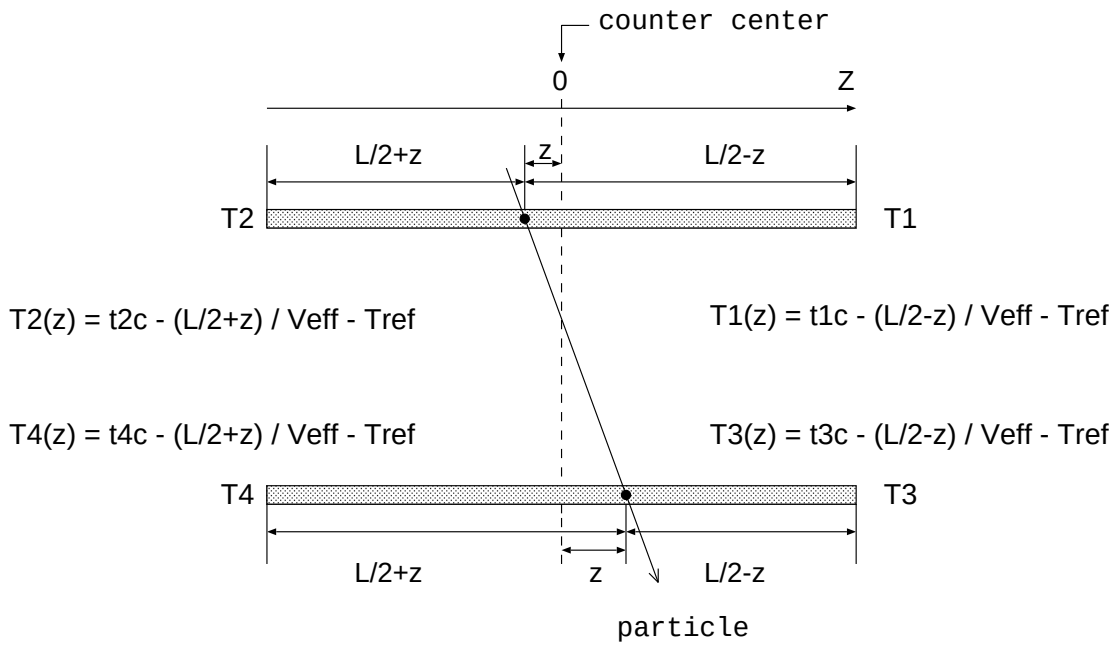

Figure 2.16: The definition of z coordinate and crossing time.

$$T_{trk} = \frac{L}{c}\beta_{trk}(R,m) = \frac{L}{c}\frac{p}{E} = \frac{L}{c}\sqrt{(ZR)^2/((ZR)^2+m^2)} \tag{2.7}$$

where L is the path length of the incidenta particles from upper to lower layer, Z the electric charge of the incident particles, R the rigidity of the incident particles, and c the velocity of light. Due to the error in R being small, the error in T_{trk} (Eq.(2.7)) is also small and the rms of ΔT represents the resolution of the TOF hodoscopes.

Figure 2.17(b) shows the $\Delta 1/\beta$ distribution during the flight by utilizing high-energy proton samples ($R > 5$ GV), the $\Delta 1/\beta$ is defined by:

$$\Delta 1/\beta = 1/\beta - 1/\beta_R$$

$$1/\beta_R = \sqrt{(M_p/R)^2 + 1}$$

where M_p denotes the proton mass, and $1/beta_R$ is the inverse velocity of protons with the rigidity of R. The $1/beta$ resolution ($\sigma_{1/\beta}$) is obtained to be 0.014 from the one sigma deviation of Gaussian fit to the distributions. From the $1/\beta$ resolution, 1, 3, and 5 σ separation of protons from e/μ particles correspond to rigidities of 5.3, 3.1, and 2.3 GV, which correspond to kinetic energies of 4.5, 2.3, and 1.6 GeV, respectively.

Figure 2.19 shows $\Delta 1/\beta$ distribution for various rigidities, i.e., 0.5-0.6, 0.7-0.8, 0.9-1.0, 2.4-2.5, and 4.9-5.0 GV from top to bottom. The center of the distribution is getting far from zero as the rigidity decreases, which was caused by following reasons. After an incident particle left a trajectory in JET chamber and IDCs, it lost energy in the lower part of thedetector and changed its velocity, and then reached the lower scintillation counters. Therefore, the measured TOF (i.e. β^{-1}) had larger value than that expected from the

measured rigidity. For lower energy particles, this effect on $\Delta 1/\beta$ was significant because of larger $\mathrm{d}E/\mathrm{d}x$. Figure 2.18 shows the β^{-1} resolution $\sigma_{1/\beta}$ as a function of rigidity.

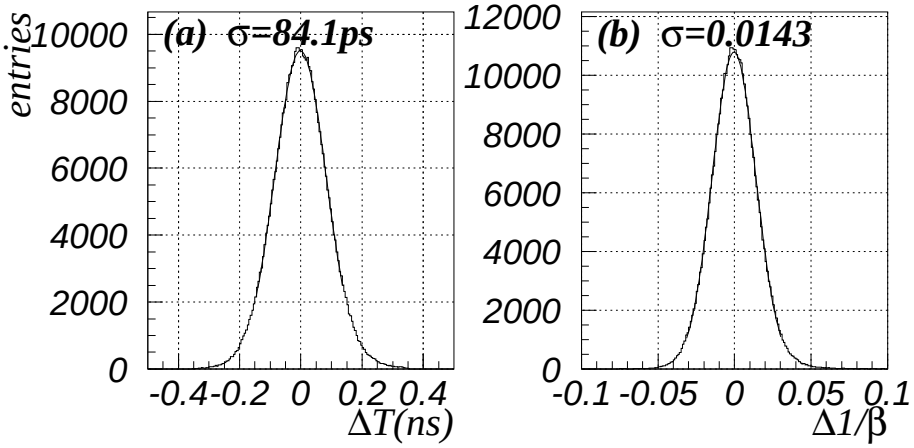

Figure 2.17: TOF performance. (a) ΔT distribution. (b) $\Delta 1/\beta$ distribution. Note that the distributions are obtained by using high-energy proton sample ($R > 5GV$).

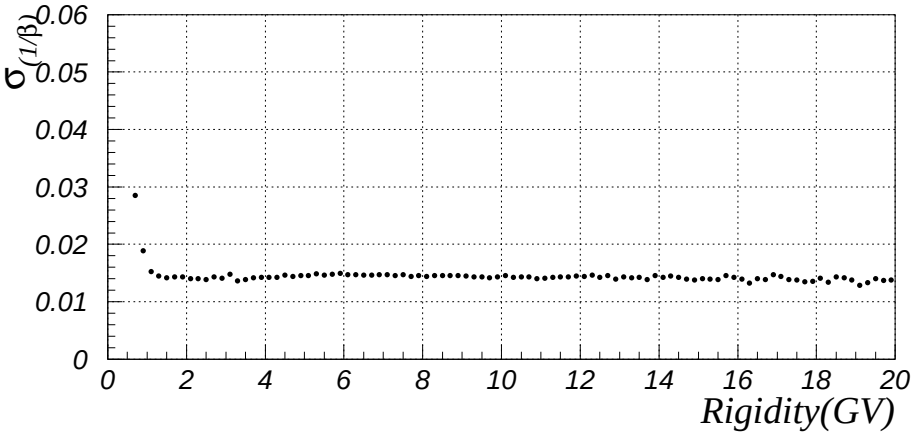

Figure 2.18: Resolution of β^{-1} distribution as a function of rigidity. Corresponding errors in each data point are too small to see in the plots.

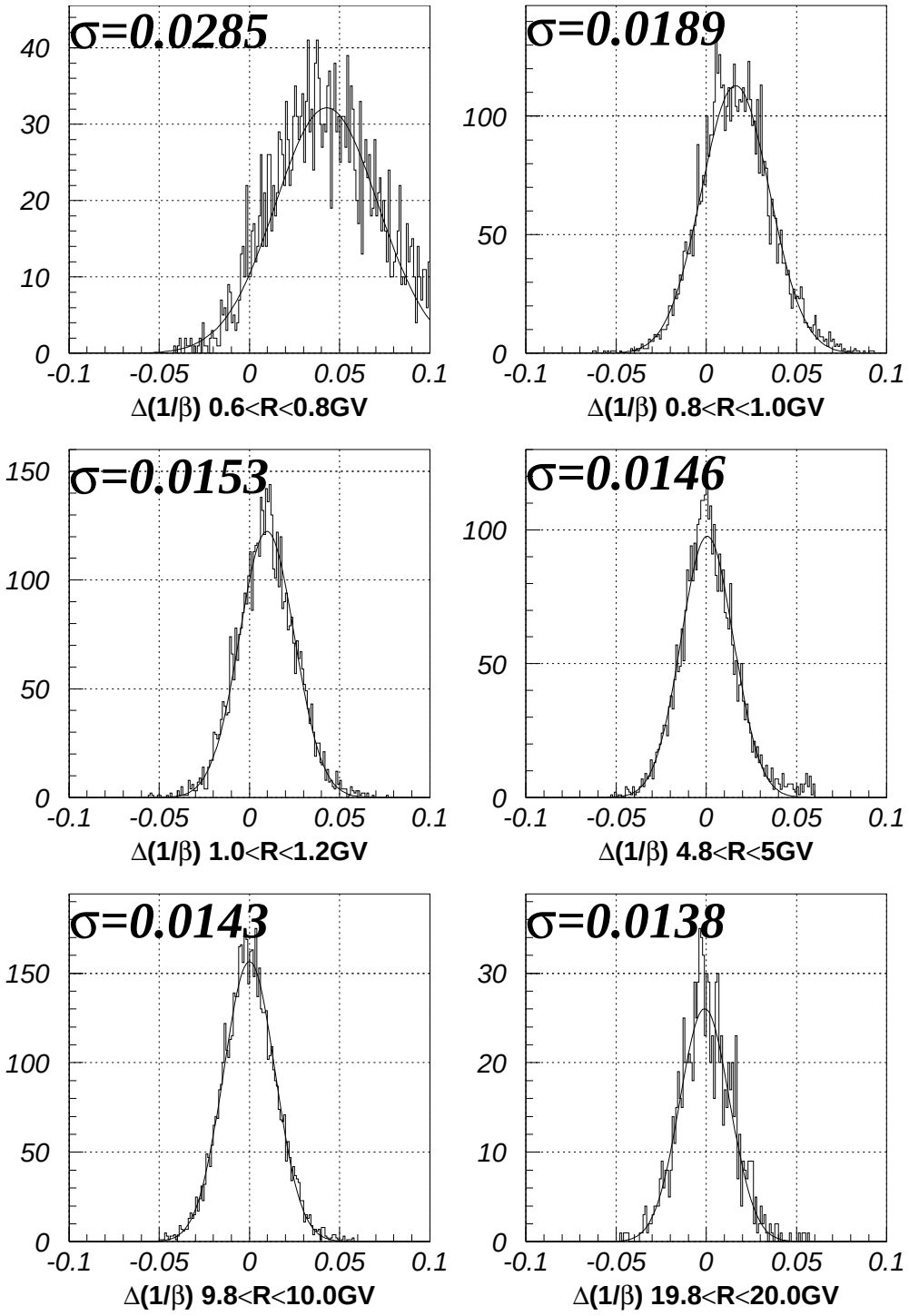

Figure 2.19: $\Delta 1/\beta$ distributions for proton samples with various rigidities: form to to bottom, 0.6-0.8, 0.8-10, 1.0-1.2, 4.8-5.0, 9.8-10.0 and 19.8-20.0 GV.

2.4.5 dE/dx Measurement

For ADC data analysis, we first subtracted its pedestal, and then normalized for the gains of the PMTs and the ADCs and for the efficiency of light collection, using the MIPs vertically traversing the center ($z = 0$) of the counter which yield about 500 photo-electrons at the photo-cathode. Coarse z-position is obtained from the ratio of these normalized ADC values of the both ends' PMTs, and is used for the matching with the extrapolated trajectory.

The dE/dx in scintillator is calculated, at first, for each PMT by dividing by the traverse length in the scintillator and by correcting for the attenuation of light in the scintillator using the extrapolated trajectory, and we finally adopted the dE/dx by averaging these dE/dx value of both ends. Although the z-position dependence of the attenuation nearly obeys an exponential law and consequently the geometrical average of both ends' ADCs is not expected to depend on the position, the obtained value have slightly position dependence especially near both ends, and the former method produced the better resolution.

Figure 2.21 shows scatter plots of dE/dx versus rigidity measured in the chambers for the top and the bottom scintillators. In the figure are shown proton and helium bands as well as their isotopes, and the energy cut-off due to the nergy losses between the top and bottom counters. Because the dE/dx distributions have longer tail on the upper side (Landau tail), we evaluated from the lower-side tail that the dE/dx resolution is 6 % for all counters for MIPs in the flight data.

In Exp-34 (2001 flight), a lead plate with a thickness of 2 radiation length (11.2 mm) was installed above the lower TOF (Figure 2.20).

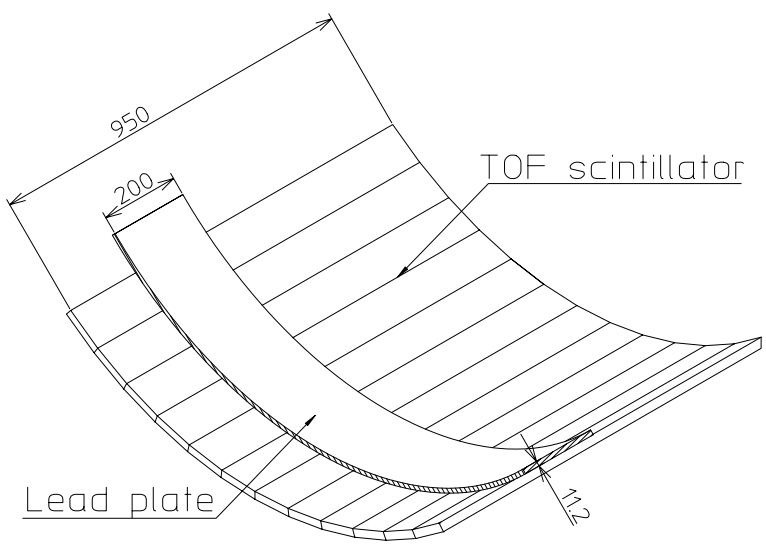

Figure 2.20: Configuration of the lead plate and lower TOF.

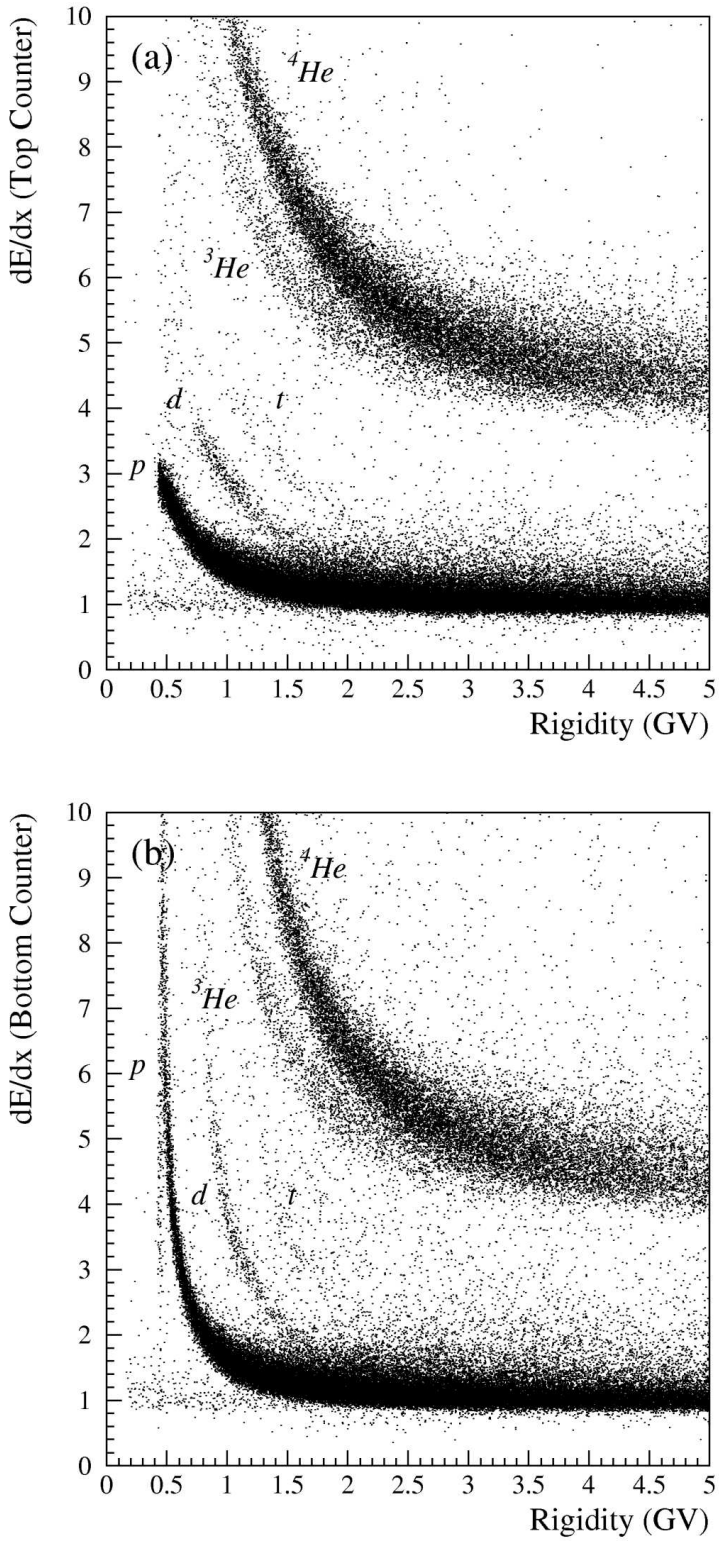

Figure 2.21: Scatter plots of $\mathrm{d}E/\mathrm{d}x$ vs rigidity for down-going positive-charge particles(a) at the top counters and (b) at bottom counters.

2.5 Aerogel Čerenkov Counters

A Čerenkov counter with a silica aerogel radiator (aerogel Čerenkov counter) has been developed in order to improve particle identification capability.

2.5.1 Design

Figure 2.22 shows an overview diagram of the aerogel Čerenkov counter, where the counter consists of a large diffusion box containing aerogel blocks viewed by 46 PMTs densely arranged at the both ends. The unit's weight and the amount of material were minimized using an aluminum-core honeycomb plate as the main structure. Choosing an effective reflector material is a key aspect in counter design since most photons generated in the diffusion box will undergo numerous reflections prior to reaching the PMTs We accordingly tested various type of sheet material, i.e., Millipore, Tibex, and Goretex; ultimately finding that Goretex, which exhibits high reflectivity in the short-wavelength region (300-400nm), is most suitable. From the standpoint of photon collection, this is consistent with the fact the number of Čerenkov photons is inversely proportional to the square of wavelength; thereby making reflectivity in short-wavelength region important.

In consideration of operating the counter in a 0.2 Tesla fringe magnetic field, we selected 2.5 inch Fine-Mesh PMTs as used in the TOF hodoscopes.

Readout electronics consists of summing amplifiers that combines 46 PMT signals into 8 channels which are digitized by a charge-integrated ADC. Blue LEDs (NLPB, NICHIA) with a peak of 450 nm are used to adjust the PMT gain such that all the PMTs provide the same ADC counts pre photoelectoron. Since PMT gain shows magnetic field dependence, final high-voltage tuning must be done in the counter after exciting the solenoidal magnet to the nominal field. Therefore, the blue LEDs were mounted on the both sides of the side plate at its center point; a configuration allowing PMT gain to be monitored throughout the experiment.

Another consideration concerns the magnetic field itself, since if the PMT axis and magnetic field direction form a nonzero angle θ, then the PMTs lose their effective photocathode are (S_{eff}), i.e., some secondary electorons produced at dynode, traveling inside the PMT in the direction of the magnetic field, cannot reach the anode. Accordingly, to avoid losing S_{eff}, each end plate on which PMTs were mounted was slanted to reduce θ. The drawback in this approach, however, is that slanting in turn leads the loss of photoelectrons. It is for this reason that during prototype testing we focused our attention on optimizing the angle of slanting such that photo-electron loss is at an acceptable level. The slanting angle was determined to be 24.5° after optimizing photo-electron loss and S_{eff}. This slanting angle reduced θ from 39° to about 18° in the lower PMTs and from 43° to about 26° in the upper PMTs, while S_{eff} increased by 20 % in comparison with not slanting. A mask of Goretex was placed over the front surface of each PMT (Figure 2.22 such that the photons hitting the insensitive photocathod area formed by residual θ would be reflected back.

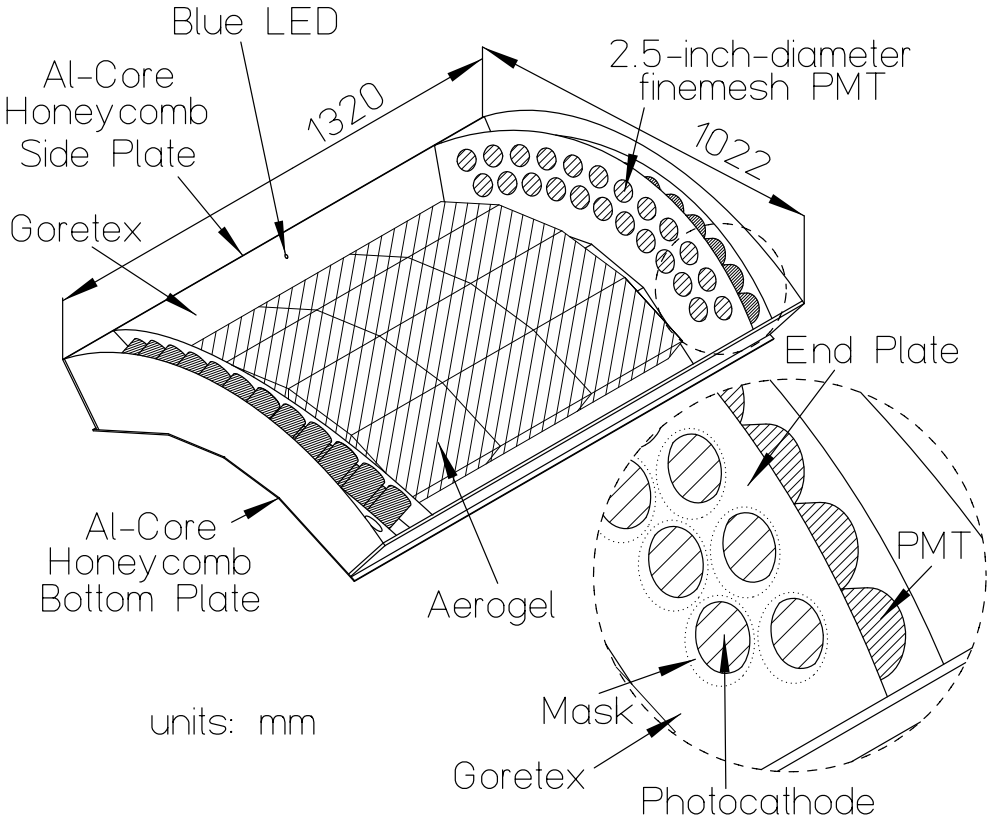

Figure 2.22: Overview of the aerogel Čerenkov counter.

2.5.2 Aerogel

As a Čerenkov radiator, we selected silica aerogel having a refractive index of 1.032 (1.022) in Exp-12 and Exp-16 (Exp-34). This aerogel was manufactured using a new method [48] which ensures that it retains its hydrophobicity such that long-term stability and good clarity are afforded. It is the aerogel's excellent clarity that allowed us to use a diffusion vs mirror box design despite being constrained by a counter thickness of ≤ 19 cm.

Figure 2.23 shows how an aerogel block was made , i.e., (Step 1) a stack of four 2-cm-thick layer pieces with a piece of Goretex sheet on their bottom were wrapped lengthwise with polyethylene film (ITOCHU SANPLUS Co. Ltd.). Then, after placing cardstock paper on the bottom side, it was again wrapped around its width (Step 2). Polyethylene film was chosen as it has good clarity in the relevant wavelength region. A string made of Kevlar was used to fix (tie) the aerogel block to the bottom honeycomb plate through a hole drilled on it. With this configuration of block fixation, no photon-absorbing surfaces such as aluminum support surfaces are present within the diffusion box. An overview diagram of an aerogel block is shown in Figure 2.24

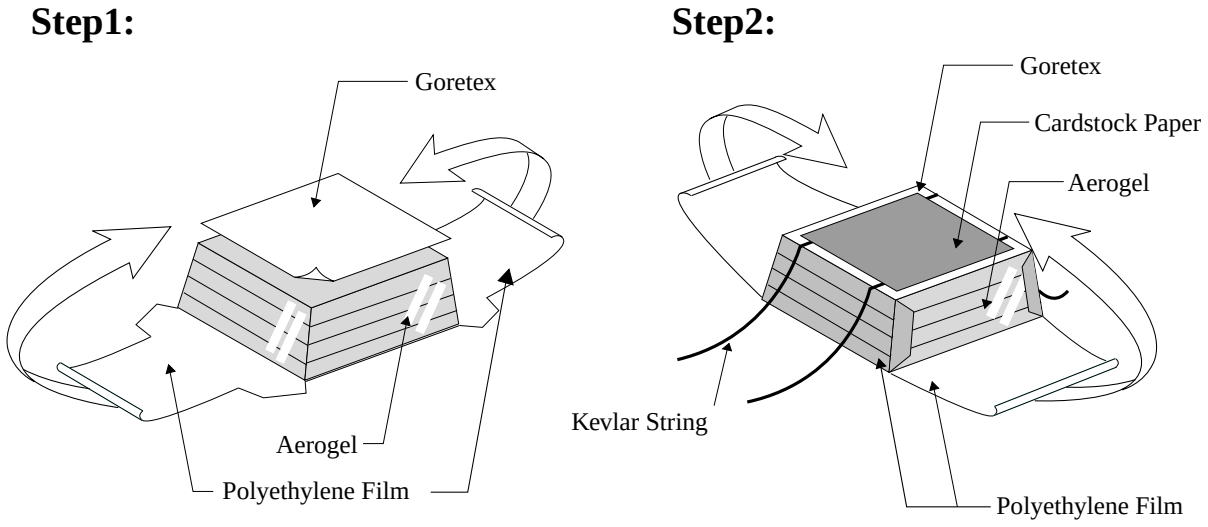

Figure 2.23: Wrapping scheme of an aerogel block.

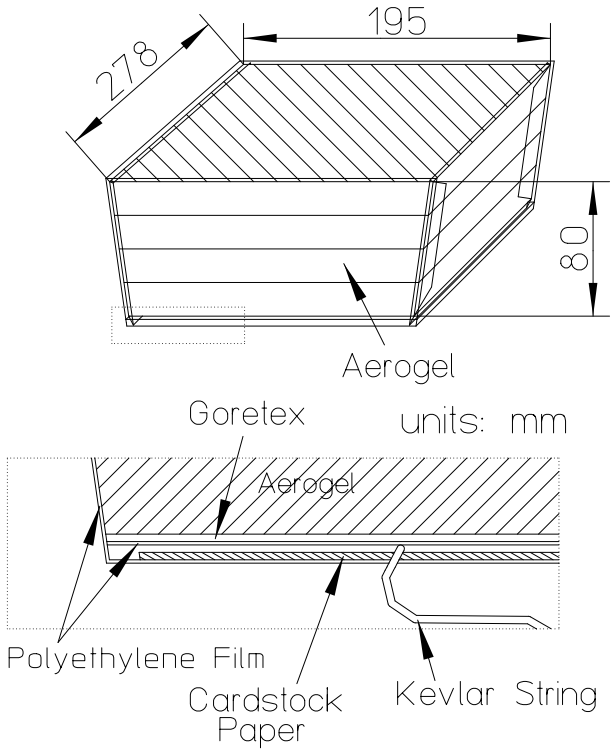

Figure 2.24: Overview of an aerogel block.

2.5.3 Upgrade of Aerogel

In 1998, the refractive indices of aerogel was changed from 1.03 to 1.02, resulting in further extension of the $\overline{p}$ detection capability up to 4.2 GeV. Figure 2.25 shows a plot of N_{pe} vs $1/\beta^2$ calculated using

$$\frac{1}{\beta^2} = \frac{m^2}{R^2} + 1$$

where R is the rigidity of the incident particle and m is mass of a proton. Closed circle represents BESS-97 data (n=1.03) while open circle represent BESS-98 data (n=1.02), both of which are plotted using flight data instead of the data taken at ground-level. $1/\beta^2$ was calculated using rigidity vice TOF measurements because the resultant value is more accurate in cases where the mass of the incident particle is known. The superimposed line represents a liner fit to the data. At the $N_{pe} = 0$, this corresponds to the square of the refractive index, *i.e.*, $n = 1.034 \pm 0.004$ for BESS-97 (Exp-12/16) and $n = 1.022 \pm 0.002$ for BESS-98.

Since number of produced photon is proportional to $1 - 1/n^2 \approx 2(n-1)$, large loss of N_{pe} was expected by the change of the refractive index from 1.03 to 1.02. However, the excellent transparency of new aerogel ($N = 1.02$) enabled us to collect 90 % of N_{pe} when comparing with $N = 1.03$. Note that new aerogel was produced using the improved technique developed by BELLE PID group [50]. Figure 2.26 shows the comparison of separation power between $n = 1.03$ (solid curve) and $n = 1.02$ (dashed curve). It is clear that a e/μ rejection factor of several thousand can be achieved while keeping the efficiency for p's above 90 %

2.6 Trigger System

Because of large geometry factor of the BESS detector, the expected rate of particles penetrating the apparatus is as high 2 kHz in the flight experiment (Exp-34), mostly low energy protons. The typical data size of a single track event is 2 kB even after zero suppression process is applied to the FADC data. If all the events were collected, the data rate would be 4 MB/s and the total data size to be recorded during a 20-hour flight exceeds 280 GB, which is beyond the on-board storage capacity. An intelligent trigger system has been developed to reduce the overall trigger rate while interesting events should not be lost.

The trigger generation proceeds in three stages. The first-level trigger (T0 trigger) is a simple coincidence between the upper and lower TOF counters and initiates digitization of various FADC/ADC/TDC modules and event building processes. The second level trigger, which is called as the track trigger (TT), is a hard-wired logic which determines the coarse track rigidity (defection^{-1}) based on the TOF/IDC hit information. In order to enrich the recorded data with negative tracks were rejected at this trigger level. However, a portion ($\sim 1/30$) of the events bypassed the TT and were recorded irrespective of their track rigidity. This event sample forms an unbiased data set and is used to study most abundant protons and helium nuclei and to evaluate various efficiencies and correction factors in the off-line analysis. The Transputer bank composed of the microprocessor

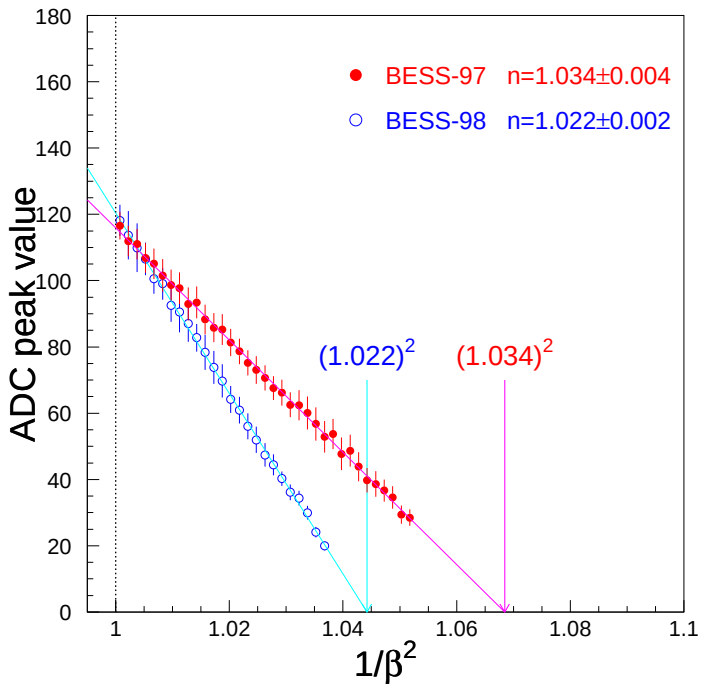

Figure 2.25: Momentum dependence of N_{pe} as a function of $1/\beta^2$. Closed circle represents $n = 1.03$ while open circle represent $n = 1.02$.

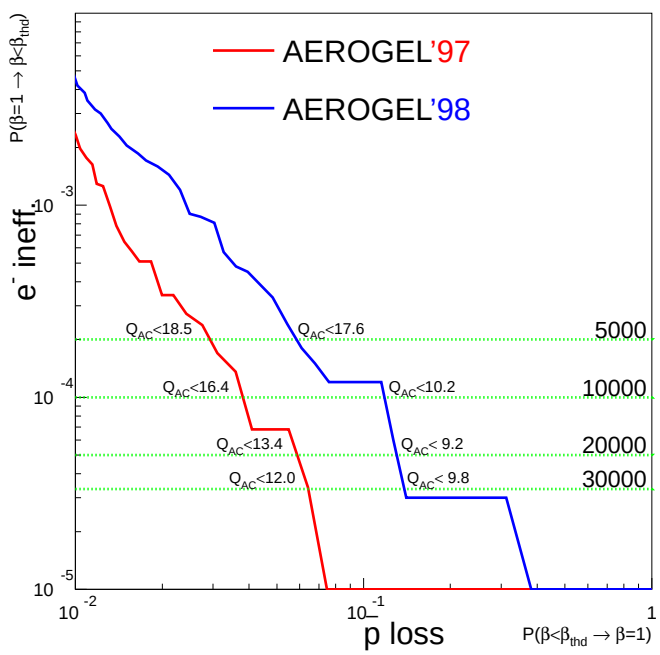

Figure 2.26: Comparison of separation power between $n = 1.03$ and $n = 1.02$. Red curve represents $n = 1.03$ while blue curve represent $n = 1.02$.

cluster performs the third level trigger, which will be described in detail in the next section.

2.6.1 First-level Trigger

The first level trigger (T0) was provided by a coincidence between the upper and the lower layers of the TOF counters. A pair of 19th dynode output pulses from PMTs at the both end of each TOF counter were integrated with a time constant of 20 ns and then linearly summed with a simple capacitor/resistor circuit. The integration was to smooth the pulse shape so that timing of the peaks were equalized irrespective of the hit position. The summation was to moderate the trigger efficiency variation along the counter.

The summed signal was discriminated and the output signal is converted to TTL compatible level. The threshold voltage should be low enough to trigger single-charged particles with good efficiency. It was set at $\sim 1/3$ of the pulse height of vertically incident MIPs at the center of the TOF counter. In order to determine the correspondence between the threshold voltage and the integrated charge of the PMT outputs normalized by the MIPs, the TOF counters were irradiated by a radioactive source (^{106}Ru) prior to each balloon flight. Figure 2.27 shows a charge distribution of the events triggered by the RI source and cosmic rays in the pre-flight test. The left peak shown in the figure arises from the continuous spectrum given by the RI source which is sharply cut by the discriminator threshold. The right peak corresponds to cosmic ray muons, which are not corrected for the incident angle. From these figures, it was verified that the threshold was set at 1/3 of the MIP signal.

The discrminated signals in each layer (top and bottom) were ORed, and the T0 trigger was generated when a coincidence was made between the top and the bottom layer. A dedicated T0-trigger modules has been developed to minimize the power consumption (1.3 W) and propagation delay and to implement a special function, "count down", denoted CD hereafter. An internal counter counts down on every trigger input starting from a preset value N, which can be set by a CAMAC command, and the output pulse is issued when the count reaches zero. The T0-CD is issued every N-th T0 trigger to collect the unbiased event sample. The rest of the vents await subsequent decision made by the TT. In Exp-34 (2001 flight), the preset value N was set at 4 for the T0-CD.

2.6.2 Second-level Trigger

The TT modules performs the hit pattern recognition and the track curvature determination. The block diagram of the circuit is shown in Figure 2.28. The TT module was implemented in a double width CAMAC module. An onboard microcode-programmable sequencer controlled the entire operation of the module as described below. The TT is enabled on receiving the T0 with a delay of $\sim 5\mu$s, the maximum drift time of the IDCs. A coincidence between the overlapping pair of cells defines a hit cell in each chamber. The TT modules is capable of receiving up to 128 inputs corresponding to 32 hit cells in the four detectors (upper TOF, upper IDC, lower IDC, lower TOF). The number of hits in each TOF/IDC is obtained from a look-up-table and is encoded into a 5-bit integer. A

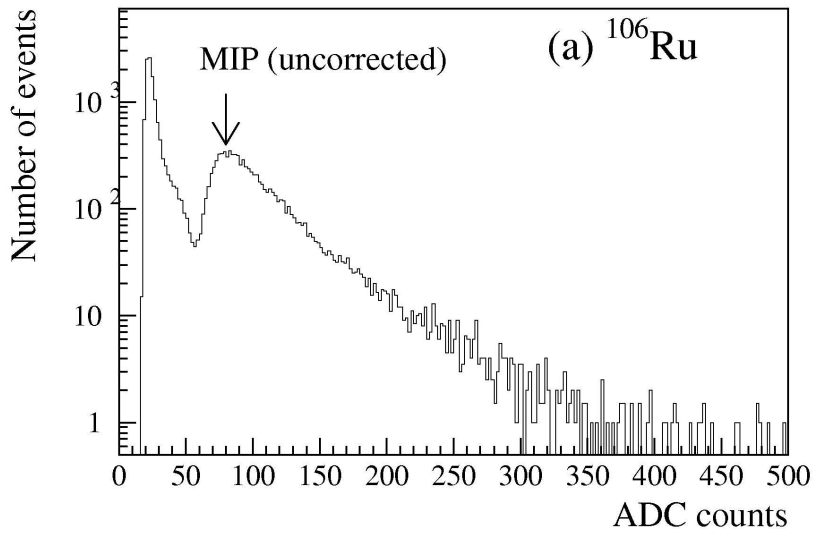

Figure 2.27: Integrated charge distribution of PMT outputs irradiating a TOF counter by a ^{106}Ru radioactive source.

20-bit *N-hit* pattern expresses the number of hits in the TOFs and IDCs.

When the *N-hit* pattern matches with one of the six acceptable patterns (see. Table 2.3) the events are subject to rigidity analysis. The micro-sequencer scans all the hit cells and picks up a combination of four hits in the four chambers. From the location of hit cells, it then retrieves a 6-bit deflection from a look-up-table. The minimum and the maximum possible deflection corresponding to each hit pattern was calculated prior to the experiment and their mean value was stored in a 16M-bit EEPROM.

Since we have variety of physics objectives, several trigger modes optimized to each objective are needed. In addition, data was collected during ascent since 1999 to study atmospheric secondary particles. The main targets for biased sampling are listed below:

- single negative charged particles, e.g., $\overline{p}$'s;
- single multiple charged particles, e.g., $\overline{He}$ (floating only);
- relativistic particles,e.g., high energy protons (p's), positron (e^+);

  This mode is equipped from 1998 flight to collect high energy protons and positrons effectively by using discriminated aerogel Čerenkov counter output.
- single positive charged particles, e.g., low energy p's (ascent only),

  This mode is equipped from 1999 flight to collect low energy protons effectively during ascent.

There are eight different threshold values prepared for the track pattern and rigidity selection in total. A 6-bit rigidity-selection flag is retrieved by specifying the 6-bit deflection. The above process repeats for all the combinations one after another. The TT can be

Table 2.3: Summary of the track trigger hit pattern selections. (i, j, k, l)$_e$ means (N_{ou}, N_{ol}, N_{iu}, N_{il}) exactly matches (i, j, k, l), while (i, j, k, l)$_p$ means the permutation (N_{ou}, N_{ol}, N_{iu}, N_{il}) matches (i, j, k, l), where N_{ou} - the number of hit-cells in upper TOF, N_{ol} - the number of hit-cells in lower TOF, N_{iu} - the number of hit-cells in upper IDC, and N_{il} - the number of hit-cells in lower IDC.

Name	Description	$N-hit$ Pattern
Clear	clean track	(1, 1, 1, 1)$_p$ (1, 1, 1, 2)$_p$
Dirty1	track with some additional hits	(1, 1, 1, 3)$_p$ (1, 1, 2, 2)$_p$ (1, 1, 1, 4)$_p$
Dirty2		(1, 1, 2, 3)$_p$ (1, 1, 2, 4)$_p$ (1, 2, 2, 2)$_p$
Dirty3		(1, 1, 1, 1)$_e$ - (1, 3, 3, 4)$_e$
Miss	missing hit in one chamber	(0, 1, 1, 1)$_p$
Anni	discontinuous hit in lower TOF	(1, 1, 1, 1)$_e$ - (1, 4, 1, 4)$_e$

switched to three hit mode in case of some trouble with one of the chambers. By combining the $N-hit$ pattern, the 6-bit rigidity-selection flag, and mask by T0 hit pattern or discriminated signal from aerogel, the final TT trigger bits are set. All the trigger modes are summarized in Table 2.4 for both ascent and floating runs. The efficiencies of three main modes of track trigger are shown in Figure 2.29(a), which uses the data taken at ground-level in the preparation process at LynnLake in 1999. In the figure, filled, open, and hatched histogram shows trigger mode for $\overline{p}$ (Mode 0-5 of track trigger), aerogel trigger (TT Mode 6), and low energy proton trigger (TT Mode 7). The inefficiency of aerogel trigger is due to limited fiducial region of aerogel. On the other hand, due to the "count down" of 1/2, the efficiency of low energy proton trigger is 0.5 at maximum. Note that these efficiencies were calculated using the events which satisfies following criteria: (i) a single down-going particle fully contained in the fiducial region of the tracking volume, (ii) only one (one or two) hit in the upper (lower) TOF hodoscope, and (iii) having acceptable track qualities.

The T0 trigger bits and the TT trigger bits are combined and the final decision to accept the event or not is made in the master trigger (MT) modules. The MT module distributes fast clear signals to all the digitizing modules for rejected events. The accepted events are subject to the Transputer bank for further on-line filtering, which is called the third level trigger in the previous section. The CD events are accepted irrespective of the TT trigger bits.

2.6.3 Third-Level Trigger

After building "an event-data" by an event builder (EBV), the process which is described in Section 2.6.6, further on-line filtering was performed by Transputer bank (TRP). The specification of Transputers used in TRP is described in Section 2.6.6. Transputers enables high-speed parallel data processing. Thus, the process in TRP does not related to "trigger ready" of the front-end electronics. It does not affect the live-data taking time, but reduces

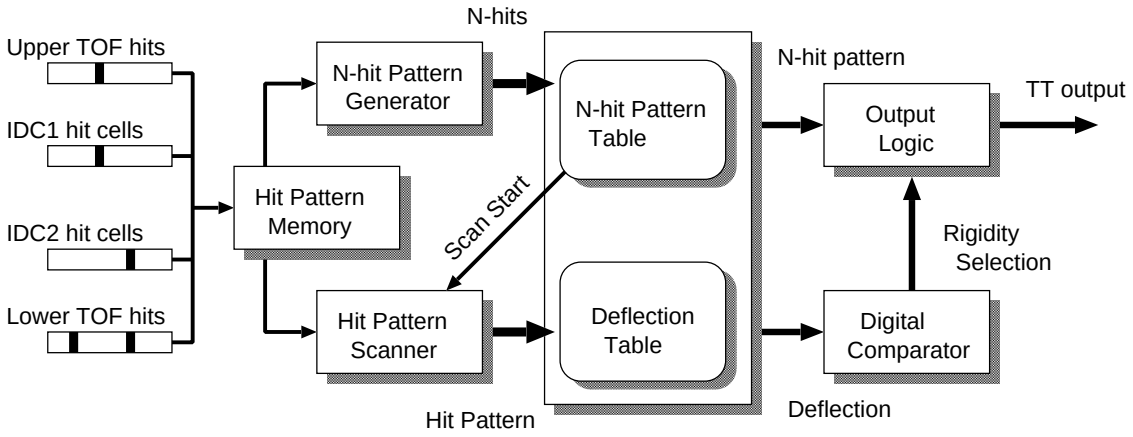

Figure 2.28: Block diagram of TT process.

data amount by rejecting not useful data.

The main role of the TRP is to select desirable evens using the whole detector information: (1) Trigger mode, (2) TOF hits, and (3) rigidity of JET tracks reconstructed using FADC data.

For JET track reconstruction and rigidity calculation, the following algorithm is employed:

(1) Determine hit position, total amount of charge, and pulse width using FADC data. Since the charge information in FADC data is the sum of pedestal and charge of the hit, the pedestal is subtracted for each hit. The pedestal value of each FADC channel is automatically updated at every 1 hour of the calibration run.

(2) Select "good" hits which are defined as hits enough charge and width.

(3) Find arrays by connecting the "good" hits in central region of JET chamber, and perform line fitting.

(4) Extrapolate each of the line trajectories to find "good" hits near the trajectory, and associate the hits to the array.

(5) Perform circular fitting on the array and the associated hits. The circular fitting algorithm is based on non-iterative method by following Karimaki [49]

(6) Scan all of "good" hits in JET chamber to check whether they are close enough to the circular trajectory or not. Only the hits passing this check are used in the following process.

(7) Perform circular fitting once more and calculate the transverse rigidity in $r - \phi$ plane.

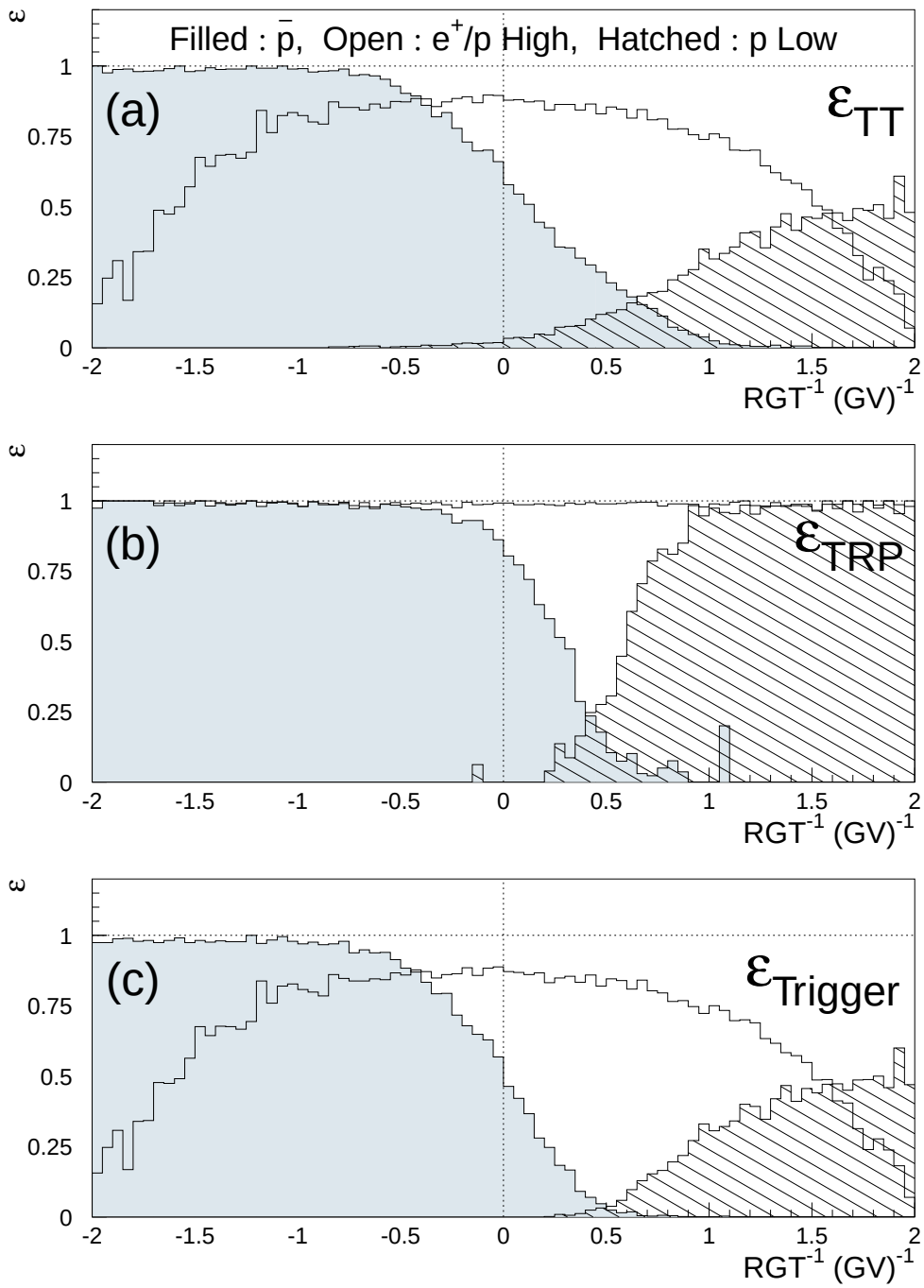

Figure 2.29: Trigger efficiencies of various trigger modes. Filled open, and hatched histogram shows trigger mode for $\overline{p}$ (Mode 0-5 of track trigger), aerogel trigger (TT Mode 6), and low energy proton trigger (TT Mode 7). (a) track trigger efficiencies (ε_{TT}), (b) trigger efficiencies of Transputer bank (ε_{TRP}), (c) combined (total) trigger efficiencies ($\varepsilon_{Trigger}$).

Table 2.4: Summary of the selection modes in the Transputer bank for Exp-34 (BESS-2001).

Mode	Target	Thres. (GeV^{-1})	Bias	TT Mode
0	$\overline{p}$	+0.150	−	0 - 5
1	e^+		+	6
2	high-E p		−	6
3	low-E p	+0.600	+	7
4	Missing	Not available		all
5	New wire / Multi	Not available		all
6	Count Down	No selection		CD bit
7	Scaler	No selection		event with scaler data

Fifteen Transputers (INMOS & SGS-Thomson) arranged in a 3×5 matrix are dedicated to this job in the TRP. They execute the same program to process events simultaneously. One of the first three Transputers receives the formatted event-data from the EVB through a Transputer link. Then the Transputer processes the event-data, or otherwise if it is already busy, the event-data is relayed down to following Transputers. Consequently, the TRP can process fifteen events concurrently. If all the Transputers are occupied and busy, the EVB stops sending event-data to the TRP.

Each Transputer executes the above task typically within 20ms. Therefore, the whole bank including fifteen Transputers is capable of processing events at 1 kHz. The accepted event-data are relayed down and are finally sent to the data-storage subsystem via Transputer link.

Table 2.4 summarizes the TRP trigger modes. Mode 1 - 4 correspond to further rigidity selection for correctly reconstructed events. In contrast, "Missing" (Mode 4) means events in which reconstructed track and TOF hits do not match. Since there is possibility of wrong reconstruction, events are accepted irrespective of their rigidity values. "Near Wire/Multi" (Mode 5) means events which can not be reconstructed while enough hits are recorded in JET. These events also accepted for safety not to reject interesting events. Count Down (Mode 6) is used to accept unbiased sample assigned in Master Trigger module. Scaler is used to accept events with scaler information such as T0 trigger rate, which is randomly assigned to some events processed in the EVB. Thus, all events rejected are (i) events correctly reconstructed and not satisfying the threshold, or (ii) garbage event (small hit in JET, etc.). The efficiencies of $\overline{p}$, aerogel trigger (e^+, p High), and p Low are shown in Figure 2.29(b). In contrast to track trigger efficiencies, sharp threshold curves were obtained. Figure 2.29(c) shows the combined efficiencies of intelligent trigger system of BESS.

2.6.4 Data Acquisition System (DAQ)

The BESS-DAQ used in Exp-12, 16 and Exp-34 are not the same. Some components were upgraded. However basic configuration is almost the same between Exp-12/16 and Exp-34. They are divide into four subsystem as illustrated Figure 2.30: (1)control, (2) event-process, (3) data-storage, (4) monitor. In addition for flight experiments Exp-34, we used the (5) communication subsystem for the communication between the payload and the ground station, which is provided by NSBF.

2.6.5 Control subsystem

Control subsystem routes (i) commands from the ground station to each subsystem, (ii) messages from each subsystem to the ground station, (iii) house-keeping data to the ground station, (iv) event-sample to the ground station.

- Control Subsystem in Exp-12/16
  In Exp-12/16 this subsystem was configured based on NEC V40 CPU and communicate with the other subsystem via Omninet. The system consists of a CPU card, a memory card, an Omninet controller card, an AMPSC controller (NEC μPD72001) card of STD BUS standard. Therefore, all the other subsystem also have had Omninet card.

- Control Subsystem in Exp-34
  In Exp-34 the control subsystem was newly developed using Mitsubishi M32R 32-bit RISC CPU. The feature of this CPU is an embedded 2MB of Dynamic RAM (DRAM) which is connected by 128-bit BUS internally. The power consumption of this CPU is about 500mW, and the processing power is 80 MIPS.

  This system consists of a CPU, four Neuron Chips to communicate with all monitors and Event-process subsystem, AMPSC controller to communicate with ground station, a 2MB of Flash memory to store their operation code, and an I/O controller specialized for this CPU. The Neuron Chip [54] is a core processor of Echelon LonWorks a technology that facilitates developments of distributed, and intelligent control networks. A LonWorks network (or shortly LON) consists of a series of nodes, each of which is implemented with a Neuron chip communicating with one another through a message-based protocol called LonTalk [55].

  The specialized I/O controller has a bus arbiter, timers, three serial controllers, 100-bit digital I/Os, and interrupt controllers. The serial controller was used for communication with the Data-Storage subsystem at 38 kbps. 8-bit digital I/Os and one interrupt line was used for receiving commands from the ground station thought a Communication subsystem.

2.6.6 Event-process Subsystem

The event-process subsystem was designed to collect digitized data from front-end electronics of sub-detectors and to build formatted data for an event. The subsystem consists

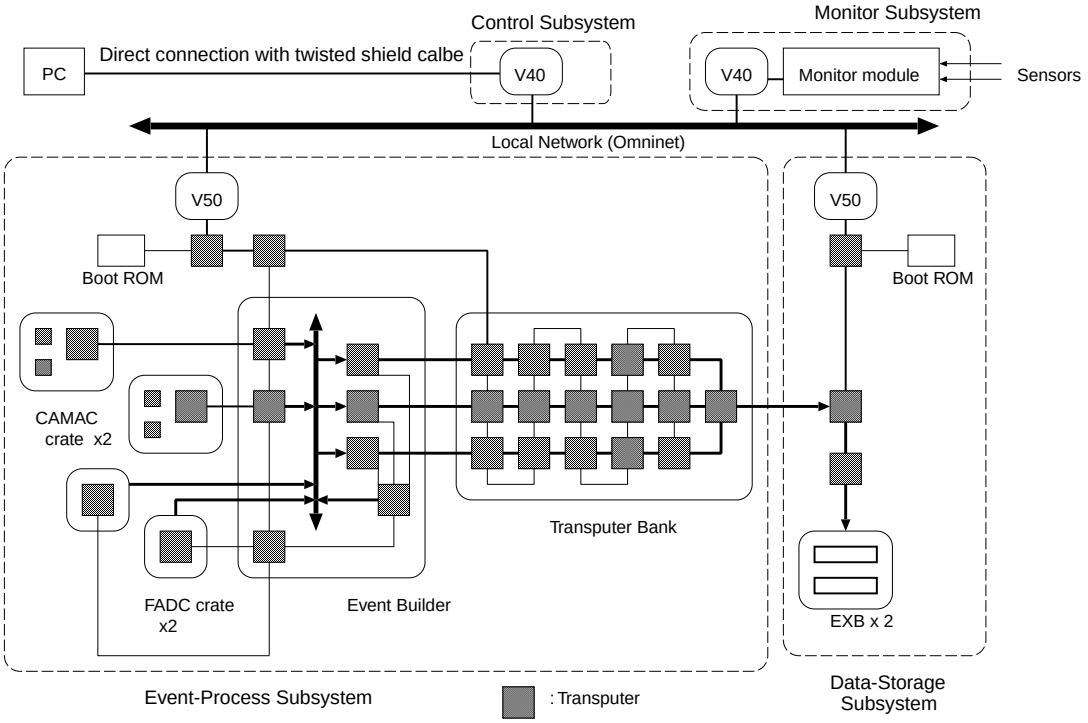

Figure 2.30: Block diagram of data acquisition system in Exp-12/16.

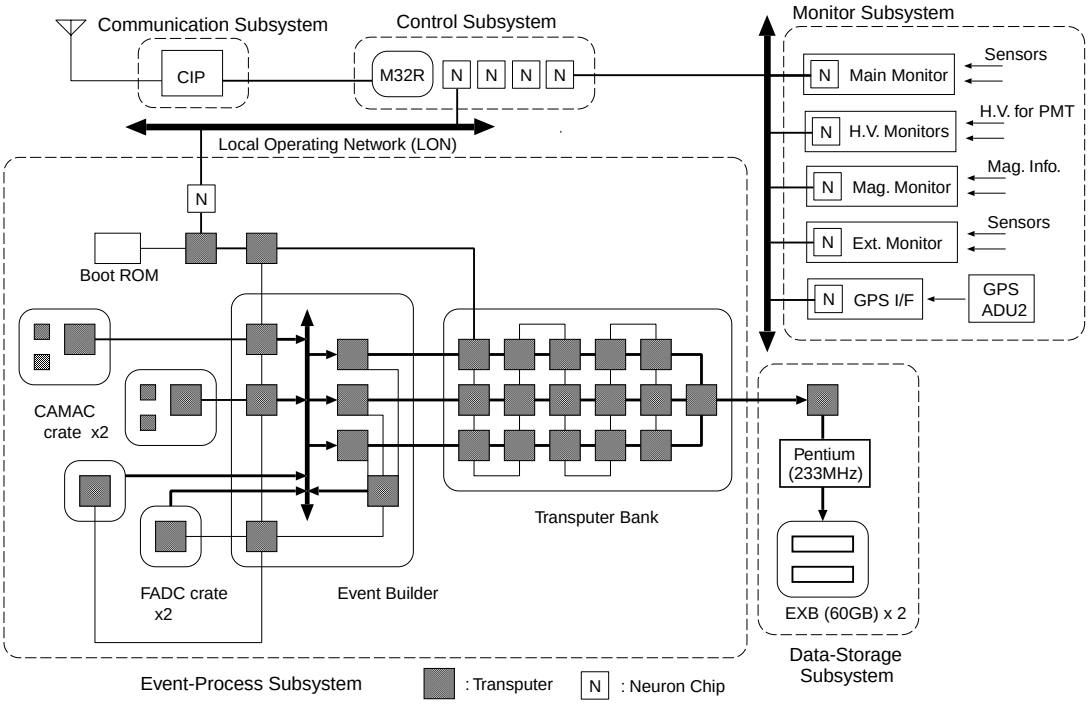

Figure 2.31: Block diagram of data acquisition system in Exp-34.

of a subsystem controller, a FADC system, a CAMAC system, an event builder (EVB), and a Transputer bank (TRP). The digitized data form FADC and CAMAC front-end modules are gathered through FADC and CAMAC Crate Controllers (CC), and processed into "an event-data" by EVB. The event-data is sent to the TRP for further on-line filtering.

In this subsystem, a total of 36 (Exp-12/16) or 34 (Exp-34) Transputers were employed. Each Transputer possesses a processing speed of 20 MIPS (million instruction per second) and supports execution of parallel tasks. In addition, each Transputer is provided with four serial bus line ports. Two Transputers can be connected with a serial "Transputer link" using these ports and can communicate each other. The Transputer link has a data transfer rate of 20 Mpbs [51]. The effective throughput is about 1 MB/s for the our particular application. Each crate controller have a Transputer inside and the TRP contained sixteen Transputers. These are connected with Transputers links to construct a "Transputer network". Programs for the Transputer network are written in OCCAM high level language [52] to utilize Transputers hardware implementation most effectively.

This unique design enabled high-speed parallel data processing and transferring of the BESS DAQ. Under typical experimental conditions, the subsystem is expected to operate at a processing time of about 250 μs per event. The maximum data size per event is 24 kB due to the limitation in buffer size.

- FADC System

  The FADC system [39] was comprised of 21 FADC modules, two data compressor module and two crate controller (FADC-CC), for read-out of the JET and IDC data.

  On receiving a first level trigger, the FADC-CC starts distributing clock signals through a back-plane of the crate and initiates digitization and zero suppression of the FADC modules. After generating 512 clock signals, a "conversion end" is issued by the FADC-CC, which then enables a scanning process of the compressor. The compressor scans all the data stored in the FADC modules channel by channel. It compresses the data size and the compressed data are stored in a FIFO memory.

  In addition to the normal event processing described above, the FADC-CC has several auxiliary functions for debugging and monitoring. Here one of the most essential functions is described shortly. The zero suppression of FADC system reduces the data size significantly, but it requires to monitor the baseline of FADC outputs which slightly drift. In order to set the zero suppression threshold to an optimum value throughout an experiment, the baseline monitoring and threshold adjustment run which is called "calibration run" is performed every one hour. It takes approximately 100 seconds for one "calibration run".

- CAMAC System

  A variety of CAMAC modules are housed in two CAMAC crate for readout of TOF, ACC data, the implementation of trigger system, and counting trigger statistics and hitting statistics of various counters. An intelligent CAMAC crate controller (ICCC) [53] has been developed specially for this experiment. The ICCC is equipped with three Transputer in it and can be naturally embedded in a Transputer network.

In the CAMAC crate which contains the master trigger module (MT), the ICCCs receives a trigger signal directly from the MT. Then two ICCCs start gathering data from CAMAC modules in parallel, and sends them to the EVB through the Transputer links.

- Event Builder

  The EVB is composed of four input ports, one DMA controller, and three output ports. Data from FADC compressors and the CAMAC-CCs are gathered by the input ports, the DMA controller merges them into formatted event-data, and the event-data is transmitted to the TRP through one of the output ports. These tasks are processed in parallel ; If the input ports receive T0 trigger, they starts gathering data from FADC compressors and CAMAC-CCs. When the fast clear signal is received, the gathering process is terminated and transfered into one of two buffers, the DMA controller starts merging and formatting these data into a event-data and at the same time the trigger lock is released. If the next T0 trigger is received, the FADC and CAMAC data of the next event can be transfered into another buffer so as to reduce readout dead-time. The event-data is transmitted through one of three output ports into the TRP. Another two output ports can transmit the next event-data. Thus the EVB may process a series of different five events concurrently. The processing speed of the EVB is about 24 MB/s, i.e., the EVB can accept the trigger rate of up to 12 kHz for typical data size of 2 kB.

- Transputer Bank

  The main role of the Transputer bank (TRP) is to select desirable events using the whole detector information: (1) Trigger mode, (2) TOF hits, and (3) rigidity of JET tracks reconstructed using FADC data. Note that these full set of event-data can be used only after the event building process.

  Details of the system are described in Section 2.6.3 as a third-level trigger.

2.6.7 Data-Storage Subsystem

The data-storage subsystem receives the event-data from the event-process subsystem via Transputer link as shown in Figures 2.30 and 2.31.

- Data storage in Exp-12/16
  In Exp-12/16, we used 20 GB of EXABYTE 8-mm magnetic tape as storage media. The tape drive for this media is called 'Mammoth' and which interface is SCSI standard. To handle this tape drive, we used the Transputer-SCSI module commercially available and the subsystem controller which CPU is NEC V50. The subsystem controller receives the data from the Omninet and transmit them to the Transputer (TRP-1) which is interfacing the V50. Another Transputer (TRP-2) is connected with both the TRP-1 and the event-process subsystem via Transputer links. The TRP-2 multiplexes the data from Omninet and the event-process subsystem to the third Transputer (TRP-3) which handle the SCSI bus interface and

records the data into the magnetic tape. The peak speed of the data transfer to the tape driver is 500 kB/s.

- Data storage in Exp-34
  In Exp-34 flight experiment, we used two set of 60 GB magnetic tape and the drive called 'Mammoth-II'. The interface of 'Mammoth-II' is SCSI-III which is advanced standard of SCSI. This drive can write the data by *sim* 4 MB/s. However, the Transputer-SCSI module described in previous paragraph can not transact such a great throughput of the data. Then we developed the small computer system which can treat the SCSI-III. The new computer system is based on Compact PCI standard and has a Pentium Processor 233 MHz as a main CPU. We used a Linux (kernel-2.2 base) as operating system, because many basic libraries such as process management routine, SCSI driver, Network driver, etc. are available freely. In addition, since it is a open source, we can tune for the balloon experiments. For example, we customized the file system to avoid the crash by an emergency power off. We also develop the PCI-Transputer interface card to transfer the event-data from the Transputer-link to the Compact PCI System.

  To have introduced this system enabled us to record the data up to few MB/s. As a result, we could increase trigger efficiency for $\overline{p}$ by loosing the trigger threshold. Furthermore, this enhancement of the throughput also produced the increase of the Count Down trigger events. This events were very useful to measure the proton or other secondary flux in Exp-34 experiment.

2.6.8 Monitor Subsystem

The monitor subsystem handles the house-keeping data which come from various sensors distributed in the payload. The transducers generate voltage outputs according to the measured value of temperature, pressure and attitude of the payload. The monitoring devices were upgraded in 2000 and 2001. Therefore we used the different monitor subsystem between Exp-12/16 and Exp-34. We describe each outline in following:

- Monitoring Devices in Exp-12/16

  In Exp-12/16 (BESS-97), A monitor modules receives up to 64-channel inputs with differential amplifiers (Analog Devices AD524): temperatures (16 points), pressures(7 points), magnet status (16 points), chamber high voltage status (15 points), and clinometers. Those are multiplexed (Analog Devices AD7501) and digitized (Analog Devices AD7572) by a single 12-bit analog-to-digital converter. The subsystem controller (NEC V40) collects the digitized values for all channels. The data are transmitted to the control subsystem via Omni-Net. In Exp-12/16, the data was to control PC via direct connection to check the detector status during the data taking.

- Monitoring Devices in Exp-34

  To obtain the higher confidence during the flight, we needed to gain more detail of detector's house-keeping information (e.g. High voltages for the PMTs of more than

100 channels, all status of the magnet, etc.). Therefore the new monitor subsystem which have a lot of channels was developed and installed in 2000. The new monitor subsystem is consists of many monitoring devices, and the feature is that each device has the network function based on a LON technology. Since it is easy to add or remove LON based devices from the LON network, we developed many kind of monitoring devices suit for the target sensors / devices as following:

(1) Main monitor box
This is alternative device of the previous BESS monitor and read the temperatures, pressures, and the Chamber High Voltages, currents. This device consists of a differential amplifier (Analog Devices AD620) which receive 0 to 5 (some special channel: -2.5 to 2.5) V, and an 12-bit analog-to-digital converter (MAXIM MAX146), and the Neuron Chip. The Neuron Chip is a 8-bit one-chip micro-computer developed by Echelon corporation. A role of the Neuron chip is to read digitized data from the ADC , and to send the data to the control subsystem by managing a network protocol called 'LON Talk'.

(2) PMT's High Voltage monitor box
The BESS detector has more than 100 PMTs. To monitor the their voltages and currents, we developed the special monitoring box. It consist of a lower power differential amplifier (Analog Devices AD623) which power consumption is 575 μA and analog-to-digital converter (MAXIM MAX146) and the Neuron chip. Since this box has 64 input channels which can receive 0 to 4.096V, we installed 3 this boxes for High Voltages of TOF (56ch), ACC (56ch), Scifi (32ch).

(3) Magnet monitor box
The magnet system has about 100 sensors to monitor its status. When we maintain the magnet system on the ground, the various informations were gathering without BESS monitor system, with direct connection before 2000. Only very import 16 informations were connected to BESS monitor subsystem. Thus, we developed the new monitor device to monitor the all information of magnet status in 2001. The new magnet monitor consists of a differential amplifier (Analog Devices AD628) and an analog-to-digital converter (MAXIM MAX146), and the Neuron chip. The AD628 require the operational current of 85 μA only and can receive input voltage of 0 to 0.5 V with 5 times gain. The features of MAX148 are (i) to operate by 2.7 V power supply, (ii) to require 1.3 mA of low operational current, (iii) to embedded the 2.5 V reference for A/D conversion. Besides a digital interface of MAX148 is compatible with MAX146 which is used other monitors. This means that we do not need to develop a new code for Neuron Chip and effort to its debug. As a result, this monitor box is ultra low power consumption and can operate low voltages (i.e. 3.3V). This excellent architecture is inherited to future long duration balloon flight BESS-Polar [**?**].

(4) External mini monitor
Some important house-keeping data is outside of the pressure vessel. One of

the such data is residual atmospheric pressure which is related with our physics deeply. The temperature of batteries are also important. If the batteries will became hot abnormally, we must turn off the DAQ system to avoid damages of detector or electronics. However, the Main monitor box described above is located inside the pressure vessel. To wire the signal cables to inside vessel, we must use the special expensive connector which can shield the vacuum. Thus, we developed and located the mini monitoring device (16ch) outside of the pressure vessel. This consists of AD623 and MAX146 and the Neuron chip described above respectively.

(5) GPS interface
We installed GPS sensor (Ashtech ADU2) in Exp-34 (BESS-2001) flight. This is the most precise GPS-based three-dimensional position and attitude determination system available, providing real-time heading pitch, and roll measurements with accurate position and velocity perfect for static and dynamic platforms. The default interface of this GPS is EIA RS-232C. Therefor, we developed the GPS management interface using Neuron chip. This device read the GPS data from RS-232S port of the GPS, then send the control subsystem via LON network.

The all monitor data is also transferred to the data-storage subsystem to be recorded for the off-line analysis.

2.6.9 Communication Subsystem

The communication subsystem manages communication between the payload and the ground station. A serial radio link is used for the transmission media. As a transceiver terminal of the radio link, Consolidated Instrument Package (CIP) is provided and attached to the payload by the National Scientific Balloon Facility (NSBF). The ground station sends commands to the payload through the radio link, and the CIP receives and interprets the commands as a 16-bit data. The control subsystem. And inversely, responses to the commands, message-data generated constantly by all subsystems, monitor-data for the house-keeping, and event-data sampled at two-second intervals are sent via the control subsystem to the CIP. Then the CIP sends them to the ground station through the radio link. Communication history is also recorded by the data-storage subsystem for off-line analysis.

2.7 Power Distribution System

2.7.1 Batteries

In spite of extensive efforts to reduce power consumption, the total power of the BESS detector amounts to 1.2 kW, which must be delivered from an on-board power source. A bank of primary (non-rechargeable) lithium batteries (Eternacell sulfur dioxide cells [57]) were used in this experiment. They have high energy density (∼35 Ah / 300g), high

current capability (3A continuous), wide operating temperature range (-40 to 85°) and relatively stable output voltage (∼2.8 V). Mode than 900 cells weighing about 240 kg were needed to drive a 24-hour flight of the BESS with some extra operations such as pre-flight test, dressed rehearsal and standby at runway.

Battery cells were stacked in series to comply with various voltages requirements of the electronics. Battery packs with 3 cells in series were used for 5 V supply allowing for some voltage droop of the battery and the voltage drop in regulators and cables. Packs with 7 (10) cells were also used for 15 (24) V supplies.

The power supply system of the BESS was subdivided into several groups; preamplifiers, high voltage supplies, CAMAC modules, FADC modules, data acquisition system, monitors and cooling fans. Each subsystem was supplied with power from separate battery banks. According to their power requirements, the appropriate number of battery packs were connected in parallel so that the possible operation time of each group well exceeds 35 hours. For safety reasons, at least two packs were used in any subsystem considering the accidental failure of the battery.

There are slight cell-to-cell differences in the output voltage of the batteries. In order to protect the batteries, which were connected in parallel from reverse bias, a low voltage drop Schottky diode was inserted in series to every battery pack.

2.7.2 Regulators

Most of the electronic circuits were implemented in custom made modules, which were housed in several crates. The power from the battery bank was directly fed to the power bus lines of the dedicated crates. The output voltage of the battery droops as time elapses. Every module of electronics was equipped with commercially available low-dropout voltage series regulators. While, we also used DC-DC converters for high voltage supplies and for Data-Storage subsystem which was located in compact magnetic shield vessel.

The Transputer bank consists of several commercial VME modules and their total load current exceeds 10 A. The distributed regulator configuration could not be applied to this system. Therefore a 5 V high current (30 A) series regulator with low dropout voltage (500 mV) has been developed to cope with requirement.

2.7.3 Control

A flexible and reliable power switch system is important to conduct the whole balloon experiment. Some of the power lines must be switched on / off simultaneously to assure proper operation of the system. Unbalanced voltage supplies might cause damage to the circuits. In addition, only a part of the apparatus is sometimes desired to be powered. In the pre-flight test with batteries, for example, the power consuming subsystem should be switched off after short checkout to save the battery power while the detector status are to be continuously monitored. The power control system is to switch on / off the individual battery groups by commands transmitted through radio link.

The BESS power control system also has been developed on the platform of Echelon LonWorks a technology. Receiving a command, the Neuron Chip interprets the command

and initiates a sequence of operations accordingly. The power control system consists of five relay nodes and a command node distributed along the local network. The command node functions as a controller of the relay nodes and issues messages to designated relay nodes, according to the commands addressed to the power control system. In the rely node the neuron, with its 11 I/O pins, is interfaced with 11 PhotoMOS relays [56]. The load currents of the power supplies varies from less than 1 A to about 50 A among the subsystem. Some of the PhotoMOS relays, which can switch a current up to 4 amperes, directly switch on / off the power supplies with lower load currents. For the higher current loads, the PhotoMOS relay s indirectly switch the power through driving solid state relays equipped with N-channel power FETs. The solid state relays are connected in parallel according to the load currents so that the voltage drops at the relays can be kept within a few tens mV.

The control system was duplicated for reliability. The power should be kept during the flight event in the case of accidental hardware failure or command loss due to bad radio link. Two relay nodes were connected in parallel and they were controlled by different sets of commands. The power was turned off only when the both switches were off.

Chapter 3

Observations

3.1 Observations at ground altitude

The BESS measurements at ground altitude were carried out during May 6-11. and Dec. 7-13. in 1997. We put the name of the experiment in May. as **'Exp-12'** and for that of the later period as **'Exp-16'**. The BESS apparatus was placed in high energy accelerator research organization (KEK), Tsukuba, Japan. The magnetic cut-off rigidity of this place is about 11.2 GV as shown in Figure 3.4. However, as will be mentioned in Chapter.6, the energy of the most contributing parent particle to the atmospheric antiprotons is more than 20 GeV. Therefore, It is no problem to observe the atmospheric antiprotons, although the observed antiproton flux does not contain the contribution of primary particles with the energy between antiproton threshold energy to cut-off energy.

Figure 3.1 shows the atmospheric pressure during the observations. During the period of these observations, the pressure change is small, and also the difference of the pressure in each period is very small. Therefore we will present the data of atmospheric antiprotons by combining the data observed in each period.

Figure 3.2 shows the temperature variation during the observations. The temperature was measured by a small thermister sensor (Analog Devices AD590J: 6.5 $\times$ 2.2 mm) attached to the JET chamber. The temperature change was within the range of 12 - 18 (9 - 17) °C in Exp-12 (Exp-16).

Tables 3.1 and 3.2 summarize the pressure, live time, dead time, and recorded number of event of each observation period respectively. The total live times were 63.1 and 114.1 hrs. in Exp-12 and Exp-16 respectively. The run number does not begin from RUN 1, as the earlier runs not listed in the tables were done for detector checking without magnetic field.

At the beginning of each run, a calibration run of 100 seconds was carried out to adjust thresholds for FADC data suppression as low as possible, because the pedestal value of FADC outputs varied depending on the temperature. Then, normal data acquisition with data suppression starts and lasts for one or two hours.

During the data acquisition runs, the live time was measured with 1 μs accuracy using a crystal oscillator. In the ground experiment, dead time fraction is smaller than 1 %.

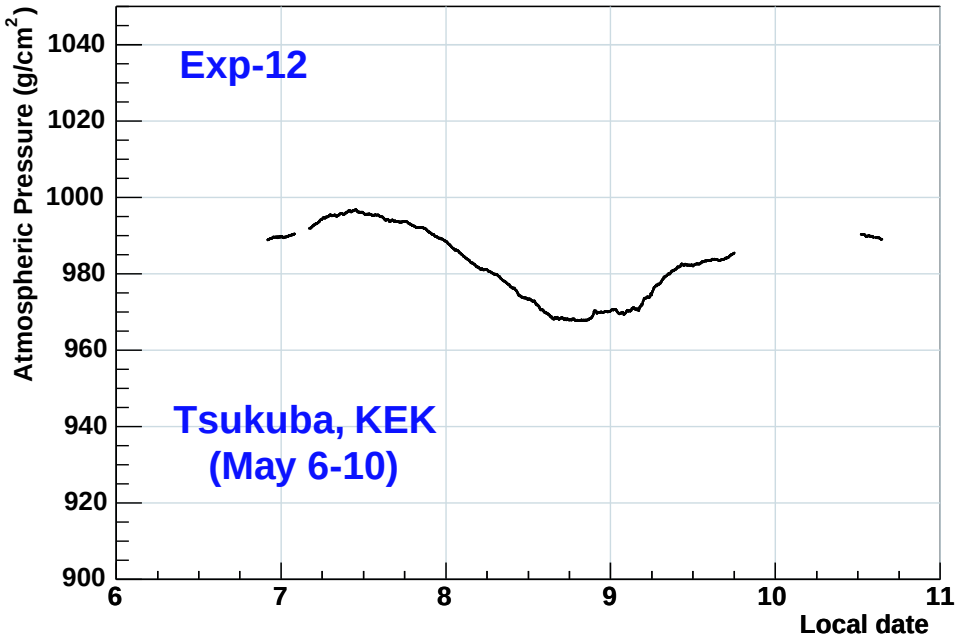

Figure 3.1: The atmospheric depth vs local date. The time is 0:00 on the grid line with the numerical label.

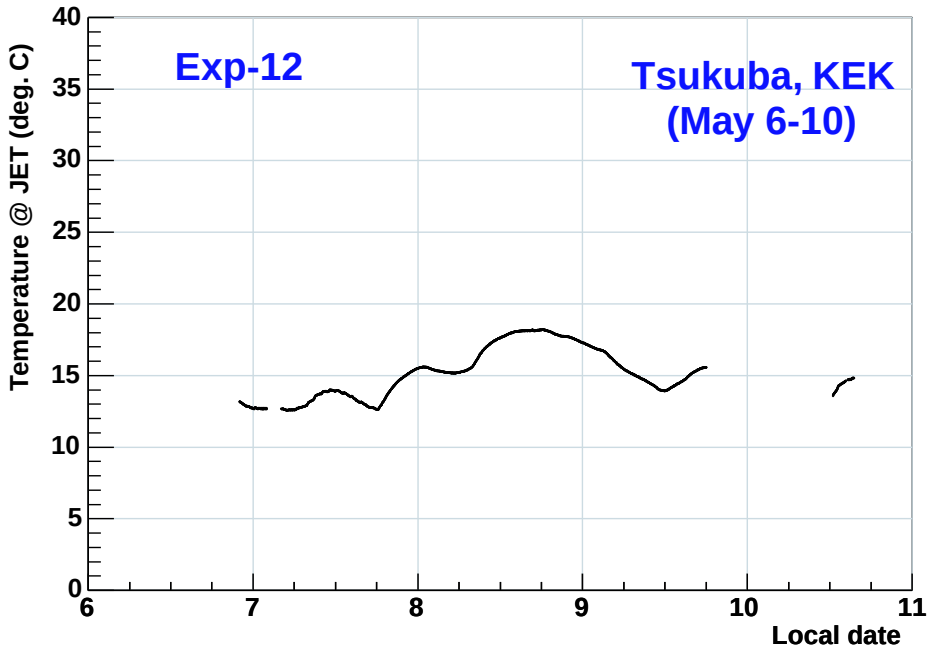

Figure 3.2: The temperature vs local date. The time is 0:00 on the grid line with the numerical label. The change is within 10 degree.

Table 3.1: Summary of Exp-12.

RUN	Local Time	Pressure (g/cm^2)	DAQ time (s)	Live time (s)	Dead time (%)	Recorded event
41	00:06 - 01:58	989.4 - 990.5	7422.1	7376.3	0.6	217278
44	08:02 - 10:03	994.9 - 996.7	6516.3	6475.8	0.6	190229
45	10:05 - 12:00	995.9 - 996.9	7207.3	7162.7	0.6	209118
46	12:01 - 14:01	995.2 - 995.9	7273.3	7228.4	0.6	210616
47	14:03 - 16:00	993.7 - 995.5	6841.7	6799.5	0.6	198473
48	16:01 - 17:59	993.5 - 994.1	7187.1	7142.4	0.6	207769
49	18:00 - 19:59	992.1 - 993.8	6992.6	6949.4	0.6	203263
50	20:01 - 22:01	990.4 - 992.2	7059.2	7015.4	0.6	205745
51	22:02 - 00:01	988.5 - 990.4	6576.4	6535.3	0.6	206525
52	00:02 - 02:00	985.5 - 988.4	7119.5	7075.2	0.6	207300
53	02:02 - 04:00	982.7 - 985.5	7113.6	7069.2	0.6	207858
54	04:01 - 05:59	981.0 - 982.7	7084.2	7039.4	0.6	208004
56	08:09 - 10:01	976.1 - 978.5	7077.3	7032.2	0.6	209371
57	10:03 - 11:59	973.3 - 976.1	7568.7	7520.2	0.6	223315
58	12:00 - 13:59	970.5 - 973.5	6712.5	6666.6	0.7	194812
59	14:01 - 15:59	968.1 - 970.7	6966.9	6921.7	0.6	205034
60	16:01 - 18:00	967.9 - 968.6	7135.5	7088.5	0.7	210792
61	18:01 - 19:58	967.6 - 968.2	7061.1	7014.5	0.7	210037
62	19:59 - 21:57	967.7 - 970.4	7135.0	7089.0	0.6	212893
63	21:59 - 23:59	969.7 - 970.3	6976.7	6932.0	0.6	208900
64	00:01 - 02:03	969.3 - 970.8	7070.0	7024.4	0.6	211463
65	02:04 - 03:59	969.7 - 971.2	7201.8	7155.3	0.6	215283
66	04:00 - 06:00	970.3 - 974.9	3560.6	3537.4	0.7	106239
67	06:02 - 07:10	974.8 - 977.6	6881.9	6836.9	0.7	206078
68	07:11 - 08:05	977.4 - 979.4	7176.9	7130.1	0.7	215241
69	08:06 - 10:02	979.5 - 981.9	4038.7	4013.4	0.6	120484
70	10:03 - 12:00	981.9 - 982.7	3201.9	3181.4	0.6	95627
71	12:02 - 14:00	982.1 - 983.4	6951.8	6907.4	0.6	206499
72	14:02 - 15:59	983.4 - 983.9	7038.2	6993.6	0.6	209440
73	16:01 - 18:00	983.5 - 985.4	7066.0	7021.4	0.6	210097
74	12:27 - 13:31	989.7 - 990.4	7035.9	6991.2	0.6	209774
75	13:33 - 14:17	989.5 - 990.0	7107.4	7062.3	0.6	211670

Table 3.2: Summary of Exp-16.

RUN	Local Time	Pressure (g/cm^2)	DAQ time (s)	Live time (s)	Dead time (%)	Recorded event
7	15:21 - 16:18	997.2 - 997.6	4705.4	4676.9	0.6	140637
8	16:19 - 17:38	997.5 - 998.4	3569.4	3547.8	0.6	106125
9	17:39 - 18:39	998.3 - 998.8	4836.9	4807.6	0.6	144808
10	18:41 - 20:01	998.8 - 999.6	3556.9	3535.4	0.6	106394
11	20:03 - 21:02	999.5 - 999.9	3393.0	3372.6	0.6	101433
12	21:04 - 22:01	999.7 - 1000.0	3516.3	3495.1	0.6	104752
13	22:02 - 23:01	999.8 - 1000.0	4079.6	4054.8	0.6	122436
14	23:03 - 00:11	999.5 - 999.9	3437.7	3416.7	0.6	103965
15	00:12 - 01:10	999.6 - 999.8	3924.7	3900.8	0.6	118196
16	01:11 - 02:17	999.2 - 999.6	3495.1	3473.6	0.6	105758
17	02:18 - 03:16	998.9 - 999.3	3864.6	3841.3	0.6	116459
18	03:18 - 04:23	998.9 - 999.2	3495.9	3474.2	0.6	105777
19	04:24 - 05:22	999.1 - 999.5	3511.5	3489.8	0.6	106236
20	05:24 - 06:23	999.6 - 999.8	3552.6	3531.0	0.6	106435
21	06:25 - 07:24	999.8 - 1000.0	4134.8	4109.6	0.6	124399
22	08:36 - 09:32	998.4 - 999.5	3355.8	3335.4	0.6	101536
23	09:34 - 10:46	996.6 - 998.3	3579.5	3557.5	0.6	108299
24	10:48 - 11:45	995.0 - 996.6	3399.9	3379.2	0.6	102676
25	11:46 - 12:43	994.0 - 995.0	3410.2	3389.4	0.6	102917
26	12:45 - 13:55	993.6 - 993.9	3444.5	3423.4	0.6	103936
27	13:56 - 15:01	993.7 - 994.0	3902.1	3878.2	0.6	117969
28	15:03 - 15:56	993.9 - 994.2	3159.7	3140.5	0.6	95781
29	15:57 - 16:55	994.2 - 994.8	3473.8	3452.4	0.6	105145
30	16:57 - 17:54	994.8 - 995.7	3392.7	3372.0	0.6	102260
31	17:55 - 18:19	995.8 - 996.3	1450.2	1441.6	0.6	43619
32	18:21 - 19:33	996.4 - 997.4	3811.1	3787.8	0.6	115216
33	19:34 - 20:34	997.3 - 997.7	3595.2	3573.1	0.6	108847
34	20:36 - 21:35	997.6 - 997.8	3507.8	3486.6	0.6	105712
35	21:36 - 22:36	997.8 - 998.1	3618.6	3596.4	0.6	109561
36	22:38 - 23:37	998.1 - 998.3	3555.9	3534.1	0.6	107527
37	23:39 - 00:37	998.2 - 998.7	3445.5	3424.5	0.6	103455
38	00:38 - 01:39	998.7 - 999.3	3641.4	3618.9	0.6	110184
39	01:40 - 02:37	999.2 - 999.6	3403.4	3382.6	0.6	102996
40	02:39 - 03:34	999.4 - 999.5	3283.6	3263.5	0.6	99298
41	03:35 - 04:36	999.5 - 1000.2	3632.9	3610.7	0.6	109707
42	04:37 - 05:35	1000.1 - 1000.6	3468.3	3447.2	0.6	104431
43	05:37 - 06:32	1000.6 - 1001.3	3290.5	3270.2	0.6	99855
44	06:33 - 07:36	1001.2 - 1002.1	3768.5	3745.4	0.6	113743

RUN	Local Time	Pressure (g/cm^2)	DAQ time (s)	Live time (s)	Dead time (%)	Recorded event
45	07:38 - 08:30	1001.7 - 1002.0	2869.1	2858.6	0.4	86362
47	10:02 - 11:07	999.6 - 1000.4	3885.1	3861.5	0.6	117276
48	11:08 - 12:00	999.0 - 999.5	3082.3	3063.3	0.6	93396
49	12:01 - 13:02	998.6 - 999.1	3679.7	3657.5	0.6	110653
50	13:04 - 14:00	998.5 - 998.9	3333.6	3313.1	0.6	100662
51	14:02 - 15:06	998.8 - 999.3	3863.0	3839.3	0.6	116314
52	15:08 - 16:05	999.3 - 999.9	3383.1	3362.6	0.6	101465
53	16:06 - 17:01	999.8 - 1000.5	3296.6	3276.5	0.6	98212
54	17:03 - 18:01	1000.5 - 1001.5	3457.6	3436.8	0.6	102766
55	18:02 - 19:01	1001.6 - 1002.8	3522.6	3501.2	0.6	105466
56	19:02 - 20:02	1002.8 - 1003.4	3596.0	3574.4	0.6	107060
57	20:04 - 21:01	1003.3 - 1003.9	3383.3	3362.8	0.6	100791
58	21:02 - 22:02	1003.9 - 1004.5	3287.1	3267.4	0.6	97425
59	22:04 - 23:05	1004.5 - 1005.0	3644.3	3622.2	0.6	108832
60	23:06 - 00:03	1005.0 - 1005.4	3434.6	3414.2	0.6	101383
61	00:05 - 01:05	1005.4 - 1005.9	3571.1	3549.5	0.6	106218
62	01:07 - 02:05	1005.7 - 1005.9	3470.2	3449.3	0.6	102742
63	02:06 - 03:05	1005.7 - 1005.9	3516.6	3495.1	0.6	105047
64	03:06 - 04:03	1005.7 - 1006.3	3378.4	3358.1	0.6	100389
65	04:04 - 05:04	1006.1 - 1006.5	3599.6	3577.6	0.6	107106
66	05:06 - 06:03	1006.4 - 1007.0	3416.6	3396.0	0.6	101960
67	06:05 - 07:09	1007.0 - 1007.6	3845.5	3822.0	0.6	114991
68	07:11 - 08:04	1007.6 - 1007.9	3214.5	3194.9	0.6	95541
69	08:06 - 09:04	1006.7 - 1007.7	3002.1	2984.0	0.6	89461
70	09:05 - 10:05	1006.2 - 1006.7	3572.2	3550.8	0.6	106289
71	10:06 - 11:15	1004.8 - 1006.2	2834.3	2817.0	0.6	84454
72	14:14 - 15:21	1003.0 - 1003.2	3567.2	3545.4	0.6	107210
73	15:22 - 16:29	1003.0 - 1003.2	4029.8	4005.5	0.6	120336
74	16:31 - 17:26	1003.0 - 1003.2	3281.8	3261.9	0.6	97824
75	17:27 - 18:29	1003.2 - 1003.5	3727.2	3704.5	0.6	111712
76	18:31 - 19:32	1003.4 - 1003.5	3625.6	3603.4	0.6	108435
77	19:33 - 21:19	1002.8 - 1003.5	6358.0	6319.4	0.6	190375
78	21:21 - 22:09	1002.5 - 1002.8	2876.0	2858.3	0.6	86391
79	22:11 - 23:13	1001.9 - 1002.5	3691.5	3669.0	0.6	110939
80	23:14 - 00:11	1001.4 - 1001.9	3392.1	3371.6	0.6	101894
81	00:12 - 01:07	1001.1 - 1001.4	3265.8	3245.9	0.6	97804
82	01:08 - 02:07	1000.9 - 1001.2	3555.7	3534.1	0.6	106929
83	02:09 - 03:04	1000.6 - 1001.0	3312.7	3292.4	0.6	99063
84	03:06 - 04:05	1000.3 - 1000.6	3544.6	3523.1	0.6	106267
85	04:07 - 05:07	1000.1 - 1000.4	3605.5	3583.3	0.6	108701

RUN	Local Time	Pressure (g/cm^2)	DAQ time (s)	Live time (s)	Dead time (%)	Recorded event
86	05:09 - 06:05	1000.3 - 1000.6	3322.4	3302.0	0.6	99396
87	06:06 - 07:06	1000.5 - 1000.9	3575.8	3554.0	0.6	107785
88	07:07 - 08:09	1000.7 - 1001.1	3711.7	3689.0	0.6	112024
89	08:11 - 09:00	1000.8 - 1001.1	2934.8	2916.9	0.6	88164
90	09:01 - 10:02	999.9 - 1001.0	3665.1	3642.6	0.6	110364
91	10:04 - 11:01	998.4 - 1000.0	3436.5	3415.4	0.6	104364
92	11:03 - 12:04	997.1 - 998.4	3623.6	3601.7	0.6	108943
93	12:05 - 12:59	996.2 - 997.0	3244.9	3225.2	0.6	98116
94	13:01 - 14:01	996.2 - 996.5	3585.9	3564.1	0.6	108047
95	14:02 - 15:01	996.4 - 997.0	3497.8	3476.5	0.6	104746
96	15:02 - 16:11	997.0 - 997.8	4071.4	4046.5	0.6	122916
97	16:12 - 17:01	997.8 - 998.4	2904.8	2886.9	0.6	87413
98	17:02 - 18:02	998.3 - 999.7	3567.9	3546.1	0.6	107364
99	18:03 - 19:03	999.6 - 1000.9	3577.8	3556.2	0.6	106814
100	19:05 - 20:02	1000.9 - 1001.8	3403.6	3382.8	0.6	102179
101	20:03 - 21:03	1001.6 - 1002.1	3586.9	3565.1	0.6	107510
102	21:05 - 22:01	1001.9 - 1002.2	3380.7	3360.1	0.6	101471
103	22:03 - 23:02	1001.7 - 1002.2	3517.3	3495.8	0.6	105593
104	23:03 - 00:02	1001.6 - 1001.9	3502.4	3481.0	0.6	104998
105	00:03 - 01:01	1001.7 - 1002.0	3475.9	3454.9	0.6	103547
106	01:03 - 02:02	1001.3 - 1001.7	3500.6	3479.3	0.6	104801
107	02:03 - 03:01	1000.8 - 1001.4	3495.5	3474.2	0.6	104958
108	03:03 - 04:01	1000.4 - 1000.8	3495.3	3473.9	0.6	105083
109	04:03 - 05:01	1000.1 - 1000.5	3496.2	3475.1	0.6	105034
110	05:03 - 06:01	1000.1 - 1000.8	3524.6	3503.2	0.6	106229
111	06:03 - 07:01	1000.7 - 1000.9	3469.2	3448.3	0.6	104266
112	07:03 - 08:00	1000.5 - 1000.9	3496.4	3475.2	0.6	105858
113	08:02 - 09:02	999.8 - 1000.8	3568.2	3546.5	0.6	107490
114	09:04 - 10:18	998.2 - 999.9	4429.1	4402.0	0.6	133253
115	10:19 - 11:07	996.3 - 998.2	2866.1	2848.5	0.6	87240
116	11:09 - 12:10	994.6 - 996.3	3673.3	3650.6	0.6	111057
117	12:12 - 13:06	993.3 - 994.5	3261.3	3241.3	0.6	98801
118	13:08 - 13:52	992.2 - 993.3	2669.8	2653.3	0.6	80699
119	15:04 - 16:17	991.2 - 992.0	1928.9	1917.0	0.6	58865
120	16:19 - 17:22	991.3 - 991.6	3754.3	3731.3	0.6	113446
121	17:23 - 18:07	991.3 - 991.6	2640.6	2624.4	0.6	80665
122	18:09 - 19:08	991.4 - 991.7	3555.3	3533.5	0.6	107607
123	19:10 - 20:02	990.9 - 991.7	3142.2	3123.3	0.6	94781
124	20:04 - 21:02	990.4 - 990.9	3452.6	3431.3	0.6	103964

3.2 Balloon Observations

The BESS apparatus was launched at Ft. Sumner, New Mexico, USA in the morning of Sep. 24. in 2001. We also put the name of **'Exp-34'** for this experiment. In this flight, 39 Mft^3 (1.1×10^6 m^3) balloon was used. The suspended weight was 3563 kg consisting of the 2,449 kg BESS apparatus, 635kg ballast and others. The balloon trajectory is shown in Figure 3.3. Through the flight, the magnetic cut off rigidity was about 4.2 GV as shown in Figure 3.4.

Figures 3.5-3.7 show the altitude and residual atmospheric depth during the flight which was monitored in every 4 second. The residual atmosphere was about 4.5 g/cm^2 in the first 2 hour of the floating, and after that the balloon descended continuously and until the residual atmosphere reached 30 g/cm^2. The observation was terminated after turning off the magnetic field and all the electronics at the end of the experiment. Then the instrument was recovered near Alberquerque, New Mexico, locating about 300 km east from Ft. Sumner.

The preparation for observation has started from afternoon of the day before the launching. First, we checked the detector status with magnetic field in a hanger where preparatory work had been done. The check was carried out by using AC power supply at first. Next we connected batteries to the BESS apparatus and checked the detector. After this check, the power of the BESS apparatus were turned off except for control, communication, and monitor subsystem. Then the BESS apparatus suspended by a launch vehicle was moved to launching point and waited for the sun rise and good wind condition.

The power for all the detector and electronics were turned on 30 minutes before launching. In this point, a tape drive was waiting mode to avoid damage by the shock of launching. The data acquisition began immediately and the data were transfered to a tape drive for recording.

Trigger parameters were carefully adjusted to achieve a desired trigger rate, based on the counting rate obtained in a short test run just before the level flight. When the detector passed through the shower max altitude (about 100 g/cm^2 of atmospheric depth), there was a possibility of hung-up of data acquisition system by a higher event rate. Therefore, we prepared the alternative trigger condition which is more safety-side criteria. If our event rate estimation was not correct, we can change the trigger condition by sending a command. In the level flight, typical recording rate was about 240 Hz.

For the change of the temperatures of the detector components (Figures 3.8-3.10), we also carried out a calibration run for adjustment of FADC at the beginning of the each run. Normal data taking with data suppression was carried out for one hour. Table 3.3 summarizes the local time, atmospheric pressure, DAQ time, and recorded event number. With an appropriate trigger setting, the dead time fraction was smaller than 10% for all runs.

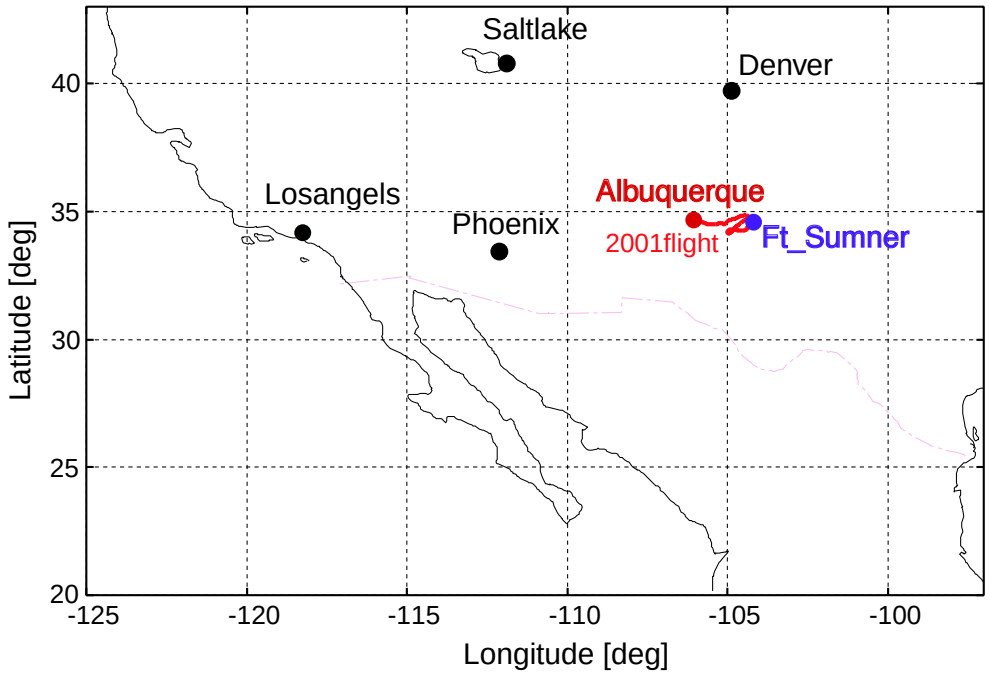

Figure 3.3: Flight path for Exp-34.

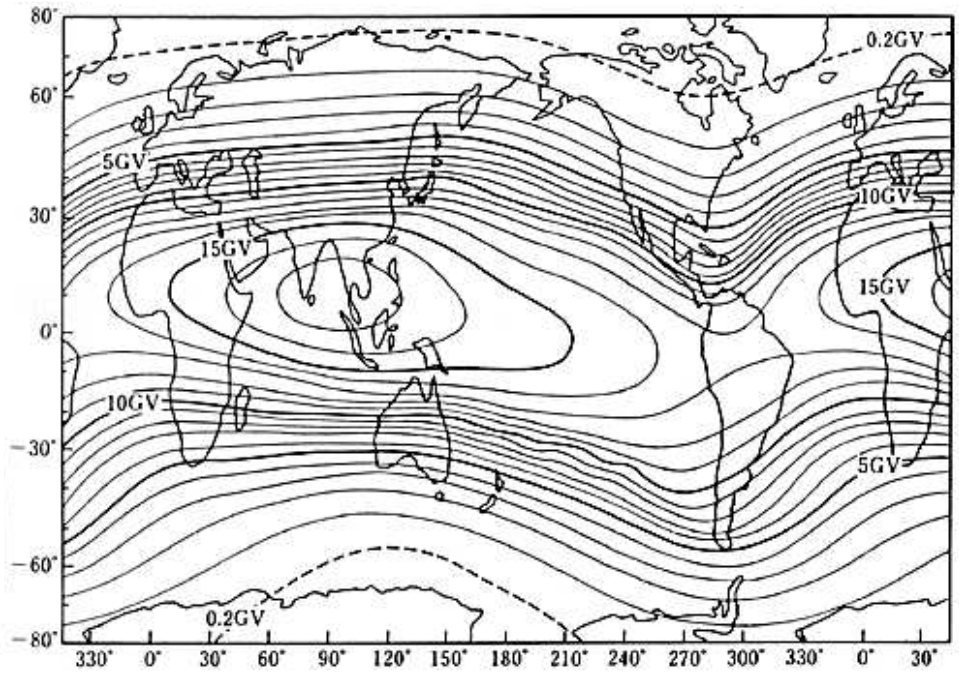

Figure 3.4: The contour map for geomagnetic cut-off rigidity.

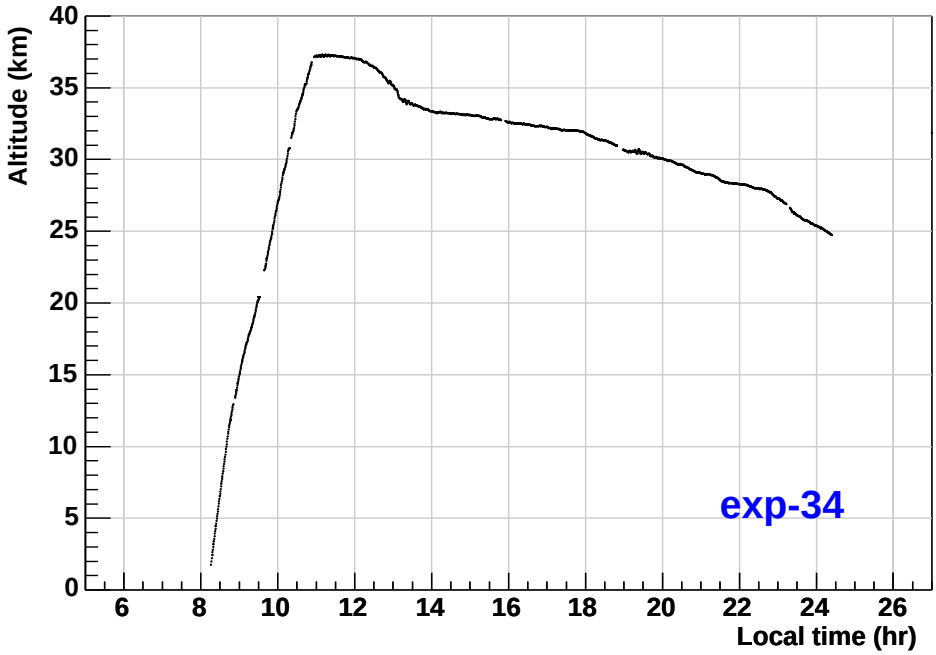

Figure 3.5: House-keeping data on float altitude.

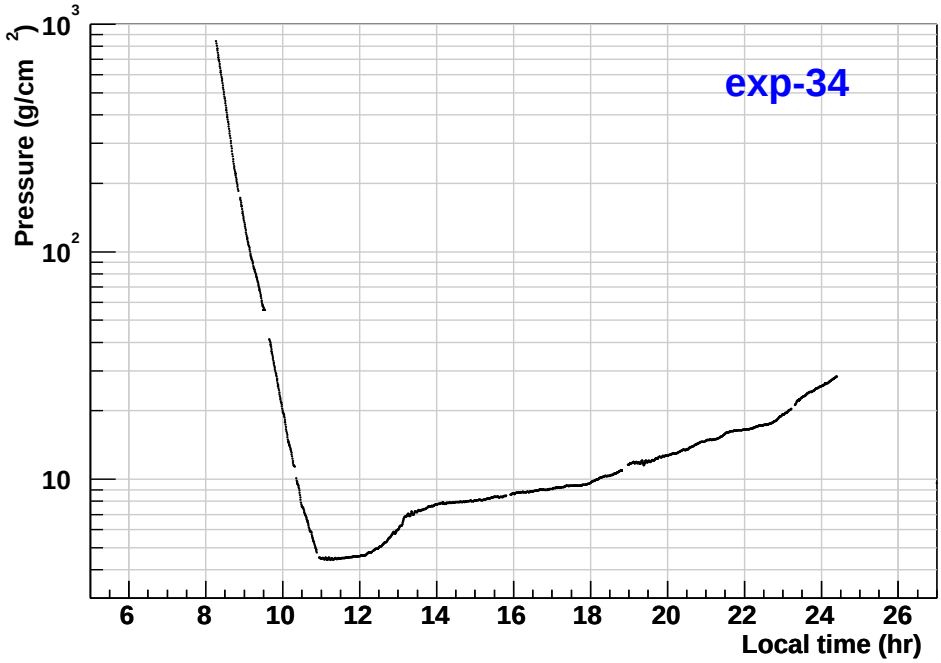

Figure 3.6: House-keeping data on atmospheric pressure.

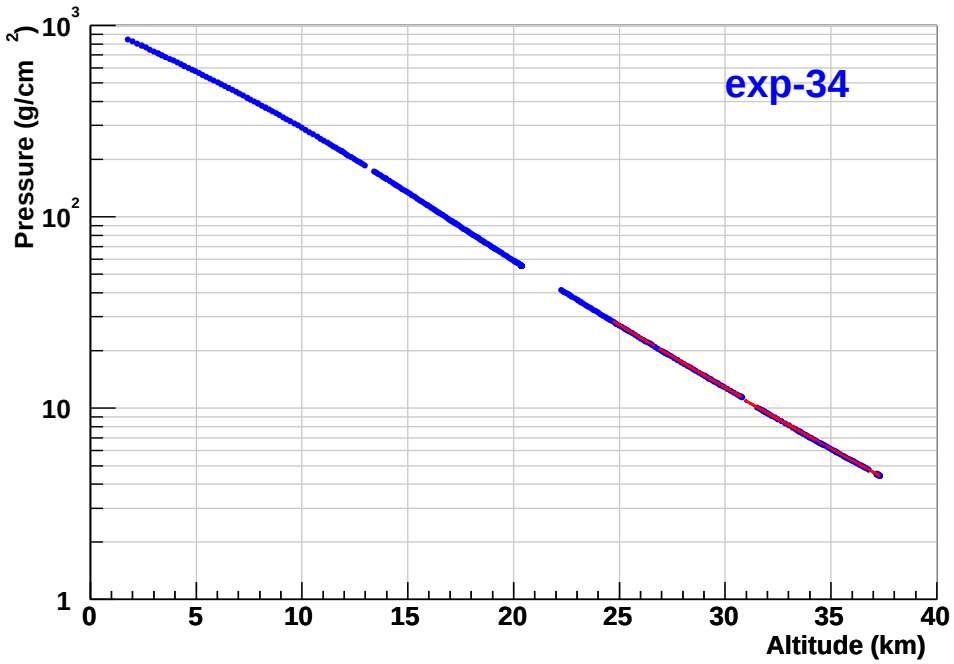

Figure 3.7: The pressure vs altitude. Blue data was gathered in ascending period and red one was gathered in floating (drooping) period. The good matching of two data indicates excellent performance of our pressure sensor and GPS.

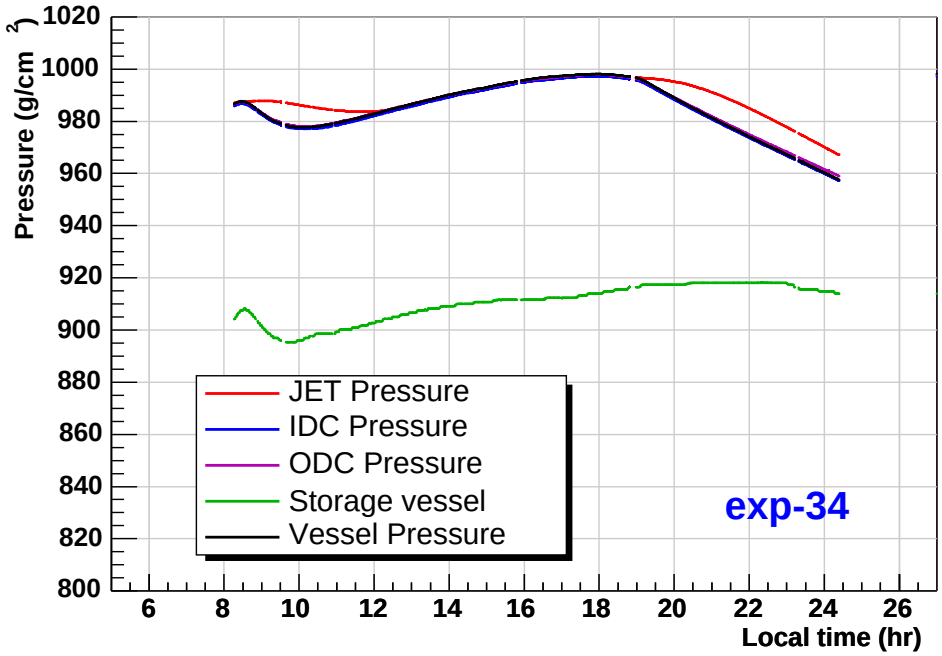

Figure 3.8: House-keeping data of pressure in the detectors.

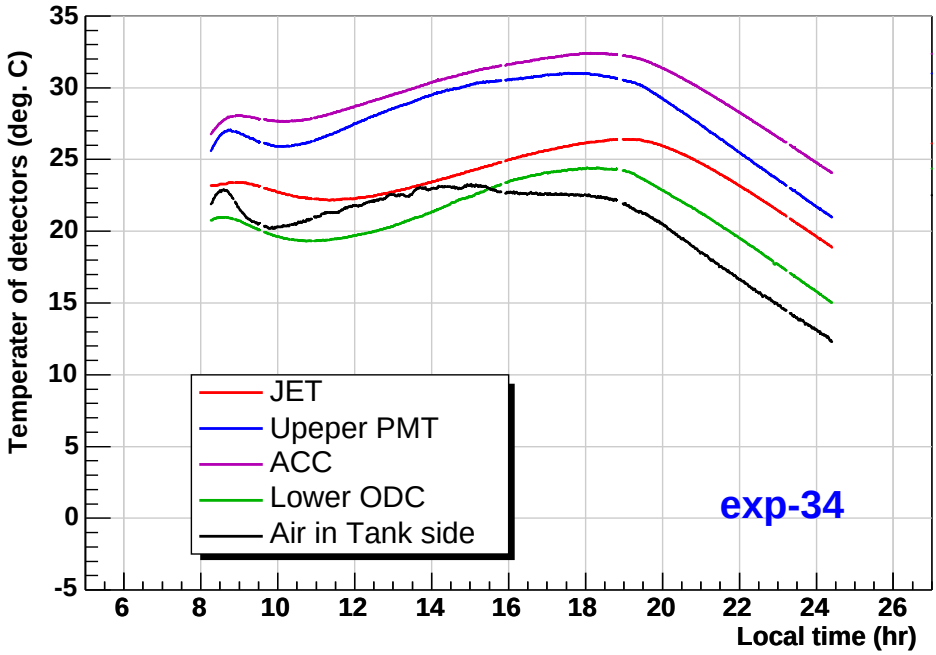

Figure 3.9: House-keeping data of detectors.

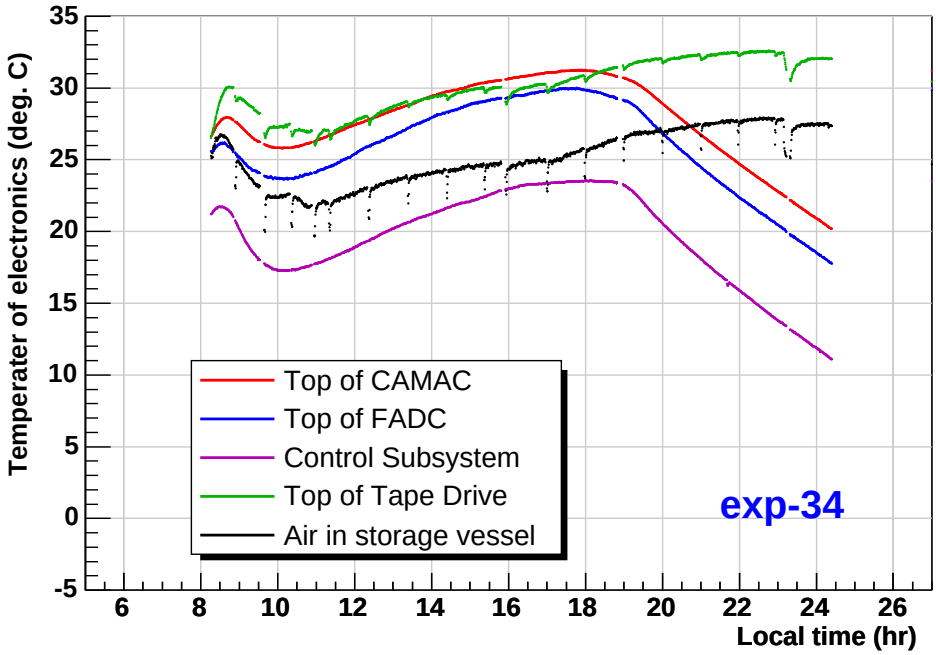

Figure 3.10: House-keeping data of electronics.

Table 3.3: Summary of Exp-34.

RUN	Local Time	Pressure (g/cm^2)	DAQ time (s)	Live time (s)	Dead time (%)	Recorded event
2	08:53 - 09:31	55.6 - 172.8	2384.9	2185.7	8.4	505403
3	09:39 - 10:18	11.4 - 41.3	2317.6	2120.3	8.5	461077
4	10:21 - 10:53	4.8 - 10.1	1829.3	1693.9	7.4	280548
5	10:56 - 11:18	4.4 - 4.5	1249.8	1165.4	6.7	186271
6	11:19 - 12:19	4.4 - 4.8	3496.5	3169.1	9.4	770080
7	12:21 - 13:21	4.9 - 7.2	3546.3	3219.0	9.2	778717
8	13:22 - 14:22	7.0 - 7.9	3528.5	3313.1	6.1	512060
9	14:23 - 15:20	7.9 - 8.2	3410.0	3106.8	8.9	803598
10	15:21 - 15:48	8.2 - 8.5	1545.8	1407.6	8.9	368402
11	15:55 - 16:57	8.6 - 9.1	3690.4	3370.8	8.7	866564
12	16:59 - 17:57	9.1 - 9.5	3400.4	3103.5	8.7	796961
13	18:00 - 17:59	9.6 - 10.9	3515.2	3203.9	8.9	839551
14	18:58 - 19:58	11.5 - 12.7	3533.7	3220.9	8.9	853442
15	19:58 - 20:57	12.7 - 14.6	3490.2	3181.4	8.8	850971
16	20:58 - 21:56	14.7 - 16.5	2909.4	2647.7	9.0	710459
17	21:57 - 22:54	16.5 - 18.8	3374.0	3050.4	9.6	829945
18	22:54 - 23:13	18.9 - 20.4	759.7	685.2	9.8	189708
19	23:18 - 00:24	21.2 - 28.3	1957.4	1762.7	9.9	503000

Chapter 4

Analysis

This chapter describes the data analysis of the flight data. Section 4.1 describes the selection of antiprotons, Then in Section 4.2, we show the properties of selected antiprotons.

4.1 Antiproton Selection

In order to measure the absolute flux of $\overline{p}$'s, we need to know its kinetic energy at the top of the instrument, detection efficiency, and background contamination. Therefore, it is inevitably important to select events (i) without interaction inside the detector, (ii) with the accurate measurements, and (iii) mass-identified as $\overline{p}$'s for $\overline{p}$ detection.

Protons are obtained with sufficient statistics, because they are the most abundant species in cosmic radiation. We applied the same selection criteria for $\overline{p}$'s and protons because non-interacting $\overline{p}$'s behave like protons except for deflection in the symmetrical configuration of BESS. Selection of $\overline{p}$'s and protons is follows into three steps, "pre-selection", "quality cut", and "identification". Pre-Selection selects non-interacting particles inside the detector. Some efficiencies in this step are determined by using the Monte Carlo simulation for BESS. Quality cut selects events having "good" conditions for measurements to ensure accurate rigidity determination. Identification is performed principally by unambiguous mass determination. The event-selection criteria is summarized in Table 4.4.

4.1.1 Pre-Selection

At the first stage of the event selection, following cuts are applied to obtain fully contained events in the fiducial region without interaction inside the detector. In this section, details of description are presented.

Selection of Non-interacted Events

- $N_{longTK} = 1$ (Figure 4.1)

  Only the events with long track are used for the analysis should be only one. The "long track" is defined as following. (i) We search for cluster of 10 or more hits

in JET chamber. (ii) For each arrays the number of JET hits expected from the trajectory (N_{expect}) is calculated. (iii) Cluster with enough hits ($> 0.6 \times N_{except}$) is regarded as a "long track".

If an accidental particle uncorrelated with a triggering particle passed through the instruments, it would leave some hits in the detectors. For multi track event, we checked if their tracks have interaction vertex. If they does not have a vertex, the other track are considered as accidental, and it is saved as an event to be analyzed. Therefore, we also define such events as $N_{longTK} = 1$.

- $N_{JET} \leq 60$ (Figure 4.1)

  Since it is difficult to derive correct information from extremely noisy events, the number of JET hits not associated to the track is limited within a certain number.

- $N_{TOF_U} = 1$, N_{TOF_L} =1 or 2 (Figure 4.2)

  There should be only one hit in the top TOF counters, and one or two hits in the bottom. The different selection for lower TOF hodoscope is accepted to save events associated with delta ray.

- $|\Delta X_U| \leq 60mm$, $|\Delta X_L| \leq 60mm$ (Figure 4.3)

  In the r-ϕ plane the extrapolated trajectory should pass through the top and bottom hit TOF counters. where

$$\Delta X_{U,L} = X_{TK_{U,L}} - X_{TOF_{U,L}}$$

  Note that $X_{TOF_{U,L}}$ represent central position of the hit of TOF counter. This condition ensure that (i) the track information and TOF information are concerned with the same particle, and (ii) the interaction events inside the coil are removed.

- $|\Delta Z_U| \leq 45mm$, $|\Delta Z_L| \leq 45mm$ (Figure 4.4)

  z position in TOF hits should be consistent with trajectory. where

$$\Delta Z_{U,L} = Z_{TK_{U,L}} - Z_{TOF_{U,L}}$$

  Expected hit position in the TOF counter along the z-coordinate can be determined from extrapolation of the trajectory determined by the JET chamber ($Z_{TK_{U,L}}$), and also determined by using the time difference between two signals from the both end of the counter($Z_{TOF_{U,L}}$). Two values of the hit position should be consistent to accept the event.

- $\mathrm{d}E/\mathrm{d}x$ in upper and lower TOF band cut

  Because of the relatively broad angular distribution of "recoil" (knock-on) protons [58], there is a non-negligible probability that incident particles escape from the BESS acceptance and only the recoil secondary protons go into the tracking volume. Such events lose large fraction of energy in the upper TOF, and gives broad tail in the $\mathrm{d}E/\mathrm{d}x$ distribution. In the low energy region (below ~ 0.5 GeV), a recoil

proton is dominant component among secondary particles of interacted events. Figure 4.5 shows a typical example of such a recoil events with large $\mathrm{d}E/\mathrm{d}x$ in upper TOF counters simulated by Monte Carlo simulation (MC) using GEANT [59]. On the other hand low energy protons do not have a tail for higher energy (Landau tail) inside $\mathrm{d}E/\mathrm{d}x$ distribution because of suppression of high energy delta-ray production. As a result, in order to (i) estimate accurately the efficiency of $\mathrm{d}E/\mathrm{d}x$ cut for $\overline{p}$'s, and (ii) determine proton flux in the low energy region, it is important to reject such recoil protons (produced by the interactions) during pre-selection. The efficiency is estimated by using the Monte Carlo simulation. Figures 4.9-4.11 show simulated $\mathrm{d}E/\mathrm{d}x$ distributions in each rigidity region together with the observed distributions. As show in these figures the simulated and observed $\mathrm{d}E/\mathrm{d}x$ distribution are well-agreed with other around their peek. Below 1 GV, however, observed distribution has long upper tail in higher energy side. The cut boundaries for $\mathrm{d}E/\mathrm{d}x$-band cut in upper TOF counters were determined to eliminate the such recoil event. The selection boundaries are indicated by solid blue curves in Figures 4.6-4.8. It should be note that ΔZ_U cut described above also plays a role to remove the "recoil-proton" influence in this selection procedure.

Definition the Fiducial Volume

- $N_{expect} \geq 16, N_{center} \geq 10$ (Figure 4.13)

  N_{expect} is described in the previous section. While, N_{center} is defined as the expected number of hits in the central region of JET chamber. The wire lines in JET chamber are divided into 4 sections. In each of the two central (side) section, 24 (16) sense wires are read out. These cuts define the fiducial region in the r-ϕ plane. We show the event sample satisfied this cut, while events unsatisfied are not shown in Figure 4.14.

- -480mm$\geq Z_{TK_{U,L}} \geq$470mm (Figure 4.15)

  By extrapolating the trajectory found in JET chamber, the expected hit positions at the top and bottom TOF counters are calculated. We require the positions to be within the scintillator of the counters. This cut defines the fiducial region in the y-z plane.

- $\beta > 0$ (Figure 4.12)

  Using this condition, the albedo particles are eliminated.

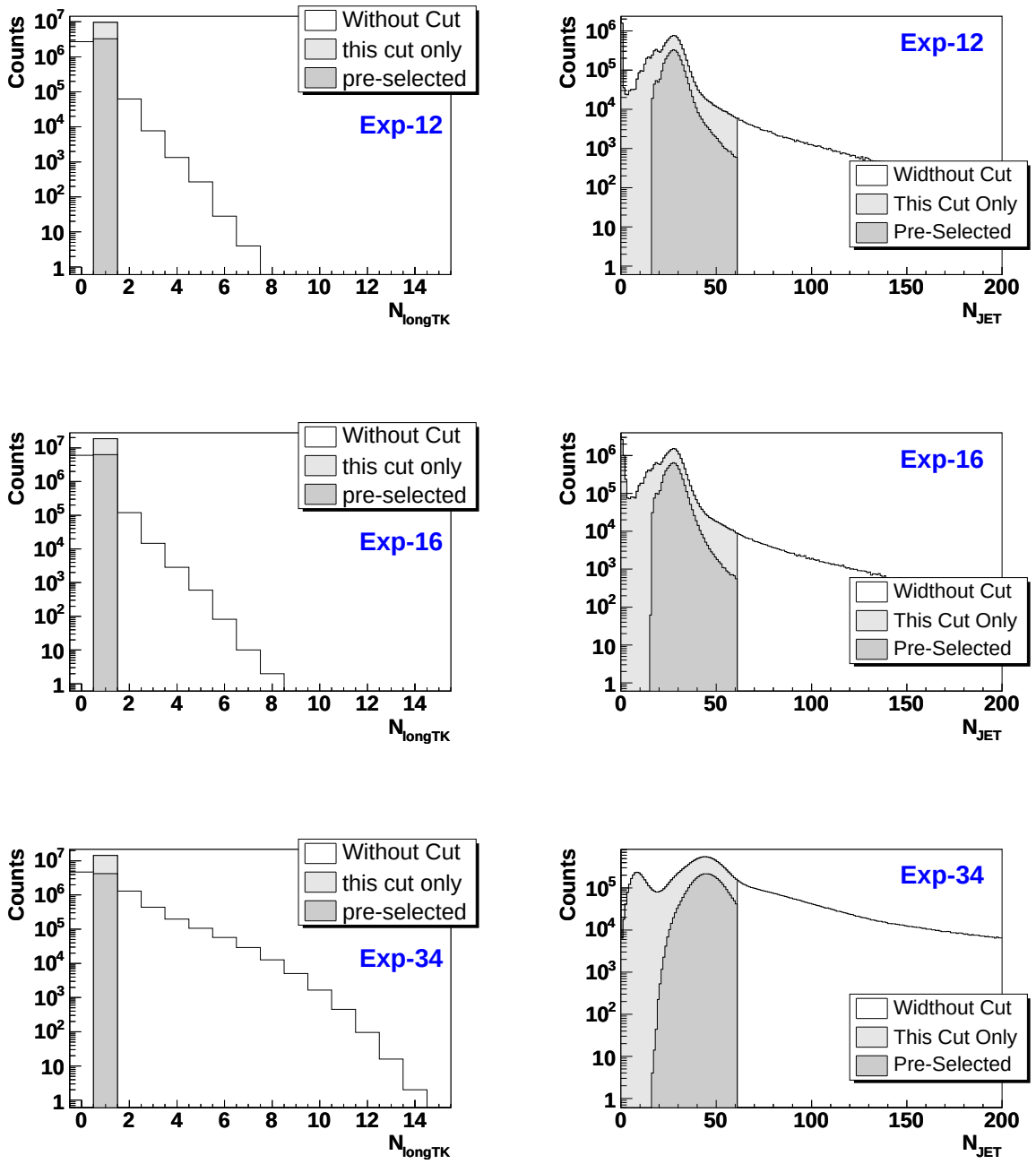

Figure 4.1: The distribution of long tracks (left) and the number of hits in JET (right).

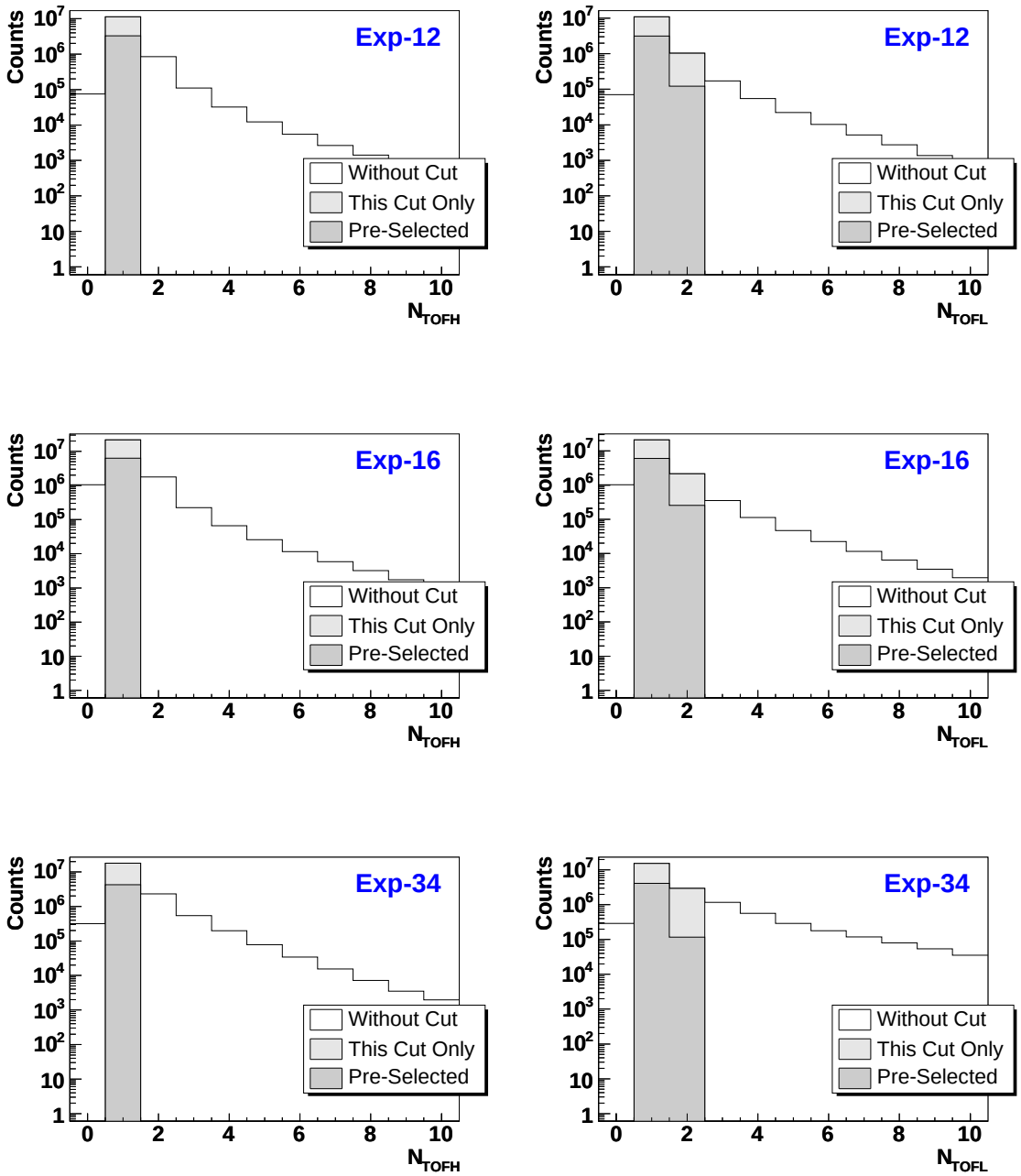

Figure 4.2: The distribution of hits in the Upper TOF (left) and the Lower TOF (right).

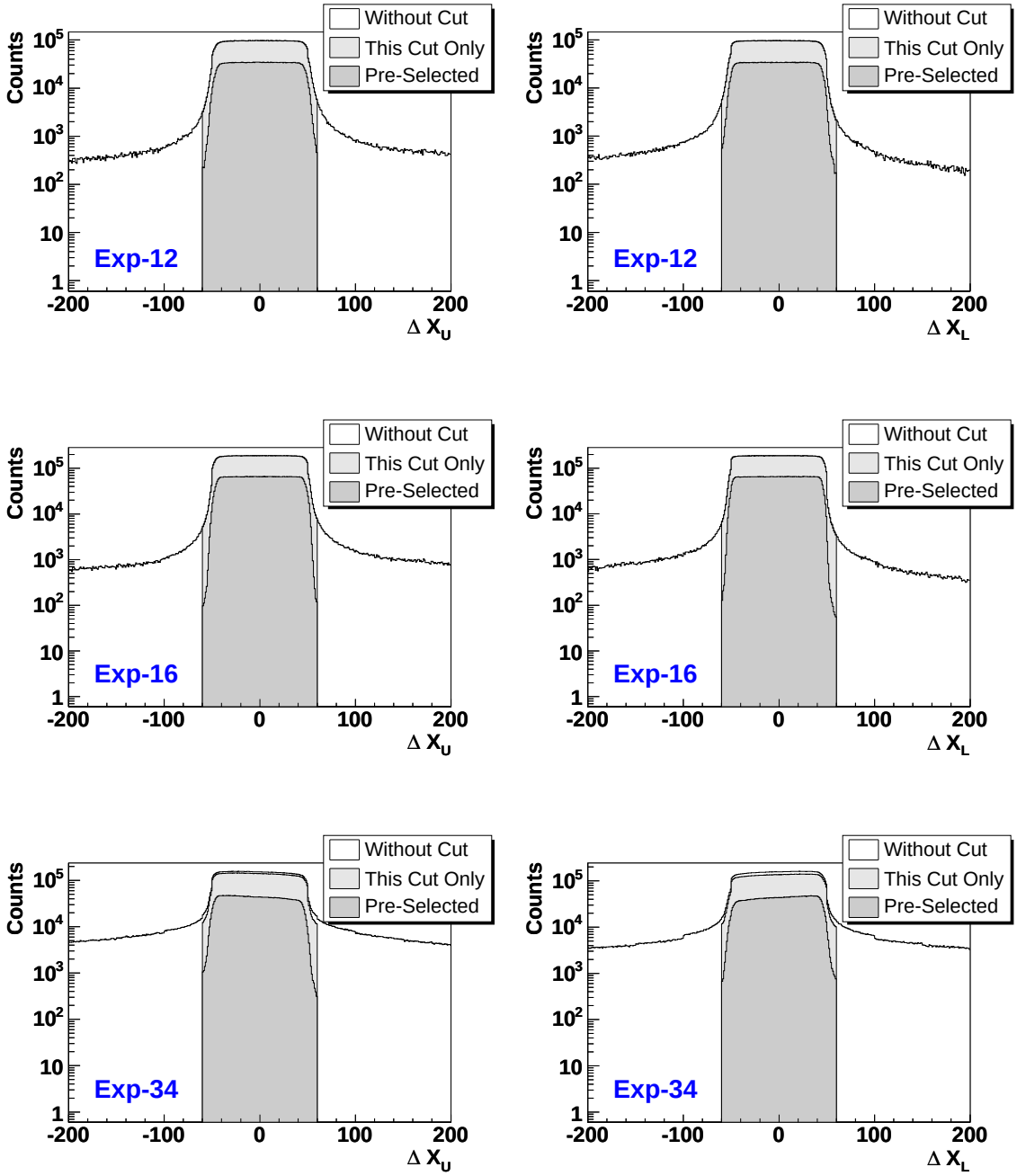

Figure 4.3: Difference of position of x between the trajectory and center of the TOF counter

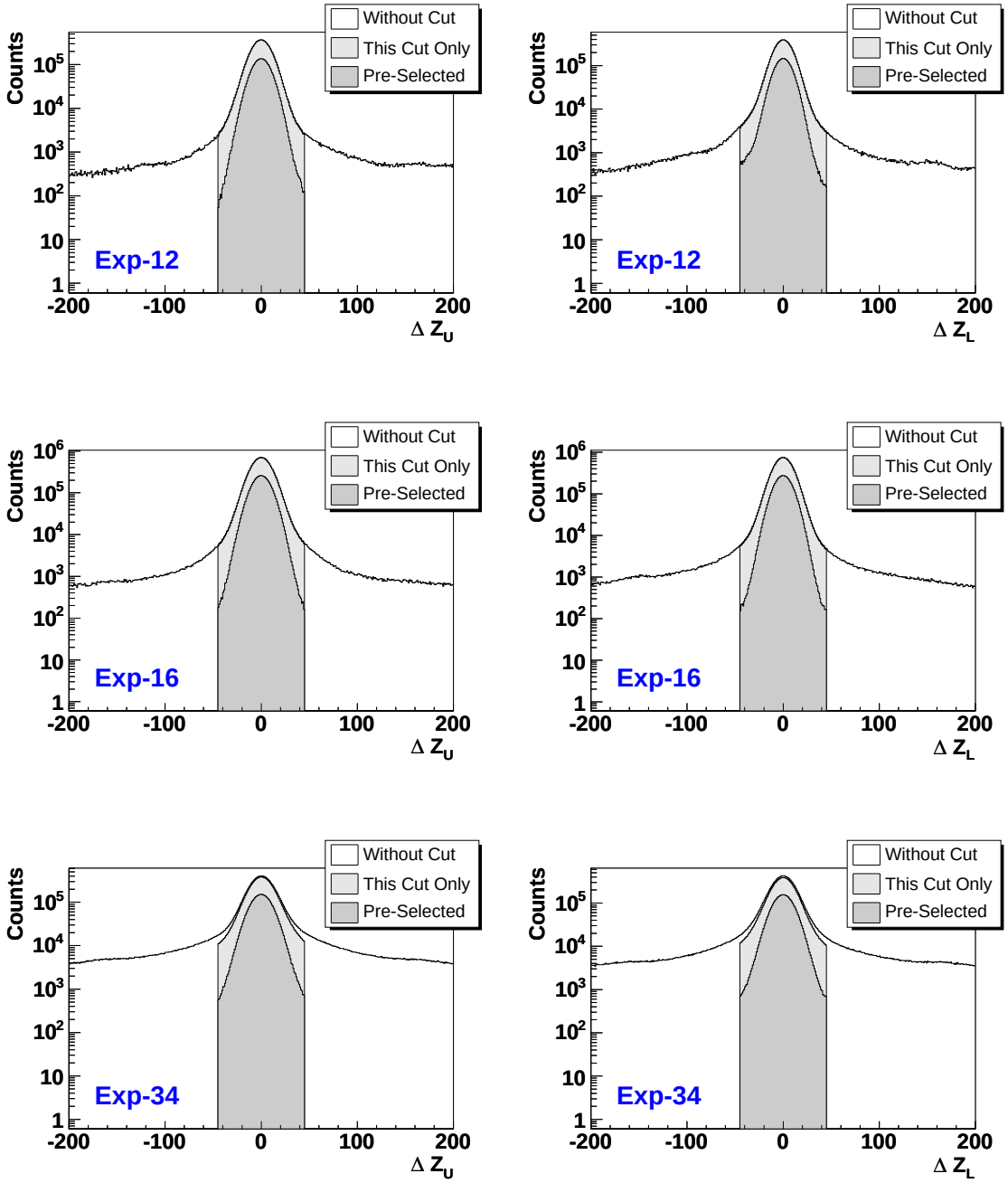

Figure 4.4: Difference of position of z between the trajectory and the TOF counter

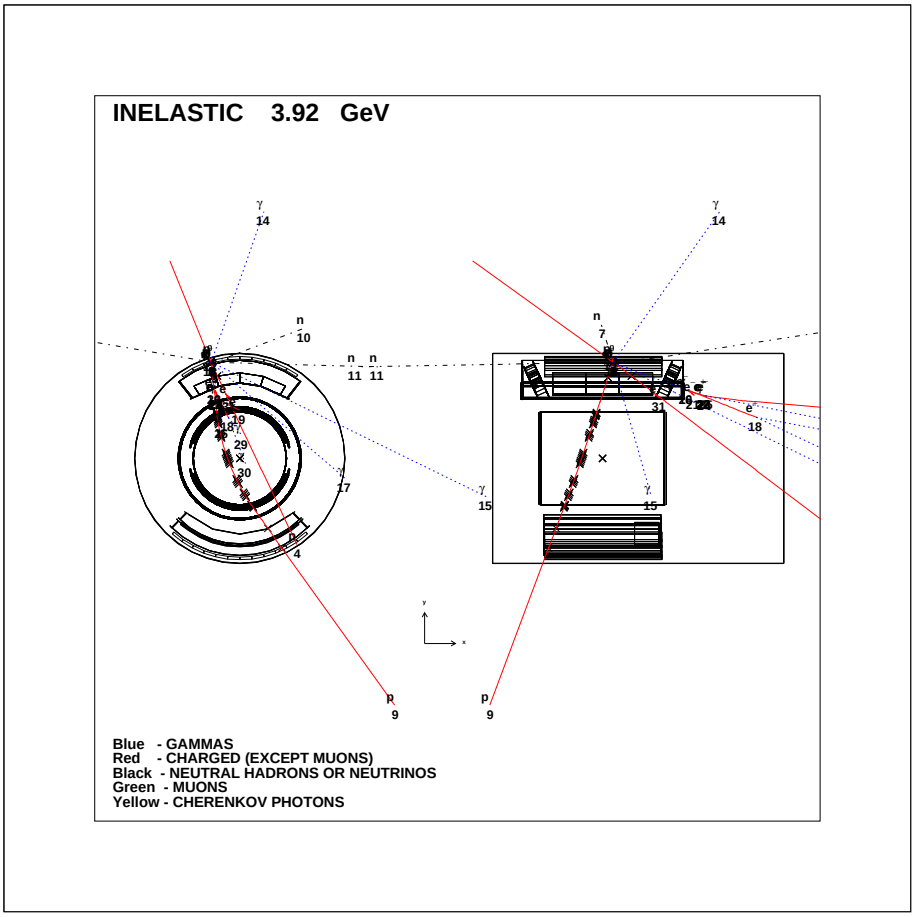

Figure 4.5: A typical example of the BESS MC events with high dE/dx in upper TOF counters.

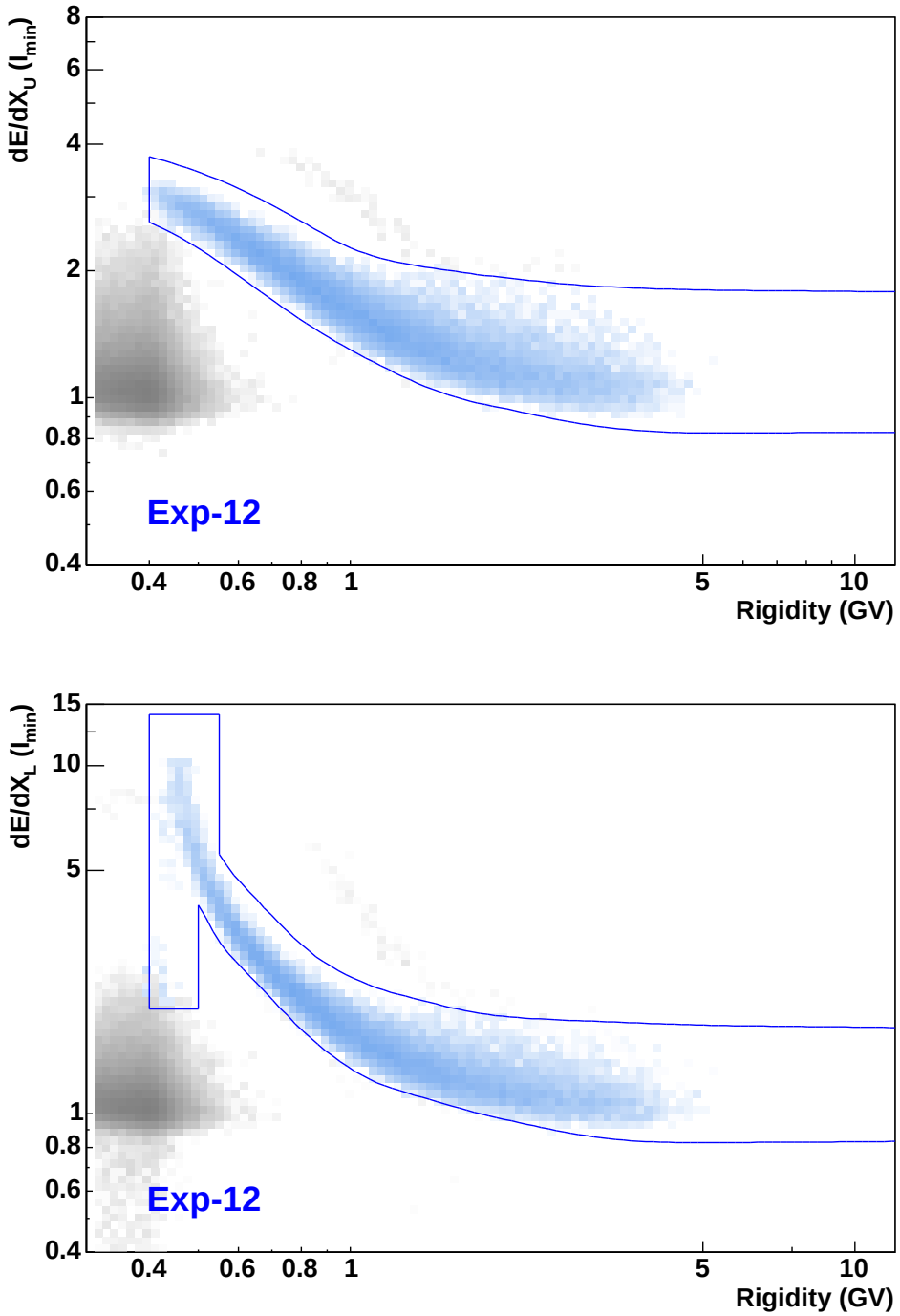

Figure 4.6: dE/dx vs Rigidity plots in Exp-12. Blue solid lines and region represent selection boundaries for non-interaction protons. Here we apply ACC cut; $Q_{AC} \leq 20$.

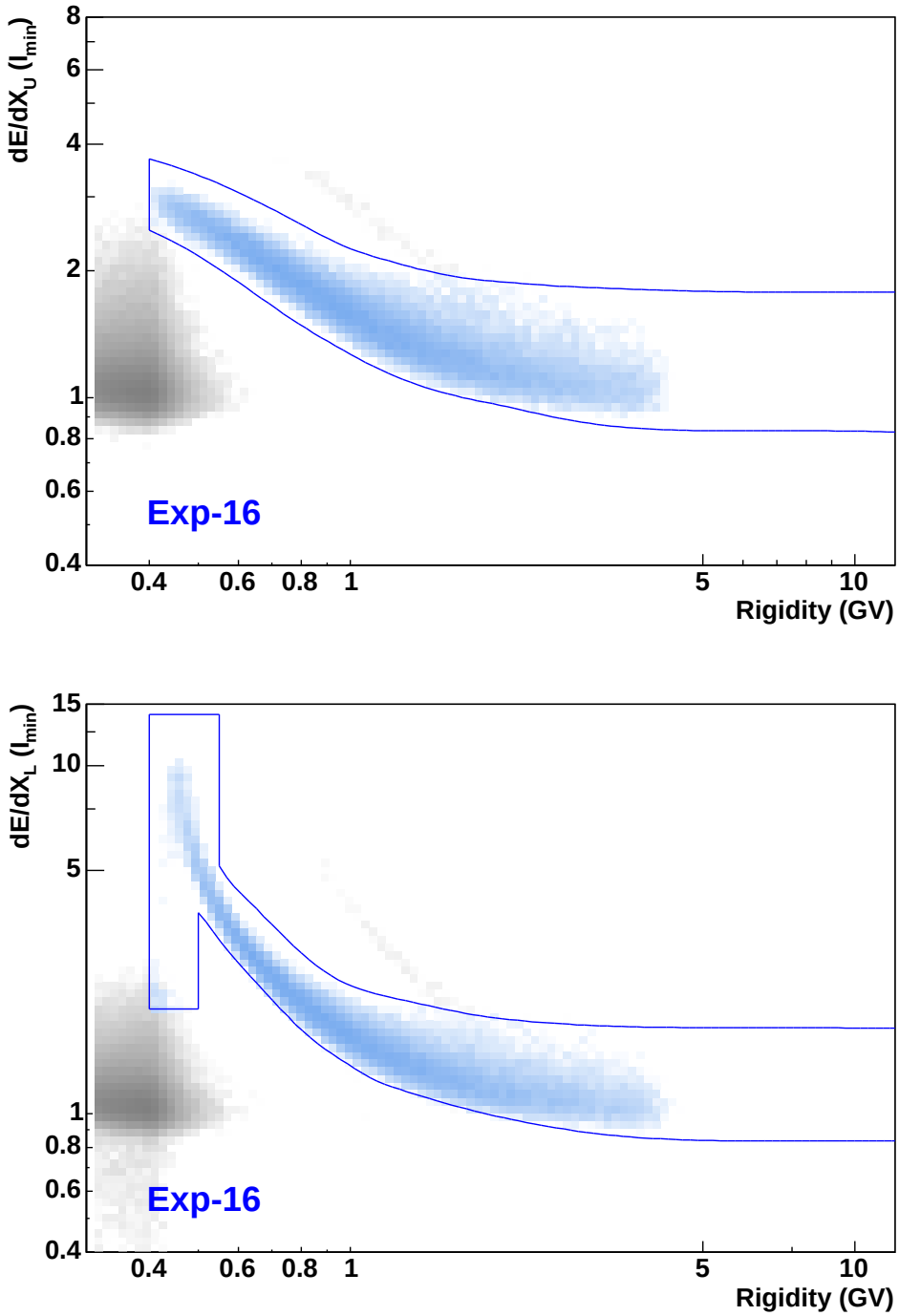

Figure 4.7: dE/dx vs Rigidity plots in Exp-16. Blue solid lines and region represent selection boundaries for non-interaction protons. Here we apply ACC cut; $Q_{AC} \leq 20$.

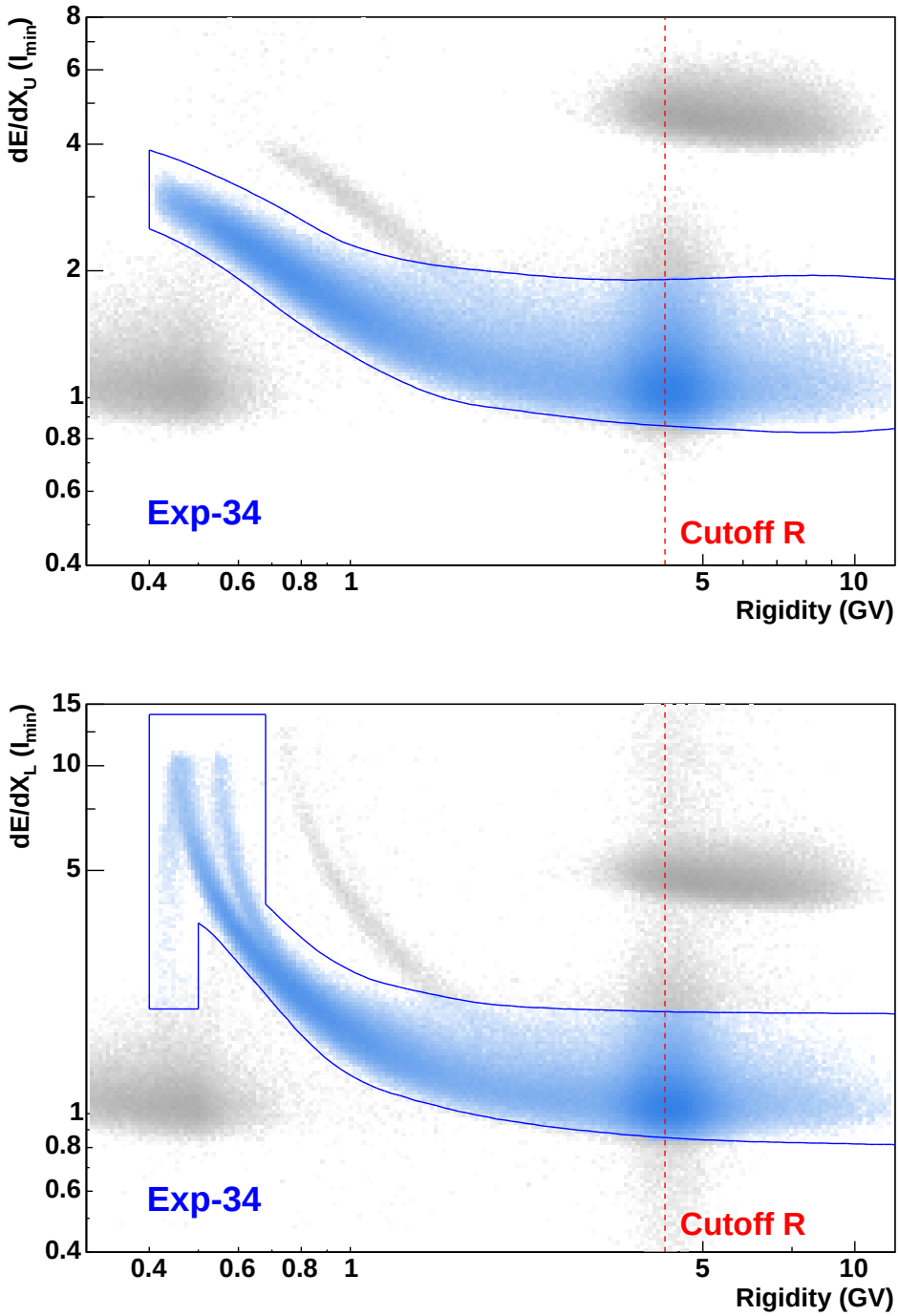

Figure 4.8: $\mathrm{d}E/\mathrm{d}x$ vs Rigidity plots in Exp-34. Blue solid lines represent selection boundaries for non-interaction protons. Here we apply ACC cut; $Q_{AC} \leq 20$. We can clearly see the geomagnetic cutoff effect for proton and He band. The separation of $\mathrm{d}E/\mathrm{d}x_L$ band at low energy is due to existence of lead region.

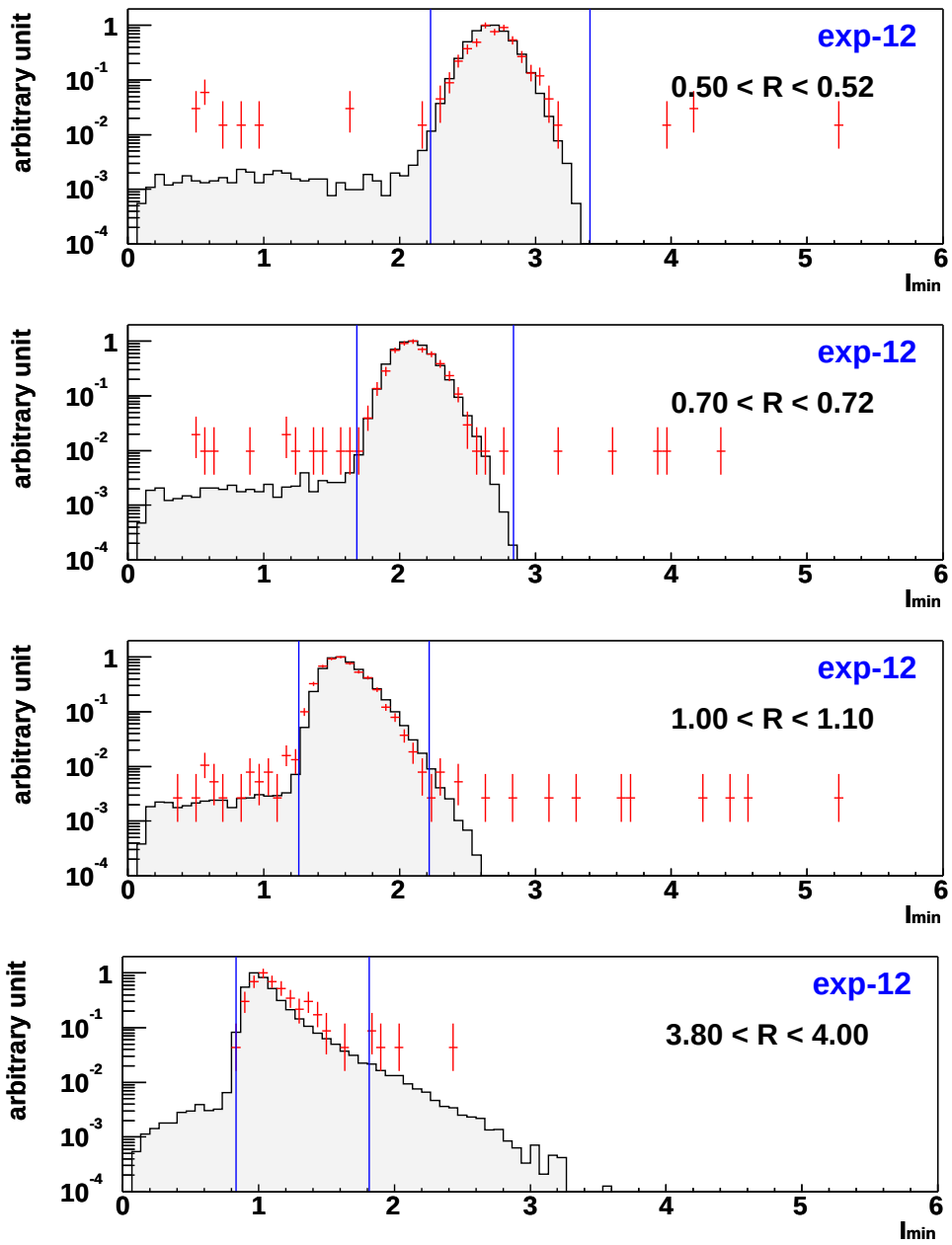

Figure 4.9: Comparison of $\mathrm{d}E/\mathrm{d}x$ distributions in upper TOF in Exp-12. Observed proton-like events are shown in red plots with error bar. Gray histogram were proton events obtained by BESS MC. Solid blue line represent the $\mathrm{d}E/\mathrm{d}x_U$ selection boundaries for protons and $\overline{p}$'s.

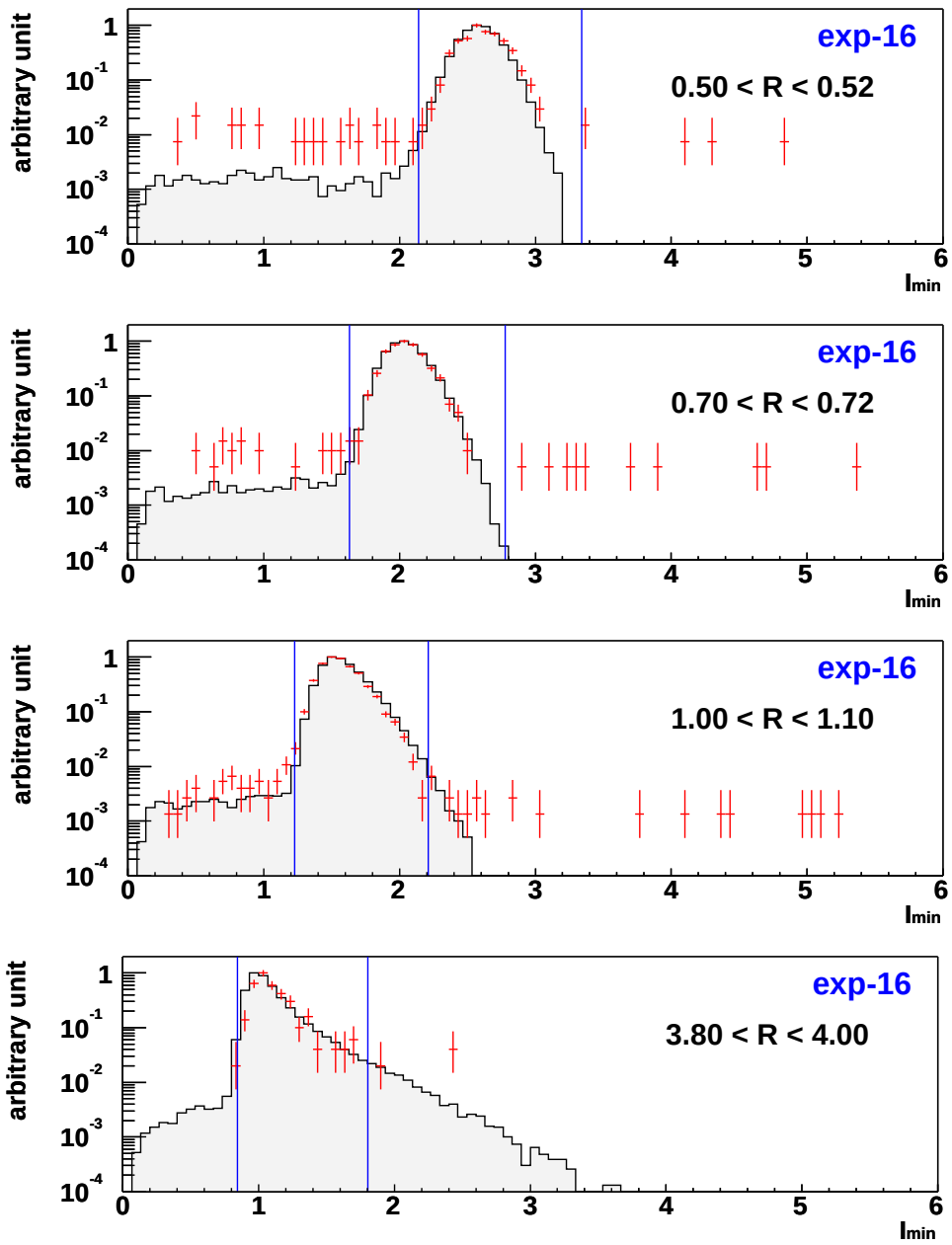

Figure 4.10: Comparison of $\mathrm{d}E/\mathrm{d}x$ distributions in upper TOF in Exp-16. Observed proton-like events are shown in red plots with error bar. Gray histogram were proton events obtained by BESS MC. Solid blue line represent the $\mathrm{d}E/\mathrm{d}x_U$ selection boundaries for protons and $\overline{p}$'s.

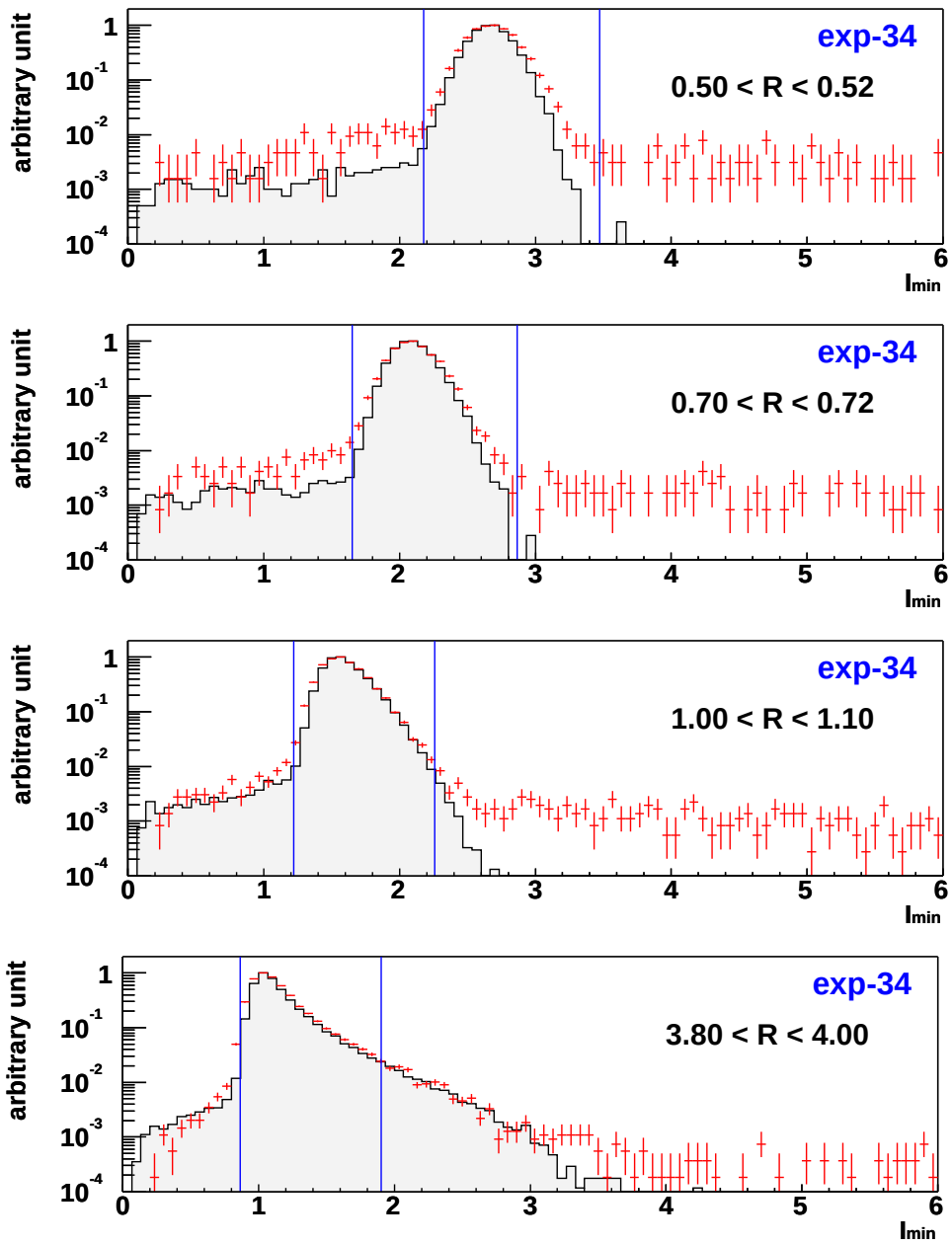

Figure 4.11: Comparison of $\mathrm{d}E/\mathrm{d}x$ distributions in upper TOF in Exp-34. Observed proton-like events are shown in red plots with error bar. Gray histogram were proton events obtained by BESS MC. Solid blue line represent the $\mathrm{d}E/\mathrm{d}x_U$ selection boundaries for protons and $\overline{p}$'s.

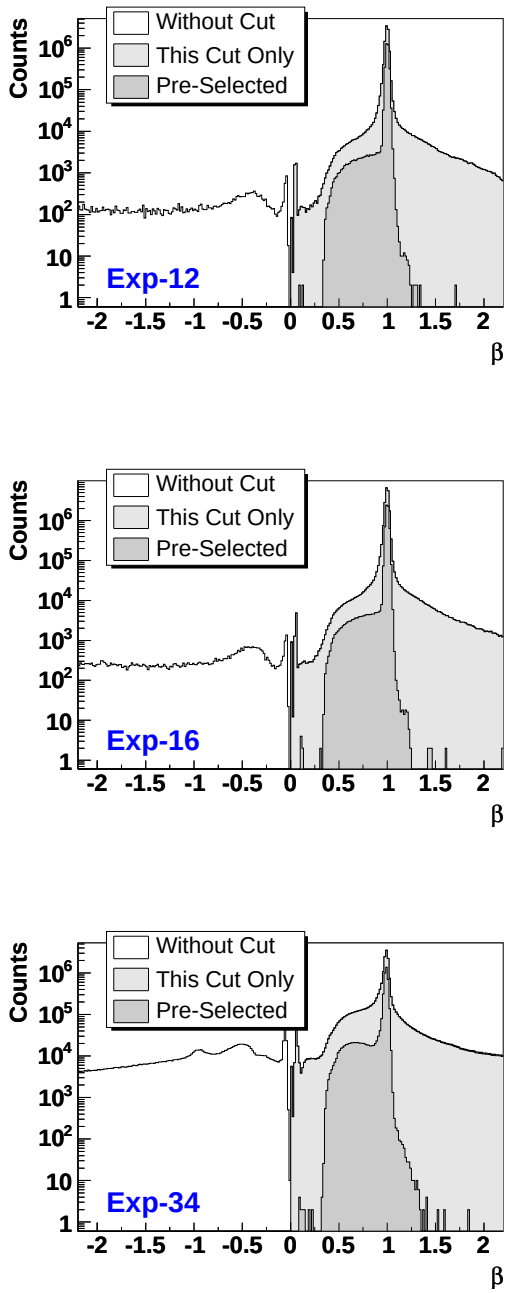

Figure 4.12: The distribution of particle velocity.

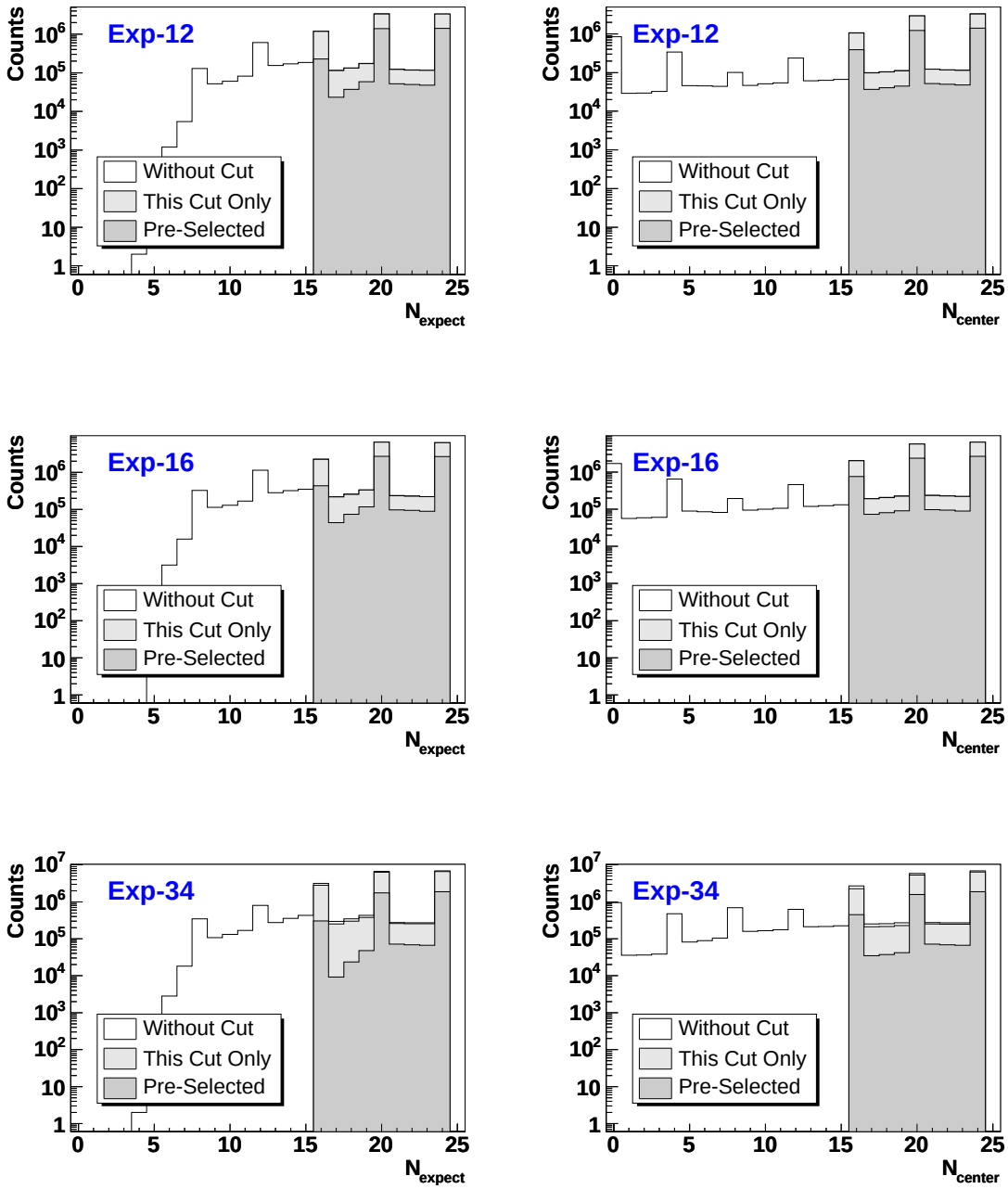

Figure 4.13: The distribution of JET hits expected from trajectory (left) and hits in the center region (right).

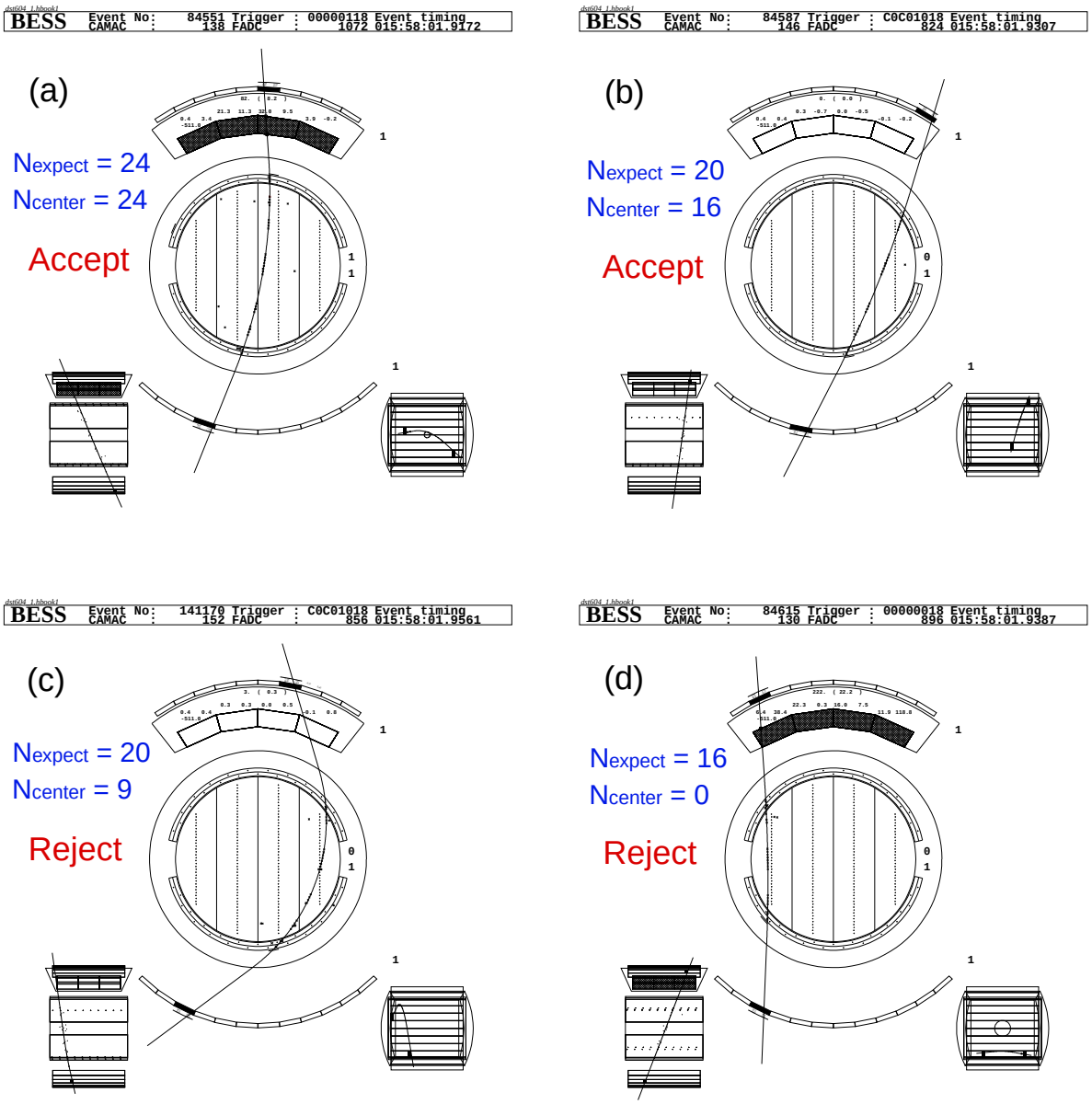

Figure 4.14: The examples of N_{expect} and $N_{ceneter}$. (a) All hits are in central region. (b) Some hits are in side region and it is satisfied the selection condition. (c) Some hits are in side region and it is not satisfied the selection condition. (d) All hits are in side region.

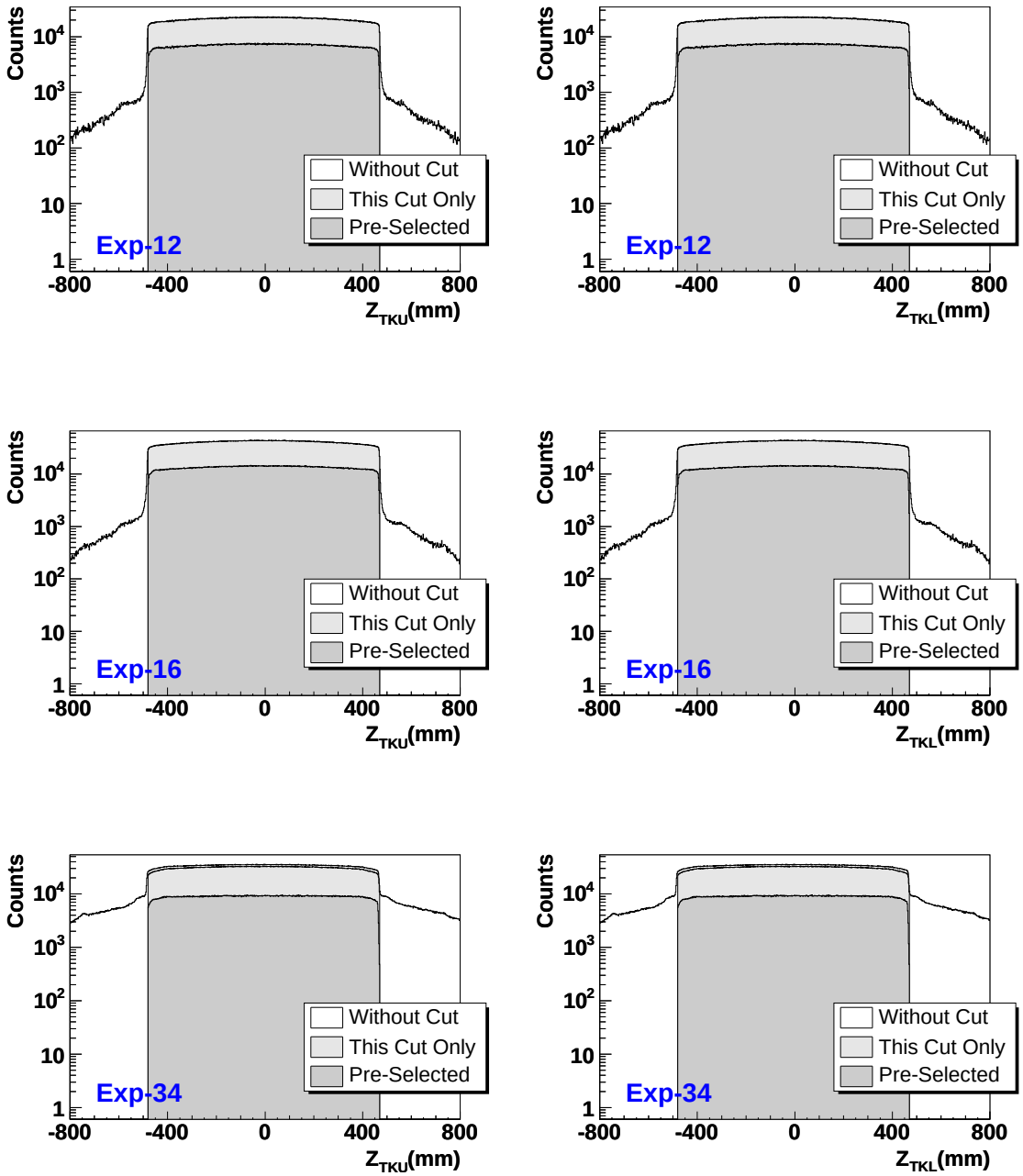

Figure 4.15: The distribution of z position extrapolating the trajectory at upper (left) and lower (right) TOF

4.1.2 Quality Cut

The main purpose of the following "quality cut" are to ensure accurate measurements the incident energy of the antiproton candidates.

Track quality cut

- $N_{r\phi-fit} \leq 10$, $N_{yz-fit} \leq 6$ (Figure 4.16) Since the number of hits used in the trajectory fitting is directly related to the accuracy of the track information, the numbers of used hits in the r-ϕ fitting ($N_{r\phi-fit}$) and in the y-z fitting (N_{yz-fit}) are required as $N_{r\phi-fit} \leq 10$, $N_{yz-fit} \leq 6$.

- $\chi^2_{r\phi} \leq 6.5$, $\chi^2_{yz} \leq 6.5$ (Figure 4.17) The goodness of the trajectory fitting are checked by using the reduced chi-square. where

$$\chi^2_{r\phi-fit} \equiv \frac{1}{N_{r\phi-fit}-3}\sqrt{\sum \frac{(\Delta r\phi_i)^2}{\sigma^2_{r,\phi,i}}}$$

$$\chi^2_{z} \equiv \frac{1}{N_{r\phi-fit}-2}\sqrt{\sum \frac{(\Delta z_i)^2}{\sigma^2_{z,i}}}$$

- $N_{drop} \leq 3$ (Figure 4.18) A "dropped" hit is defined by a JET hit satisfying the following two conditions; (i) which is expected from the trajectory (ii) while actually not existing close to the expected position. We count the number of "dropped" hits (N_{drop}), which should be 4 or less to avoid wrong reconstruction of the trajectory.

TOF quality cut

- $|\Delta R_U| \leq 0.3$, $|\Delta R_L| \leq 0.3$ (Figure 4.19) The ratio of the amplitude of the signals from two ends of a counter will be a monotone function of z. Since the z-dependence is due to attenuation and loss, the amplitude of a signal read out from a end of a TOF counter will be expressed as:

$$A \simeq \exp(a + bz)$$

where a and b are constant for the each read out channel. The logarithm of ratio of the amplitude from two sides, A_L/A_R, will then be proportional to z

$$R \simeq \log(A_L/A_R) \simeq cz$$

where c is constant specific to the each counter. Actually, the value A deviates from the exponential function of z, and so R deviates slightly from the linear function of z:

$$R = f(z) \simeq cz + \varepsilon(z)$$

Thus, value $\Delta R \equiv R - f(z)$ will offer a good parameter to check the consistency between the hit and the trajectory.

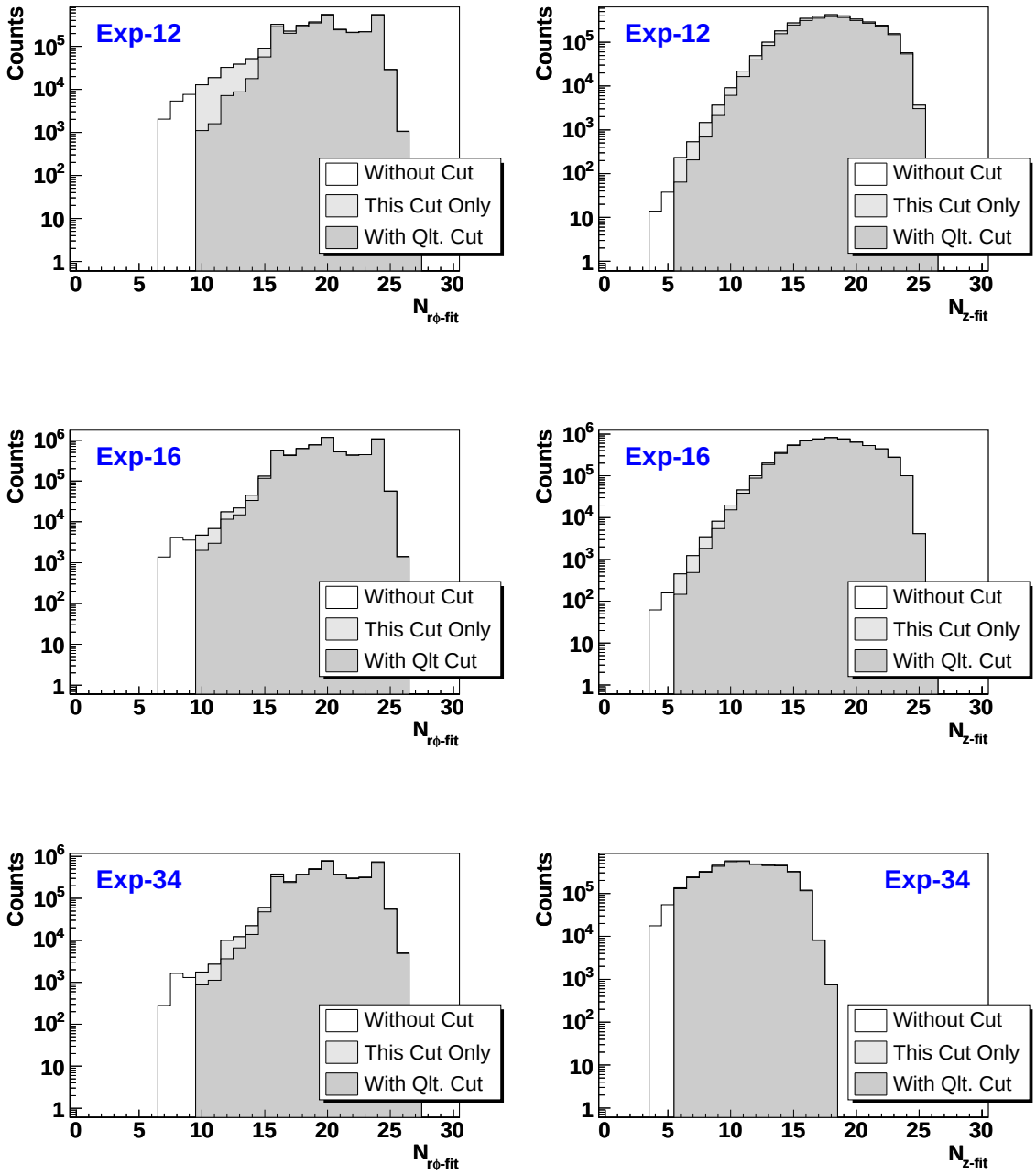

Figure 4.16: The number used fitting the trajectory.

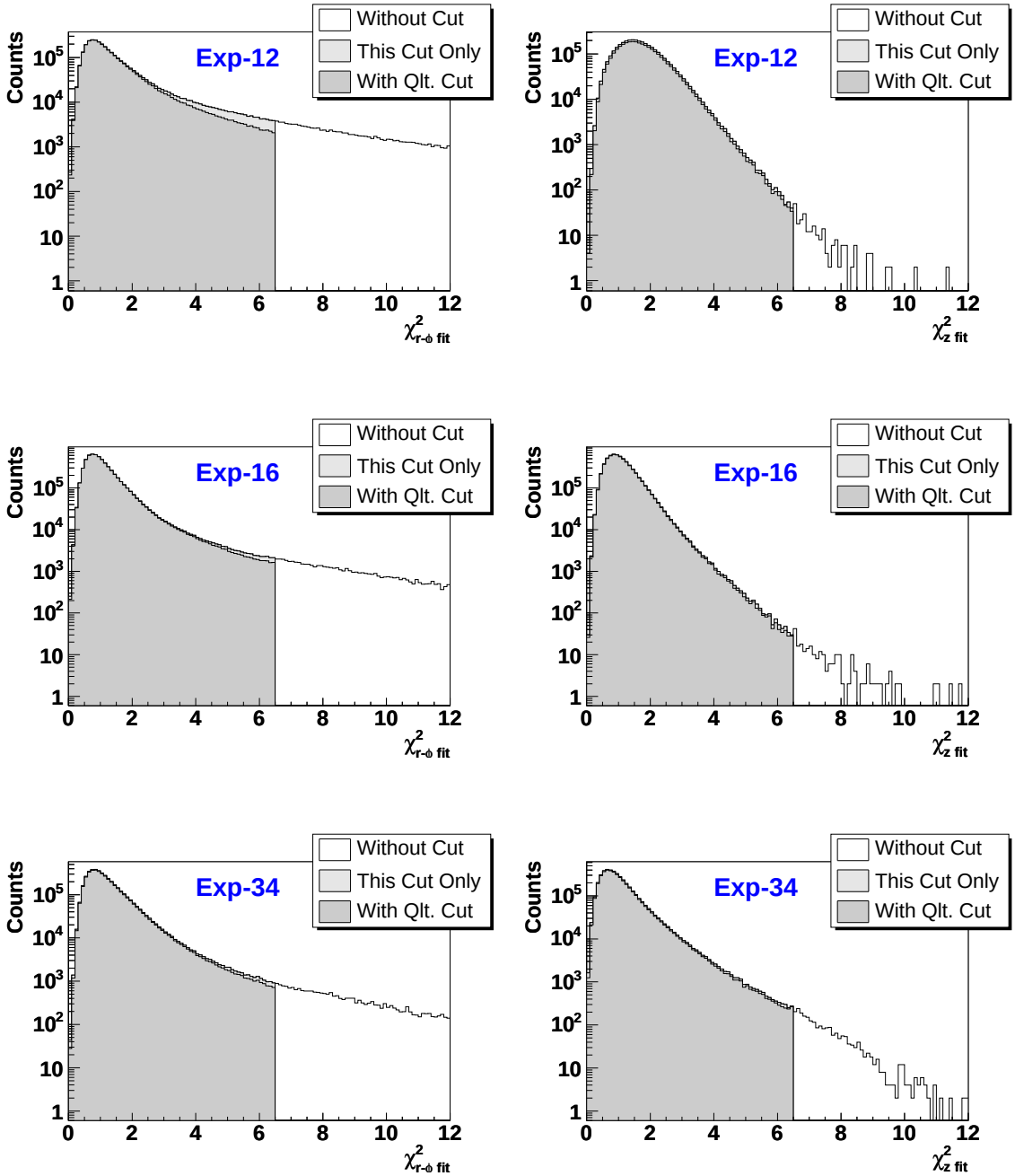

Figure 4.17: The distribution of χ^2 of the fitting.

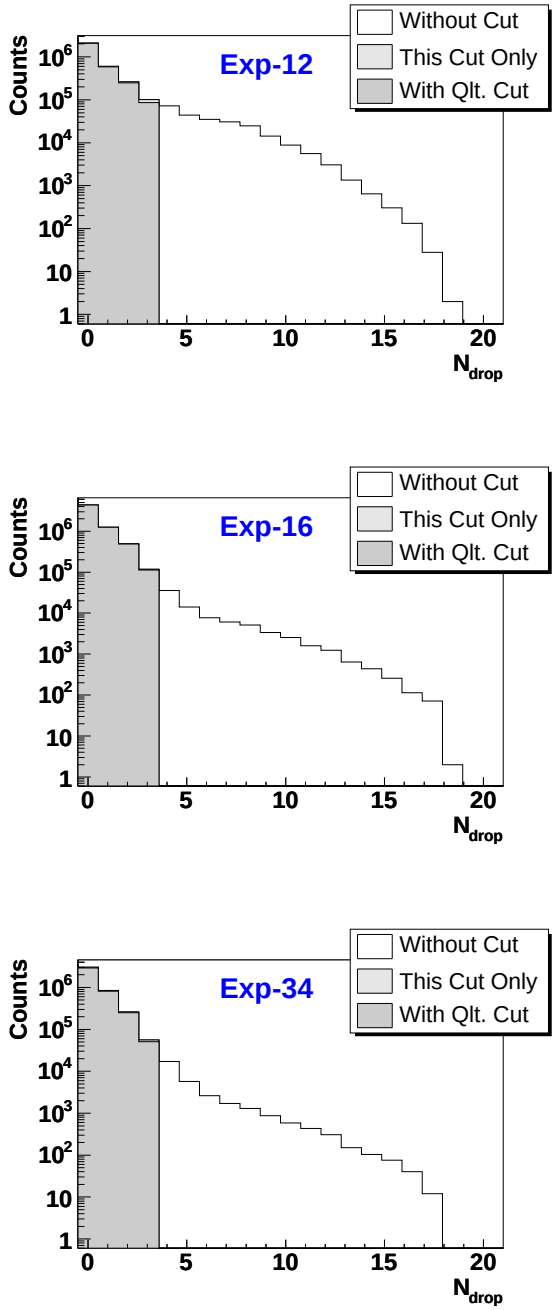

Figure 4.18: The distribution of N_{drop}

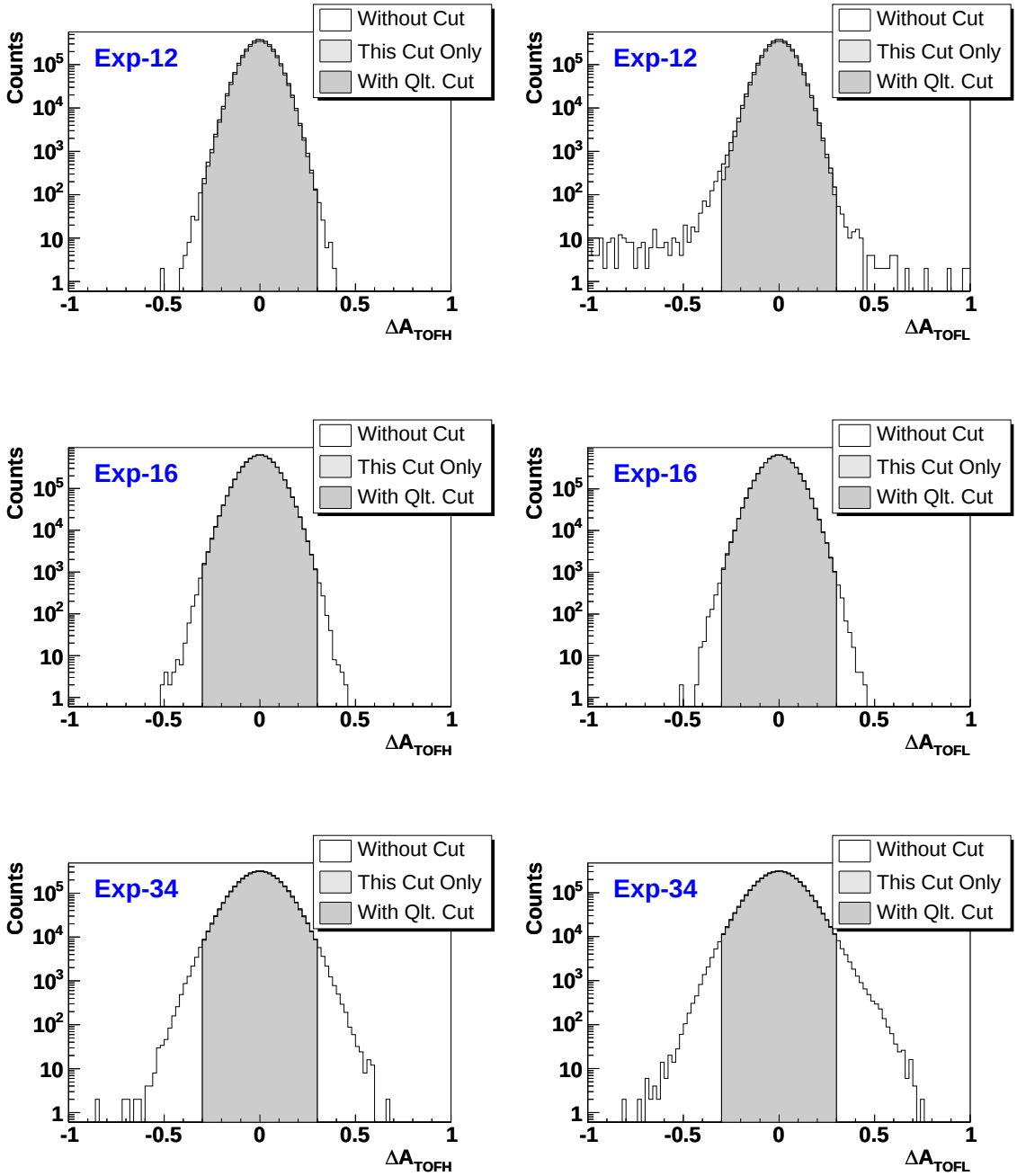

Figure 4.19: The distribution of ΔA_{tof}.

4.1.3 Identification

To identify $\overline{p}$'s, we made analysis in the following way.

- Aerogel Čerenkov veto

  At the balloon altitude, there are many negative charged particles (i.e. μ^-, e^- and π^-). They became a major background for $\overline{p}$'s and we must eliminate those particles. For this purposes, we apply a cut by using Aerogel Čerenkov counter with following conditions.

  (1) The fiducial volume The particle should cross an aerogel fiducial volume shown in Table 4.1-4.3 for each experiments. The fiducial volume is defined to be well smaller than the actual size of the aerogel blocks, since Čerenkov output were not obtained enough when the particles pass through the edge of the aerogel blocks or the gaps between the blocks (Figure 4.20-4.31). To find the location of the gap, we used two independent method. One is to find the area where N_{pe} is smaller than other place. The other way is detect the area where Čerenkov light was not observed although relative particles passed though. In the Figures 4.20-4.31, we show the location by following parameters defined by

  $$Xc \equiv (X_{ACU} + X_{ACL})/2$$

  $$Zc \equiv (Z_{ACU} + X_{ZCL})/2$$

  where X_{ACU} (X_{ACL}) is x-position of particle's incoming point at upper (lower) surface of the ACC. Similarly Z_{ACU} (Z_{ACL}) is z-position of incoming point. Both method are consistent and we can see gaps clearly.
  We applied fiducial volume cut to $\beta^{-1} \leq 1.1$ region only, because in $\beta^{-1} > 1.1$ region $\overline{p}$'s can be identified by JET dE/dx band cut and β^{-1} vs R cut described in later.

  (2) The threshold The Čerenkov output should be smaller values of than the threshold, values which we put Q_{AC} =12, 12, 10 (Exp-12, 16, 34 respectively). Where Q_{AC} means the sum of ADC counts from Čerenkov outputs. The threshold is determined from the trade of between the following quantities; (i) A probability that a slow proton ($\beta < 1/n_{aerogel}$) gave a higher signal than the threshold, where $n_{aerogel} \sim 1.03$ (Exp-12, 16) 1.02 (Exp-34) denotes the refractive index of the silica-aerogel radiator. (ii) A probability that a relativistic particle ($\beta > 1/n_{aerogel}$) gave a lower signal than the threshold.

- JET dE/dx band cut (Figure 4.35 4.39, 4.43) We utilize energy deposit in the JET chamber (dE/dx_J) to identify low-energy $\overline{p}$'s. As shown in Figure 4.35, 4.39, 4.43, the band structures in dE/dx_J vs Rigidity plots for protons demonstrates clear difference $dE/dx_J = 1$ of the minimum ionized particles in the low energy region. Therefore, dE/dx_J can be used as a powerful identification tool of low-energy $\overline{p}$'s. Selection boundaries are indicated in the figures as solid lines.

- Mass determination Figure 4.44-4.49 show the β^{-1} vs R plot for the surviving events after Čerenkov veto and JET dE/dx band cut. In this figure, $\overline{p}$ candidates are mass-identified up to about 4 or 5 GV (Exp-12, 16 or 34) using the combination of Čerenkov veto and excellent resolution of β^{-1} measurements. We see a clean narrow band of $\overline{p}$ candidates at the exact mirror position of the protons. Here, we take $\pm 3.89\sigma$ of the distribution for p and $\overline{p}$ boundaries. Thus, it is clear that majority of final $\overline{p}$ candidates are real $\overline{p}$'s. Nevertheless, the $\overline{p}$ band is slightly contaminated with the e^- and μ^{-1} backgrounds due to the inefficiency of the aerogel Čerenkov counter. The estimation of contribution of such backgrounds is discussed in the next chapter.

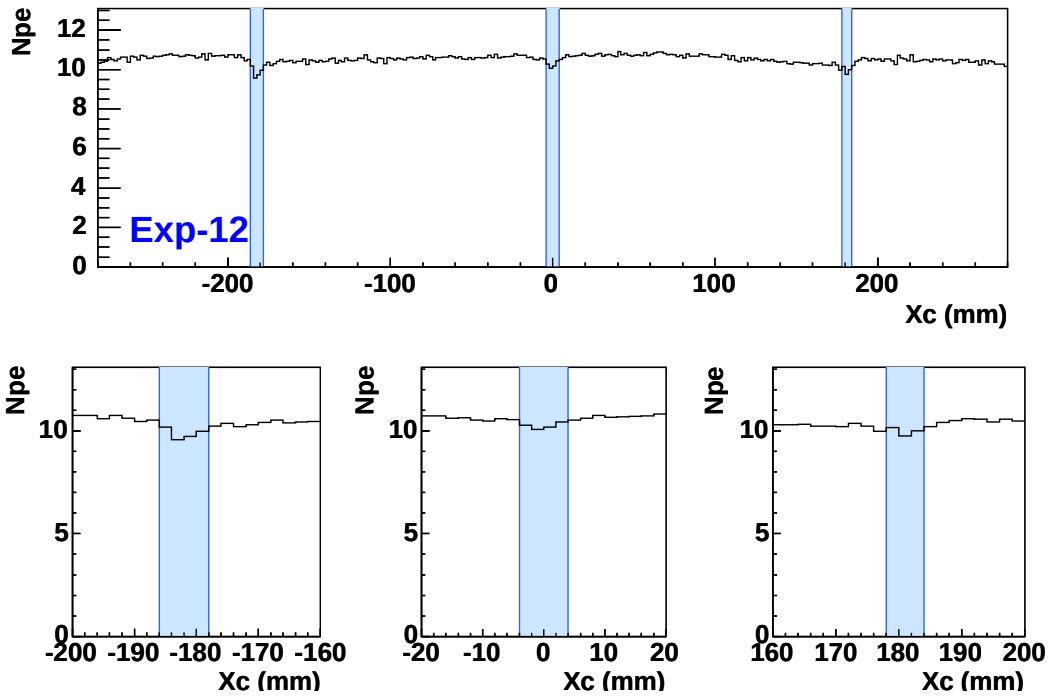

Figure 4.20: The N_{pe} distribution in r-ϕ plane in Exp-12. The blue regions represent the location of the gaps

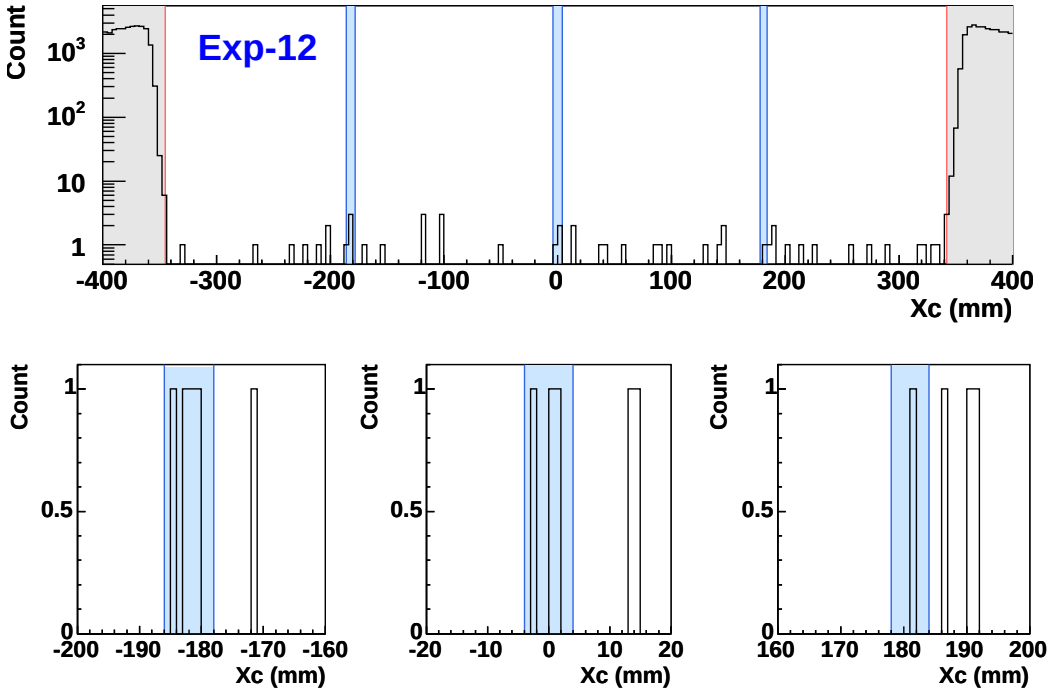

Figure 4.21: The effect of edge and gaps of Aerogel along the r-ϕ plane in Exp-12. The gray regions represent the edge and the blue regions are the location of the gaps.

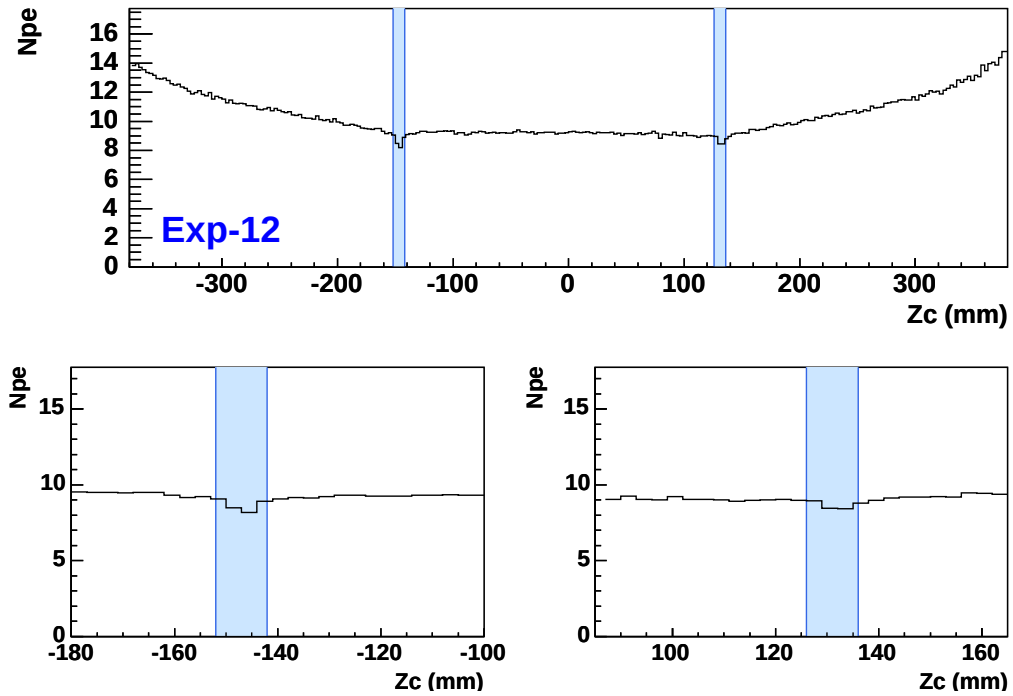

Figure 4.22: The N_{pe} distribtuions along the z-axis in Exp-12. The blue regions represent the location of the gaps.

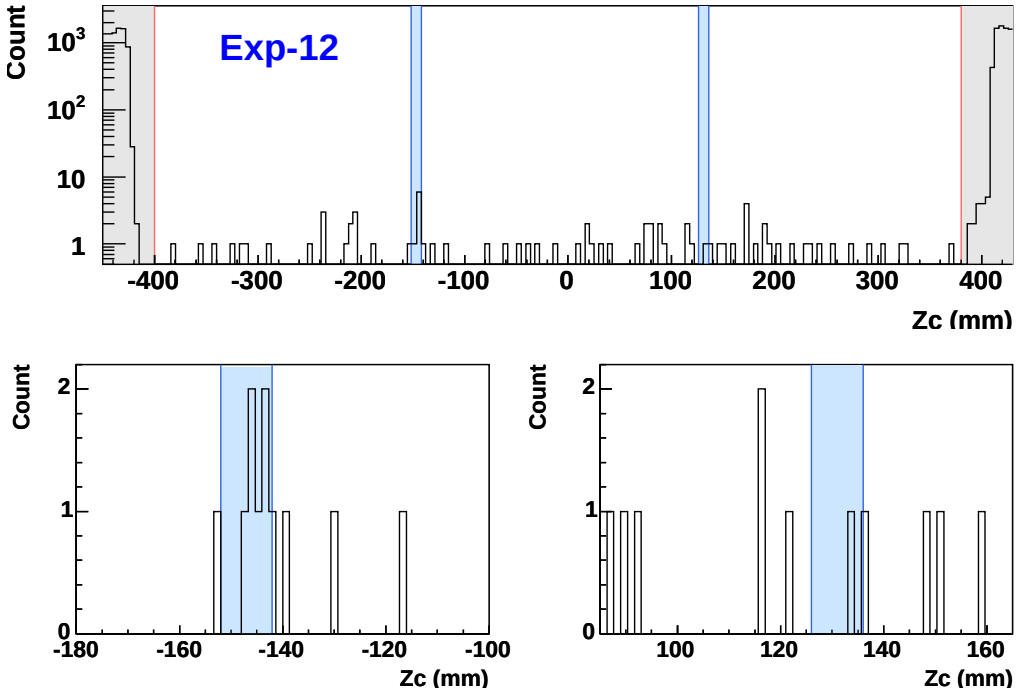

Figure 4.23: The effect of edge and gaps of Aerogel along the z-axis in Exp-12. The gray regions represent the edge and the blue regions are the location of the gaps.

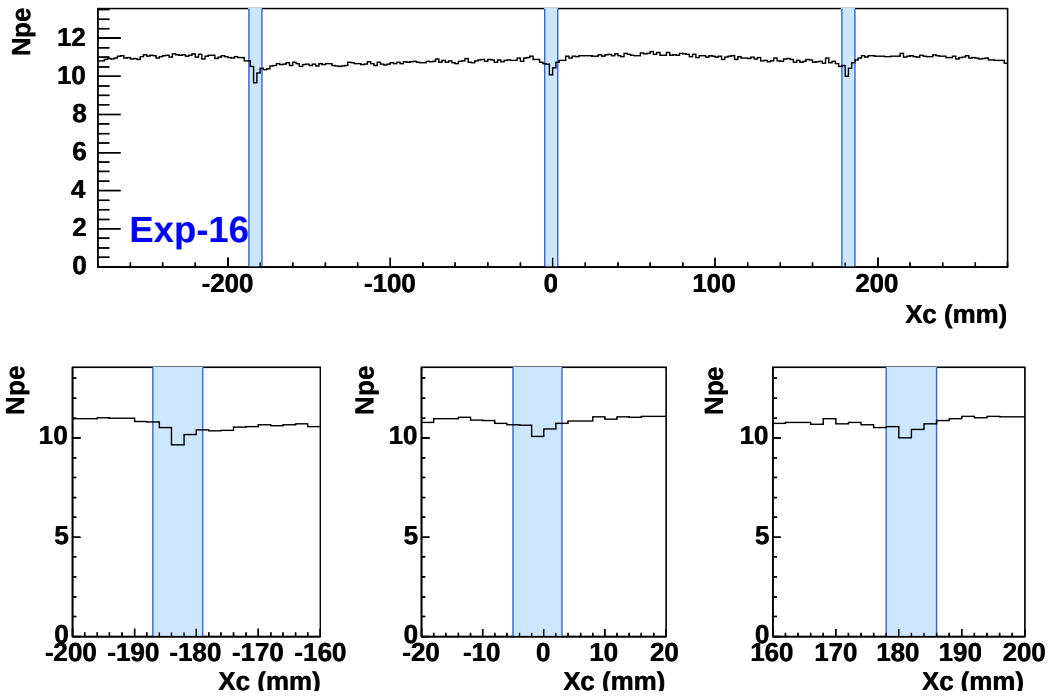

Figure 4.24: The N_{pe} distributions in the r-ϕ plane in Exp-16. The Blue regions represent the location of the gaps. Perhaps aerogel blocks were closed tightly.

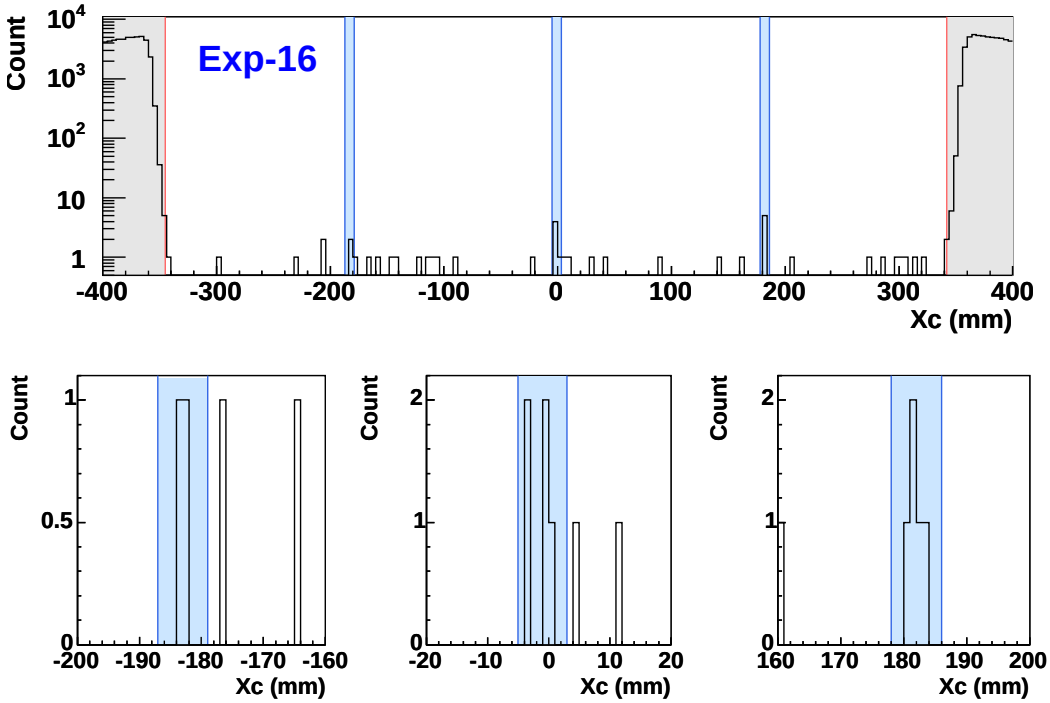

Figure 4.25: The effect of edge and gaps of Aerogel along the r-ϕ plane in Exp-16. The gray regions represent the edge and the blue regions are the location of the gaps.

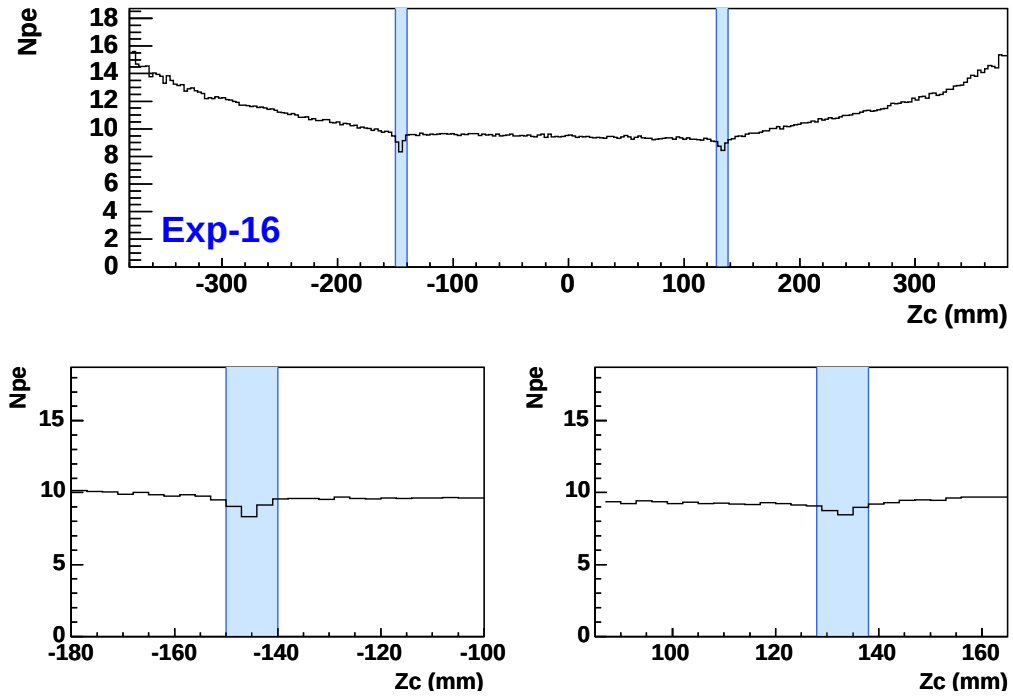

Figure 4.26: The N_{pe} distributions along the z-axis in Exp-16. The blue regions represent the location of the gaps.

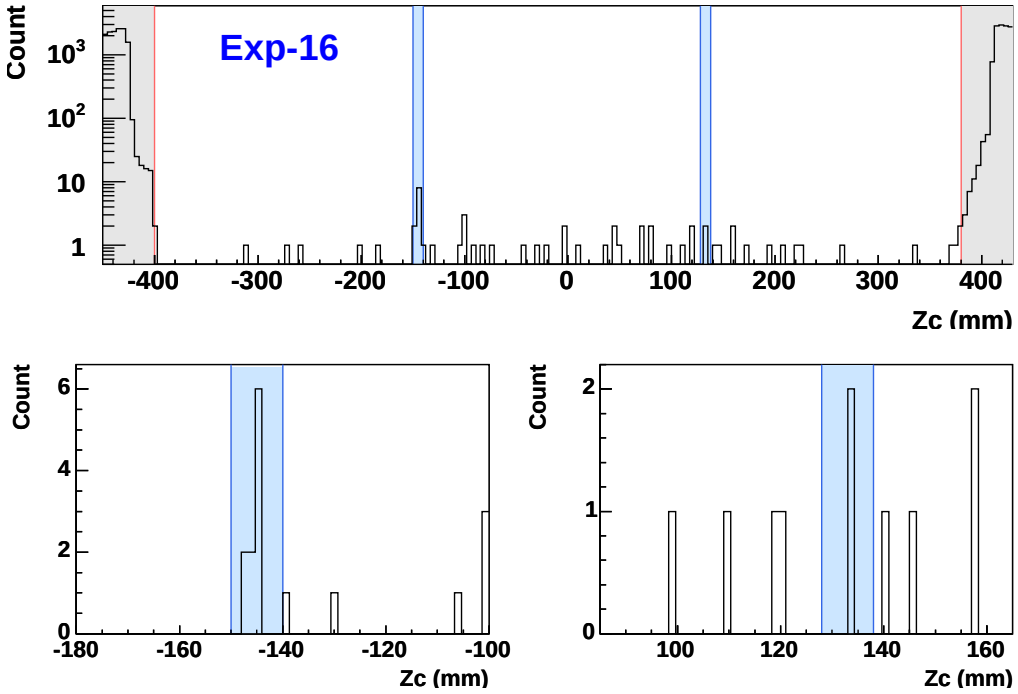

Figure 4.27: The effect of edge and gaps of Aerogel along the z-axis in Exp-16. The gray regions represent the edge and the blue regions are the location of the gaps.

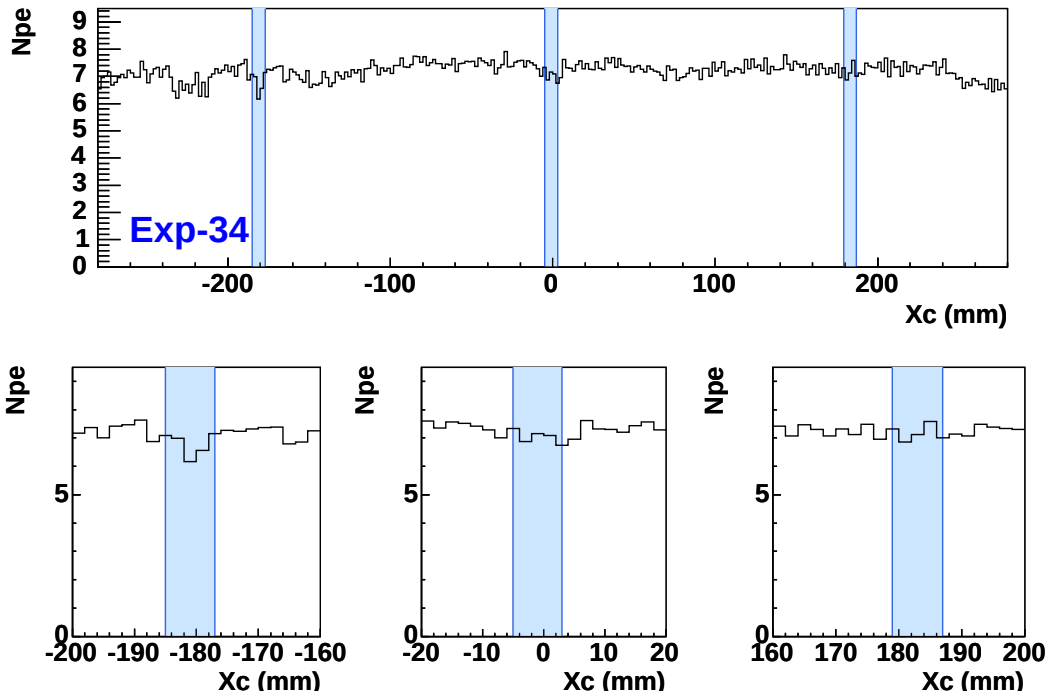

Figure 4.28: The N_{pe} in the r-ϕ plane in Exp-34. The blue regions represent the location of the gaps. In this experiment, we can't see the gaps clearly. It is considered that aerogel blocks were closed tightly.

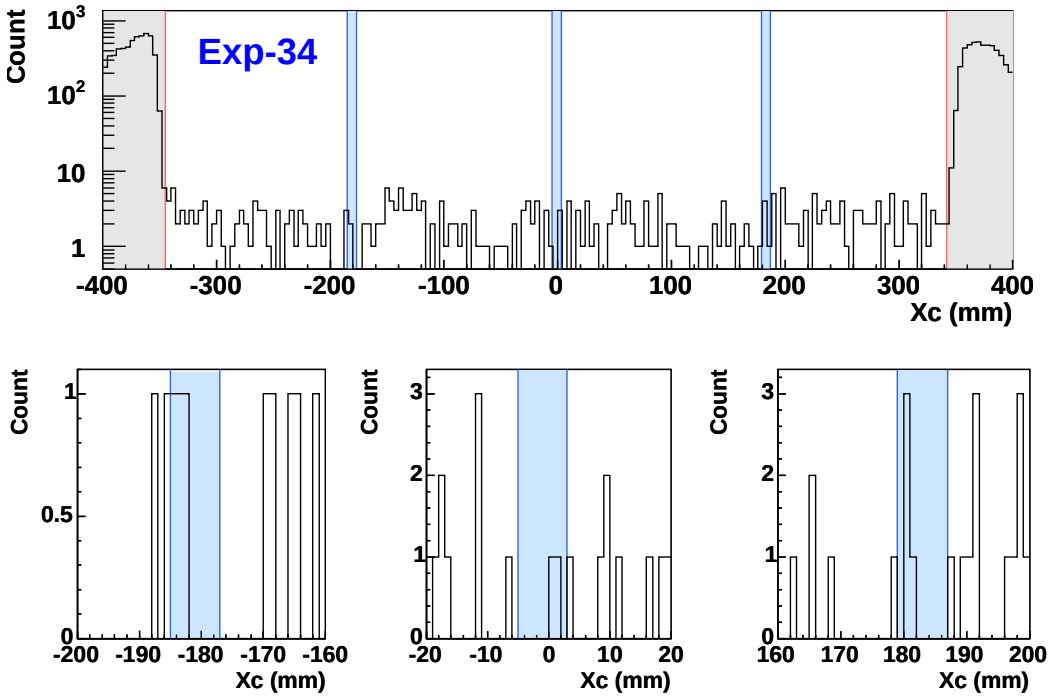

Figure 4.29: The effect of edge and gaps of Aerogel along the r-ϕ plane in Exp-34. The gray regions represent the edge and the blue regions are the location of the gaps.

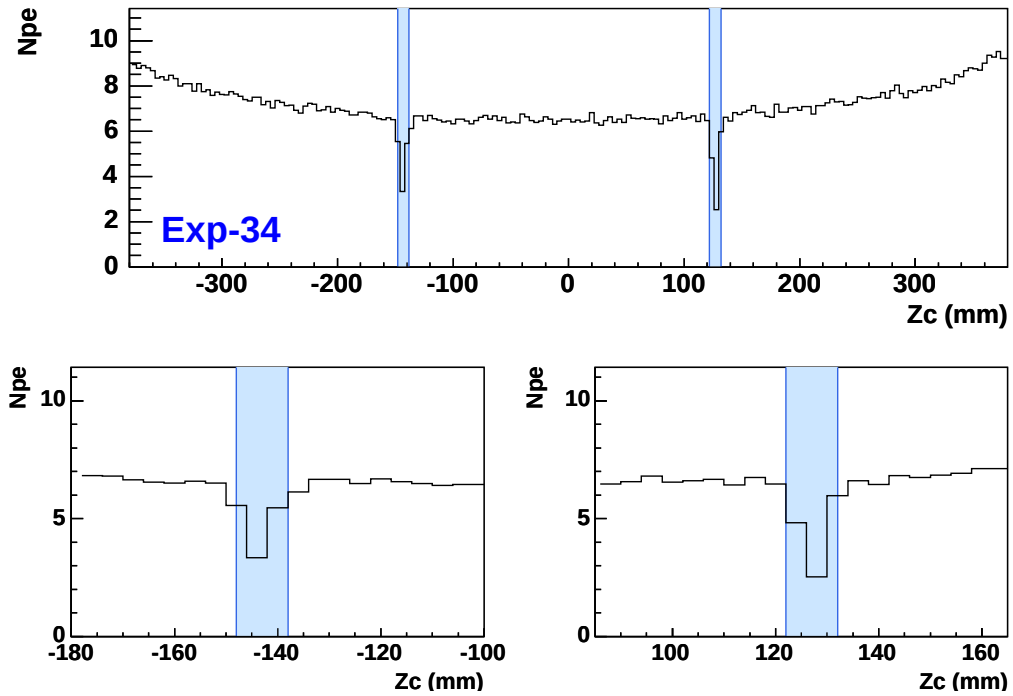

Figure 4.30: The N_{pe} distributions along the z-axis in Exp-34. The blue regions represent the location of the gaps.

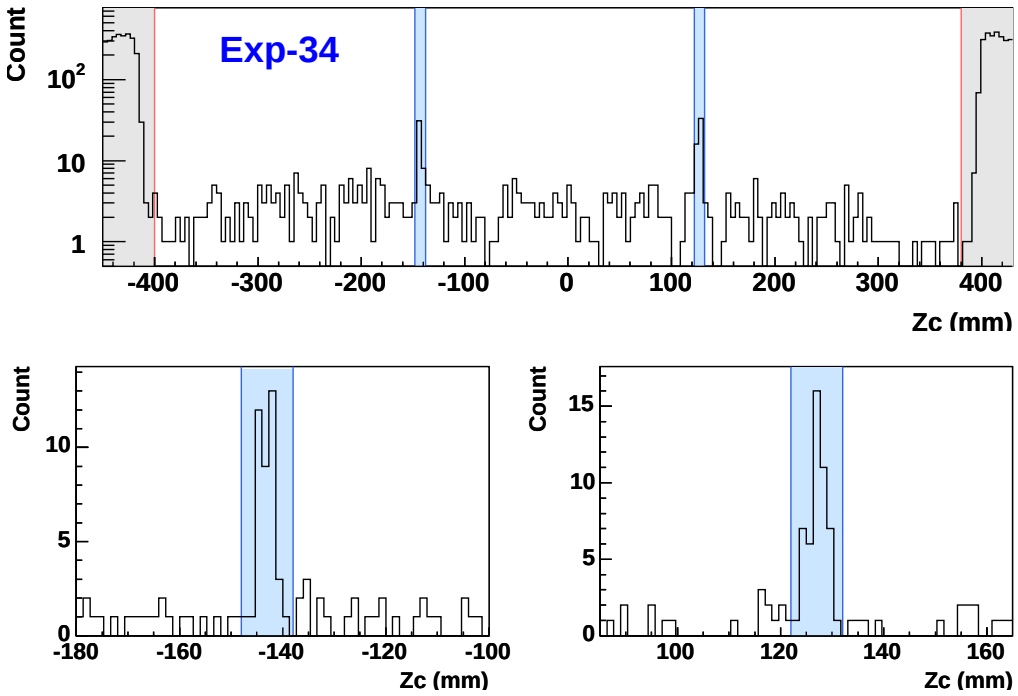

Figure 4.31: The effect of edge and gaps of Aerogel along the z-axis in Exp-34. The gray regions represent the edge and the blue regions are the location of the gaps.

Table 4.1: Summary of the Aerogel fiducial region in Exp-12.

0.	Bellow cuts are applied for $\beta^{-1} < 1.1$ events						
1.		-360 $< X_{AC_U} <$ 360	and		-320 $< X_{AC_L} <$ 320		
2.		590 $< Y_{AC_U} <$ 700	and		520 $< Y_{AC_L} <$ 620		
3.		-400 $< Z_{AC_U} <$ 380	and		-400 $< Z_{AC_L} <$ 380		
4.	except for	$\lvert X_{AC_U} - X_{AC_L} + 24\rvert$	≤ 10	and	-186	$< (X_{AC_U} + X_{AC_L})/2 <$	-178
5.	except for	$\lvert X_{AC_U} - X_{AC_L}\rvert$	≤ 10	and	-4	$< (X_{AC_U} + X_{AC_L})/2 <$	4
6.	except for	$\lvert X_{AC_U} - X_{AC_L} - 24\rvert$	≤ 10	and	178	$< (X_{AC_U} + X_{AC_L})/2 <$	184
7.	except for	$\lvert Z_{AC_U} - Z_{AC_L}\rvert$	≤ 10	and	-152	$< (Z_{AC_U} + Z_{AC_L})/2 <$	-142
8.	except for	$\lvert Z_{AC_U} - Z_{AC_L}\rvert$	≤ 10	and	126	$< (Z_{AC_U} + Z_{AC_L})/2 <$	136

Table 4.2: Summary of the Aerogel fiducial region in Exp-16.

0.	Bellow cuts are applied for $\beta^{-1} < 1.1$ events						
1.		-360 $< X_{AC_U} <$ 360	and		-320 $< X_{AC_L} <$ 320		
2.		590 $< Y_{AC_U} <$ 700	and		520 $< Y_{AC_L} <$ 620		
3.		-400 $< Z_{AC_U} <$ 380	and		-400 $< Z_{AC_L} <$ 380		
4.	except for	$\lvert X_{AC_U} - X_{AC_L} + 24\rvert$	≤ 10	and	-187	$< (X_{AC_U} + X_{AC_L})/2 <$	-179
5.	except for	$\lvert X_{AC_U} - X_{AC_L}\rvert$	≤ 10	and	-5	$< (X_{AC_U} + X_{AC_L})/2 <$	3
6.	except for	$\lvert X_{AC_U} - X_{AC_L} - 24\rvert$	≤ 10	and	178	$< (X_{AC_U} + X_{AC_L})/2 <$	186
7.	except for	$\lvert Z_{AC_U} - Z_{AC_L}\rvert$	≤ 10	and	-150	$< (Z_{AC_U} + Z_{AC_L})/2 <$	-138
8.	except for	$\lvert Z_{AC_U} - Z_{AC_L}\rvert$	≤ 10	and	128	$< (Z_{AC_U} + Z_{AC_L})/2 <$	138

Table 4.3: Summary of the Aerogel fiducial region in Exp-34

0.	Bellow cuts are applied for $\beta^{-1} < 1.1$ events						
1.		-360 $< X_{AC_U} <$ 360	and		-325 $< X_{AC_L} <$ 325		
2.		590 $< Y_{AC_U} <$ 700	and		515 $< Y_{AC_L} <$ 620		
3.		-400 $< Z_{AC_U} <$ 380	and		-400 $< Z_{AC_L} <$ 380		
4.	except for	$\lvert X_{AC_U} - X_{AC_L} + 24\rvert$	≤ 10	and	-185	$< (X_{AC_U} + X_{AC_L})/2 <$	-177
5.	except for	$\lvert X_{AC_U} - X_{AC_L}\rvert$	≤ 10	and	-5	$< (X_{AC_U} + X_{AC_L})/2 <$	3
6.	except for	$\lvert X_{AC_U} - X_{AC_L} - 24\rvert$	≤ 10	and	179	$< (X_{AC_U} + X_{AC_L})/2 <$	187
7.	except for	$\lvert Z_{AC_U} - Z_{AC_L}\rvert$	≤ 10	and	-148	$< (Z_{AC_U} + Z_{AC_L})/2 <$	-138
8.	except for	$\lvert Z_{AC_U} - Z_{AC_L}\rvert$	≤ 10	and	122	$< (Z_{AC_U} + Z_{AC_L})/2 <$	132

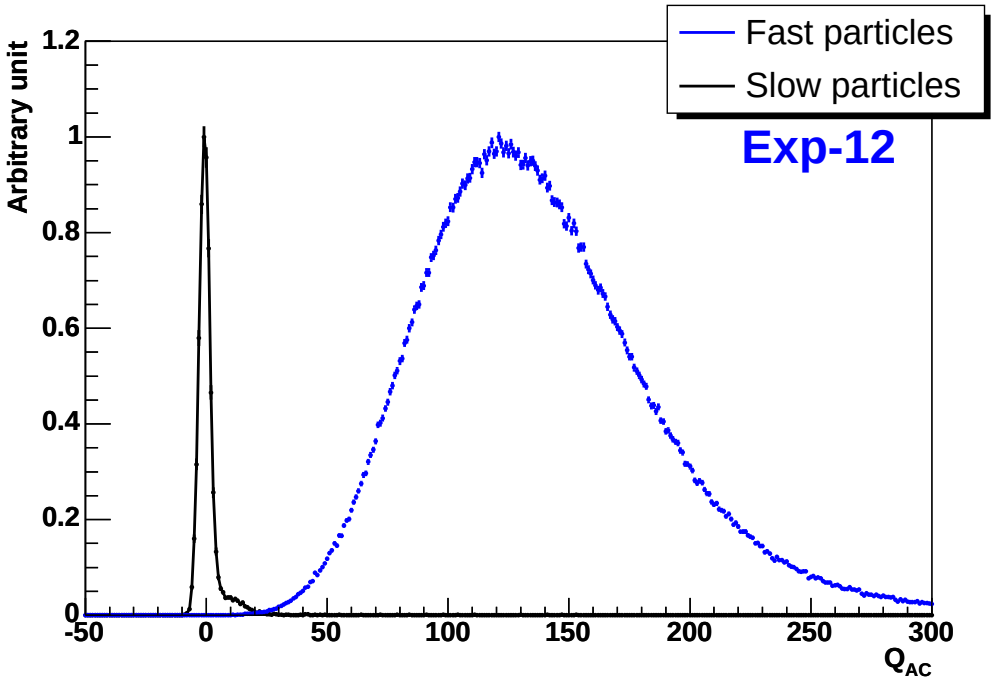

Figure 4.32: The Čerenkov output distribution for slow (black) and relative (blue) particles. Where we used proton samples which is $R > 25$ GeV ($R < 2$GeV) as Fast (Slow) particles.

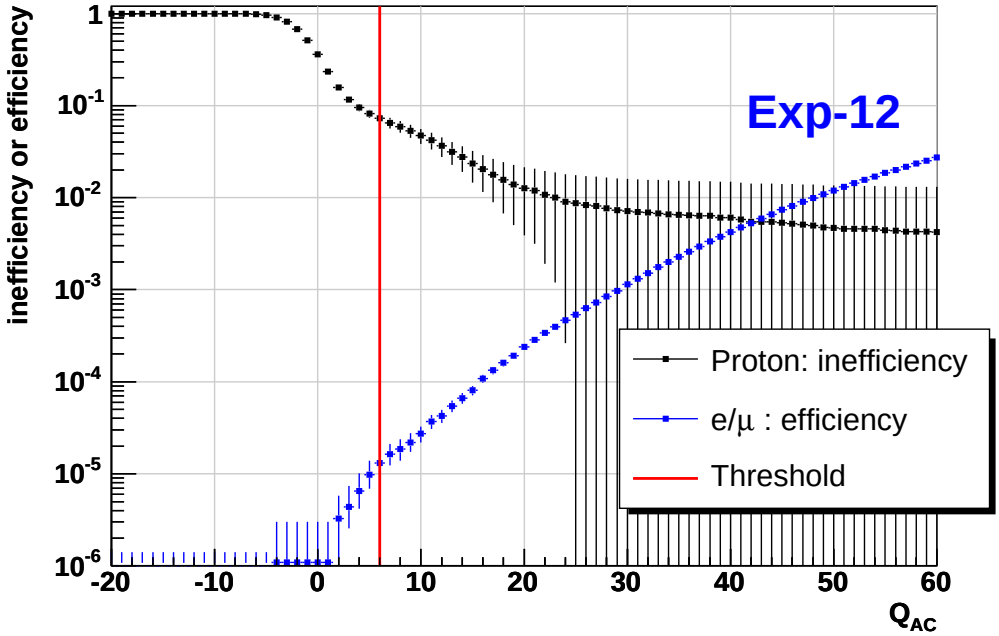

Figure 4.33: The inefficiency and efficiency of Čerenkov cut as a function of ADC threshold. Note that the error bars are taken into account for statistical errors only.

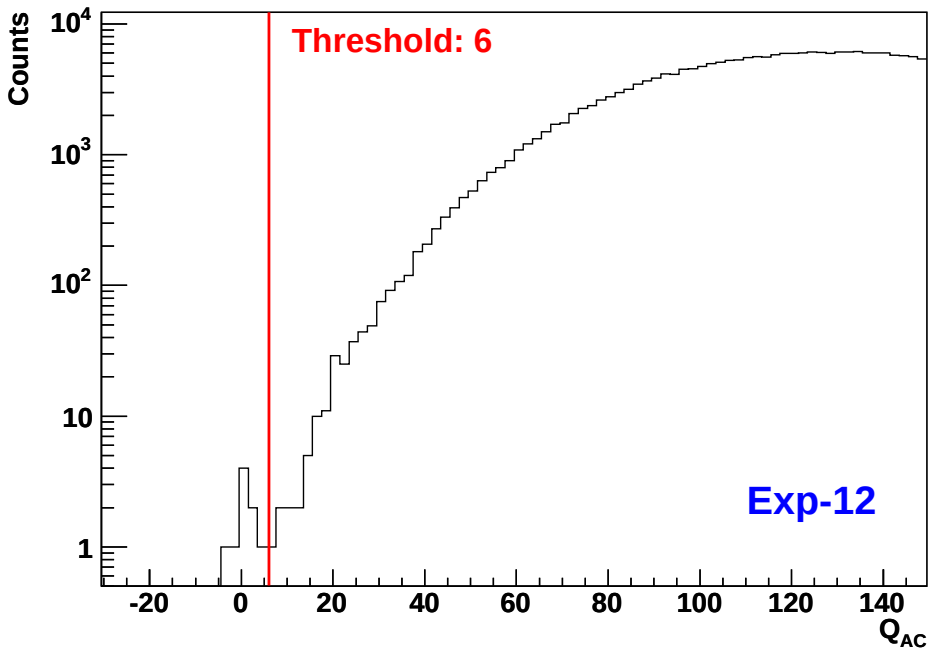

Figure 4.34: Q_{AC} distribution which is applied to all cut for $\overline{p}$ identification expect for Čerenkov cut.

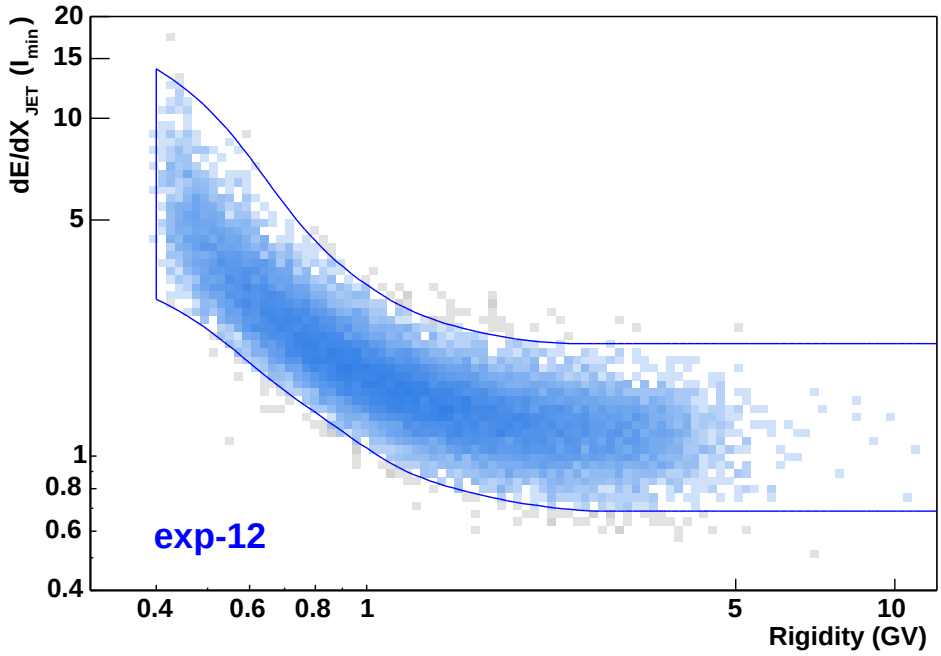

Figure 4.35: Antiproton selection with $\mathrm{d}E/\mathrm{d}x$ chamber. Solid lines represent selection boundaries.

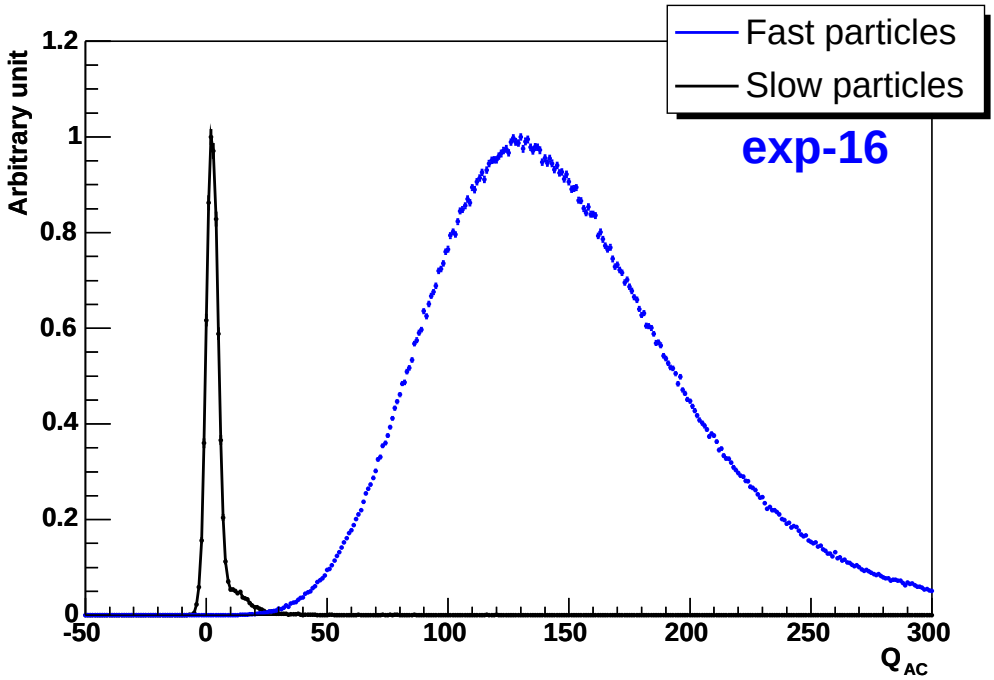

Figure 4.36: The Čerenkov output distribution for slow (black) and relative (blue) paticles. Where we used proton samples which is $R > 25$ GeV ($R < 2$GeV) as Fast (Slow) particles.

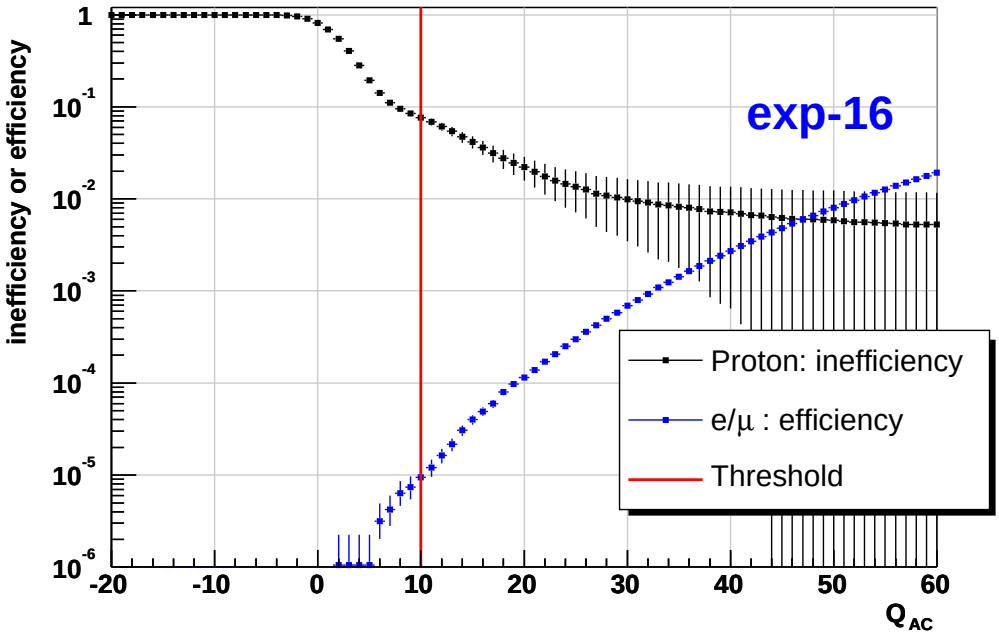

Figure 4.37: The inefficiency and efficiency of Čerenkov cut as a function of ADC threshold. Note that the error bars are taken into account of statistical errors only.

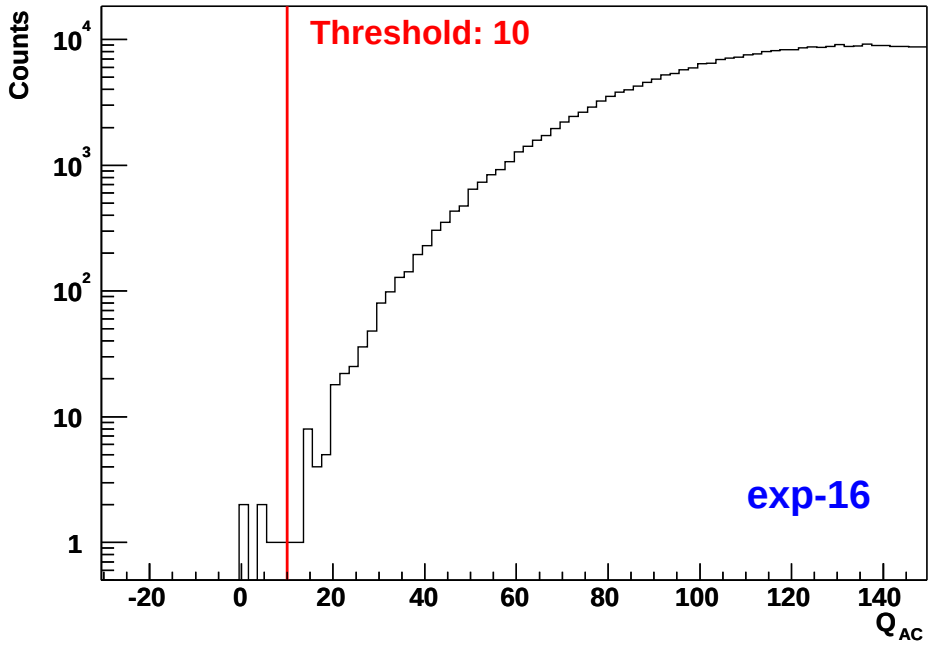

Figure 4.38: Q_{AC} distribution which is applied to all cut for $\overline{p}$ identification expect for Čerenkov cut.

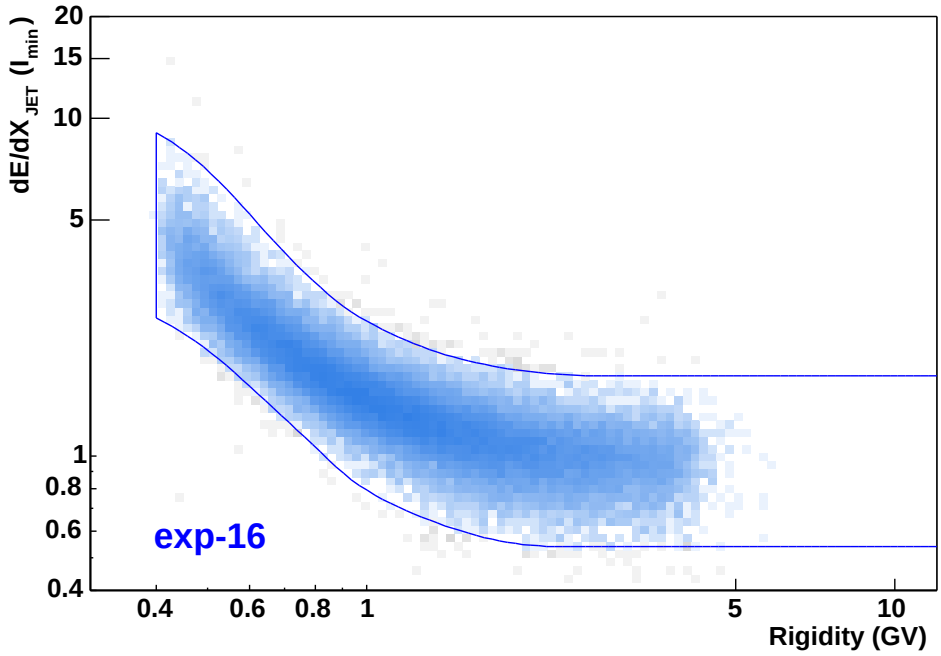

Figure 4.39: Antiproton selection with $\mathrm{d}E/\mathrm{d}x$ chamber. Solid lines represent selection boundaries.

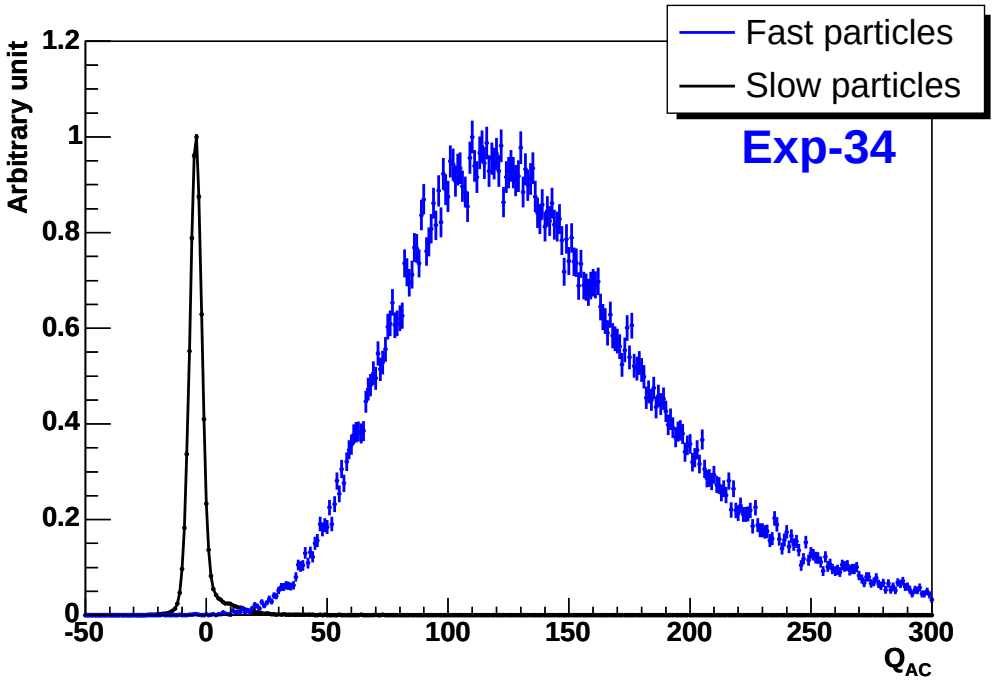

Figure 4.40: The Čerenkov output distribution for slow (black) and relative (blue) particles. Where we used proton samples which is $R > 25$ GeV ($R < 2$GeV) as Fast (Slow) particles.

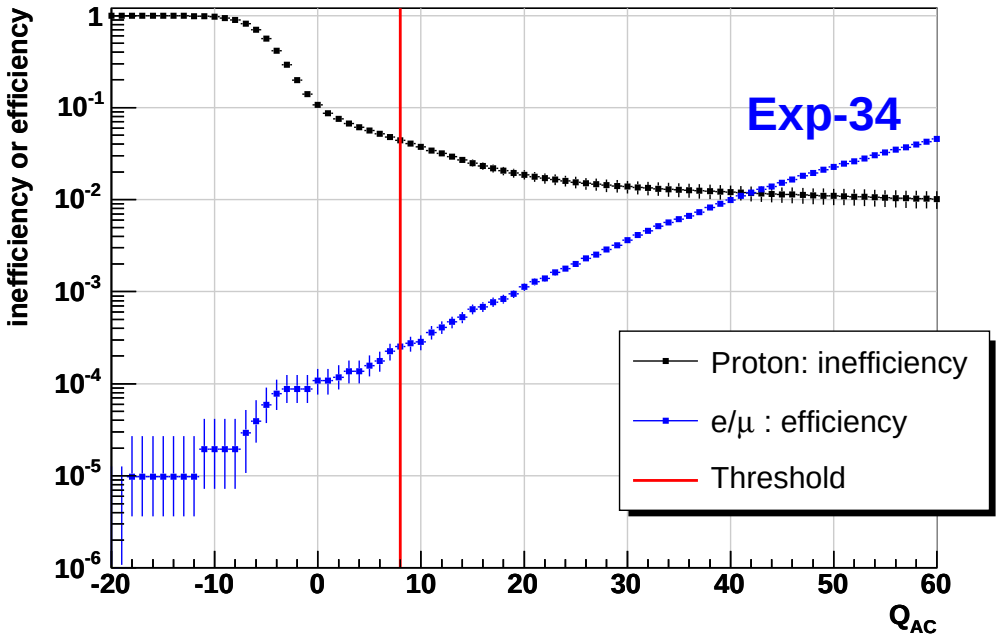

Figure 4.41: The inefficiency and efficiency of Čerenkov cut as a function of ADC threshold. Note that the error bars are taken into account of the statistical errors only.

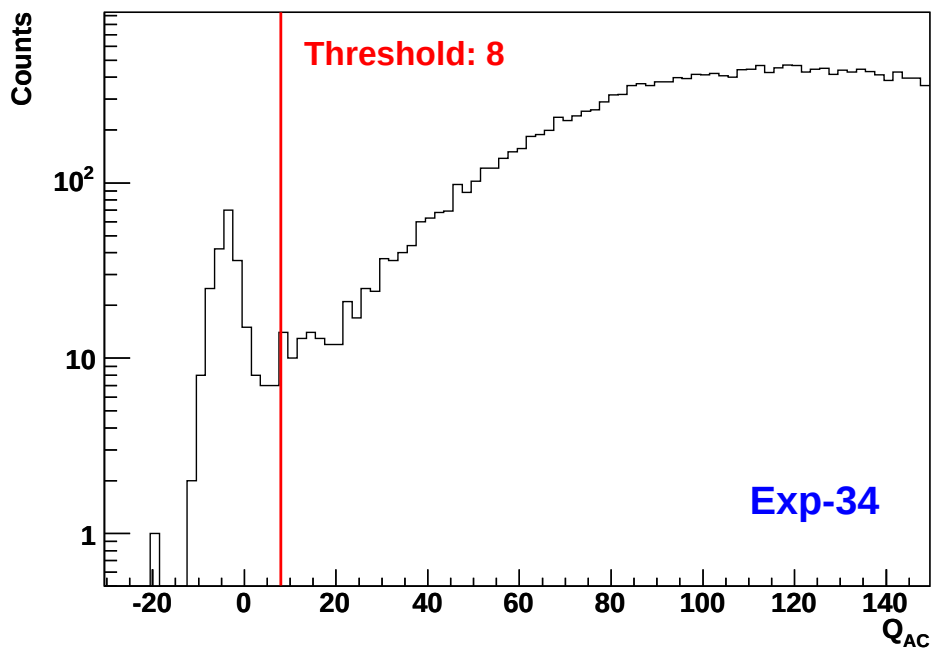

Figure 4.42: Q_{AC} distribution which is applied to all cut for $\overline{p}$ identification expect for Čerenkov cut.

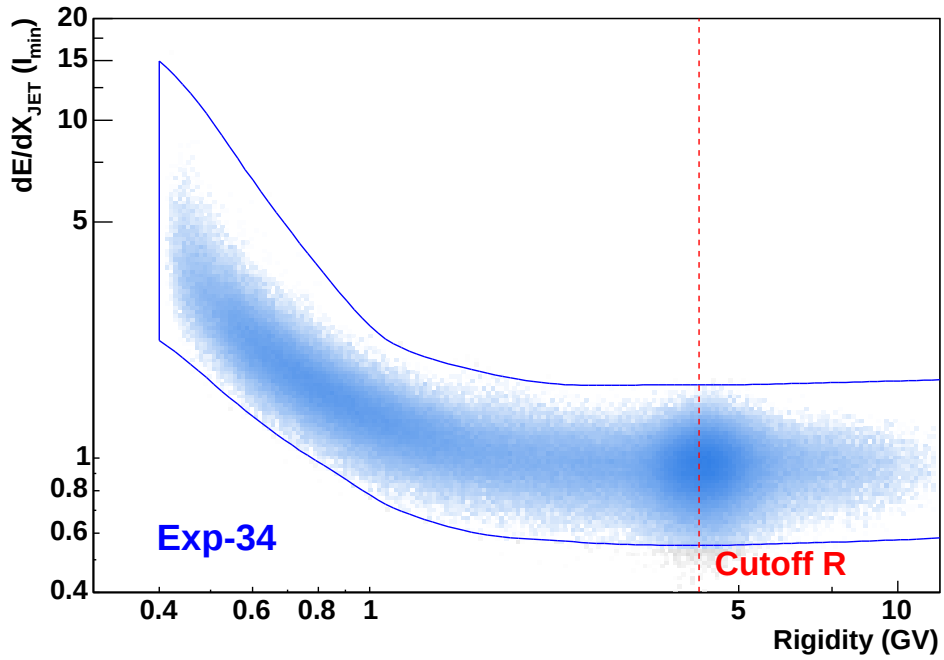

Figure 4.43: Antiproton selection with $\mathrm{d}E/\mathrm{d}x$ chamber. Solid lines represent selection boundaries.

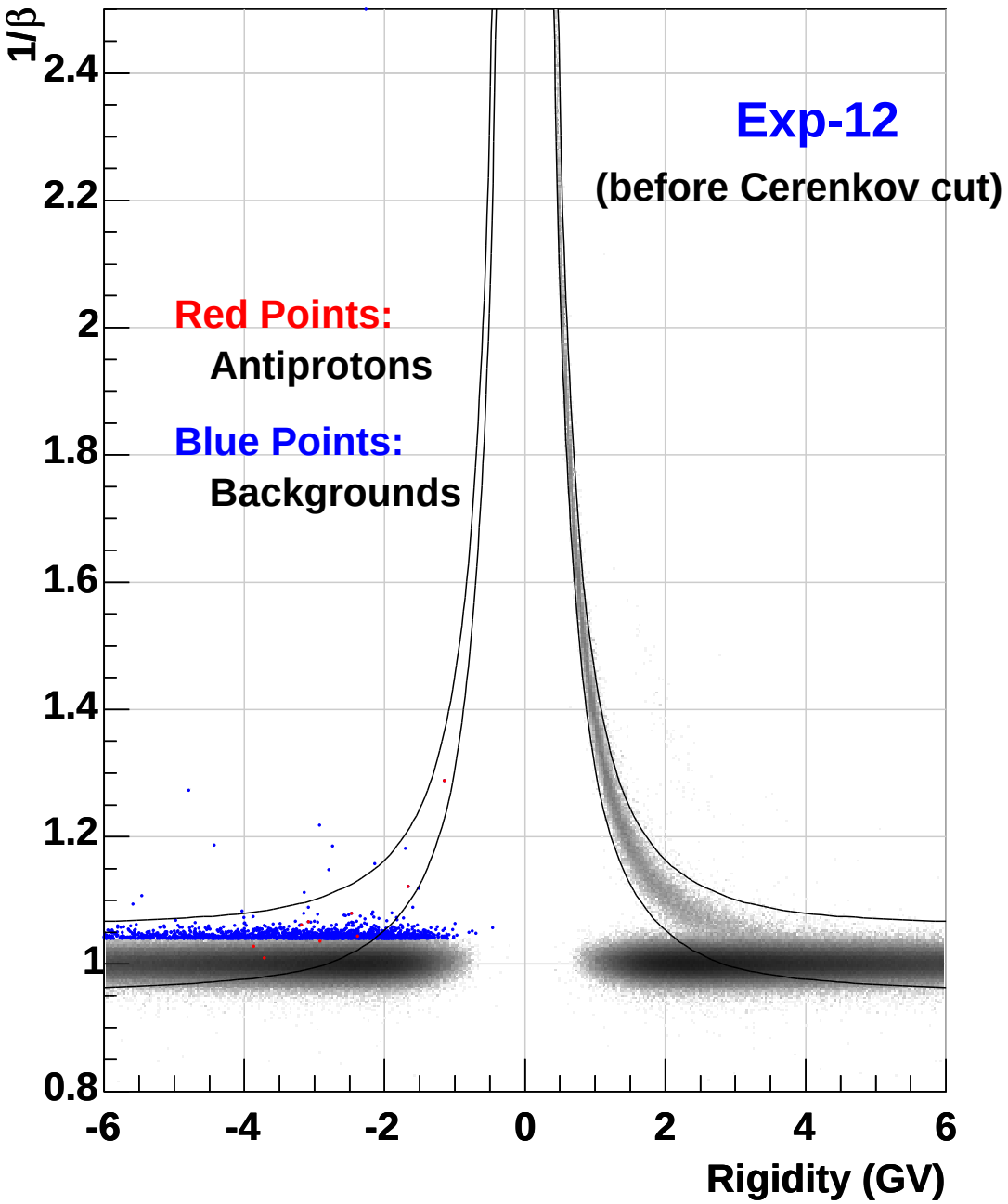

Figure 4.44: β^{-1} vs Rigidity plots before Čerenkov cut. The red points represent $\overline{p}$ events and the blue points represent background particles that are $\beta^{-1} \geq 1.1$. The gray scaled regions represent the event density remaining after Quality cut. In high rigidity region it is impossible to identify $\overline{p}$ events due to the overwhelming backgrounds of e^-, μ^- and π^-.

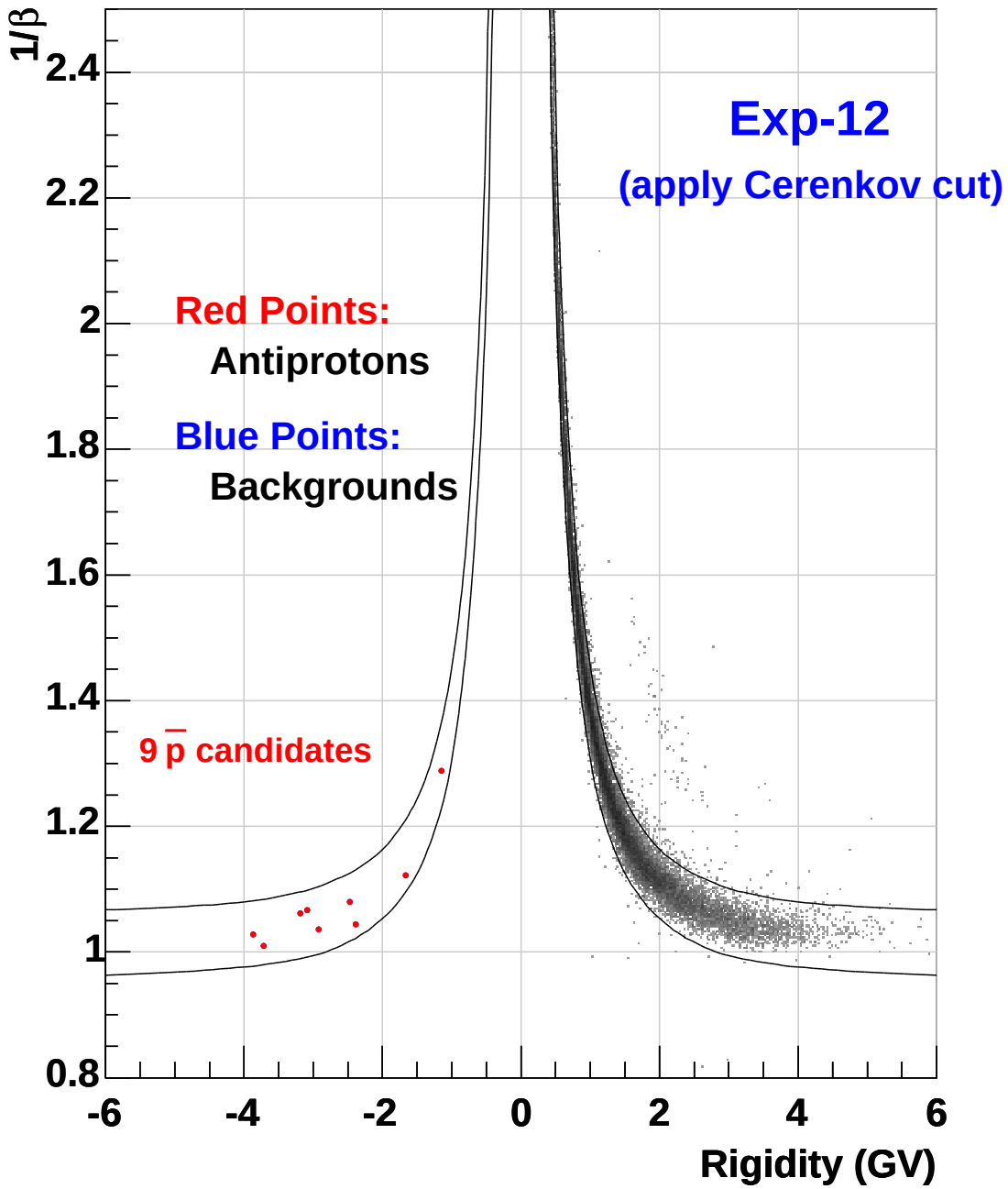

Figure 4.45: β^{-1} vs Rigidity plots after Čerenkov cut. The solid lines represent boundaries of β-band cut. a clean narrow band of $\overline{p}$'s can be seen at the exact mirror position of the protons.

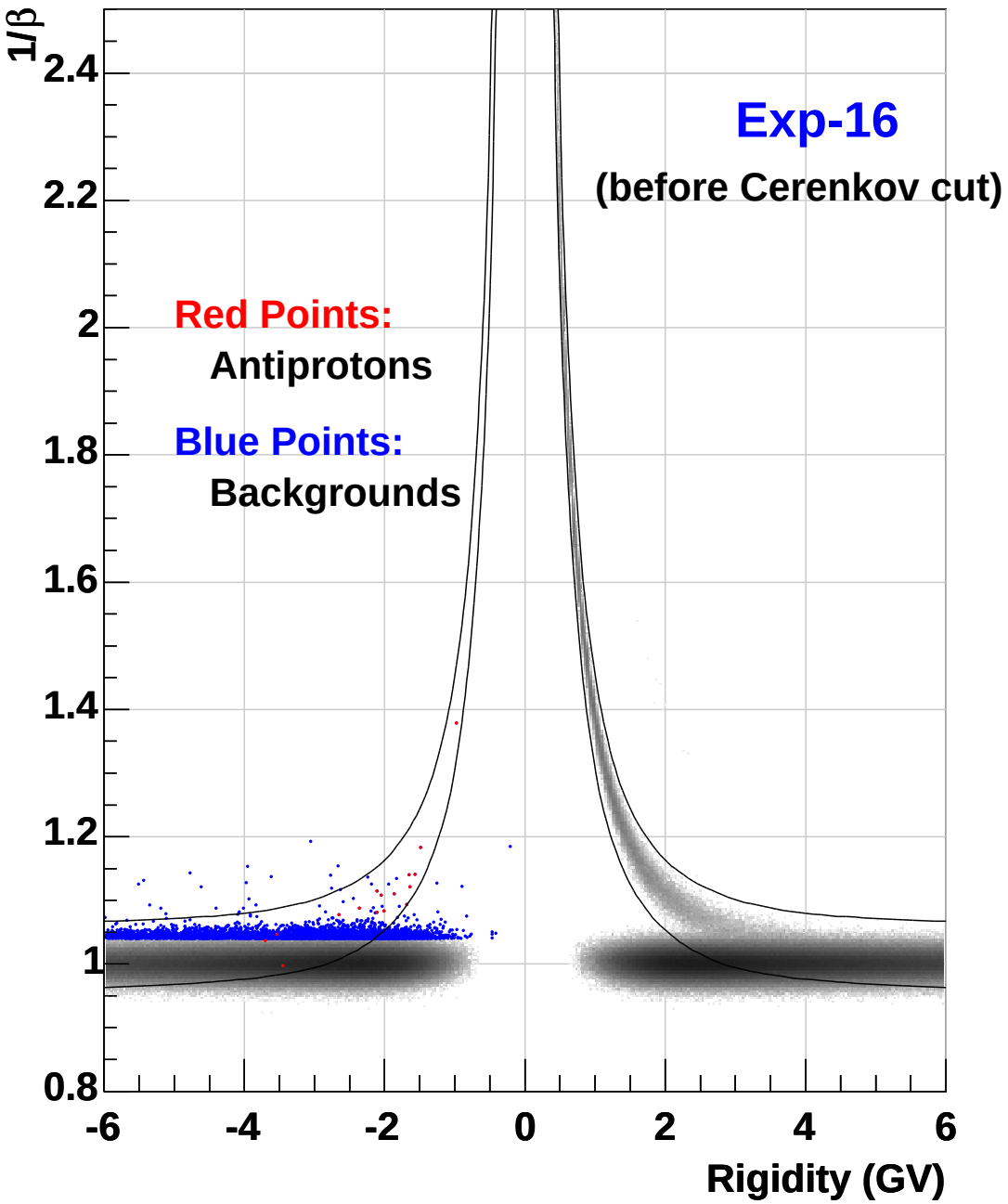

Figure 4.46: β^{-1} vs Rigidity plots before Čerenkov cut. The red points represent $\overline{p}$ events and the blue points represent background particles that are $\beta^{-1} \geq 1.1$. The gray scaled regions represent the event density remaining after Quality cut. In high rigidity region it is impossible to identify $\overline{p}$ events due to the overwhelming backgrounds of e^-, μ^- and π^-.

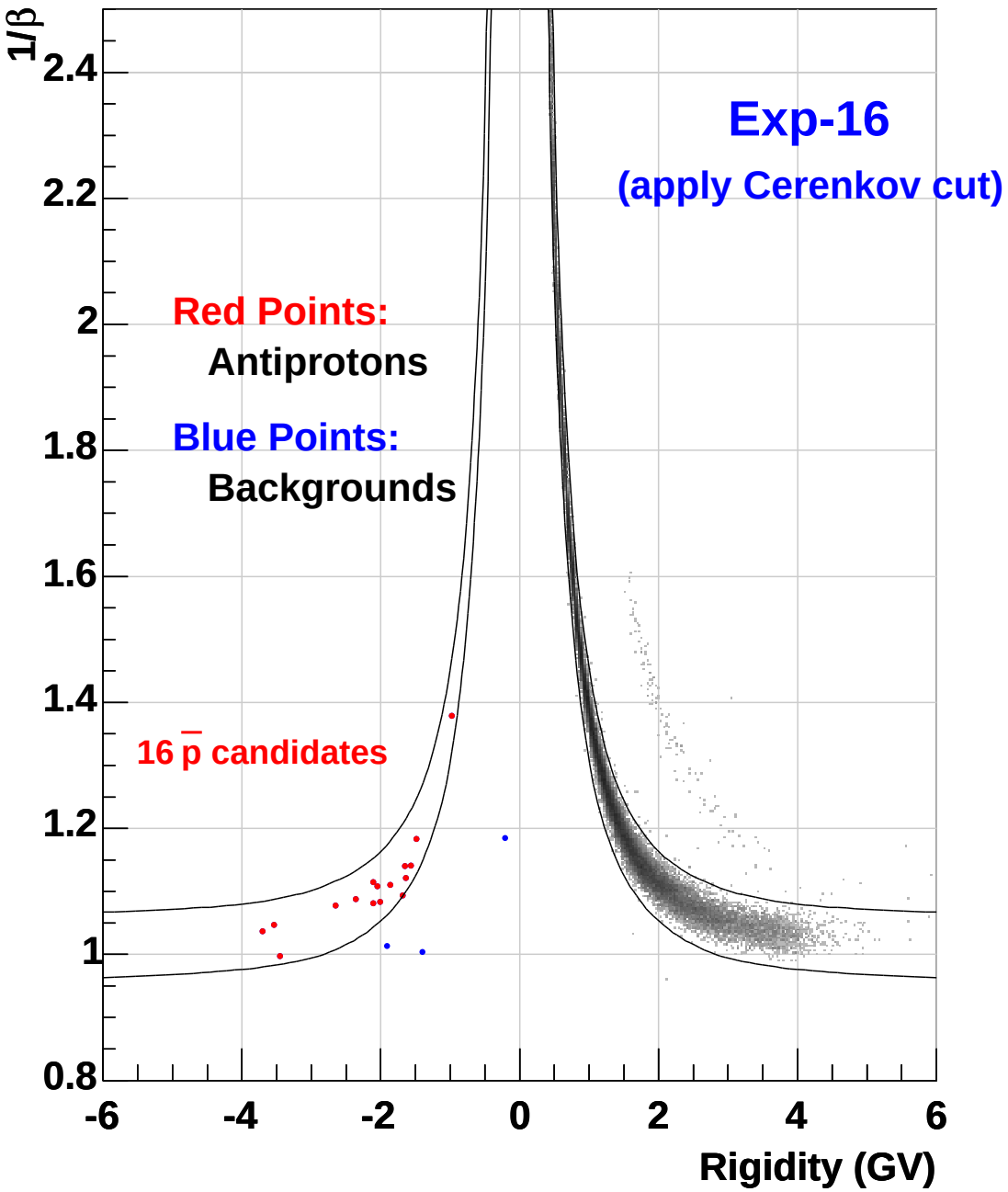

Figure 4.47: β^{-1} vs Rigidity plots after Čerenkov cut. The solid lines represent boundaries of β-band cut. a clean narrow band of $\overline{p}$'s can be seen at the exact mirror position of the protons.

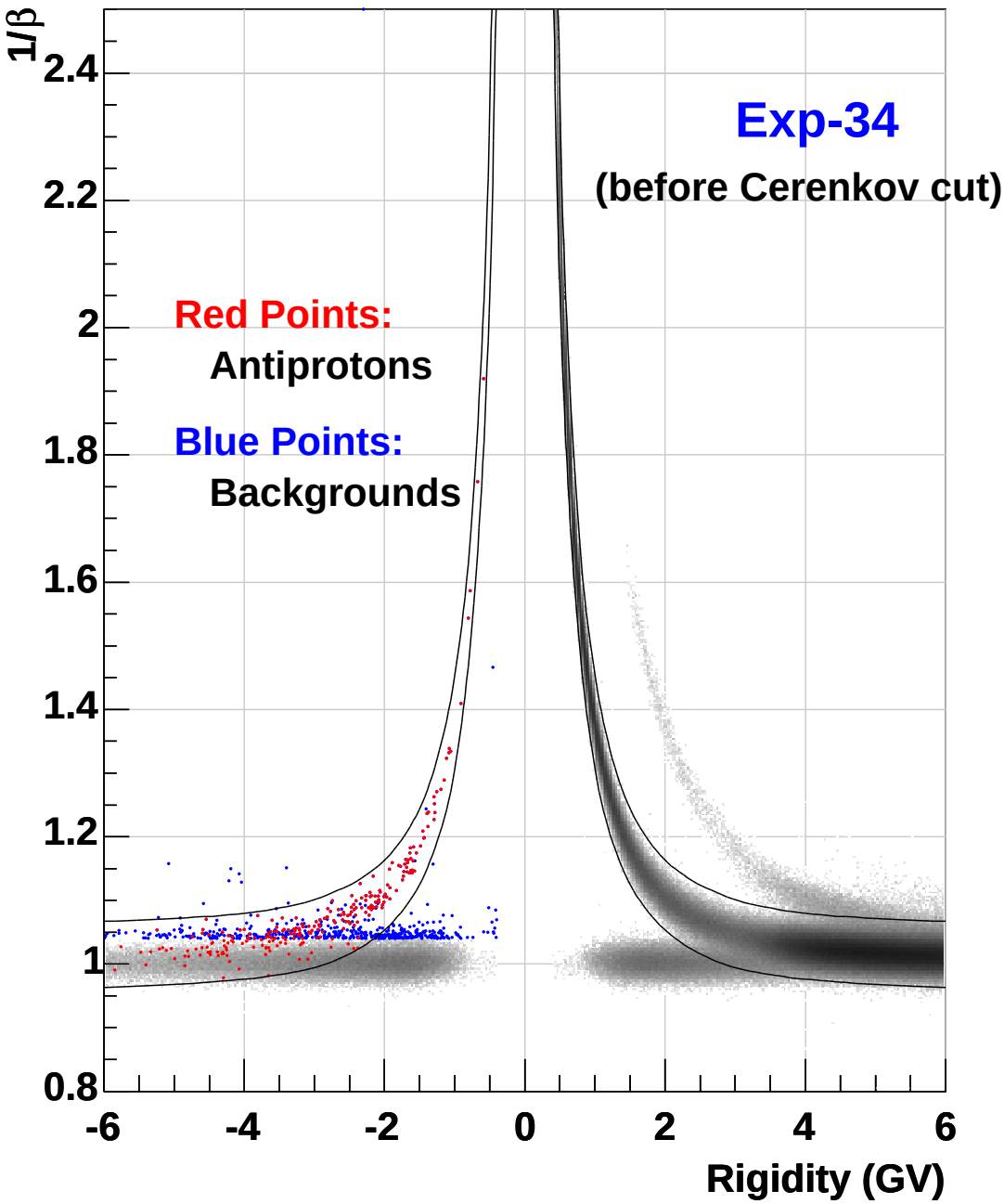

Figure 4.48: β^{-1} vs Rigidity plots before Čerenkov cut. The red points represent $\overline{p}$ events and the blue points represent background particles that are $\beta^{-1} \geq 1.1$. The gray scaled regions represent the event density remaining after Quality cut. In high rigidity region it is impossible to identify $\overline{p}$ events due to the overwhelming backgrounds of e^-, μ^- and π^-

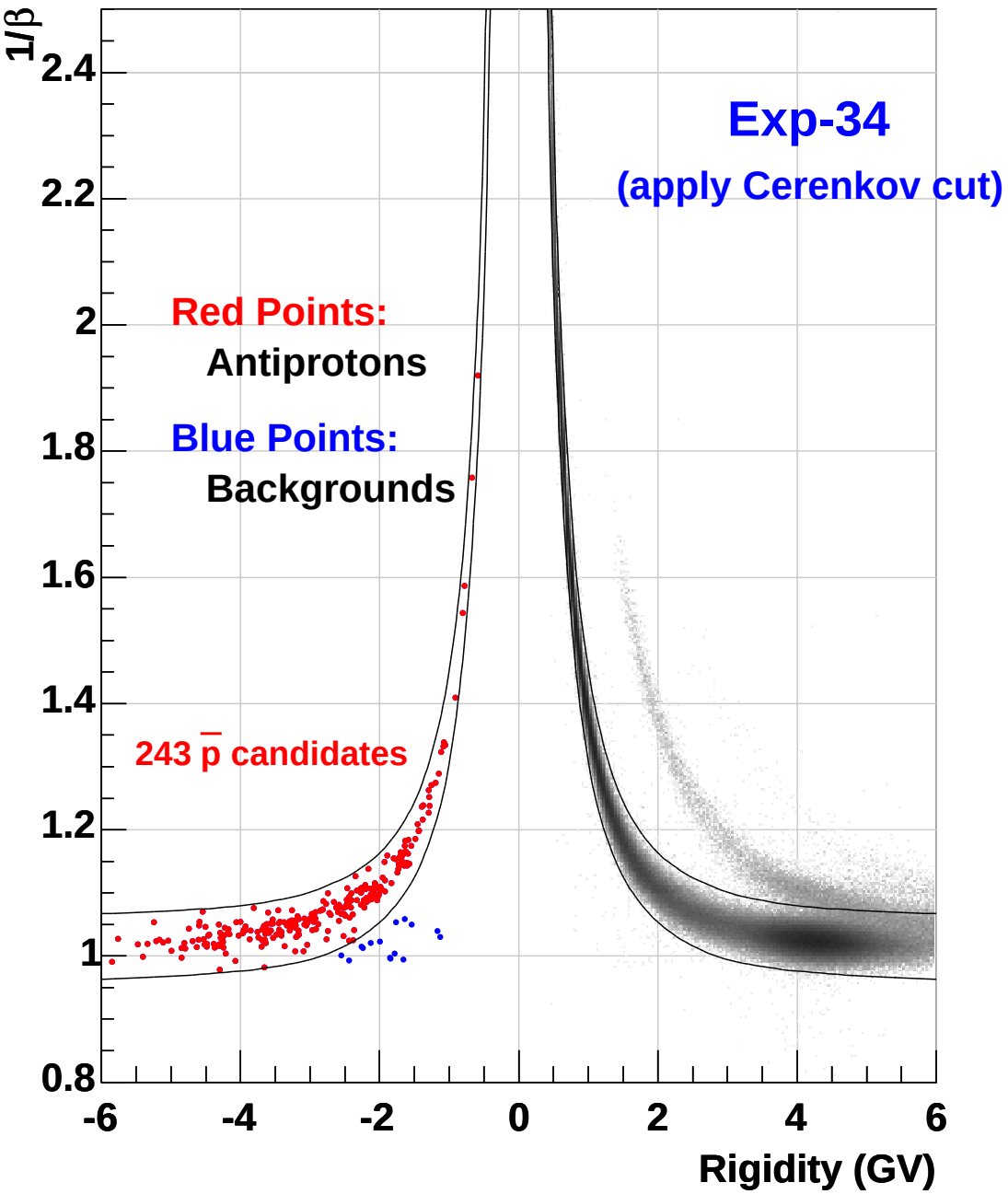

Figure 4.49: β^{-1} vs Rigidity plots after Čerenkov cut. The solid lines represent boundaries of β-band cut. a clean narrow band of $\overline{p}$'s can be seen at the exact mirror position of the protons. There are some event in negative R region plotted as blue points, but there is no such event in positive R region. This is due to plot the all events in negative R region only. Since proton events are many, we show density of proton events as gray scale in positive R region.

Table 4.4: Summary of the event-selection criteria

Pre-selection	
1. Number of long track (including accidental tracks)	$N_{longTK} = 1$
2. Hits in JET	$N_{JET} \leq 60$
3. Hits in TOF	-480mm $\geq Z_{TK_{U,L}} \geq$ 470mm
4. Consistency: TOF and track (r-ϕ)	$\lvert\Delta X_U\rvert \leq$ 60mm, $\lvert\Delta X_L\rvert \leq$ 60mm
5. Consistency: TOF and track (z)	$\lvert\Delta Z_U\rvert \leq$ 45mm, $\lvert\Delta Z_L\rvert \leq$ 45mm
6. Upper TOF dE/dx band cut	dE/dx_U vs R cut (Figure 4.6, 4.7, 4.8)
7. Lower TOF dE/dx band cut	dE/dx_L vs R cut (Figure 4.6, 4.7, 4.8)
8. Expected hits in JET	$N_{expect} \leq 16$, $N_{cneter} \leq 10$
9. z hit-position in TOF	$-480mm \geq Z_{TK_{U,L}} \geq$ 470mm
10. Albedo rejection	$\beta > 0$
Quality cut	
1. Hits used in trajectory fitting	$N_{r\phi-fit} \geq 10$, $N_{z-fit} \geq 6$
2. χ^2 in trajectory fitting	$\chi^2_{r\phi-fit} \leq 6.5$, $\chi^2_{z-fit} \leq 6.5$
3. Dropped hits	$N_{drop} \leq 3$
4. Validity of R_{amp}	$\lvert\Delta R_U\rvert \leq 0.3$, $\lvert\Delta R_L\rvert \leq 0.3$
Identification	
1. Aerogel Čerenkov veto	$Q_{AC} \leq 25$ (for $\beta^{-1} \geq 1.1$ events)
Exp-12 :	$Q_{AC} \leq 6$ (for $beta^{-1} < 1.1$ events)
Exp-16 :	$Q_{AC} \leq 10$ (for $beta^{-1} < 1.1$ events)
Exp-34 :	$Q_{AC} \leq 8$ (for $beta^{-1} < 1.1$ events)
	with fiducial volume cut (Table 4.1-4.3)
2. Energy deposit in JET	dE/dx_J vs R cut (Figure 4.35, 4.39, 4.43)
3. Mass determination	$1/\beta$ vs R cut (Figure 4.45, 4.47, 4.49)

4.2 Properties of Antiproton Candidates

4.2.1 Energy Deposit in the Scintillators and JET chamber

Figures 4.50-4.52 show the $\mathrm{d}E/\mathrm{d}x$ distribution of $\overline{p}$ (red circles) and protons (background gray dots) candidates in upper and lower TOF hodoscopes, respectively. Figure 4.53, 4.55, 4.57 also show the energy deposit in JET chamber. Each distribution is shown after applying all cuts other than the $\mathrm{d}E/\mathrm{d}x$ cut. Solid curves define the selection boundaries.

4.2.2 Light Output in Aerogel Čerenkov Counter

The rigidity dependence of aerogel Čerenkov output(Q_{AC}) for $\overline{p}$ (large solid circles) candidates are shown in Figure 4.54, 4.56, 4.58. Solid lines represent selection boundaries.

4.2.3 Particle Direction and Zenith Angle Distribution

Figure 4.61-4.62 shows the incoming direction of $\overline{p}$ candidates together with those of protons. Figure 4.64 shows the zenith angle distributions of the $\overline{p}$ candidates compared with those of proton candidates. From top to bottom, the plots correspond to energy range of 0.2-1.3, 1.3-3.3, and 3.3-4.2 GeV. In all plots, the distribution are consistent between $\overline{p}$'s and protons. Since zenith angle dependence of the proton flux and that of the antiproton flux is not same, distribution of antiproton is not necessary to agree with distribution of protons. Here, we can check that antiprotons came from acceptable (normal) region, and there is no unusual bias of incoming direction.

4.2.4 Distributions of Cut Parameters

Pre-selection cut parameters

We checked cut parameters used in the "pre-selection" for all candidates. Figures 4.65-4.68 shows the distribution of pre-selection cut parameter for $\overline{p}$ and proton candidates. Open histograms show the distributions for protons, and filled histograms show those for $\overline{p}$'s. For Exp-34 a Fill color shows the observed atmospheric depth. The most light gray represents 4 - 6.5 g/cm^2. As atmospheric depth are increased, the fill color becomes deep.

Quality cut parameters

We also checked parameters used in the quality cut for all candidates. Figures 4.69-4.72 show the distributions of quality cut parameters for $\overline{p}$ and proton candidates. Open histograms show the distributions for protons, and filled histograms show those for $\overline{p}$'s. Although statistics of $\overline{p}$'s is not enough, the distributions of $\overline{p}$'s and protons are consistent with each other. Thus we concluded that all candidates have no problem about the event quality.

4.2.5 Low Energy Antiproton Candidates

Here, we show the event display of $\overline{p}$ candidates (4.73-4.75). Top figure of each page is the lowest energy event observed in each experiment. Other selected events are also illustrated in the figures as typical events with kinetic energy $1 \sim 2$ GeV.

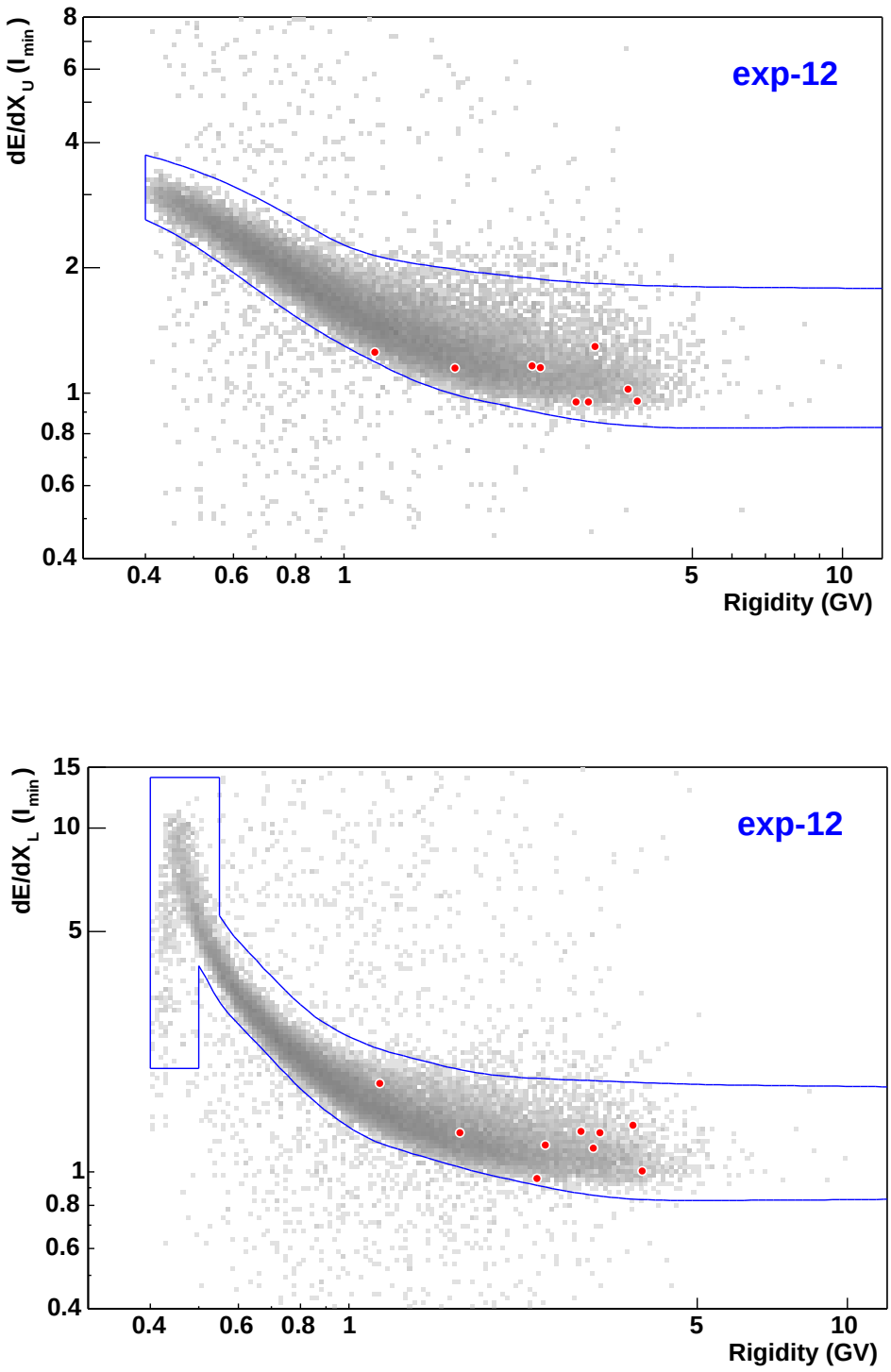

Figure 4.50: Scatter plot of $\mathrm{d}E/\mathrm{d}x$ in upper and lower TOF hodoscope vs $\overline{p}$ rigidity together with the final $\overline{p}$ candidates (large solid circles). Solid line represent selection boundaries.

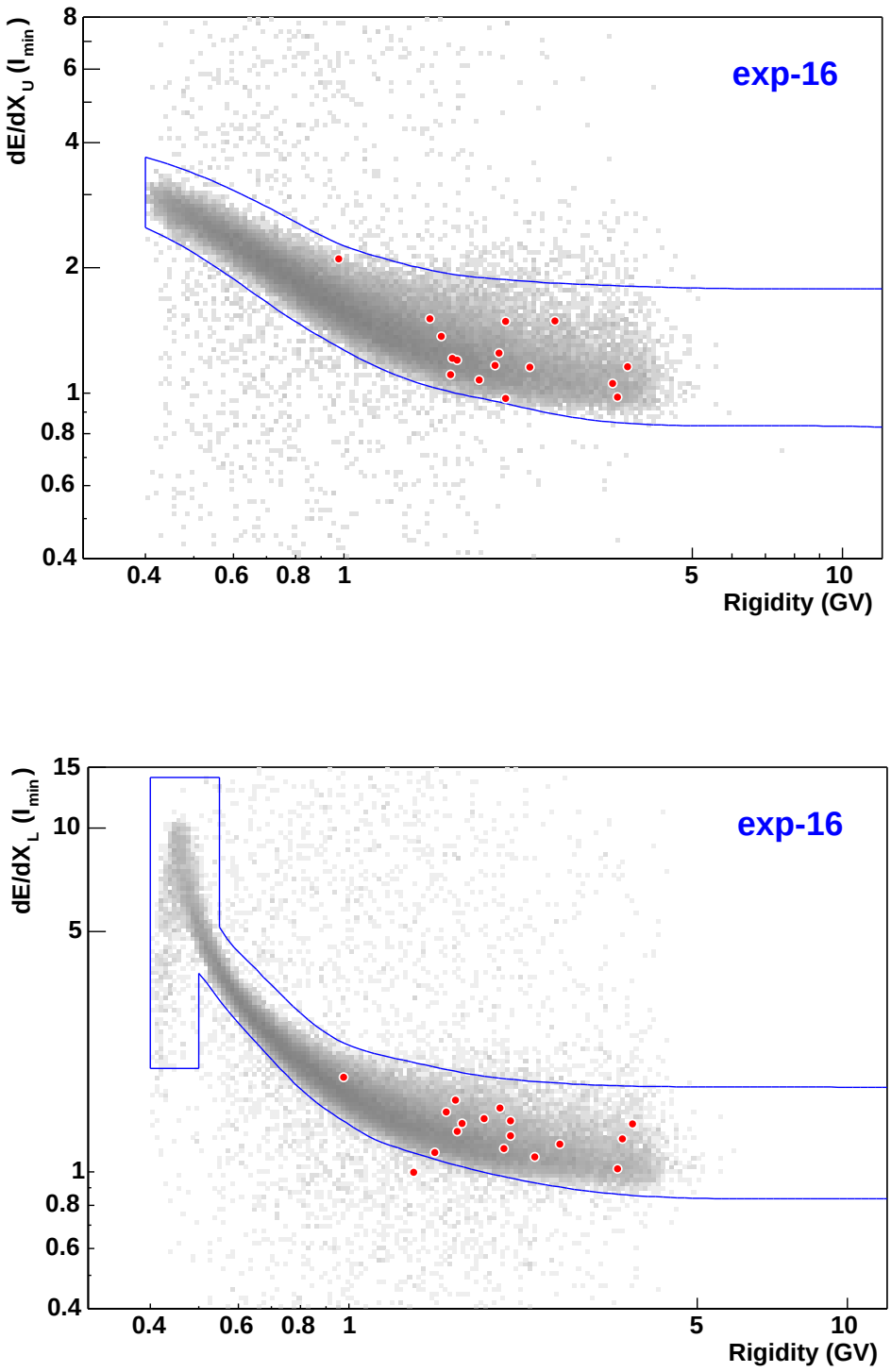

Figure 4.51: Scatter plot of $\mathrm{d}E/\mathrm{d}x$ in upper and lower TOF hodoscope vs $\overline{p}$ rigidity together with the final $\overline{p}$ candidates (large solid circles). Solid line represent selection boundaries.

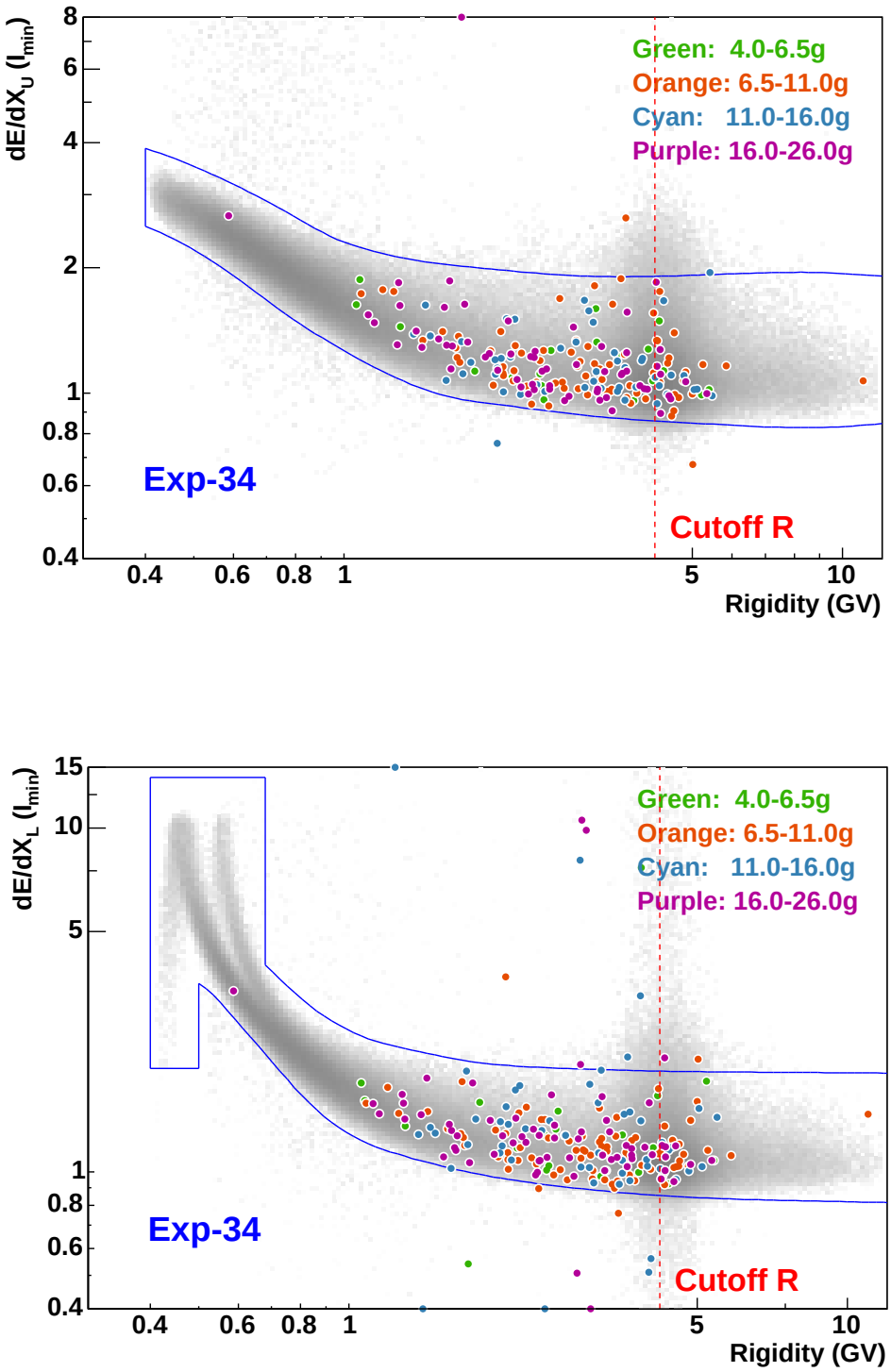

Figure 4.52: Scatter plot of $\mathrm{d}E/\mathrm{d}x$ in upper and lower TOF hodoscope vs $\overline{p}$ rigidity together with the final $\overline{p}$ candidates (large solid circles). Solid line represent selection boundaries.

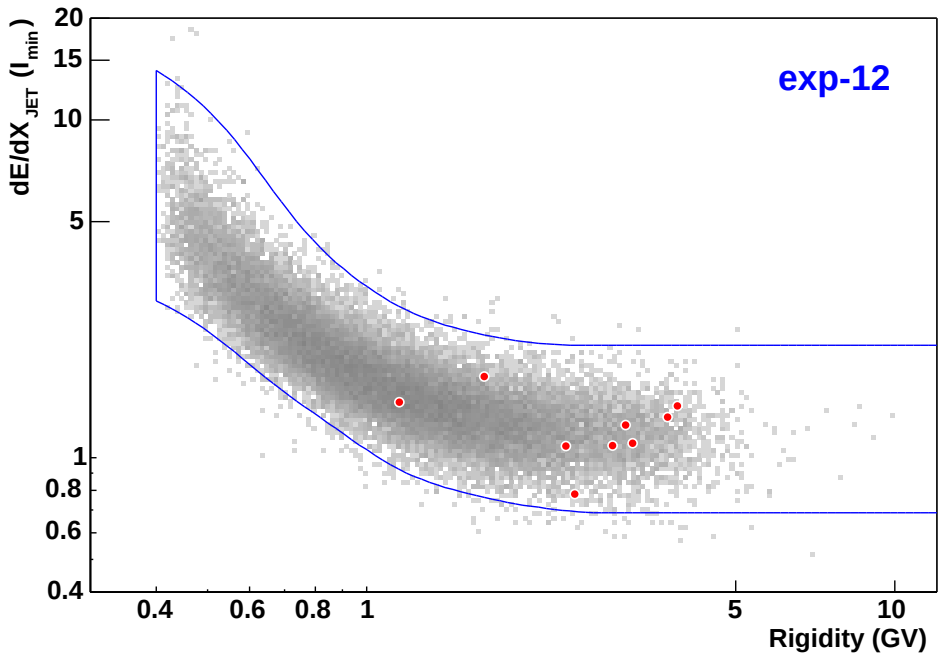

Figure 4.53: Scatter plot of $\mathrm{d}E/\mathrm{d}x$ in JET chamber vs Rigidity in Exp-12.

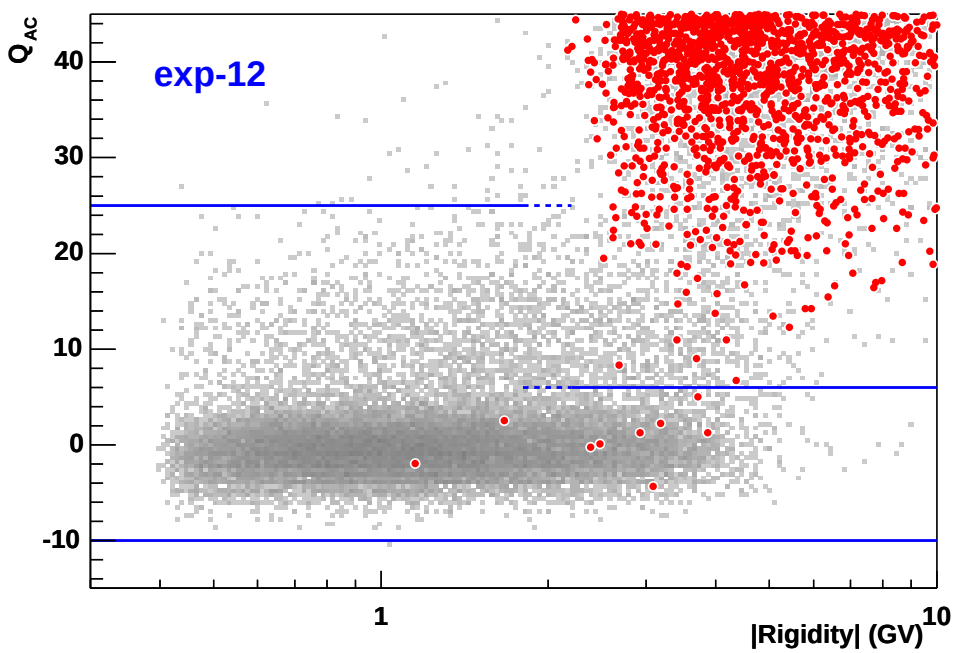

Figure 4.54: Scatter plot of Q_{AC} vs Rigidity in Exp-12.

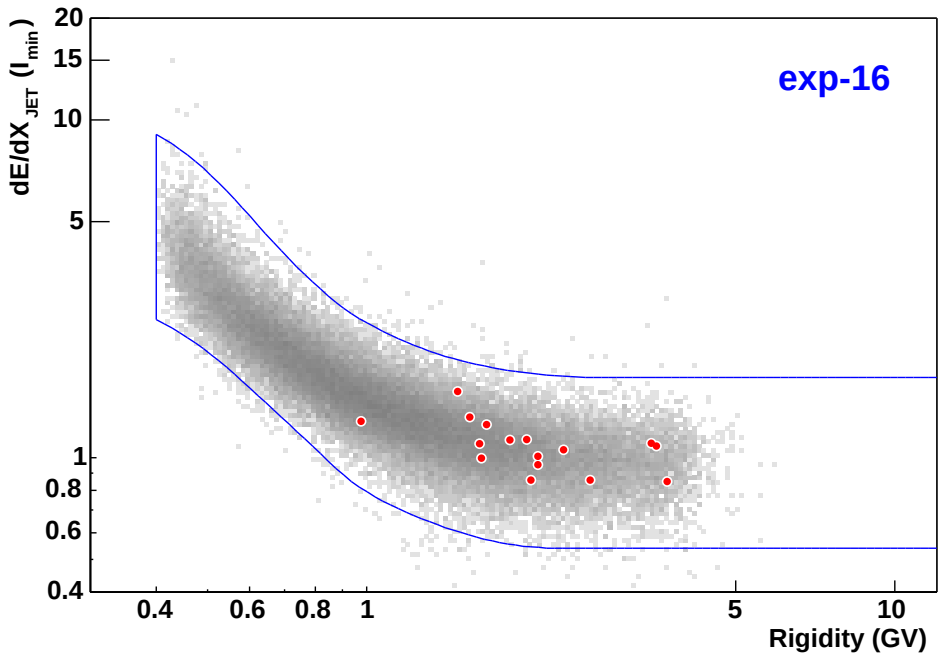

Figure 4.55: Scatter plot of $\mathrm{d}E/\mathrm{d}x$ in JET chamber vs Rigidity in Exp-16.

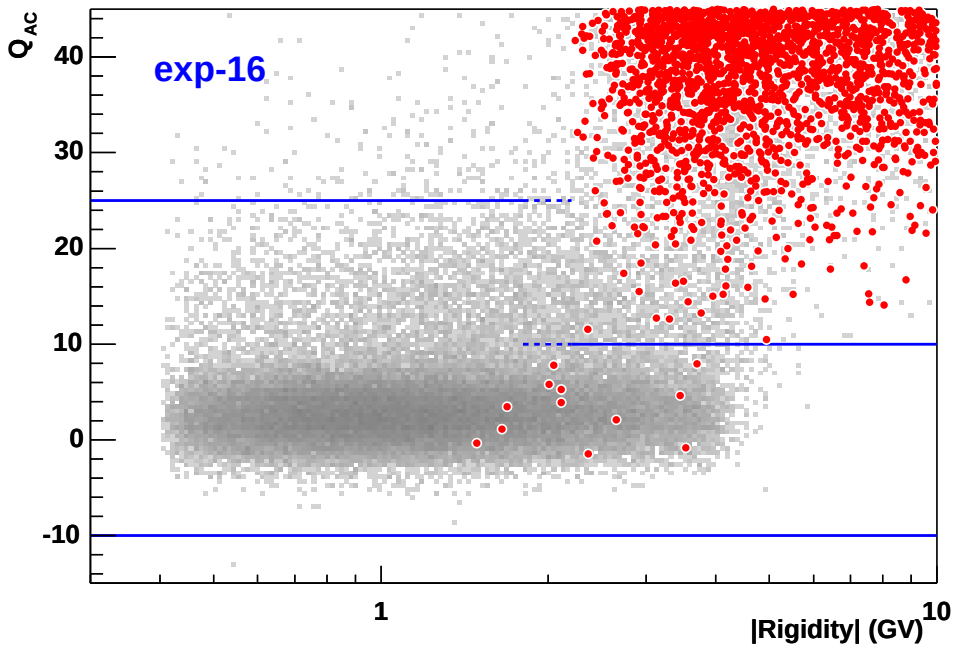

Figure 4.56: Scatter plot of Q_{AC} vs Rigidity in Exp-16.

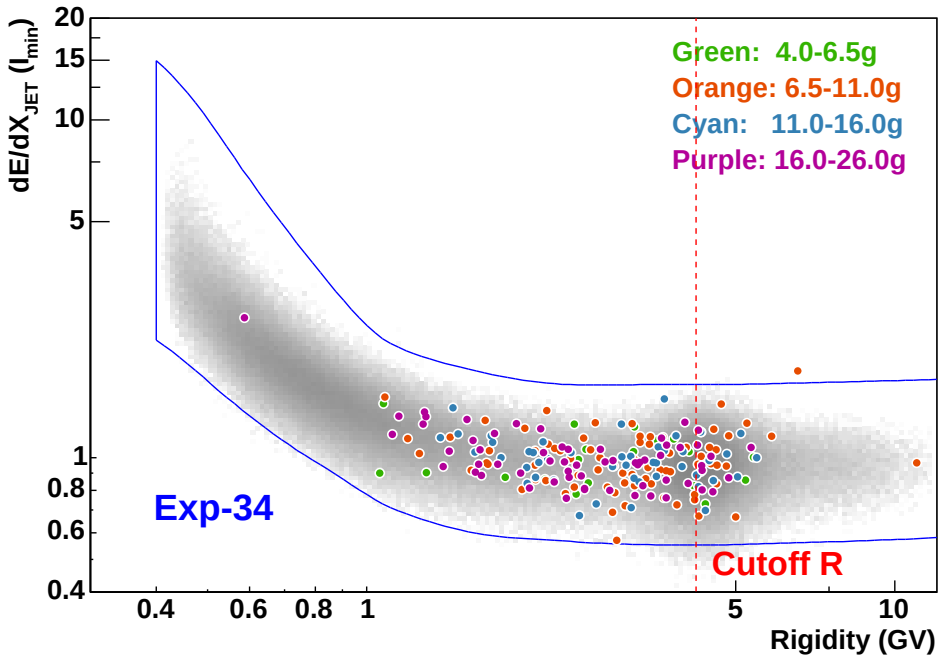

Figure 4.57: Scatter plot of $\mathrm{d}E/\mathrm{d}x$ in JET chamber vs Rigidity in Exp-34.

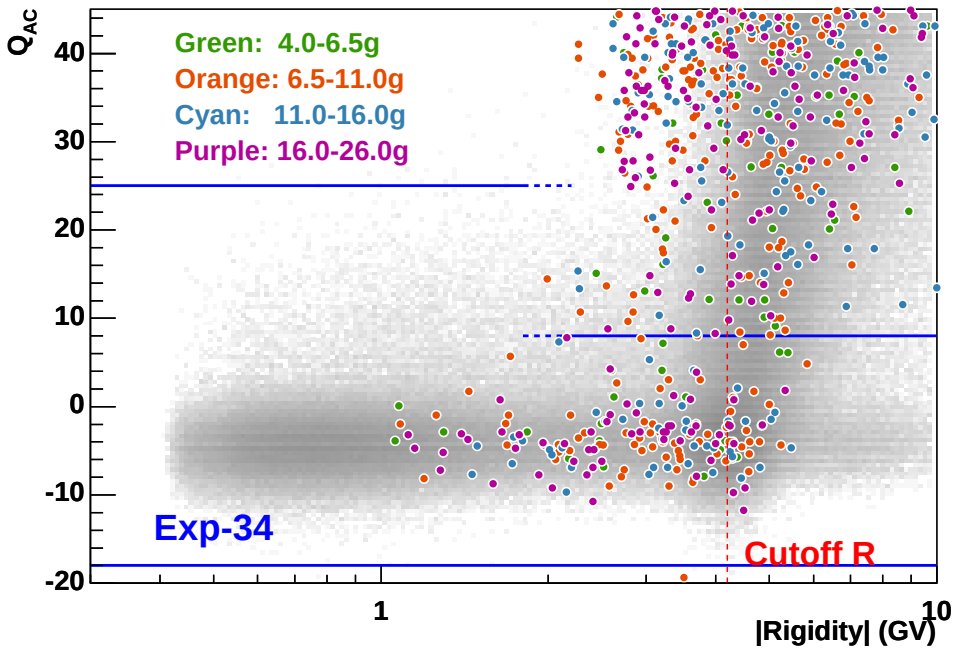

Figure 4.58: Scatter plot of Q_{AC} vs Rigidity in Exp-34.

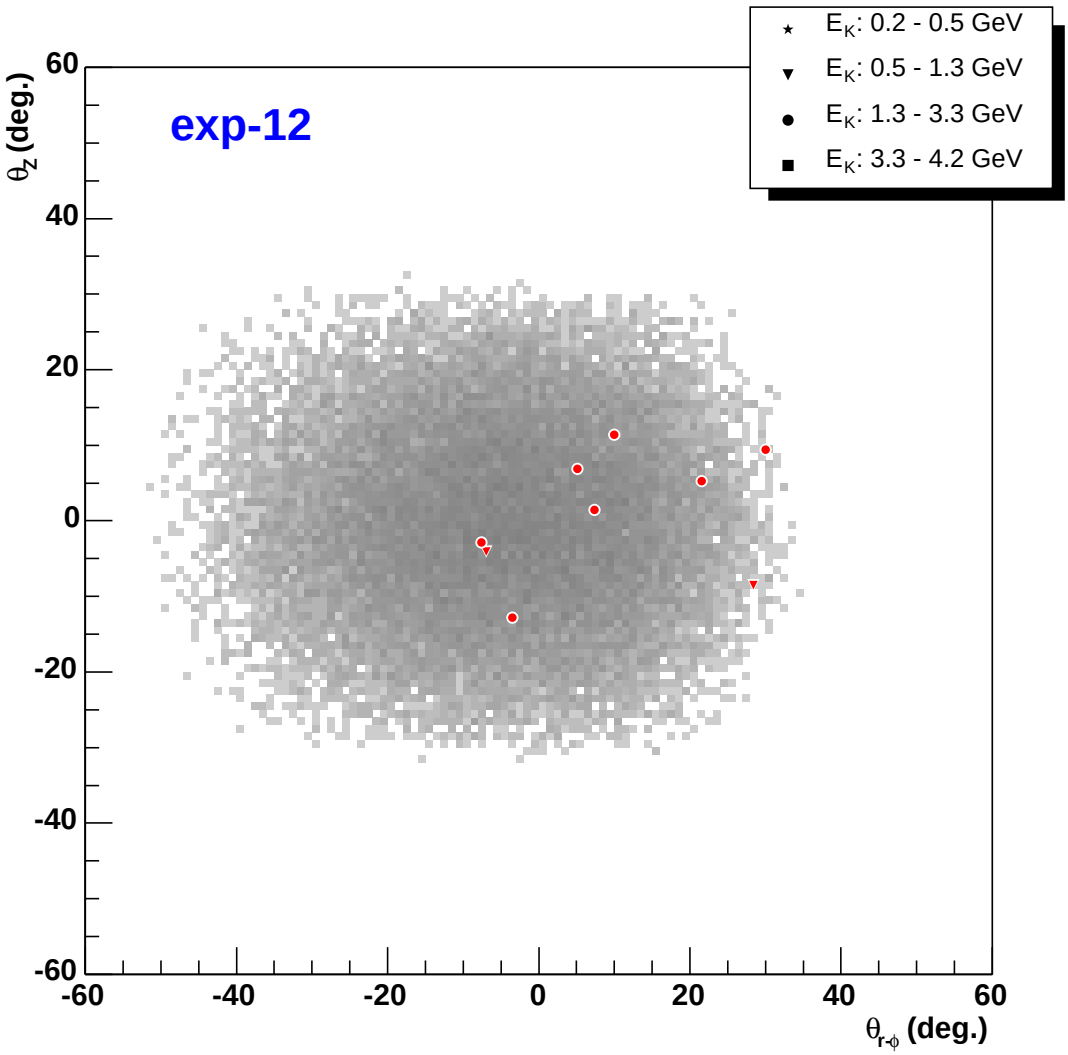

Figure 4.59: The incident direction of $\overline{p}$ candidates in $\theta_{r\phi}$ vs θ_z. Behind gray square represent direction of incoming protons. For compared with $\overline{p}$'s, it is reversed in $\theta_{r\phi}$.

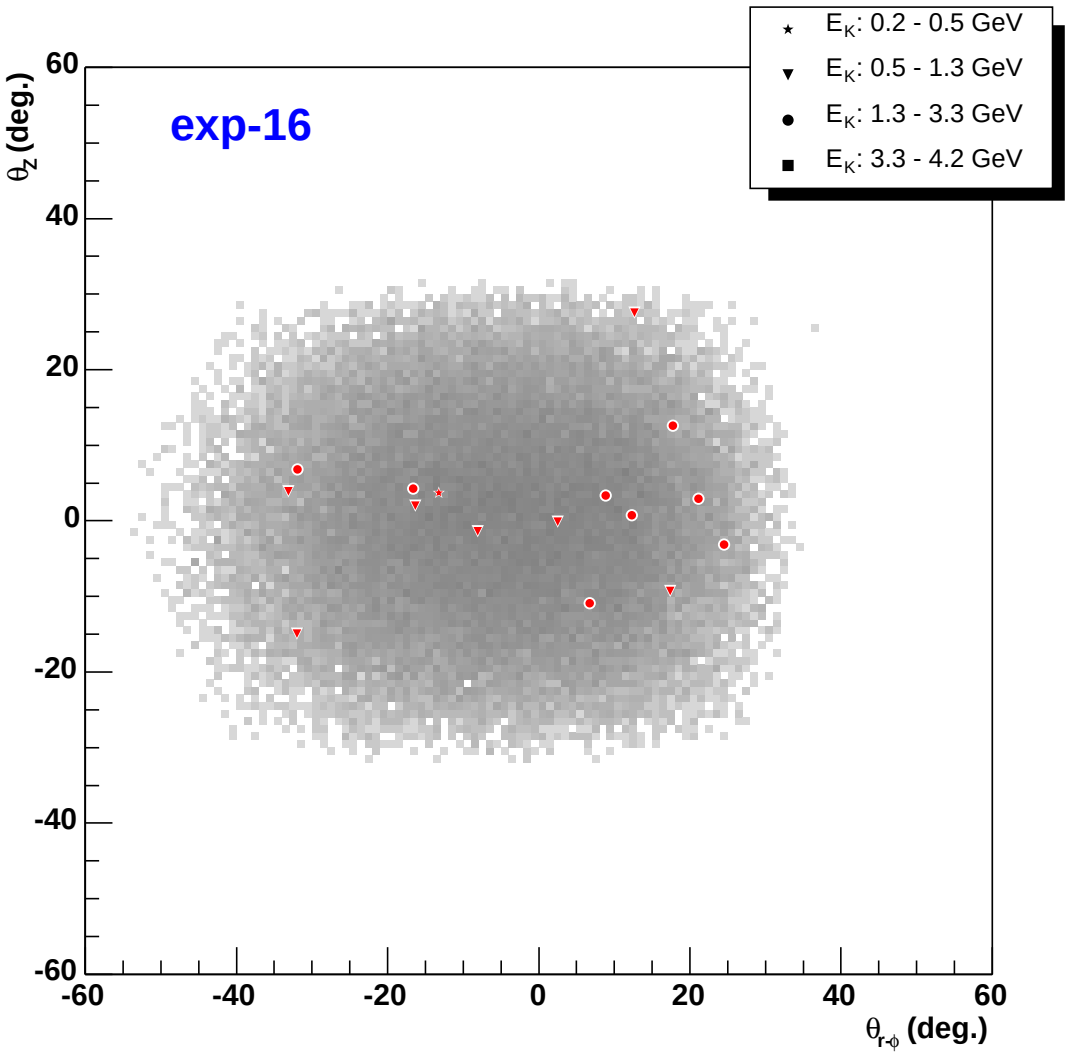

Figure 4.60: The incident angle of $\overline{p}$ candidates in $\theta_{r\phi}$ vs θ_z. Behind gray square represent direction of incoming protons. For compared with $\overline{p}$'s, it is reversed in $\theta_{r\phi}$.

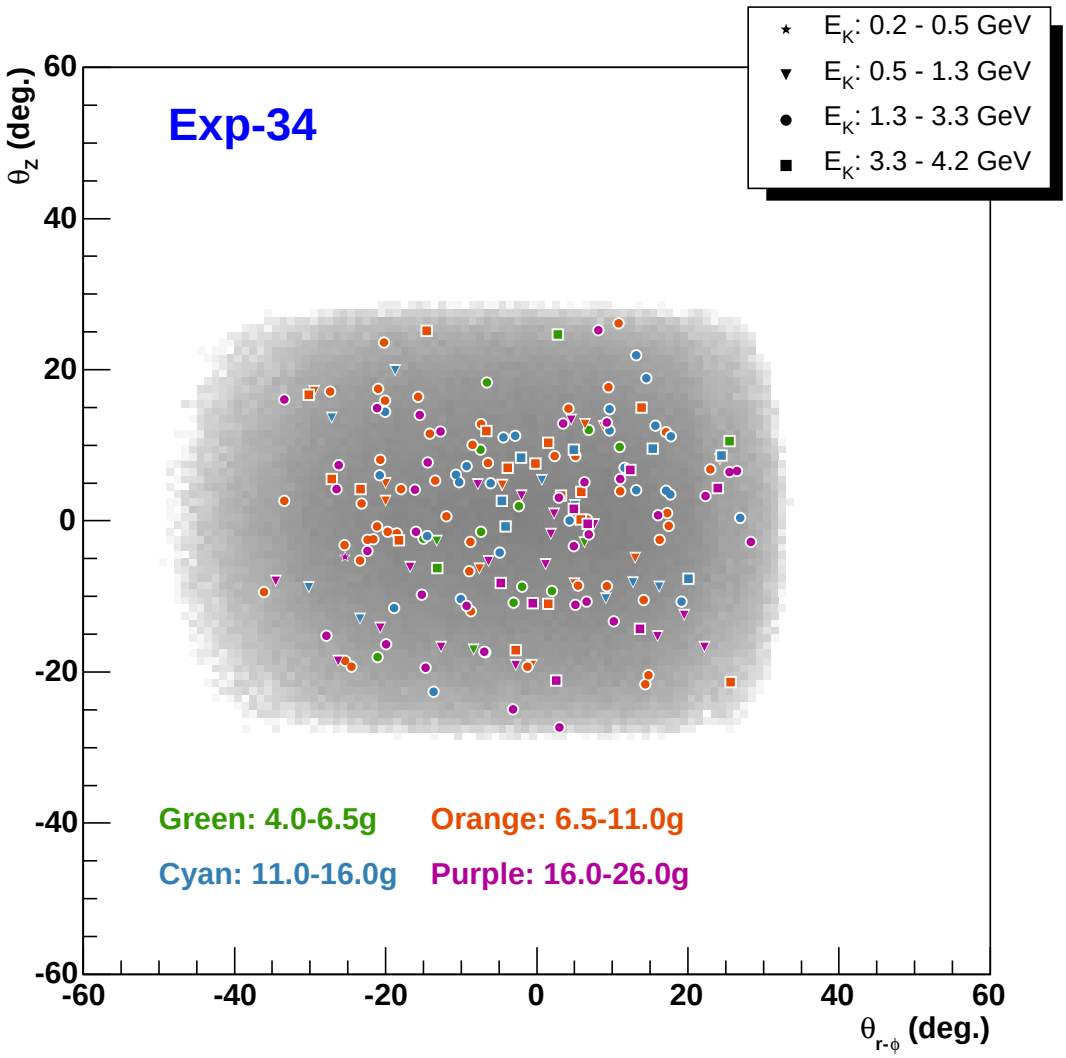

Figure 4.61: The incident angle of $\overline{p}$ candidates in $\theta_{r\phi}$ vs θ_z. Behind gray square represent direction of incoming protons. For compared with $\overline{p}$'s, it is reversed in $\theta_{r\phi}$.

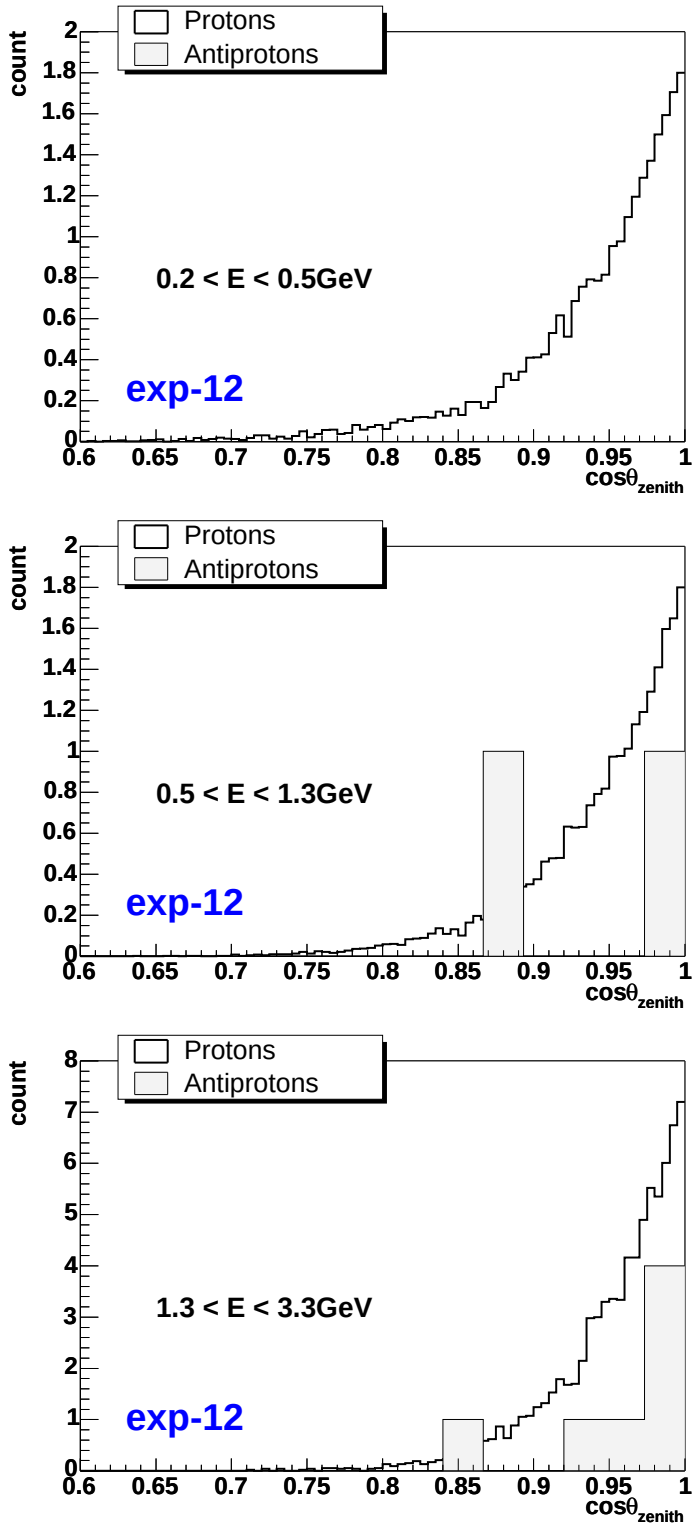

Figure 4.62: Comparison of zenith angle distribution of $\overline{p}$ and proton candidates in energy range of 0.2-0.5, 0.5-1.3 and 1.3-3.3 GeV at TOI.

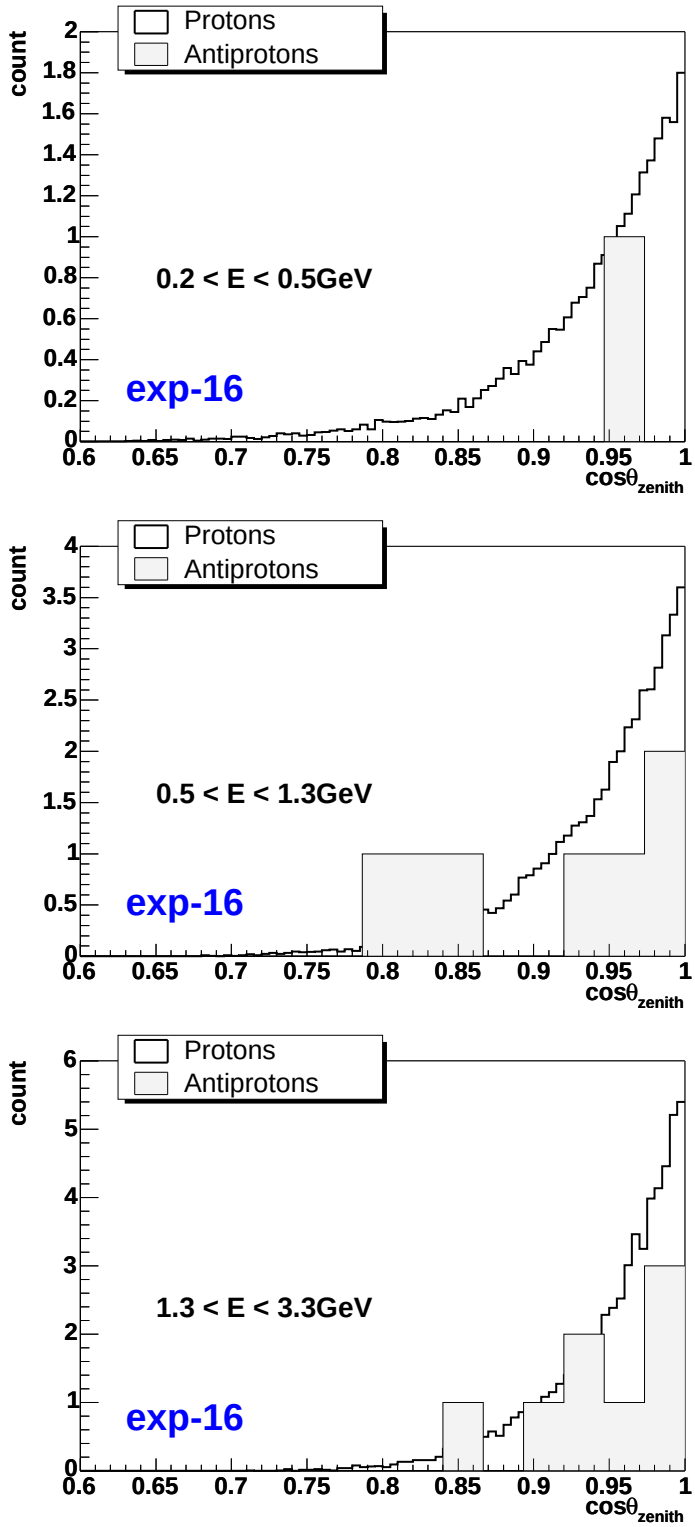

Figure 4.63: Comparison of zenith angle distribution of $\overline{p}$ and proton candidates in energy range of 0.2-0.5, 0.5-1.3 and 1.3-3.3 GeV at TOI.

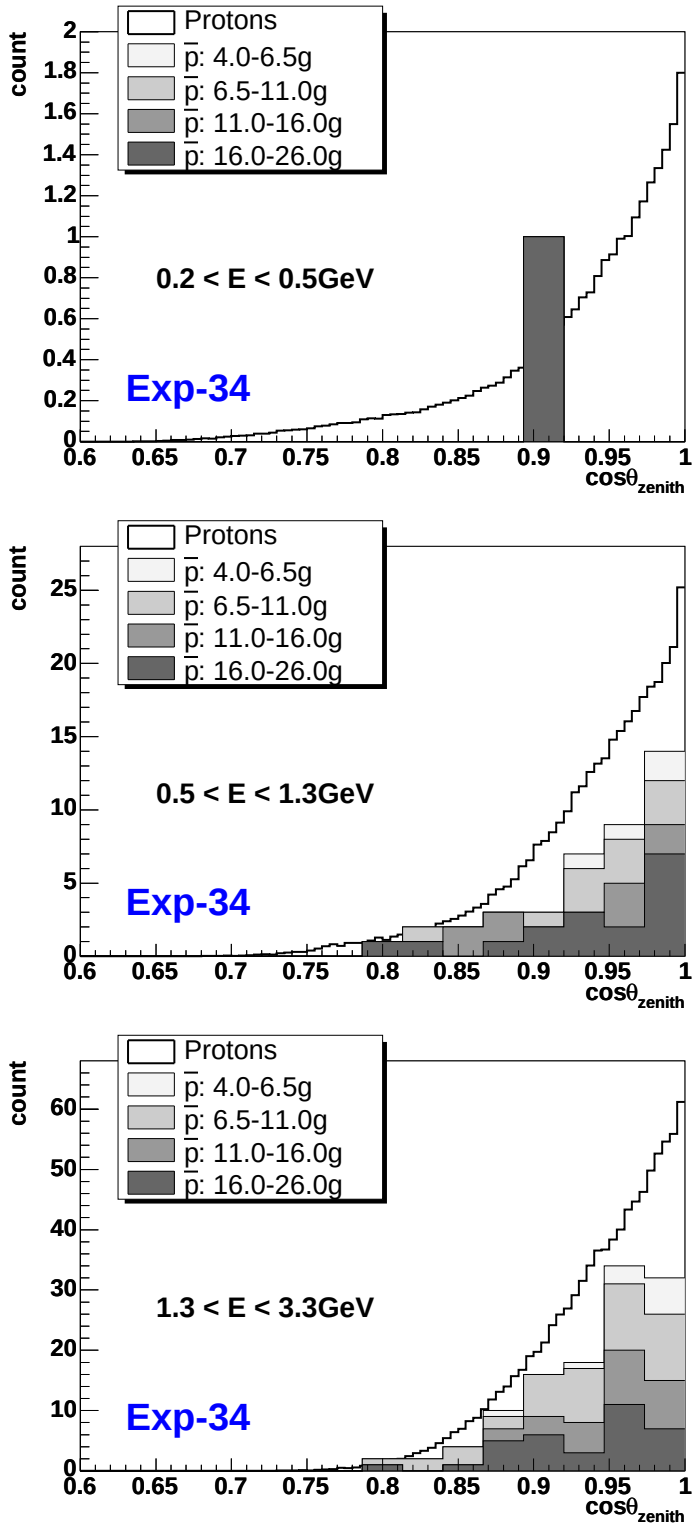

Figure 4.64: Comparison of zenith angle distribution of $\overline{p}$ and proton candidates in energy range of 0.2-0.5, 0.5-1.3 and 1.3-3.3 GeV at TOI.

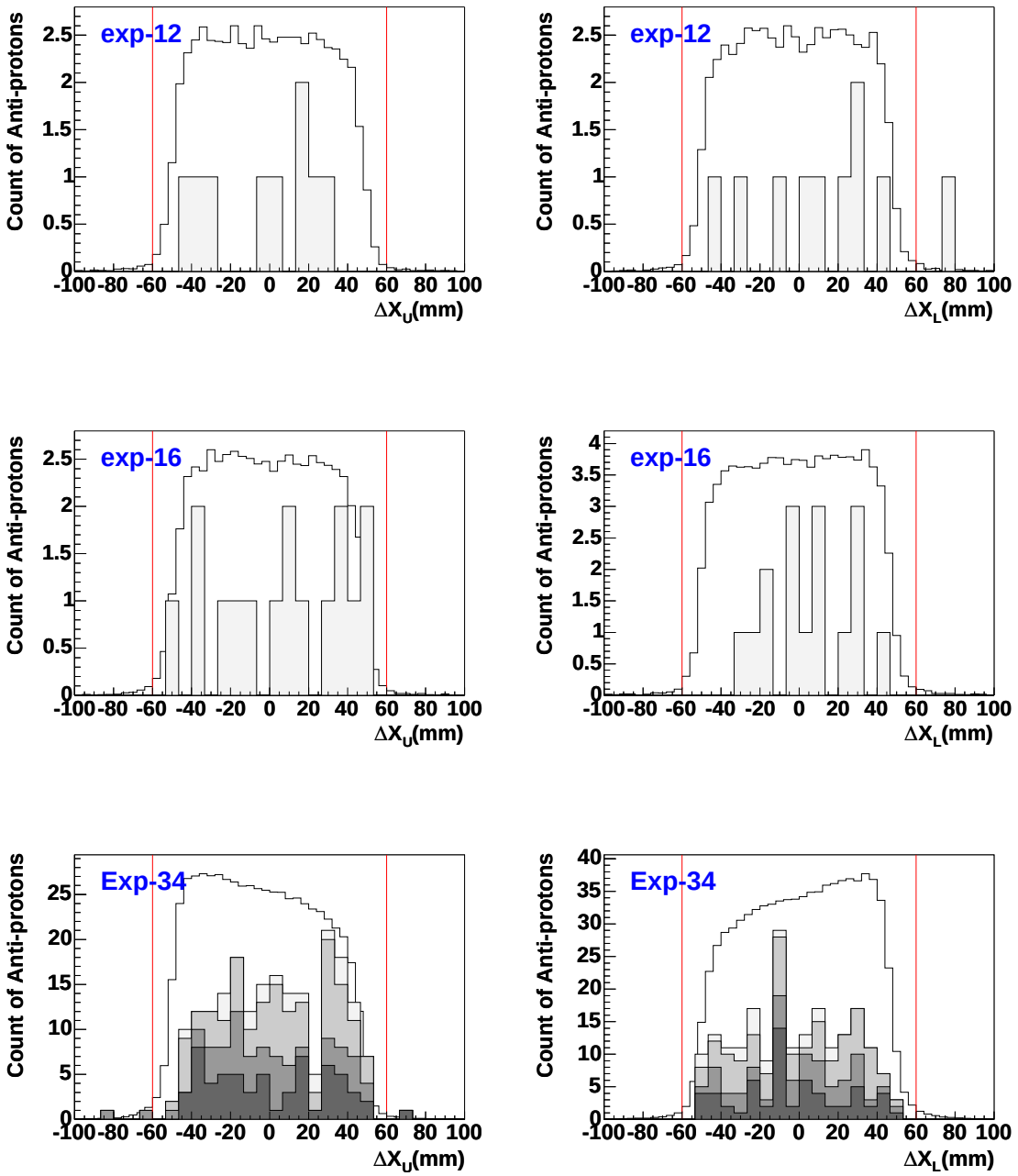

Figure 4.65: Distributions of ΔX parameters for $\overline{p}$ (filled) and proton (open) candidates.

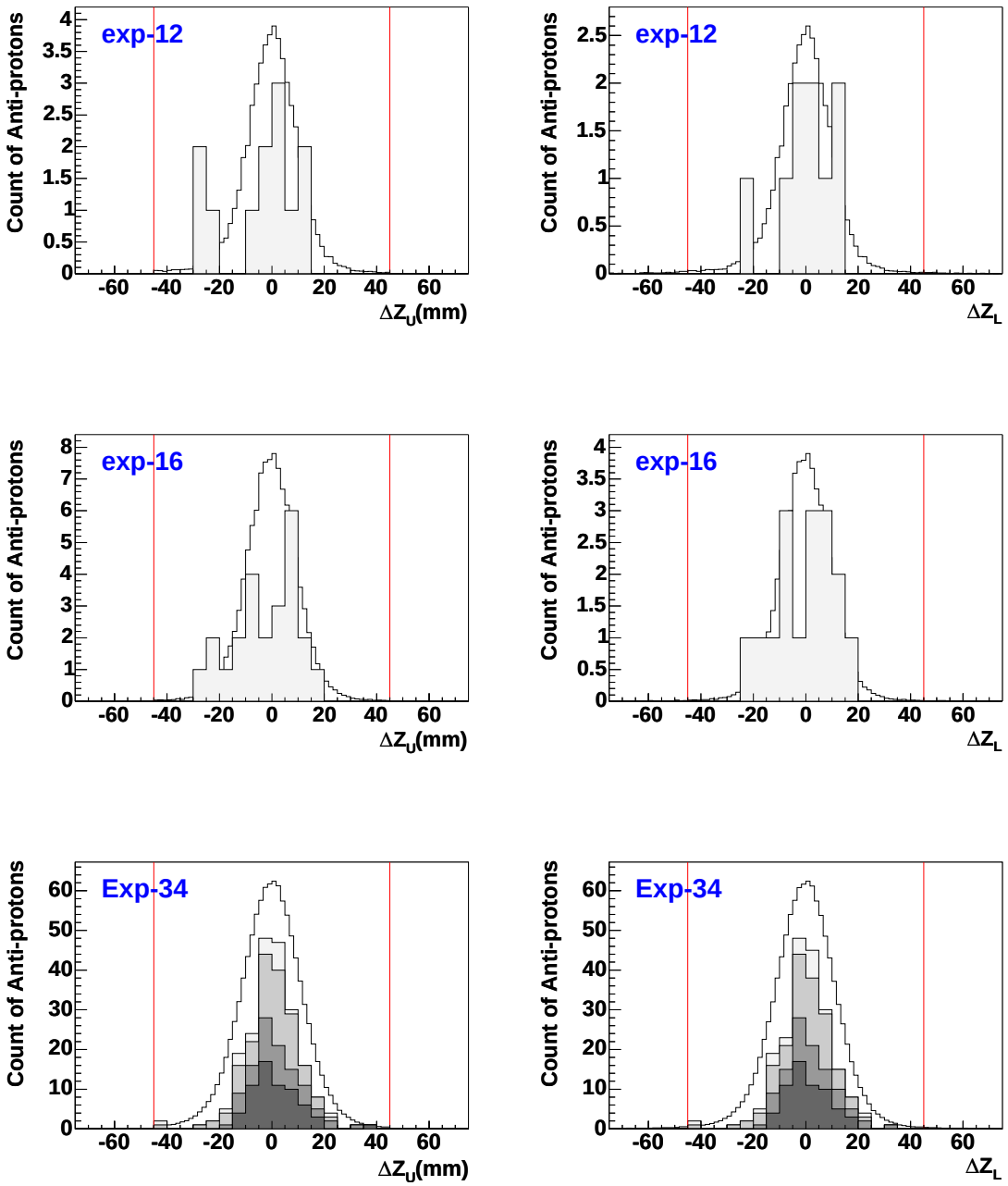

Figure 4.66: Distributions of ΔZ parameters for $\overline{p}$ (filled) and proton (open) candidates.

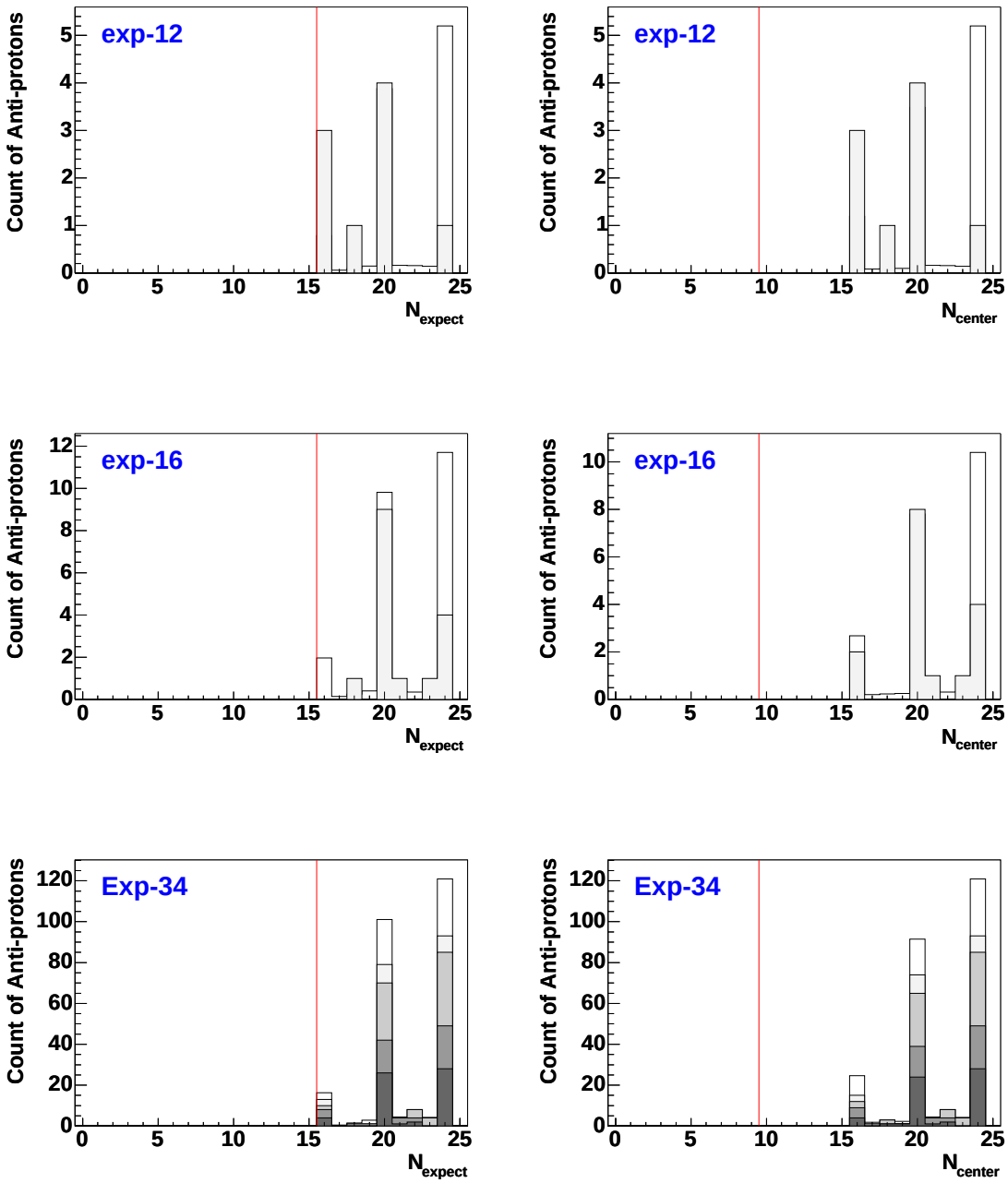

Figure 4.67: Distributions of N_{expect} and N_{center} parameters for $\overline{p}$ (filled) and proton (open) candidates.

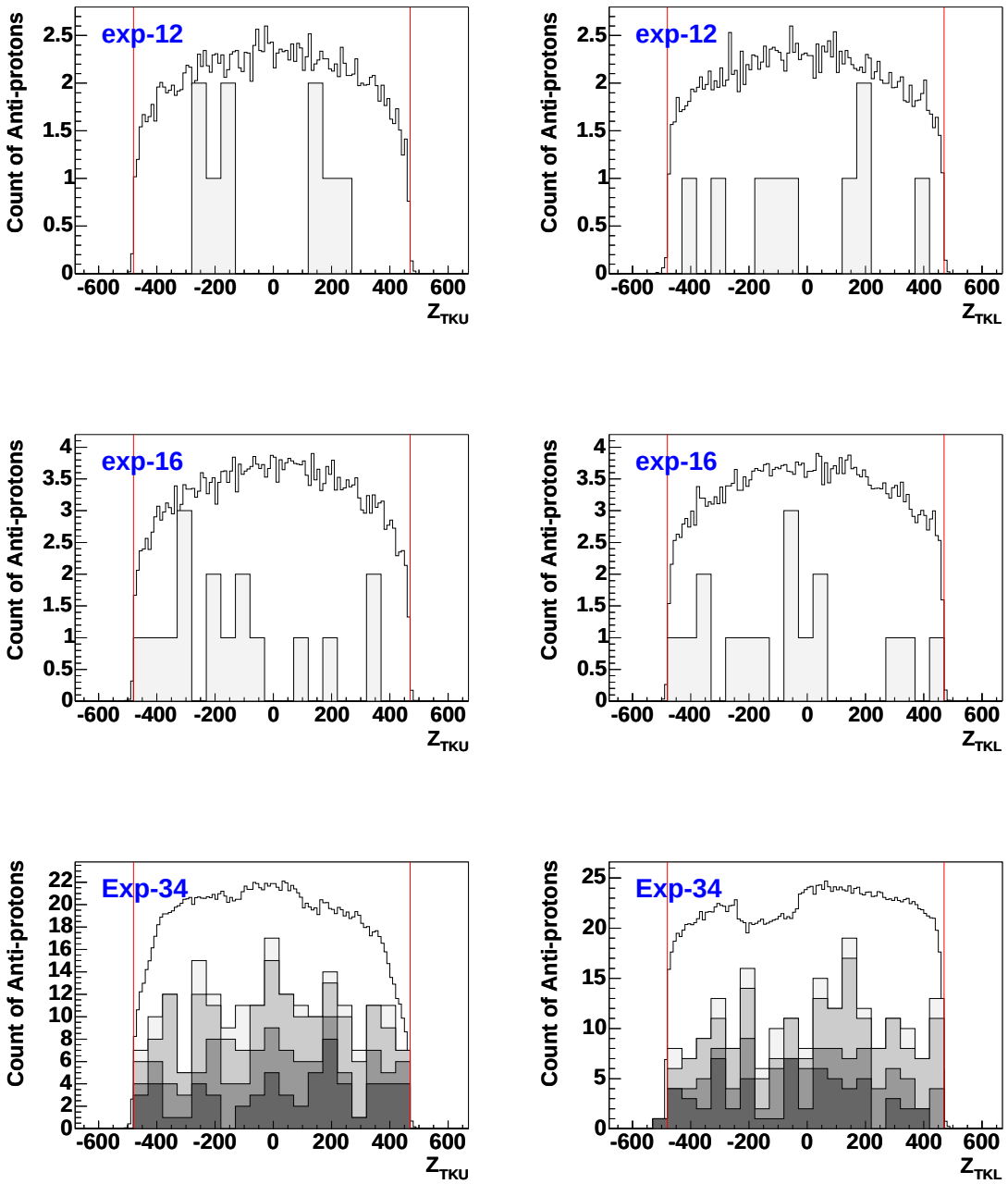

Figure 4.68: Distributions of Z_{TK} at TOF parameters for $\overline{p}$ (filled) and proton (open) candidates.

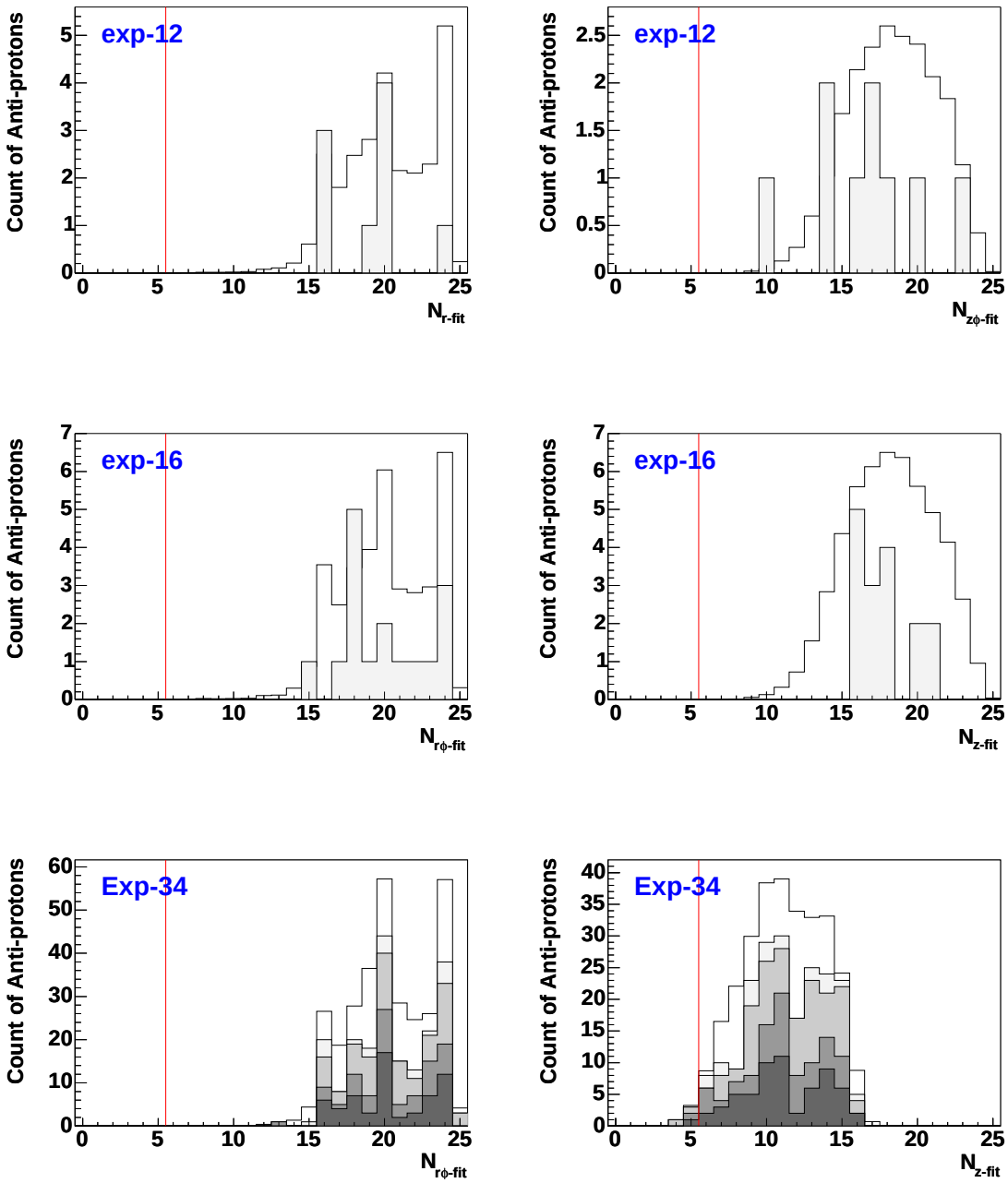

Figure 4.69: Distributions of N_{fit} parameters for $\overline{p}$ (filled) and proton (open) candidates.

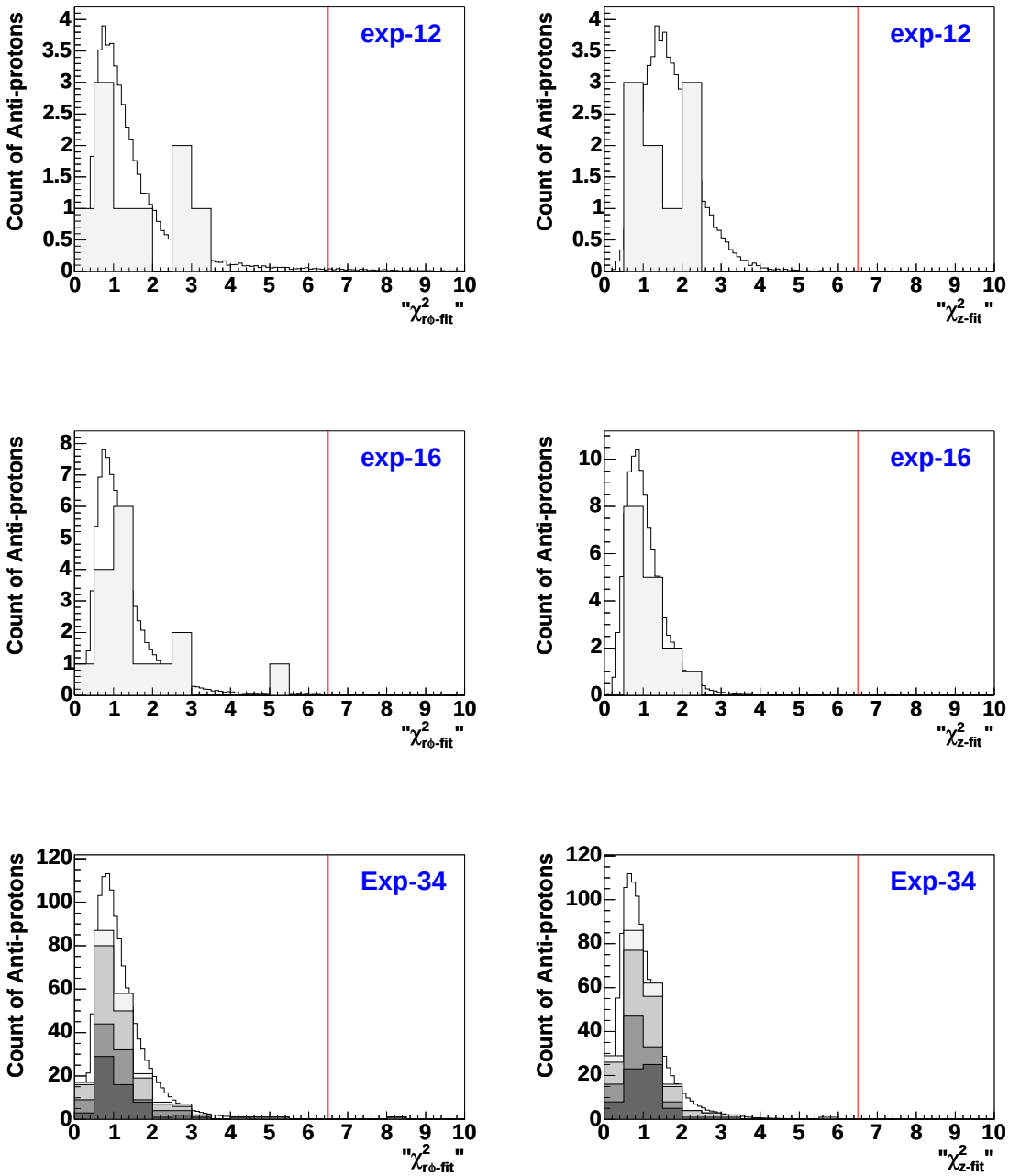

Figure 4.70: Distributions of χ^2 parameters for $\overline{p}$ (filled) and proton (open) candidates.

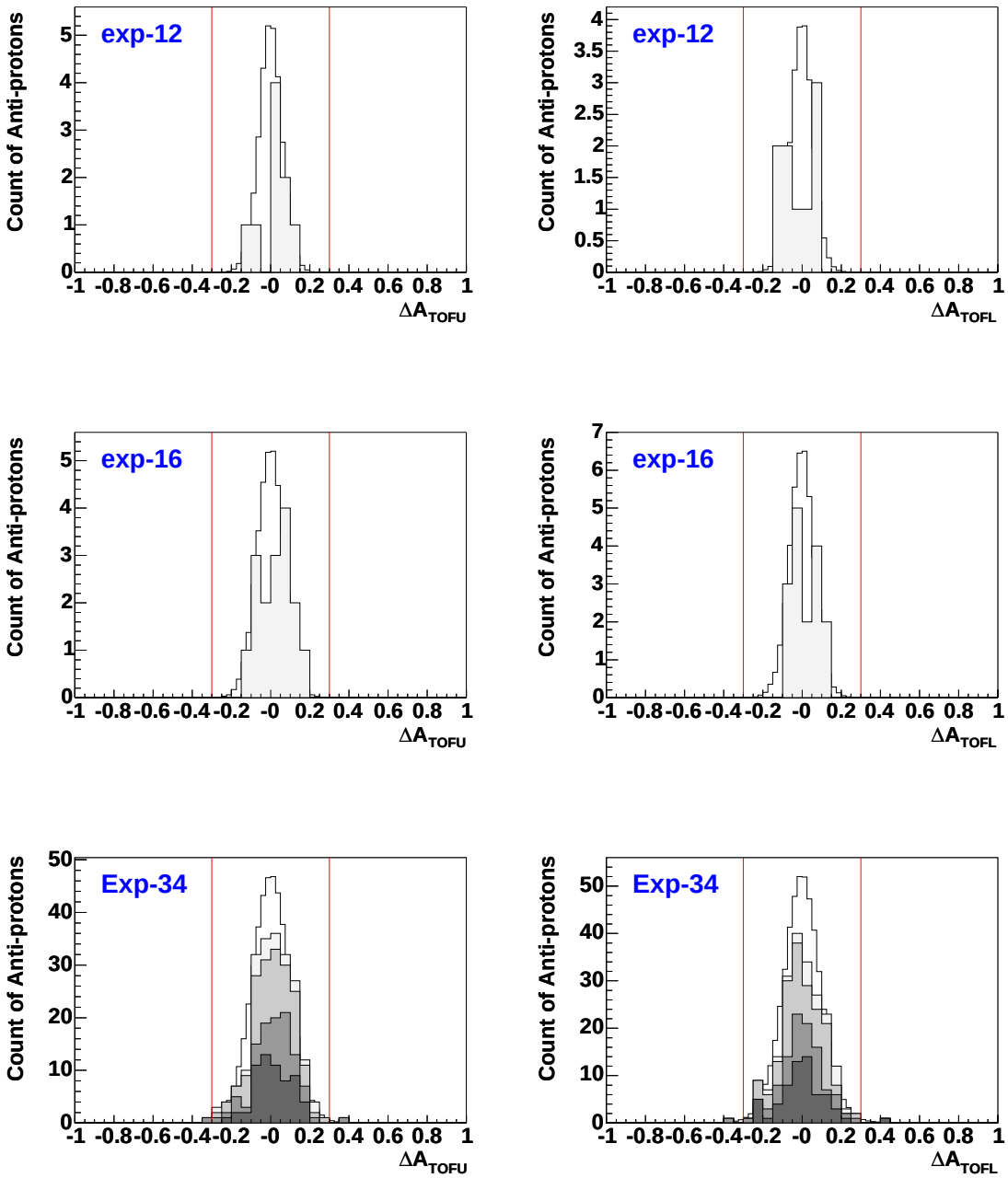

Figure 4.71: Distributions of ΔA_{tof} parameters for $\overline{p}$ (filled) and proton (open) candidates.

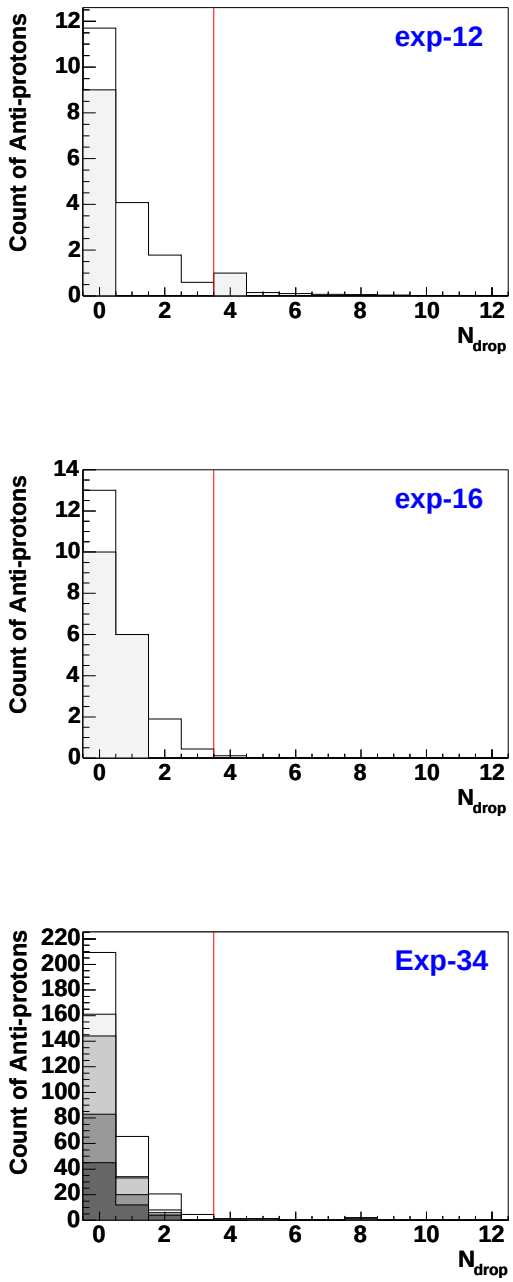

Figure 4.72: Distributions of N_{drop} parameters for $\overline{p}$ (filled) and proton (open) candidates.

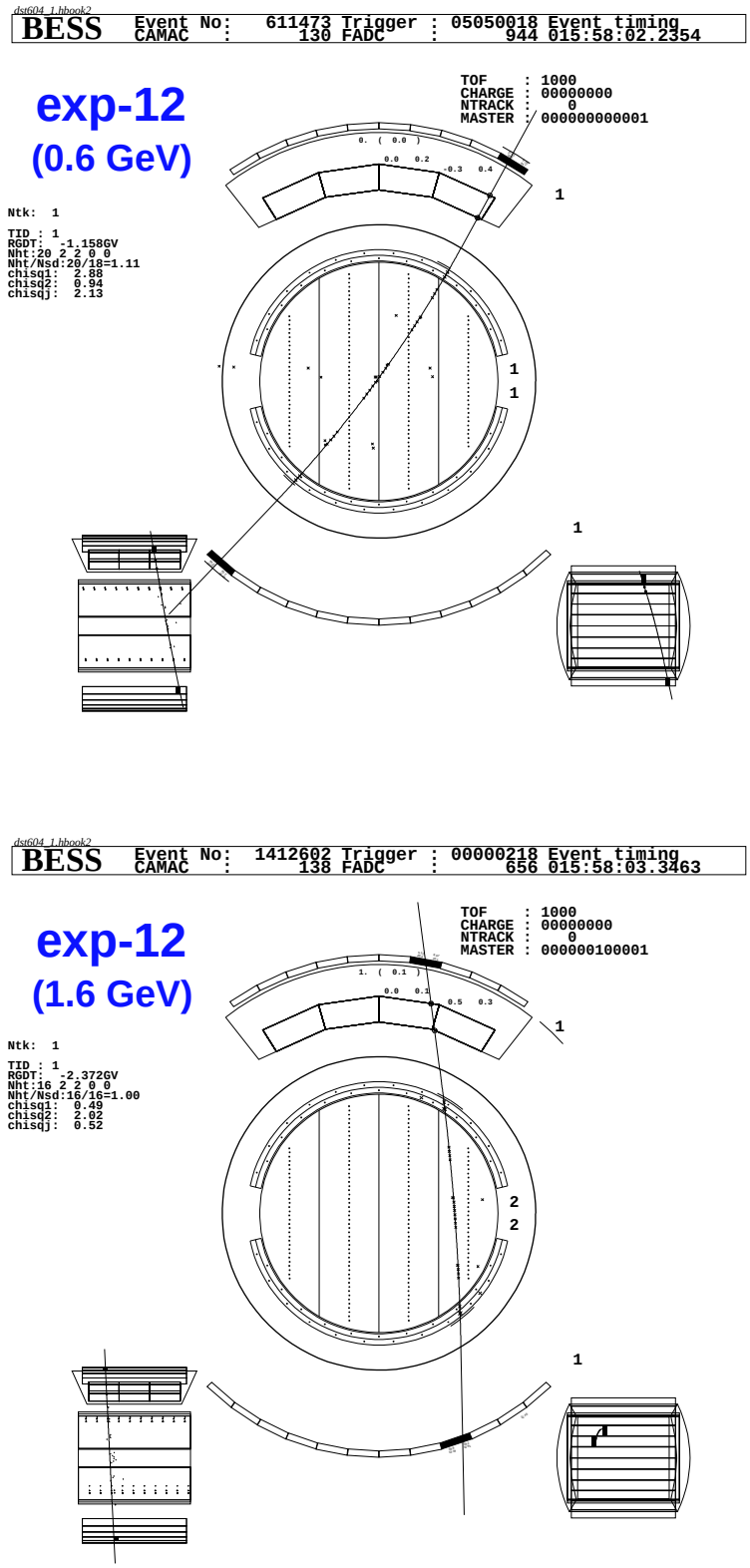

Figure 4.73: Event display of $\overline{p}$ candidates in Exp-12. Top figure is the lowest energy event in this experiment.

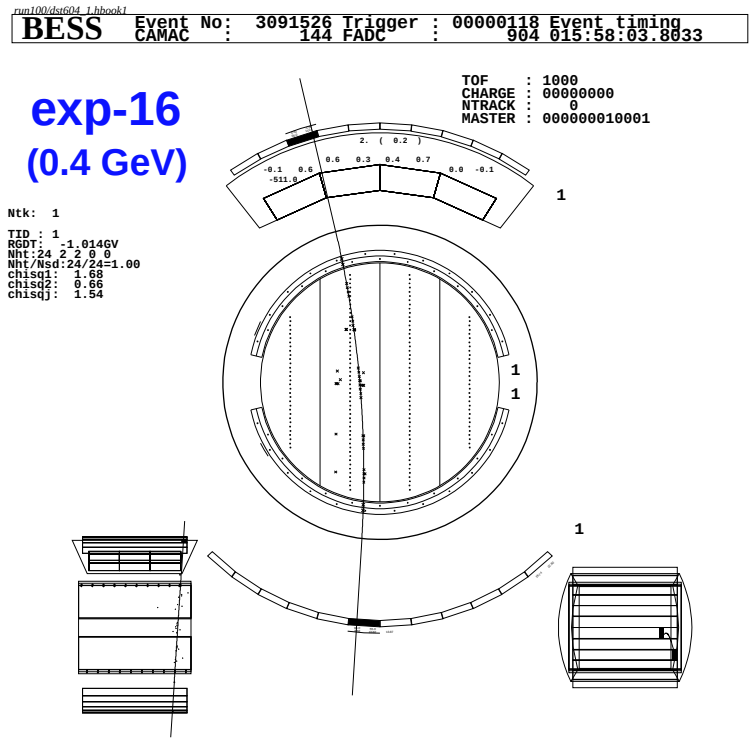

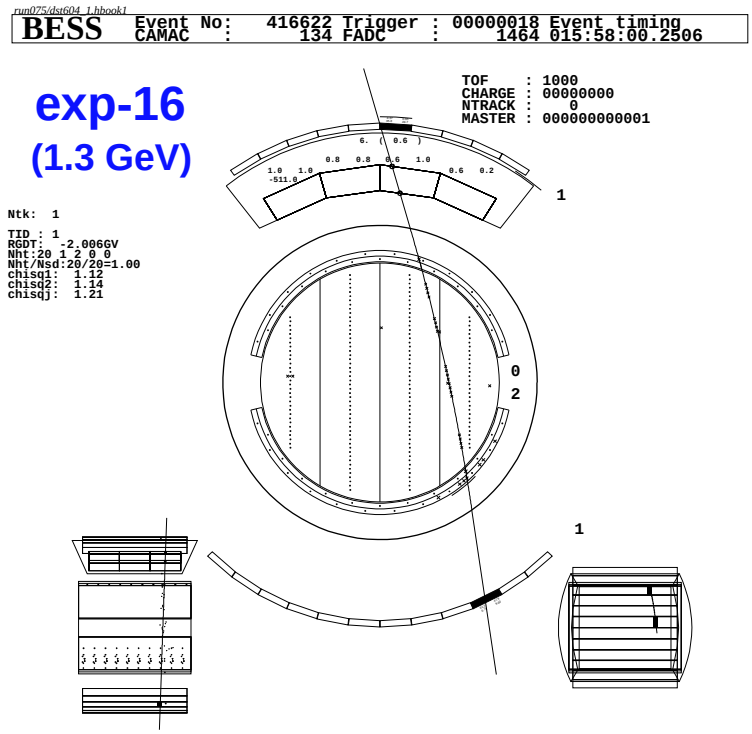

Figure 4.74: Event display of $\overline{p}$ candidates in Exp-16. Top figure is the lowest energy event in this experiment.

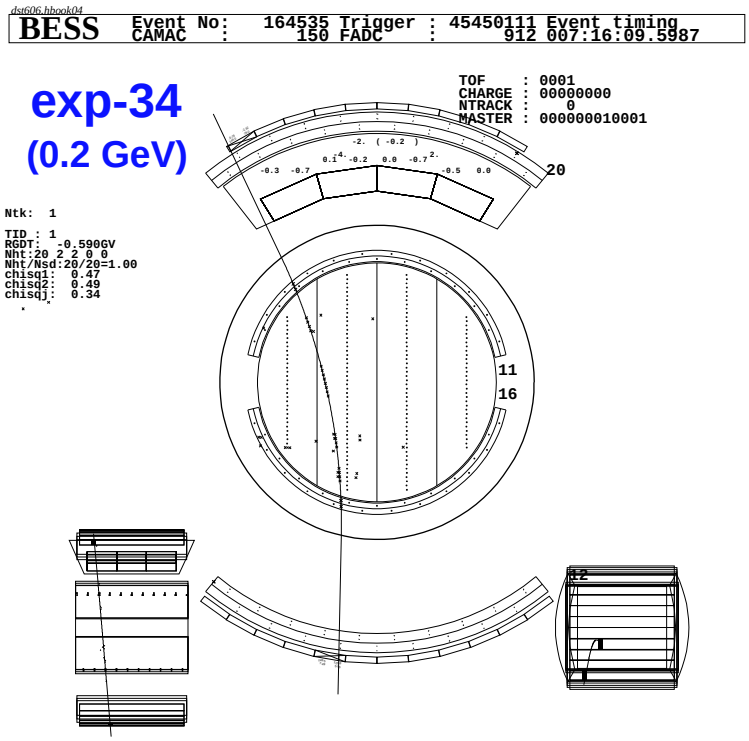

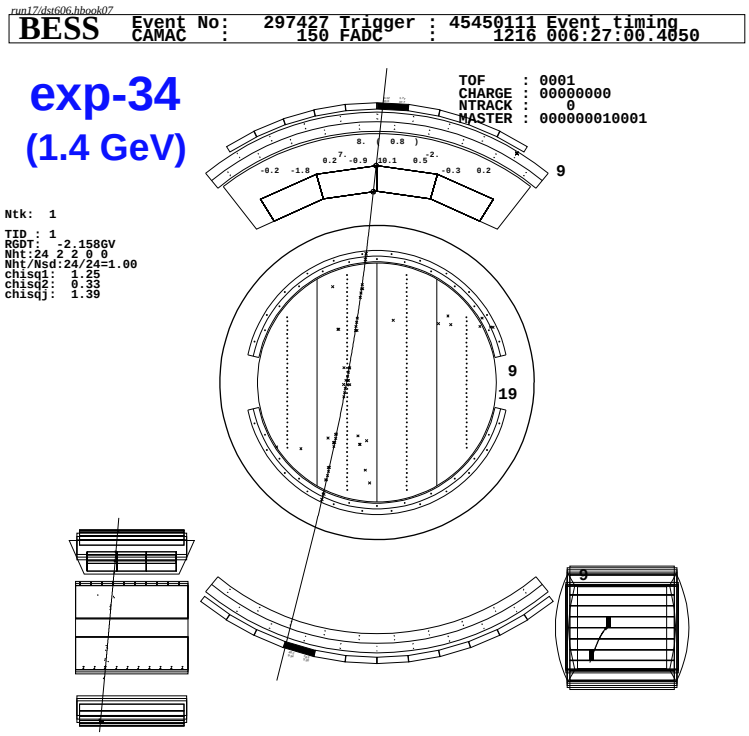

Figure 4.75: Event display of $\overline{p}$ candidates in Exp-34. Top figure is the lowest energy event in this experiment.

Chapter 5

Flux Determination

This chapter describes flux determination processes based on the observed candidates of antiprotons.

5.1 Derivation of Flux Calculation

The differential flux of $\overline{p}$'s at the top of instrument (J_{TOI}) integrated in an energy bin dE can be expressed as follows:

$$J_{TOI} = \frac{N_{TOI}}{S\Omega \cdot T_{live} \cdot dE} \tag{5.1}$$

$$N_{TOI} = (N_{obs} - N_{BG})/\varepsilon \tag{5.2}$$

where

N_{TOI}	: number of $\overline{p}$'s at the top of the instrument
$S\Omega$	: geometrical acceptance
T_{live}	: the live time period
N_{obs}	: number of observed $\overline{p}$ candidates
N_{BG}	: number of expected background contaminated in the candidates
ε	: detection efficiency of $\overline{p}$'s

5.2 Corrections

5.2.1 Ionization Energy Losses

The observed $\overline{p}'s$ lose their energies while they traverse the material in the upper half of the instrument before they are detected at the JET chamber. The energy of a particle after traversing the thickness of the material of a depth x g/cm^2 ($E(x)$) is given by:

$$E(x) = E(0) - \int_0^x \frac{dE}{dx}(E, x)\, dx$$

where $E(0)$ is to the particle energy at the top of instrument. The actual thickness of the material for a particle to traverse depends on the particle trajectory. The energy loss was calculated for each track by summing up the energy losses at every steps in the detector components.

5.2.2 Exposure Factor

Exposure factor consists of geometrical acceptance (SΩ) and live time (T_{live}).

$$\text{Exposure Factor} = S\Omega \cdot T_{live}$$

(1) Geometrical Acceptance ($S\Omega$)

The geometrical acceptance is determined by the geometry of the BESS. Since trajectory of a particle has a curvature in the magnetic field depending on the particle energy, a geometrical acceptance also depend on the energy. It can be calculated reliably by a Monte Carlo simulation in the following way:

(1) Define a sphere (A) of radius R_A which include the whole instrument.

(2) The geometrical acceptance of A for isotropic down-going flux can be easily calculated as:

$$S\Omega_A = \frac{1}{2} \cdot 4\pi \cdot \pi R_A^2$$

because the sphere with a radius of R_A is recognized as area of πR_A^2 from any angle of observation. Note that the factor of 1/2 multiplied to 4π corresponds to down-going incidence of measured flux.

(3) Using the isotropically injected particles from A, we trace the particles through the instrument with GEANT with a solenoidal magnetic field of 1 Tesla by ignore the interaction and energy losses in the detector.

(4) We applied a fiducial volume cut to the MC events, where the fiducial volume cut is defined as pre-selection.

(5) The efficiency of the fiducial volume cut is obtained as the ratio ($r_{fiducial}$).

$$r_{fiducial} = \frac{\text{number of events passing Step (4)}}{\text{total number of events generated in Step (3)}}$$

The geometrical acceptance ($S\Omega$) of the detector is calculated from $S\Omega_A$ and $r_{fiducial}$ as:

$$S\Omega = S\Omega_A \cdot r_{fiducial}$$

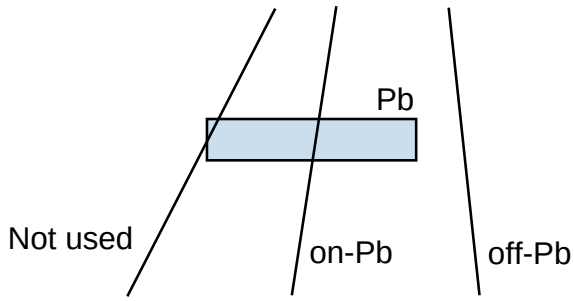

Figure 5.1: The definition of a track passing through the lead region or or not.

Figures 5.2 show the calculated geometrical acceptance for each experiment. The legends in the figures have statistical error bar. The statistical error is very small because M.C. can generate enough number of events. For Exp-34, we calculated the acceptance for Lead region (on-Pb) and Not Lead region (off-Pb) respectively. A red line represents $S\Omega$ not passing the Pb region. A blue line represents $S\Omega$ passing through the Pb region. We take the definition of 'on-Pb' and 'off-Pb' in Figure 5.1. In the Figure 5.2, 'Whole acceptance' does not agree with the value of the summation of 'on-Pb' and 'off-Pb', because we have 'Not used' region shown in Figure 5.1.

Note that we use isotropic flux to calculate the acceptance, in spite of intensity of the atmospheric antiproton depend on the zenith angle. We present only the measured flux at top of the BESS detector in this chapter. The discussion including the effect of the zenith angle dependency is presented in the chapter 6.

(2) Live Time (T_{live})

The live time of observation was directly measured by 1 MHz-clock pulse generator and scalers. The Live times are 59.4, 112.0, 11.86 hours (Exp-12, Exp-16, Exp-34 respectively). For Exp-34, the analysis was performed in 4 regions of air depth. While for Exp-12 and 16, the analysis was performed in one region. The live time vs residual air depth is shown in Figure. 5.3

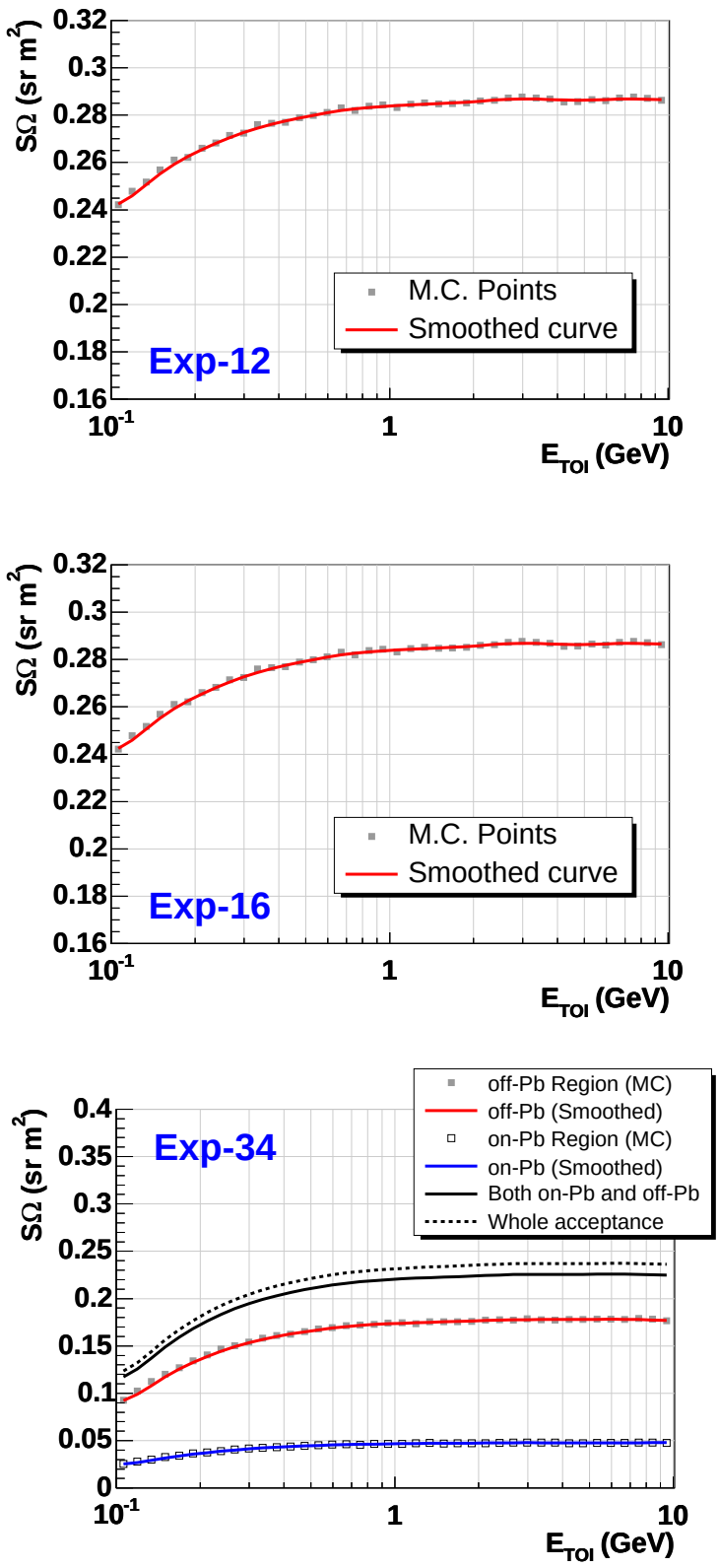

Figure 5.2: The geometrical acceptance ($S\Omega$) as function of the energy for each experiment.

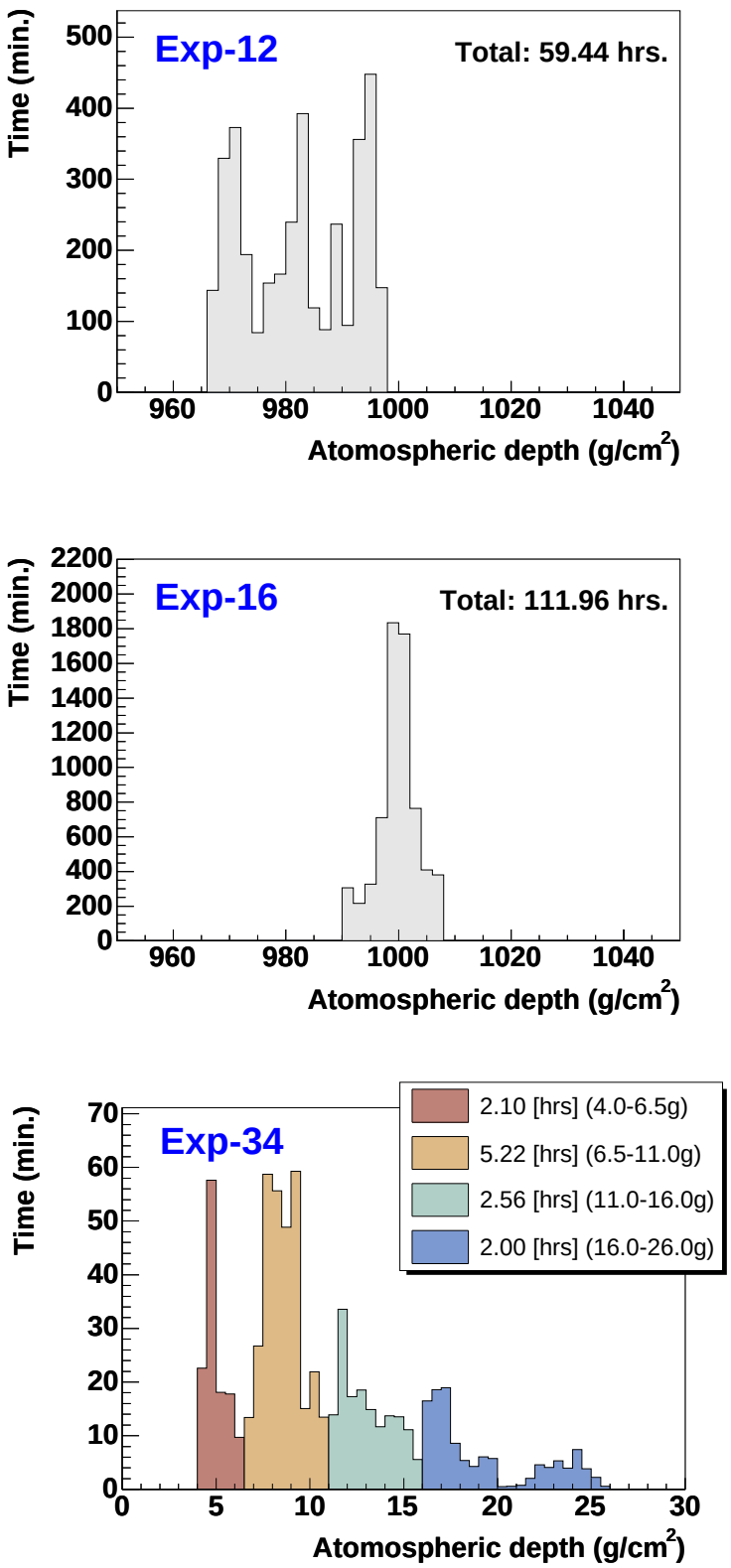

Figure 5.3: The live-time vs air depth

5.2.3 Detection Efficiency (ε)

The detection efficiency ε is defined as

$$\varepsilon = \frac{N_{obs}}{N_{inc}}$$

where N_{inc} is the number of particles within acceptance of the detector, and N_{obs} is the number of observed particles. The detection efficiency is decomposed into five factors:

$$\varepsilon = \varepsilon_{trig} \cdot \varepsilon_{rec} \cdot \varepsilon_{acc} \cdot \varepsilon_{non-int} \cdot \varepsilon_{Q-ID}$$

ε_{trig}	: the trigger efficiency
ε_{rec}	: the track-reconstruction efficiency
ε_{acc}	: the probability of events without accidental hits
$\varepsilon_{non-int}$	: the efficiency of pre-selection
ε_{Q-ID}	: the efficiency of quality cut and particle identification

Note that the efficiencies ε_{Q-ID}, ε_{rec}, ε_{acc} for antiprotons are identical to protons. While $\varepsilon_{non-int}$ and ε_{trig} are different for $\overline{p}$'s and protons. Since above efficiencies are not related to the interactions, these efficiencies can be obtained using the proton samples in the experiment.

(1) Triggering efficiencies (ε_{Trig})

The triggering efficiency for $\overline{p}$'s can be decomposed into three factors:

$$\varepsilon_{Trig} = \varepsilon_{TT(PAT)} \cdot \varepsilon_{TT(RGT)} \cdot \varepsilon_{TRP}$$

, where $\varepsilon_{TT(PAT)}$, $\varepsilon_{TT(RGT)}$, and ε_{TRP} represent the efficiency of pattern selection of Track Trigger (TT), rigidity selection of TT, and online filtering by Transputer bank (TRP) respectively. These efficiencies were also estimated by using unbiased samples. Unbiased samples are recorded at every few events which is unrelated to judgements of the trigger system. Figure 5.19 shows these efficiencies in E_{TOI} and rigidity.

This efficiency is related with Exp-34 only. In the measurements on the ground, BESS detector can take all cosmic-ray events except for dead-time period because T0 trigger rate is about 30Hz.

(2) Track reconstruction efficiencies (ε_{rec})

Since JET chamber and IDC's have insensitive region very close to sense wires due to the dead time of FADC, failures to reconstruct the trajectory could happen. In these events no trajectory is found (i.e. $N_{longTk} = 0$), while enough hits are left in JET chamber and IDC's. In order to estimate the track reconstruction efficiency (ε_{rec}), we scan 1000 unbiased events with appropriate TOF hits and enough JET hits, among which only2 events are failed to be reconstructed. As a result, we estimate

$$\varepsilon_{rec} = 99.8 \pm 0.1\%$$

(3) Accidental hits (ε_{acc})

When an accidental particle passed through the TOF and left "accidental hits", the pre-selection would eliminate the events. The inefficiency from accidental hits can be estimated by utilizing the random trigger samples, not by the BESS MC which does not simulate such accidental hits. Random triggers were made at every 0.8 second during the flight independent of T0 trigger. Therefore, the number of hits in the random trigger samples corresponds to the number of accidental hits. Figure 5.20 shows the number of hits in the upper and the lower TOF for all random trigger samples in Exp-34. As shown in this figure, there would exist one or more "accidental hits". Since pre-selection allows one (two) in the upper (lower) counter, following events are eliminated due to the "accidental hits".

For ground experiment (Exp-12, 16), this efficiency is very small because T0 trigger rate is about 1/70 compared with balloon borne situation. Therefore we ignore this efficiency for Exp-12 and 16.

$$
\begin{array}{lcrl}
1-\varepsilon_{acc} = 0.11 \pm 0.03\ \% & (& 4.0 \text{ - } 7.5 & \text{g/cm}^2\ ) \\
1-\varepsilon_{acc} = 0.11 \pm 0.02\ \% & (& 7.5 \text{ - } 14.0 & \text{g/cm}^2\ ) \\
1-\varepsilon_{acc} = 0.10 \pm 0.03\ \% & (& 14.0 \text{ - } 26.0 & \text{g/cm}^2\ ) \\
1-\varepsilon_{acc} = 0.11 \pm 0.01\ \% & (& 4.0 \text{ - } 26.0 & \text{g/cm}^2\ )
\end{array}
$$

(4) Interaction losses ($\varepsilon_{non-int}$)

Top two of the figure 5.4 shows the non-interaction efficiencies for $\overline{p}$'s in the ground experiment in which we do not include Pb region. In the figures, the gray markers represent data points generated by MC with enough statistics. The red lines are smoothed curve of the MC points. The bottom of figure 5.4 shows the non-interaction efficiency in Exp-34. In the figure, the lower blue line shows the efficiency when incident particles passes through Pb region, and upper red curve shows the efficiency when incident particles does not pass through Pb region. Since the efficiency drops significantly below about 0.20 GeV, only the events with E_{TOI} above 0.2 GeV were analyzed.

(5) Antiproton Selection Efficiency (ε_{Q-ID})

The efficiency of Quality and Identification cuts can be decomposed into four factors:

$$\varepsilon_{Q-ID} = \varepsilon_Q \cdot \varepsilon_{dE/dx} \cdot \varepsilon_{agl} \cdot \varepsilon_{mass}\ ,$$

where $\varepsilon_Q, \varepsilon_{dE/dx}, \varepsilon_{agl}$, and ε_{mass} are the efficiency of Quality cut, dE/dx-band aerogel Čerenkov veto, and $1/\beta$-band cut respectively.

- Quality cut efficiency ε_Q ($ref.$ Figure 4.15-4.18, 4.68-4.71)

  Figures 5.5 show the efficiencies of Quality cut. These are obtained by using the observed proton samples. For Exp-34, we show 'on-Pb' region and 'off-Pb' region respectively. A difference of the quality cut in each region is not caused by existence of Lead, but the geometrical difference of the existence of lead plate. A lead plate is

placed in almost center in z-axis. There are many small χ^2 events in central region rather than end of chamber region. This was confirmed by choosing events at mirror position in z-axis where there is no lead plate.

- $\mathrm{d}E/\mathrm{d}x$ cut efficiency $\varepsilon_{dE/dx}$ (*see*. Figure 4.6-4.8, 4.49-4.51)

  Figure 5.7-5.12 shows $\mathrm{d}E/\mathrm{d}x$ cut efficiency. A cut efficiency of $\mathrm{d}E/\mathrm{d}x$ in TOF was obtained by using MC simulation data. While, a cut efficiency of $\mathrm{d}E/\mathrm{d}x$ in JET chamber was estimated by real proton samples. All efficiencies tend to lower values as increasing kinetic energy. This is due to the increase of the tail of energy deposit of Landau distribution. In lower TOF, the efficiency is notably high at low energy due to shape of their cut boundary.

  For Exp-34 we also show the efficiency in on-Pb and off-Pb region respectively in Figures 5.10 and 5.11. These efficiencies are agree well with expectation in upper TOF. However, in lower TOF, they are different with each other clearly. The reason of this are that at low energy side, an energy deposit distribution is narrowed. While, at higher energy, an energy side deposit distribution became broad due to production of electromagnetic shower.

- Aerogel Čerenkov cut efficiency ε_{agl}

  To know the energy dependency of ε_{agl}, we need pure proton samples. In the flight experiment at low cutoff rigidity area (ordinary BESS flight in Lynnlake), unbiased samples can be used as proton samples because almost cosmic-rays are protons. However at ground (Exp-12, 16) altitude, unbiased samples are almost muons. While at high cutoff rigidity area (i.e. Ft.Sumner flight: Exp-34), unbiased samples are many secondary protons with some muons below the cutoff rigidity. Then, we used different way to obtain the ε_{agl} for the ground experiment (Exp-12, 16) and flight experiment (Exp-34) respectively.

For ground experiment

ε_{agl} can be decomposed into

$$\varepsilon_{agl} = \varepsilon_{radiator} \times \varepsilon_{fiducial-cut}$$

, where $\varepsilon_{radiator}$ is the efficiency in the case that protons pass through the fiducial volume fully. $\varepsilon_{fiducial-cut}$ is the efficiency of Aerogel fiducial cut including β dependence as defined in chapter 4. Then these efficiencies can be decomposed again into

$$\varepsilon_{radiator} = R_0\,\varepsilon_{thr0} + R_1\,\varepsilon_{thr1}\ ,$$
$$\varepsilon_{fiducial-cut} = R_0\,\varepsilon_{fid0} + R_1\,\varepsilon_{fid1}\ ,$$
$$R_0 = \frac{N_0}{N_0+N_1},\ R_1 = \frac{N_1}{N_0+N_1}\ ,$$

where, ε_{thr0} (ε_{thr1}) is the efficiency in the threshold for $\beta^{-1} \geq 1.1$ ($\beta^{-1} < 1.1$). ε_{fid0} (ε_{fid1}) is the efficiecy of ACC fiducial cut for $\beta^{-1} \geq 1.1$ ($\beta^{-1} < 1.1$) described in Section 4.1.3. In fact $\varepsilon_{fid0} = 1$, because we do not apply the fiducial cut for $\beta^{-1} \geq 1.1$.

N_0 and N_1 is a number of proton events with $\beta^{-1} \geq 1.1$ and $\beta^{-1} < 1.1$ respectively in each corespoing energy bin.

We obtained ε_{thr0} and ε_{thr1} from BESS97 flight called 'Exp-14' which was performed during the period of Exp-12 and Exp-16. These efficiencies are shown in Figure 5.13 and 5.15. ε_{fid1} and N_0, N_1 is not obtained form 'Exp-14', but from the each real data (i.e. Exp-12 or Exp-16). Then total Aerogel efficiencies are shown in Figure 5.14 and 5.16.

For Ft.Sumner flight

As Described in above, unbiased samples contain some muons below cutoff rigidity in Ft.Sumner flight. Therefore we obtained aerogel efficiency by subtracting expected muon contamination from unbiased samples. Red points in figure 5.17 are observed number of μ^- events in antiproton band. Since we applied all cuts for antiprotons including $1/beta$ selection in the figure, Muons are above ~1.5 GeV. Then, blue points (i.e. number of μ^+) were estimated by assuming $\mu^+/\mu^- = 1.3 \pm 0.1$. The final Aerogel efficiency is shown in Figure 5.18. We also show the ε_{agl} applied fiducial cut to all energy (or β) region by purple circles. Below 1 GeV the purple points are confident because we can neglect muon contamination in such energy. The connection between purple points and final ε_{agl} is good. Consequently, our estimation can be trusted.

- $1/\beta$ vs R cut efficiency ε_{mass}
  Particle mass is related to rigidity R, velocity β and charge Z as;

$$M^2 = R^2\, Z^2 (\frac{1}{\beta} - 1)$$

By selecting $|Z| = 1$ particles with $\mathrm{d}E/\mathrm{d}x$ cut and applying ACC cut, we can identify protons by using R and β. The band width of $1/\beta$-band cut was set to $3.89\,\sigma$. Therefore the efficiency ε_{mass} is very close to unity (99.99% in the case of Gaussian distribution).

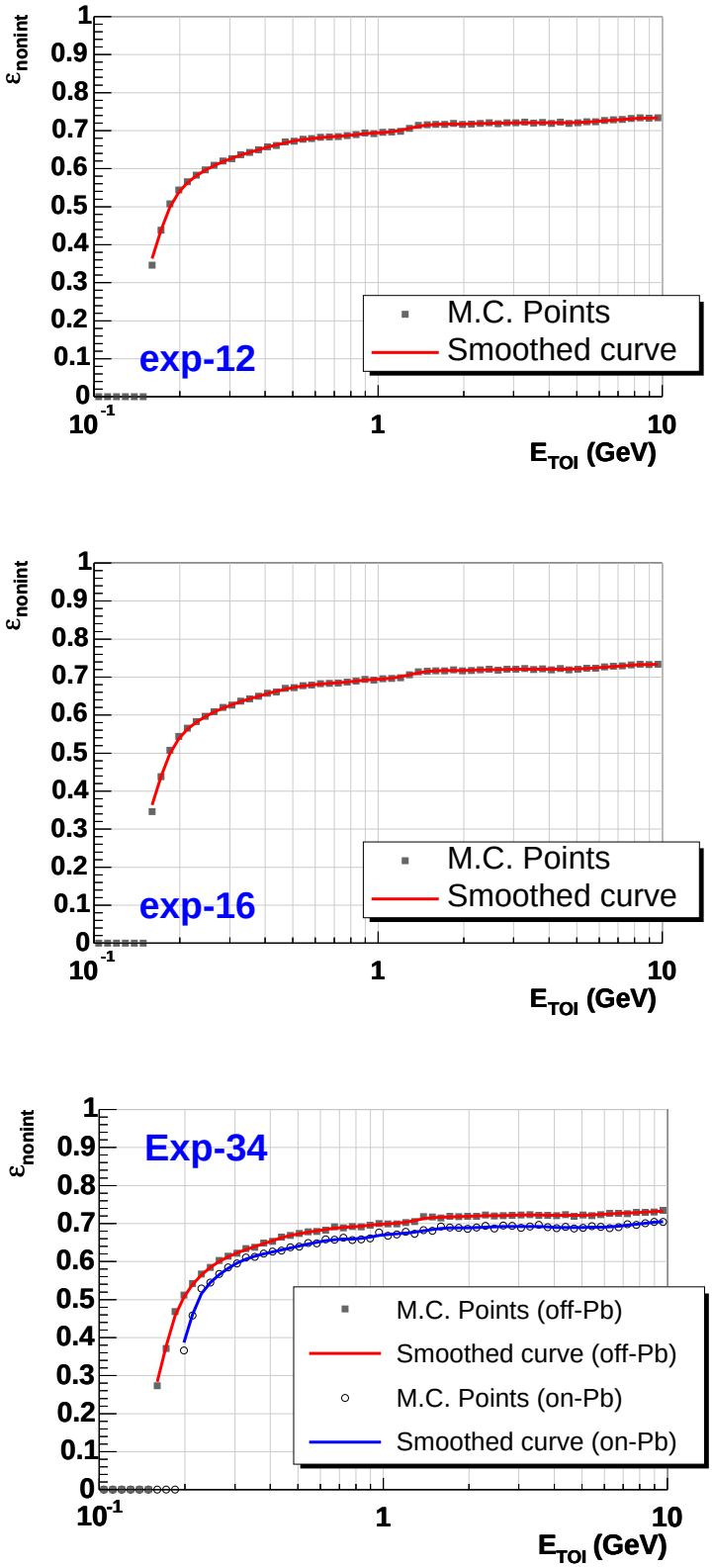

Figure 5.4: Non-interacting efficiency for each experiment.

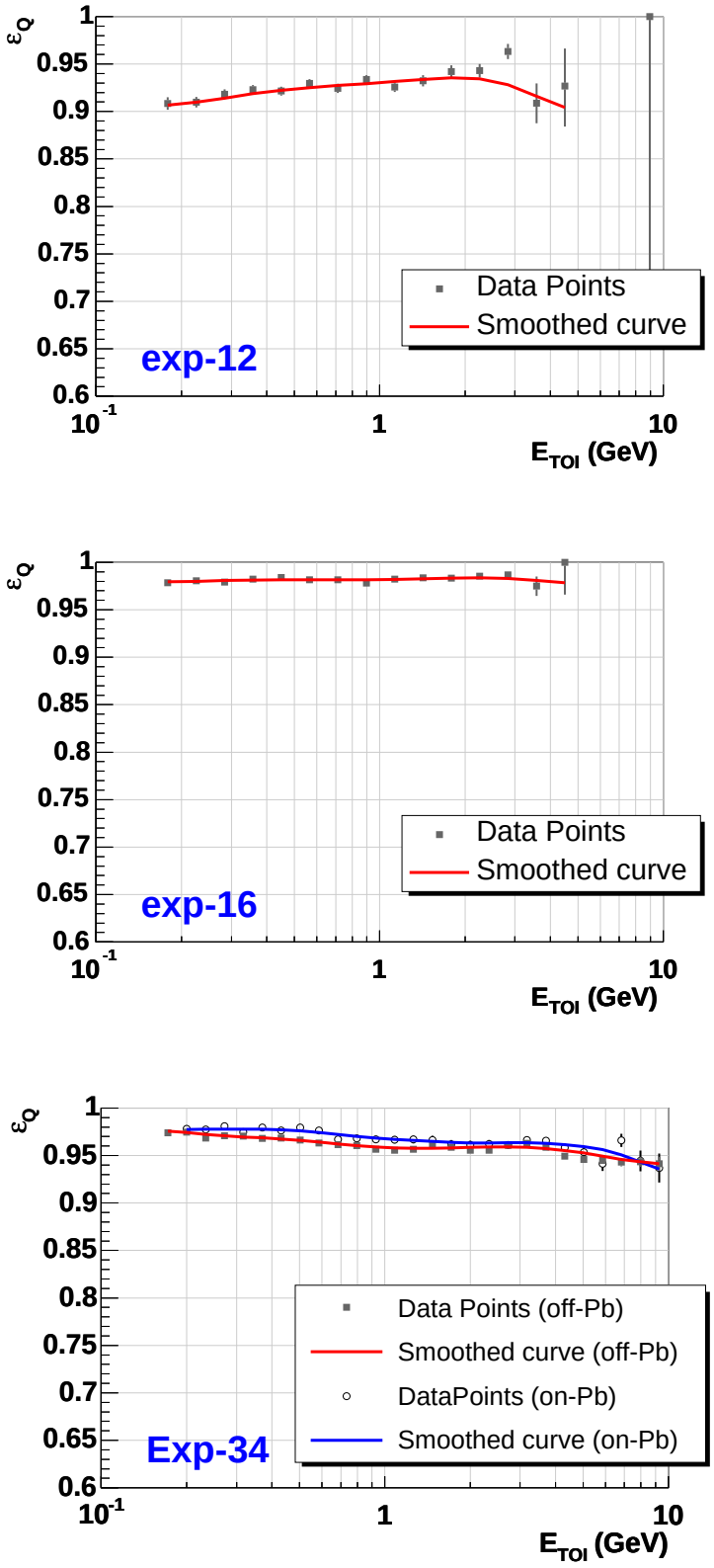

Figure 5.5: Quality Cut efficiency for each experiment.

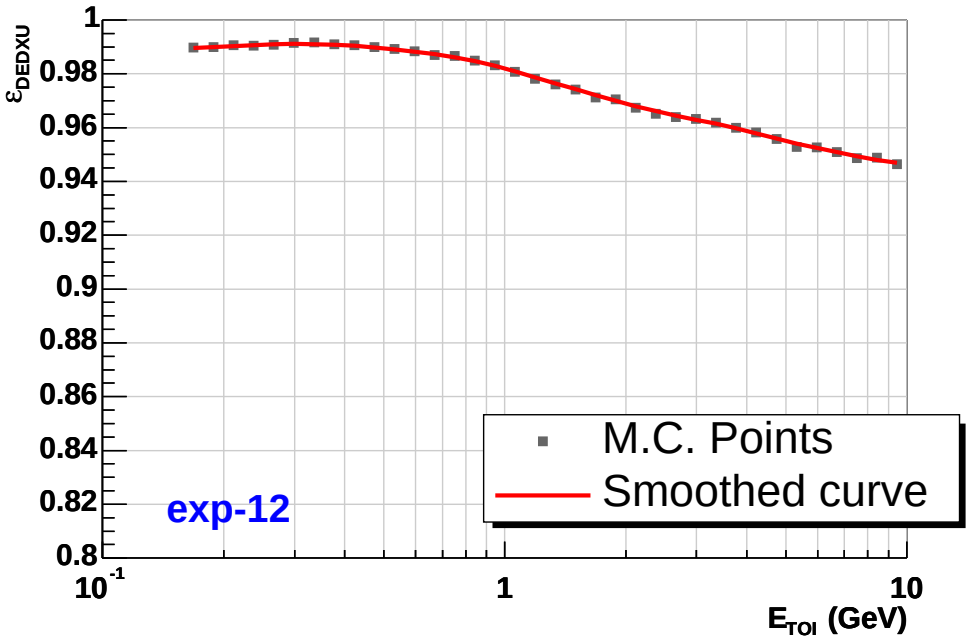

Figure 5.6: Selection efficiency for $\mathrm{d}E/\mathrm{d}x_U$ in Exp-12

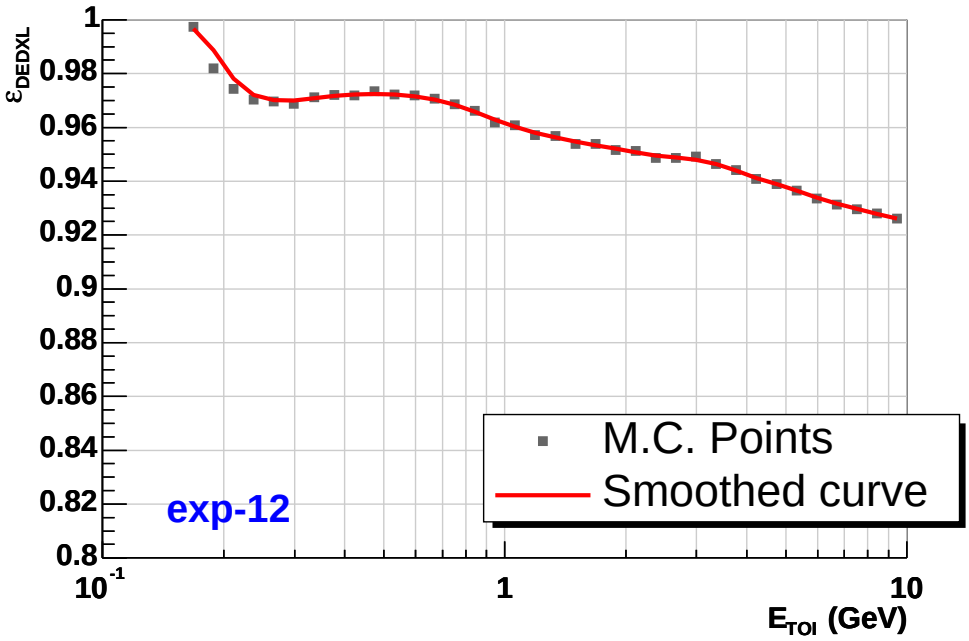

Figure 5.7: Selection efficiency for $\mathrm{d}E/\mathrm{d}x_L$ in Exp-12

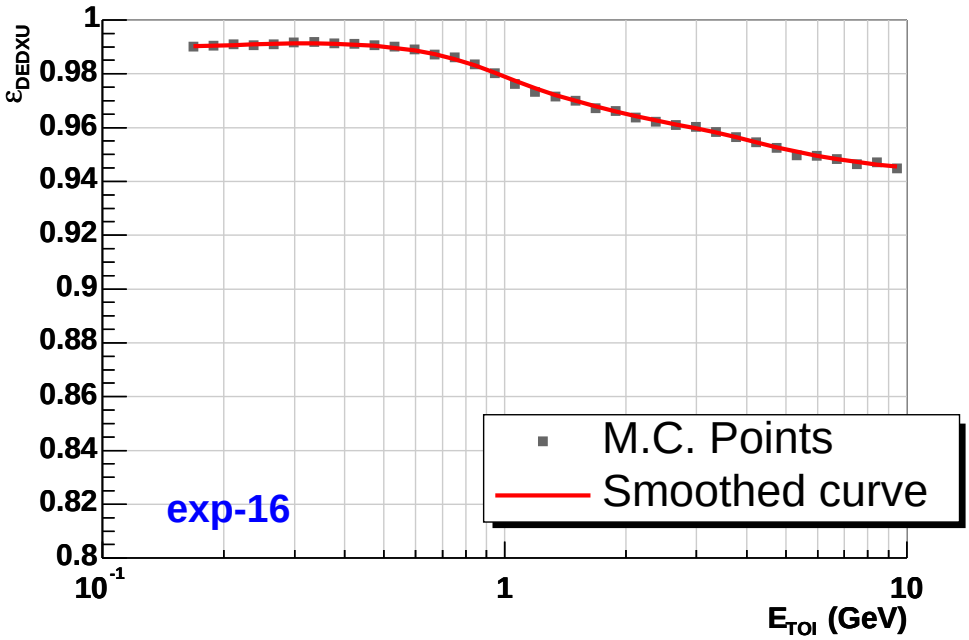

Figure 5.8: Selection efficiency for $\mathrm{d}E/\mathrm{d}x_U$ in Exp-16

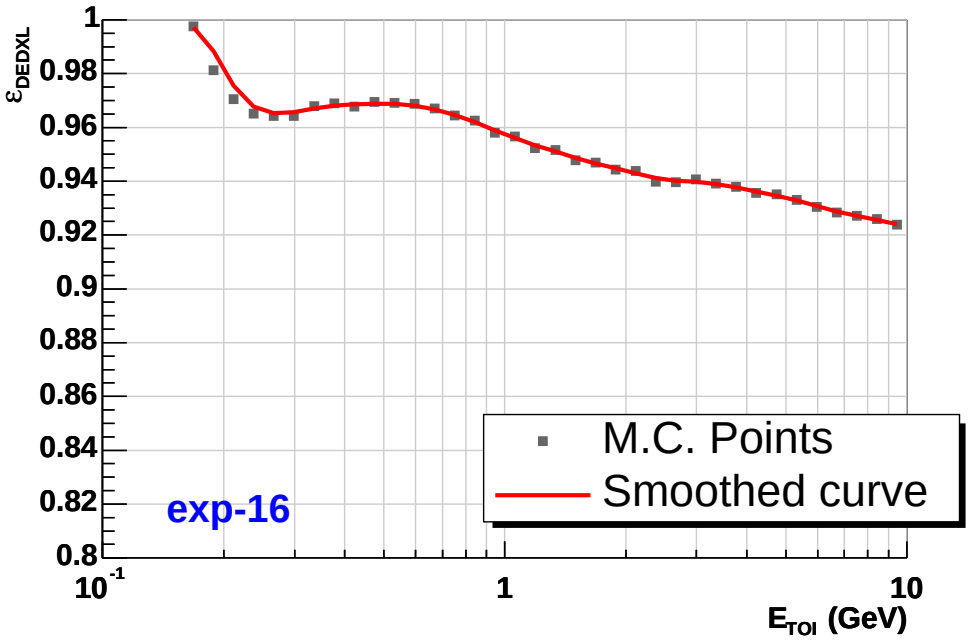

Figure 5.9: Selection efficiency for $\mathrm{d}E/\mathrm{d}x_L$ in Exp-16

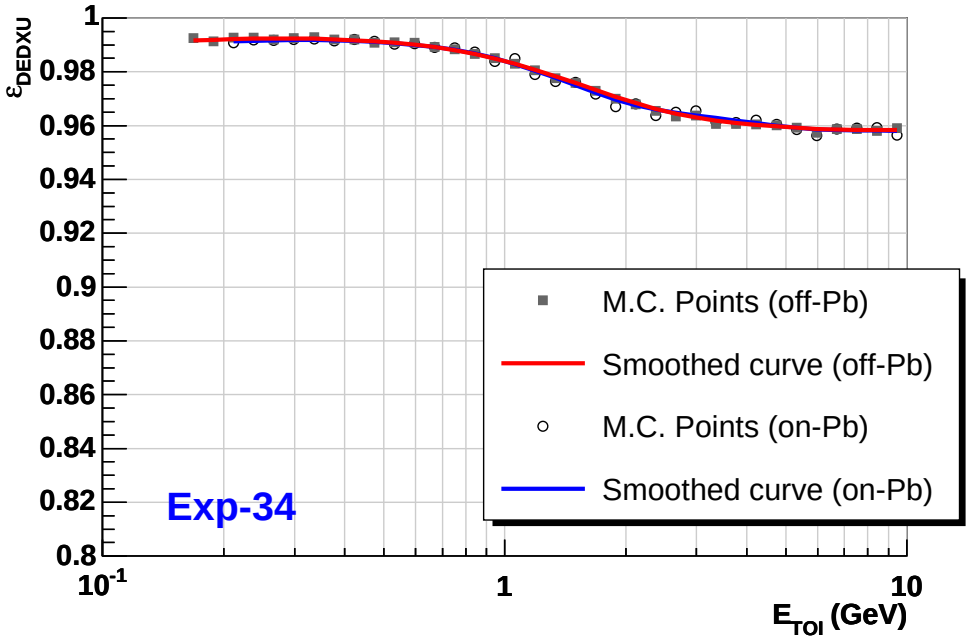

Figure 5.10: Selection efficiency for $\mathrm{d}E/\mathrm{d}x_U$ in Exp-34

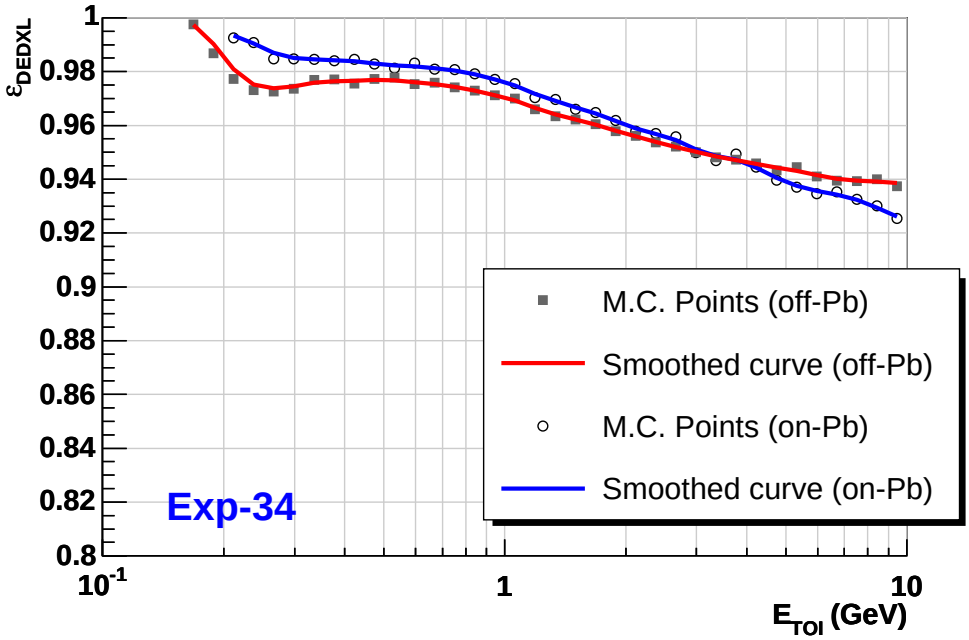

Figure 5.11: Selection efficiency for $\mathrm{d}E/\mathrm{d}x_L$ in Exp-34

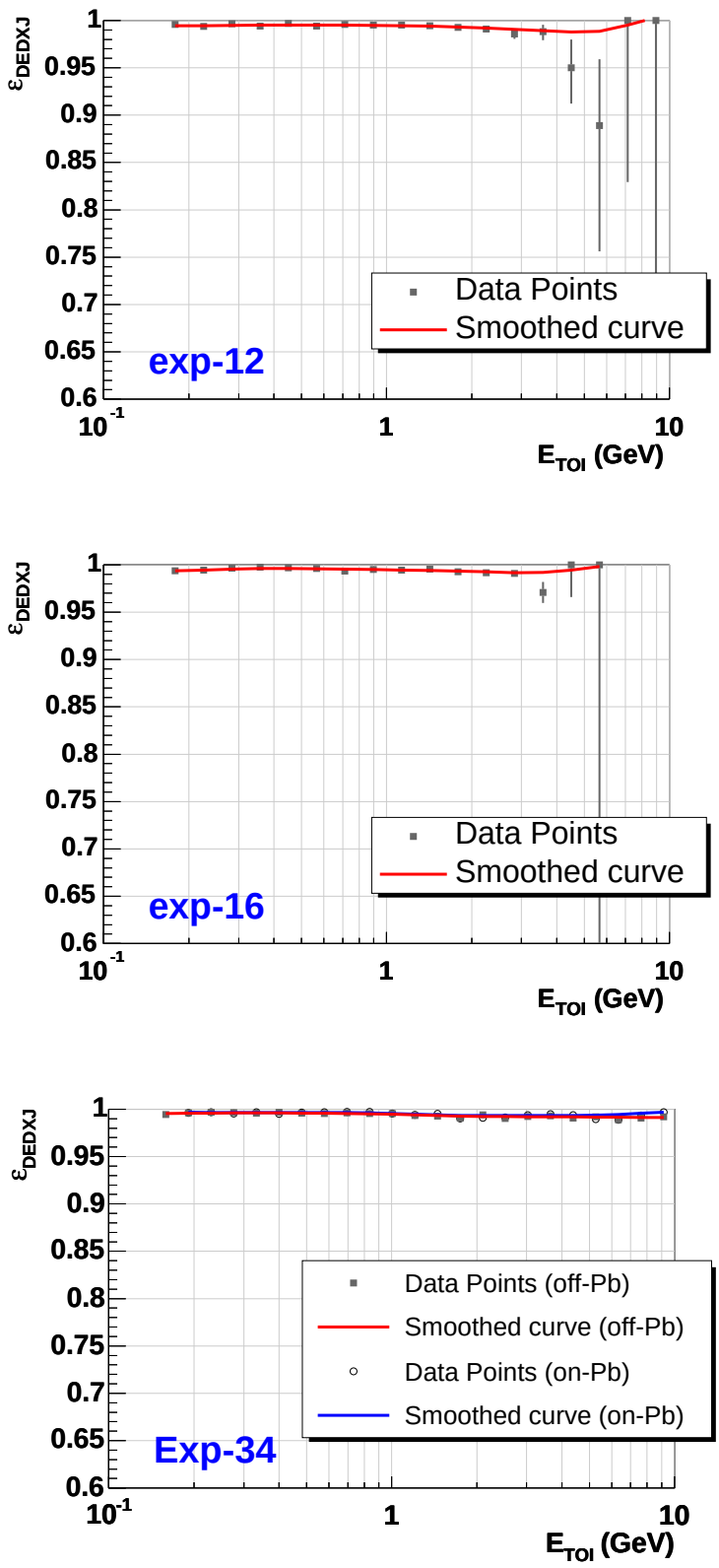

Figure 5.12: Selection efficiency for $\mathrm{d}E/\mathrm{d}x$ in the JET chamber for each experiment.

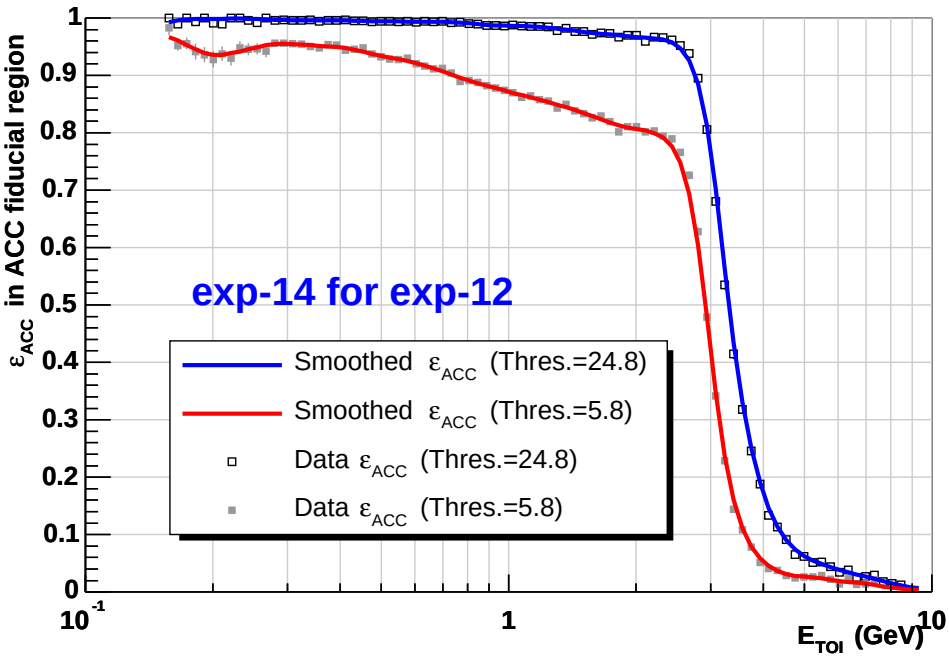

Figure 5.13: Aerogel efficiency in fiducial (effective) region in Exp-14.

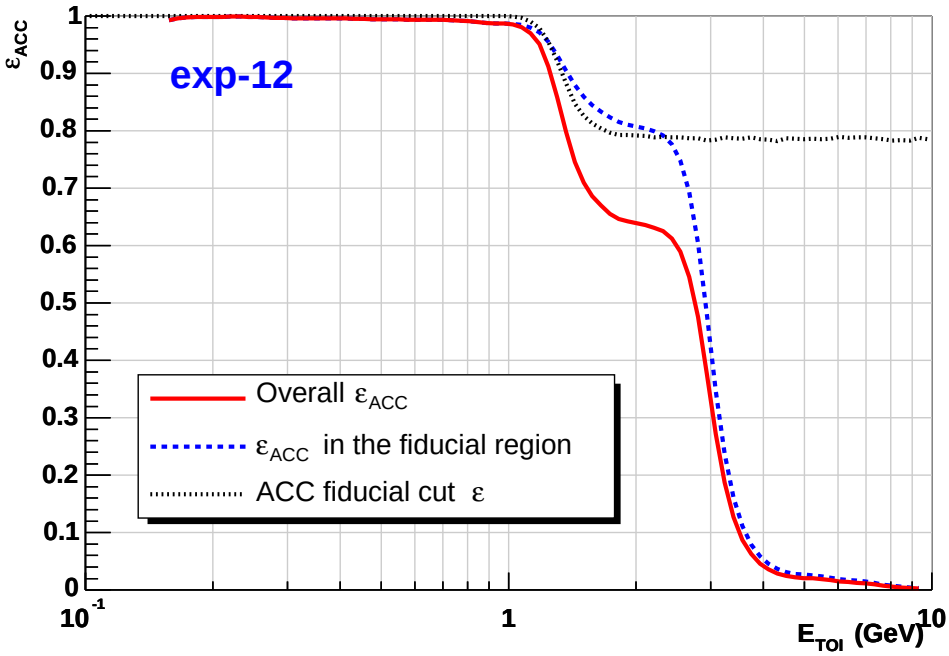

Figure 5.14: Overall Aerogel efficiency in in Exp-12.

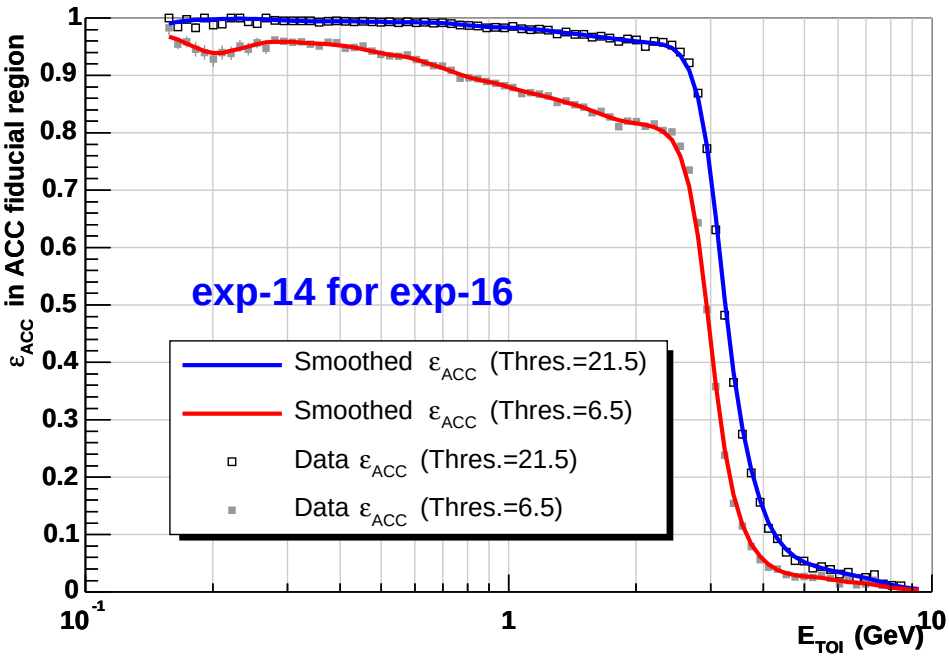

Figure 5.15: Aerogel efficiency in fiducial (effective) region in Exp-14.

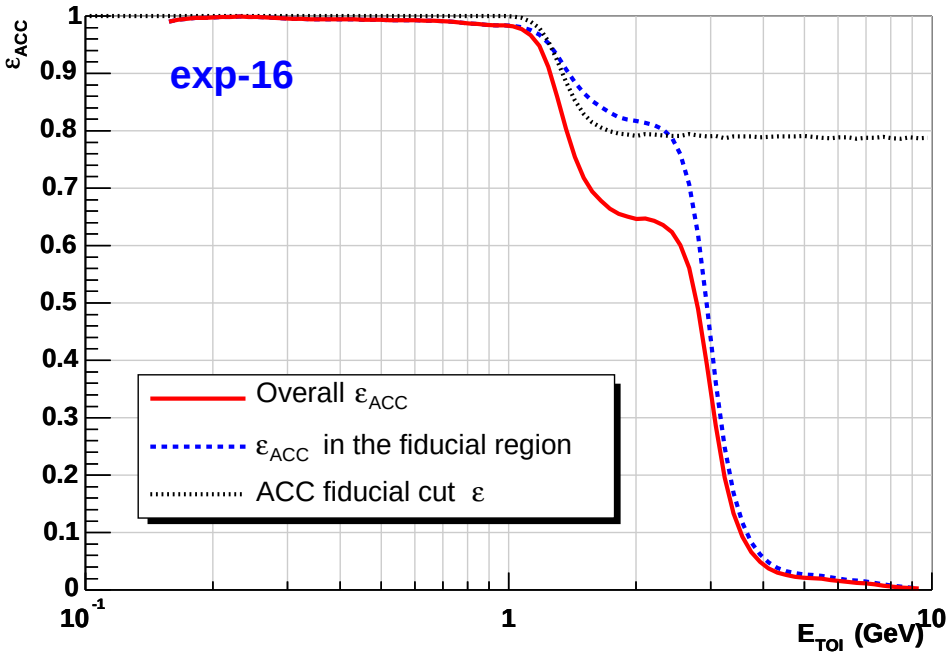

Figure 5.16: Overall Aerogel efficiency in in Exp-16.

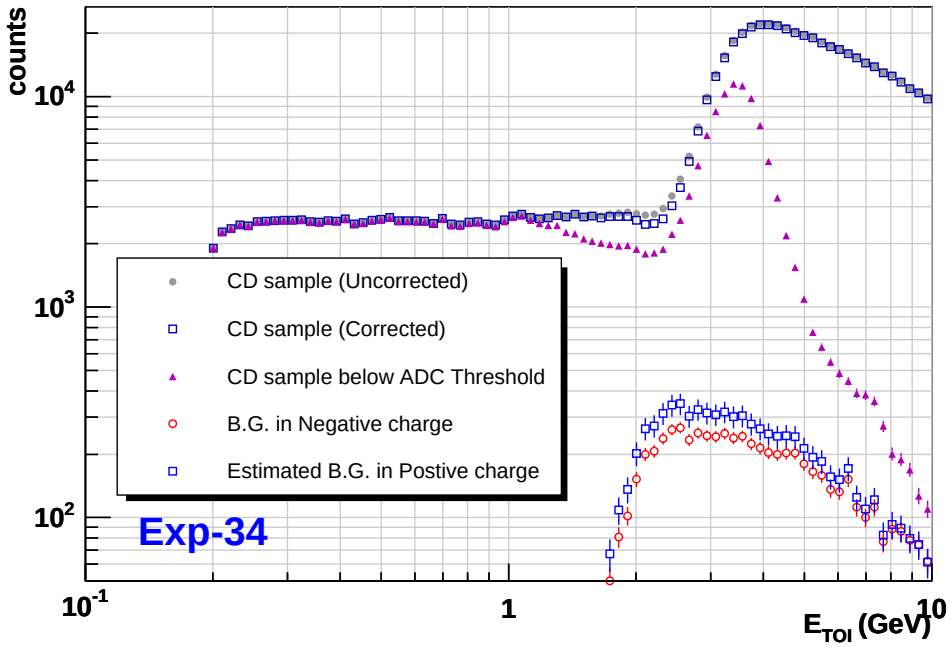

Figure 5.17: Number of unbiased samples and Background. B.G. events are remaining events after applying all cuts for $\overline{p}$'s. Therefore it seems to have a peak.

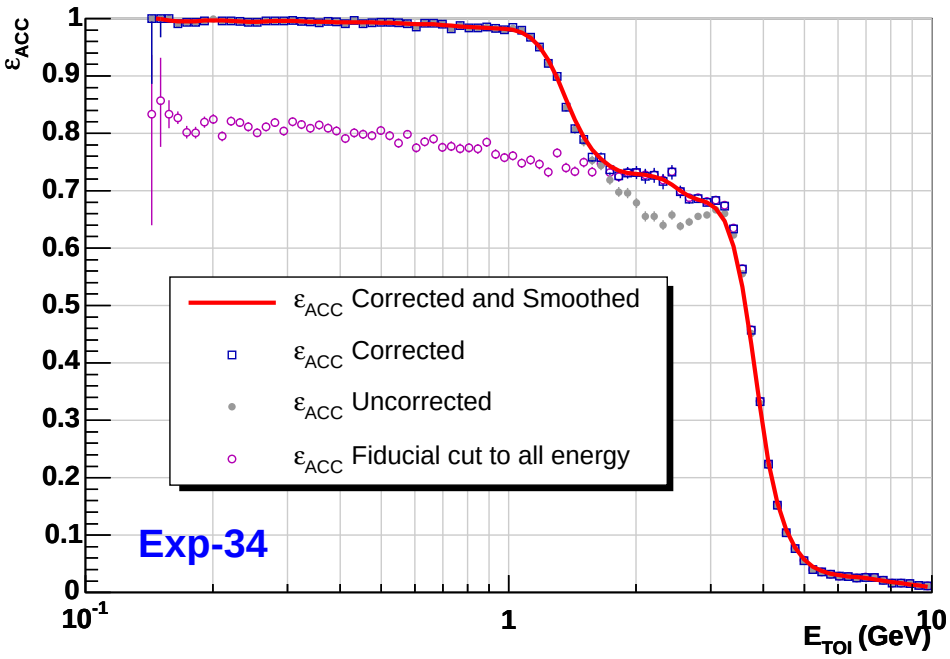

Figure 5.18: Aerogel Cut efficiencies.

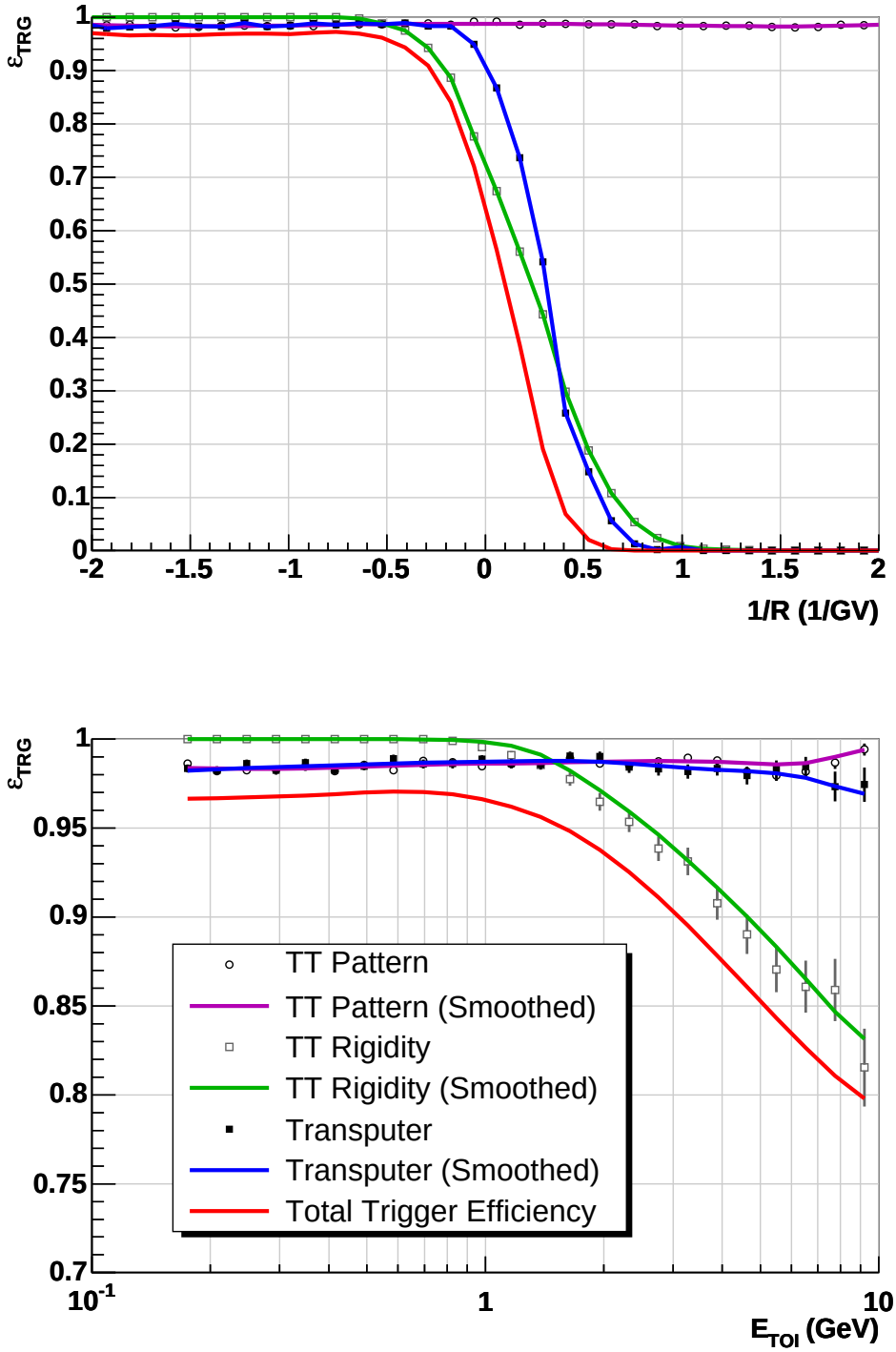

Figure 5.19: Triggering efficiency for $\overline{p}$'s estimated by using unbiased proton samples. Purple, green, blue lines represent efficiencies of Track Trigger pattern selection, of Track Trigger rigidity selection, and of Transputer selection, respectively.

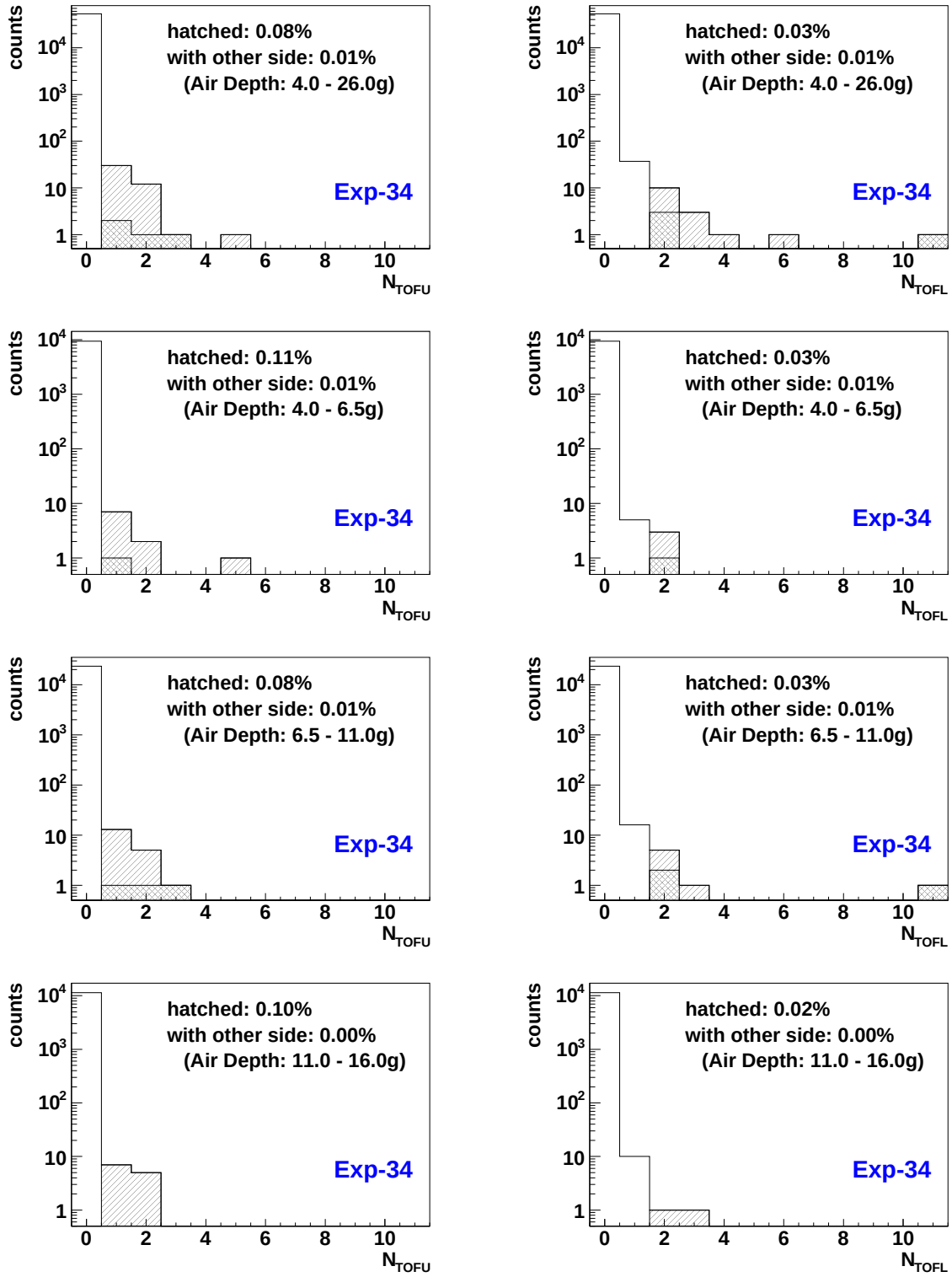

Figure 5.20: Distributions of number of TOF hits in the random trigger samples at various air depth. Distributions in the upper (lower) TOF are shown in the left (right) column.

5.3 Background Estimation

5.3.1 Čerenkov inefficiency ($N_{e/\mu}$)

To estimate e and μ contamination in the $\overline{p}$ candidates, we need to know two quantities, i,e., (i) rejection factor for μ/e contamination and (ii) total number of potential background. From the performance check in Section 4, we already know the rejection factor. The total number of potential background (i.e. number of negative particle in $\overline{p}$ band) can be obtained easily from data.

Figure 5.21-5.26 summarizes the estimation of the contamination electrons and muons in the final $\overline{p}$ candidates. In the figure, Red points indicate the number of the $\overline{p}$ candidates. Open histograms represent the total number of e/μ particles identified by $\mathrm{d}E/\mathrm{d}x$ and $1/\beta$ distributions. Hatched histograms represent the number of e/μ particles in $\overline{p}$ band, estimated by applying all cuts but aerogel Čerenkov veto. Only the e/μ particles drawn by hatched histograms contribute to the contamination for $\overline{p}$ candidates. It is seen no contamination of e/μ particles is expected below 1GeV, Using the rejection factor mentioned above, the contamination of e/μ particles are estimated, and shown as blue points obtained by hatched histogram multiplied by the rejection factor. The contamination ratio ($N_{e/\mu}/N_{obs}$) is shown in Figure 5.27-5.28, demonstrating that the e/μ contamination is below one percent except for most highest bin of 1.8 - 3.4 GeV. In the highest bin, contaminations are about 40 % in Exp-12 and Exp-16, and about 5 $\sim$ 7 % in off-Pb region of Exp-34, about 5 $\sim$ 10 % in Lead region of Exp-34.

5.3.2 Antiproton production in the parachute

A parachute was put above the BESS detector during the balloon experiment. Dimensions of the folded parachute were 1 m in radius 100 m long. Total weight of the parachute was 400 kg. Although the weight of the parachute was heavy, it covered only a small part of field of view of the BESS detector. We expected that backgrounds from the parachute should be negligible. Using the Monte Carlo simulation, we estimated secondary particles produced in the parachute material. Two different hadronic packages, GHEISHA [62] and GEANT-FLUKA [63], were used in this simulation. As the primary flux hitting to the parachute, we used the observed proton flux which passed the detector. First, we normalized the proton flux in the simulation at the pressure of 4.58 g/cm^2. Calculated flux and our final observation result (4 - 6.5 g/cm^2) not including this contamination are shown in Figure 5.29. In the figure, blue histogram show GHEISHA result and green histogram show GEANT-FLUKA result. The GEANT-FLUKA code produce the $\overline{p}$ greater than GEISHA. We show the average of two packages as red line in the figure.

The ratio of $\overline{p}$'s from the parachute to the most small flux bin of observed $\overline{p}$'s are about 1 %. However, It is negligible small compared to statistical errors of corresponding observed flux. For other bin or range of air depth, the contamination is estimated below 1%. Because values are so small compared with the statistical errors, we didn't subtract these backgrounds from our final observed flux.

5.3.3 Antiprotons produced inside the Instrument

Antiprotons can also be produced by the interactions of high energy cosmic-rays with materials of the instrument. Most of them are expected to be eliminated, because most of events with such $\overline{p}$'s cannot pass the imposed cuts. However, the small fraction of them would pass the cuts and contaminate the $\overline{p}$ candidates. We estimated the number of the contamination by utilizing kaon samples. Since the life time of kaon is about 12 ns ($c\tau = 3.7$m), we can consider the detected kaons were produced only in the parachute or the instrument and their origin could not be the atmosphere. The kaon samples were extracted from the observed data in the similar way as the $\overline{p}$'s. Figure 5.30 shows the resultant β^{-1} vs R plots in which 1 event of kaon are identified, where we limited $\beta^{-} \geq 1.1$ to avoid the contamination of $e/\mu/\pi$. This kaon might be produced in the parachute, but even if the Kaon-like events shown in Figure 5.30 were produced in the instrument, we can neglect such instrumental antiproton, because the number is so small.

The production ratio of $\overline{p}$ to K^{-} was estimated as ~ 0.13, by convolving the production cross section [64] with proton spectrum [65]. That is, the number of $\overline{p}$'s produced in the instrument was estimated as 0.13 events, which corresponds to 0.36 % of the $\overline{p}$ samples of 36 events in $E_{TOI} \leq 1.0$ GeV. Accordingly, we neglected this contamination.

5.3.4 Other Source of Background

As other possible sources of background for $\overline{p}$'s, one can consider (i) spillover of positive particles and (ii) albedo particles. However, such backgrounds were completely negligible because of the excellent R and β^{-1} resolutions.

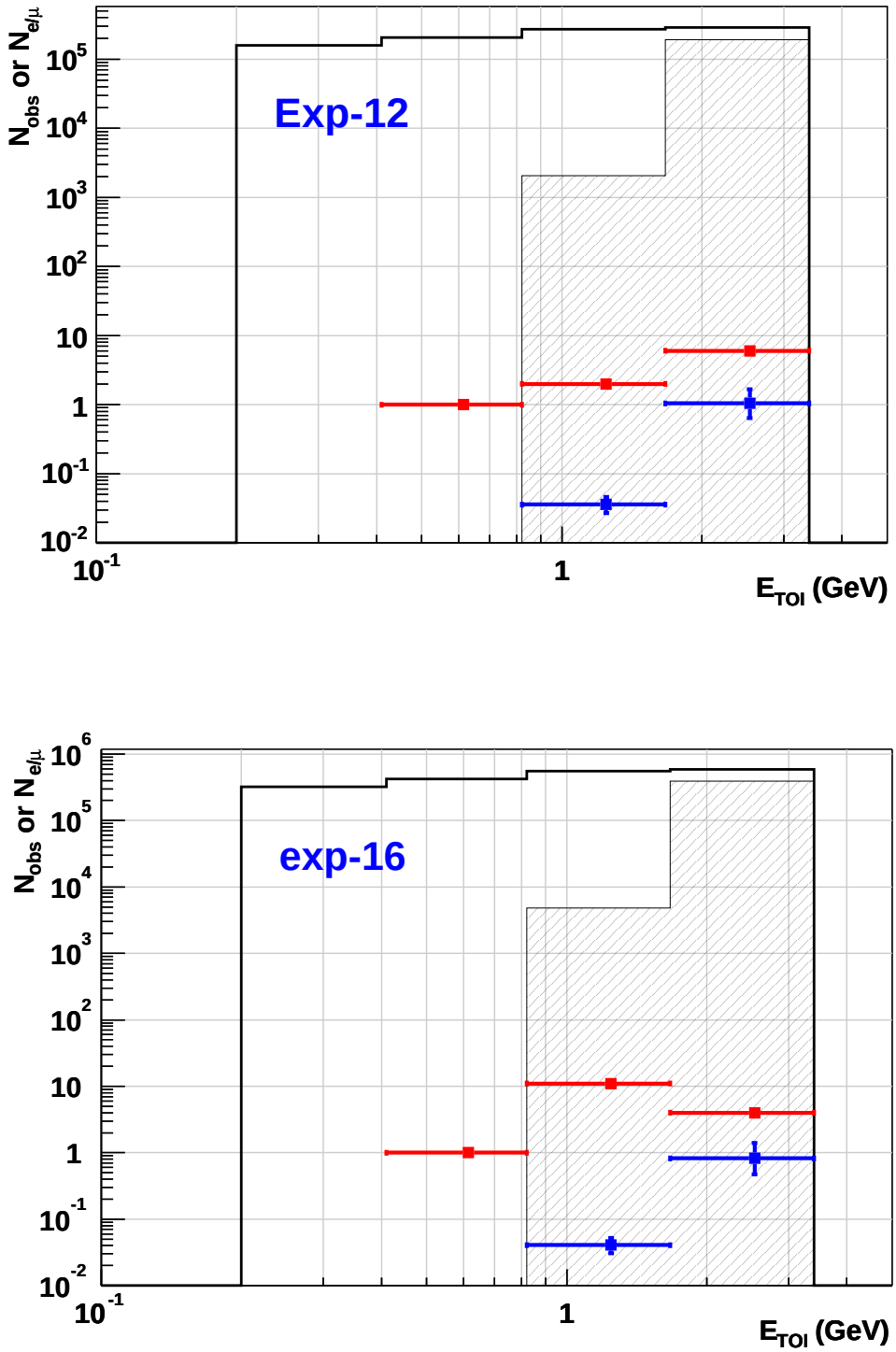

Figure 5.21: Background for e and μ particles with $\overline{p}$ candidates in Exp-12 and Exp-16. Open Histogram is total number of events with negative charge. Hatched Histogram is number of negative charged events in $\overline{p}$-band. Red points represent the number of antiproton candidates. Blue points represent the expected number of contaminated events.

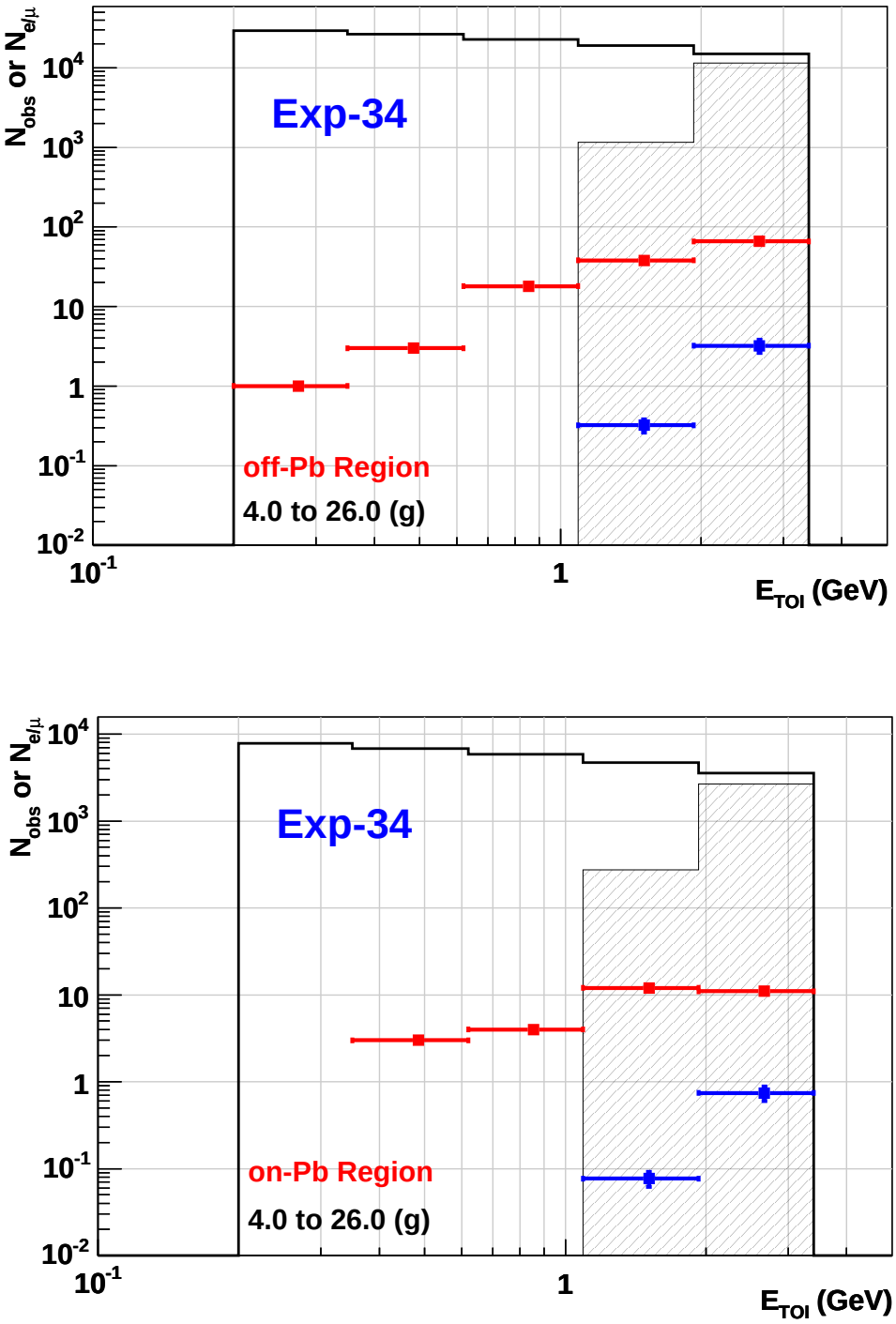

Figure 5.22: Background (blue points) for e and μ particles (hatched histogram) with $\overline{p}$ candidates (red points) in Exp-34 (4 to 26 g/cm^2). Open Histogram is total number of events with negative charge. Hatched Histogram is number of negative charged events in $\overline{p}$-band. Red points represent the number of antiproton candidates. Blue points represent the expected number of contaminated events.

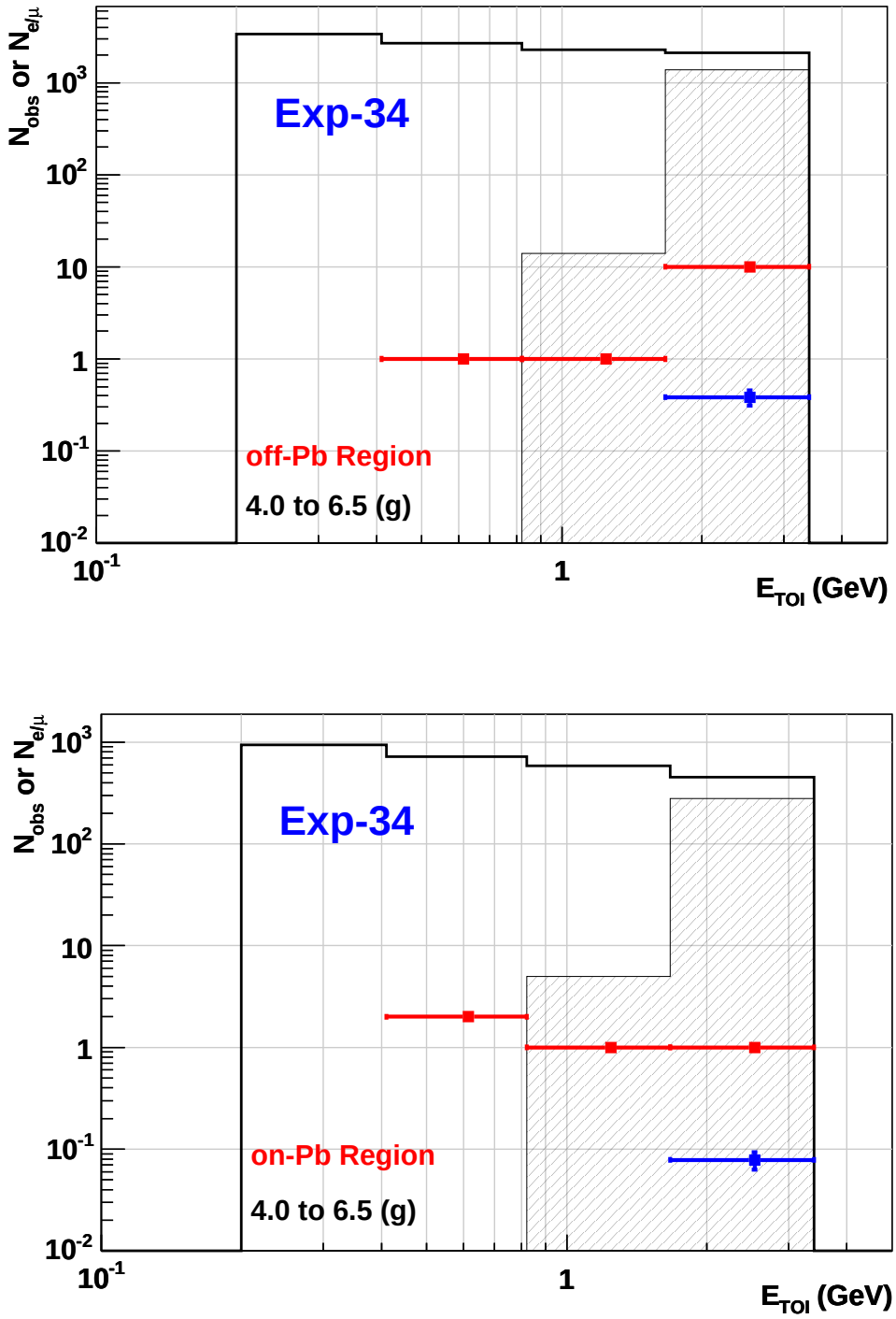

Figure 5.23: Background (blue points) for e and μ particles (hatched histogram) with $\overline{p}$ candidates (red points) in Exp-34 (4 to 6.5 g/cm^2). Open Histogram is total number of events with negative charge. Hatched Histogram is number of negative charged events in $\overline{p}$-band. Red points represent the number of antiproton candidates. Blue points represent the expected number of contaminated events.

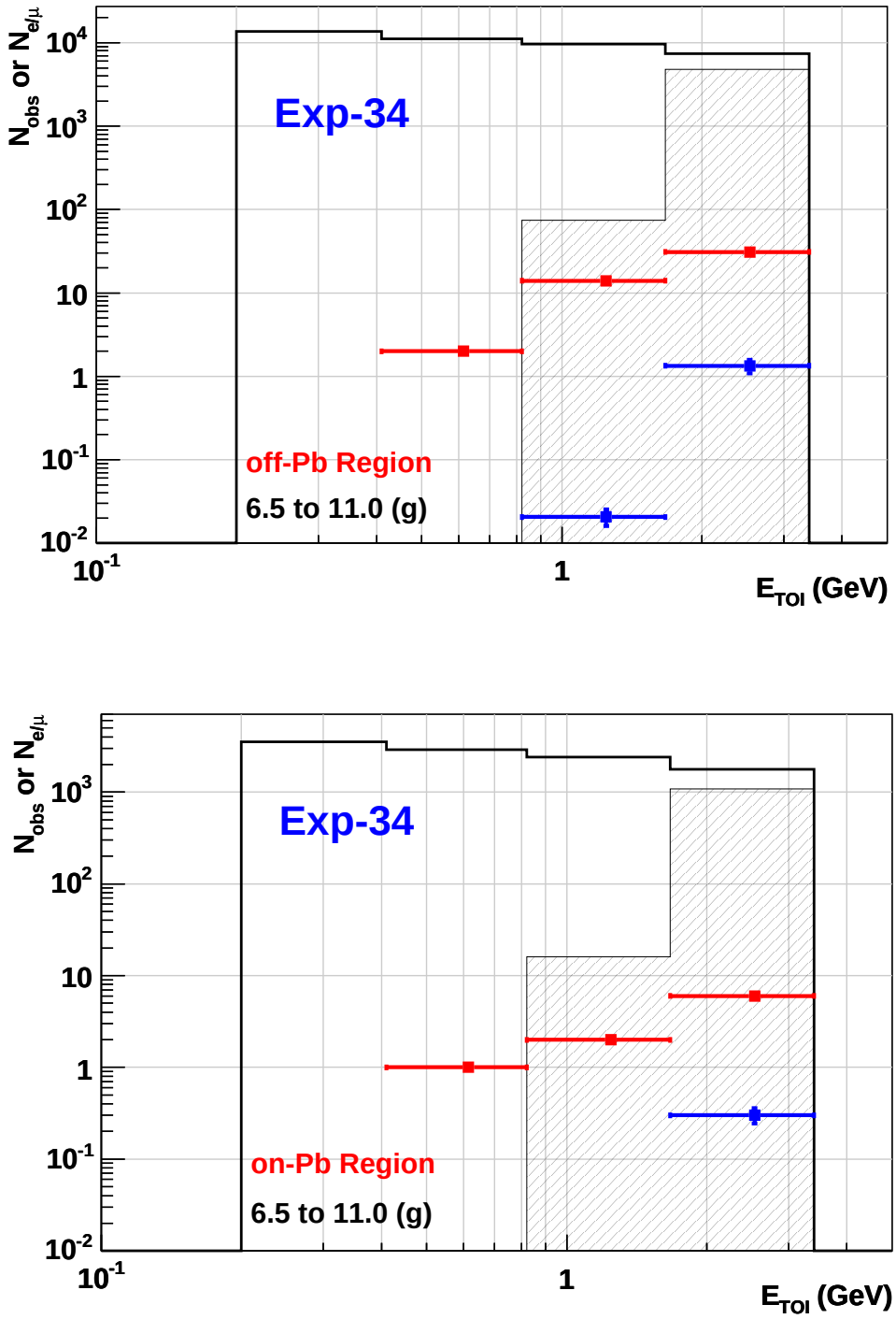

Figure 5.24: Background (blue points) for e and μ particles (hatched histogram) with $\overline{p}$ candidates (red points) in Exp-34 (6.5 to 11 g/cm^2). Open Histogram is total number of events with negative charge. Hatched Histogram is number of negative charged events in $\overline{p}$-band. Red points represent the number of antiproton candidates. Blue points represent the expected number of contaminated events.

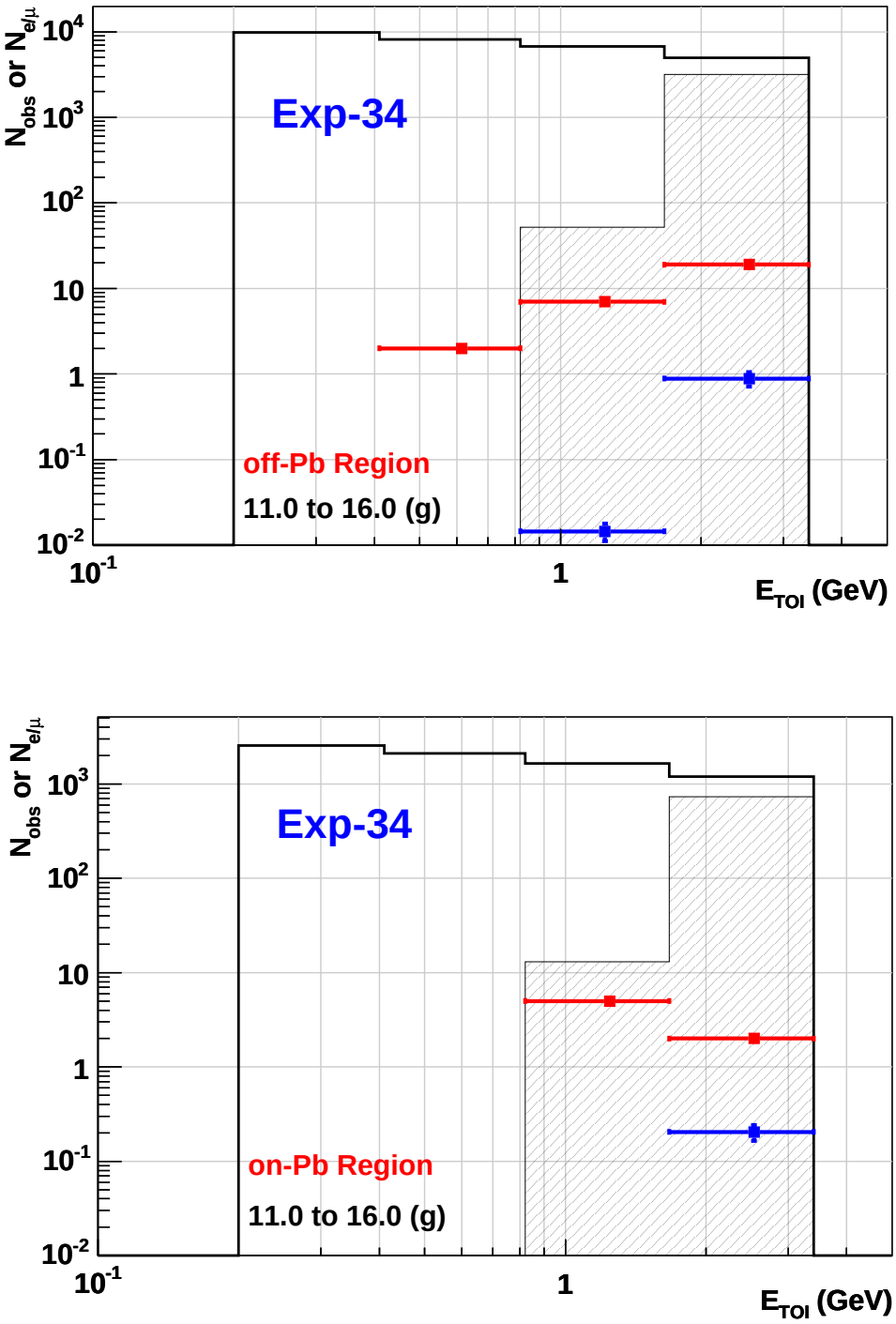

Figure 5.25: Background (blue points) for e and μ particles (hatched histogram) with $\overline{p}$ candidates (red points) in Exp-34 (11 to 16 g/cm^2). Open Histogram is total number of events with negative charge. Hatched Histogram is number of negative charged events in $\overline{p}$-band. Red points represent the number of antiproton candidates. Blue points represent the expected number of contaminated events.

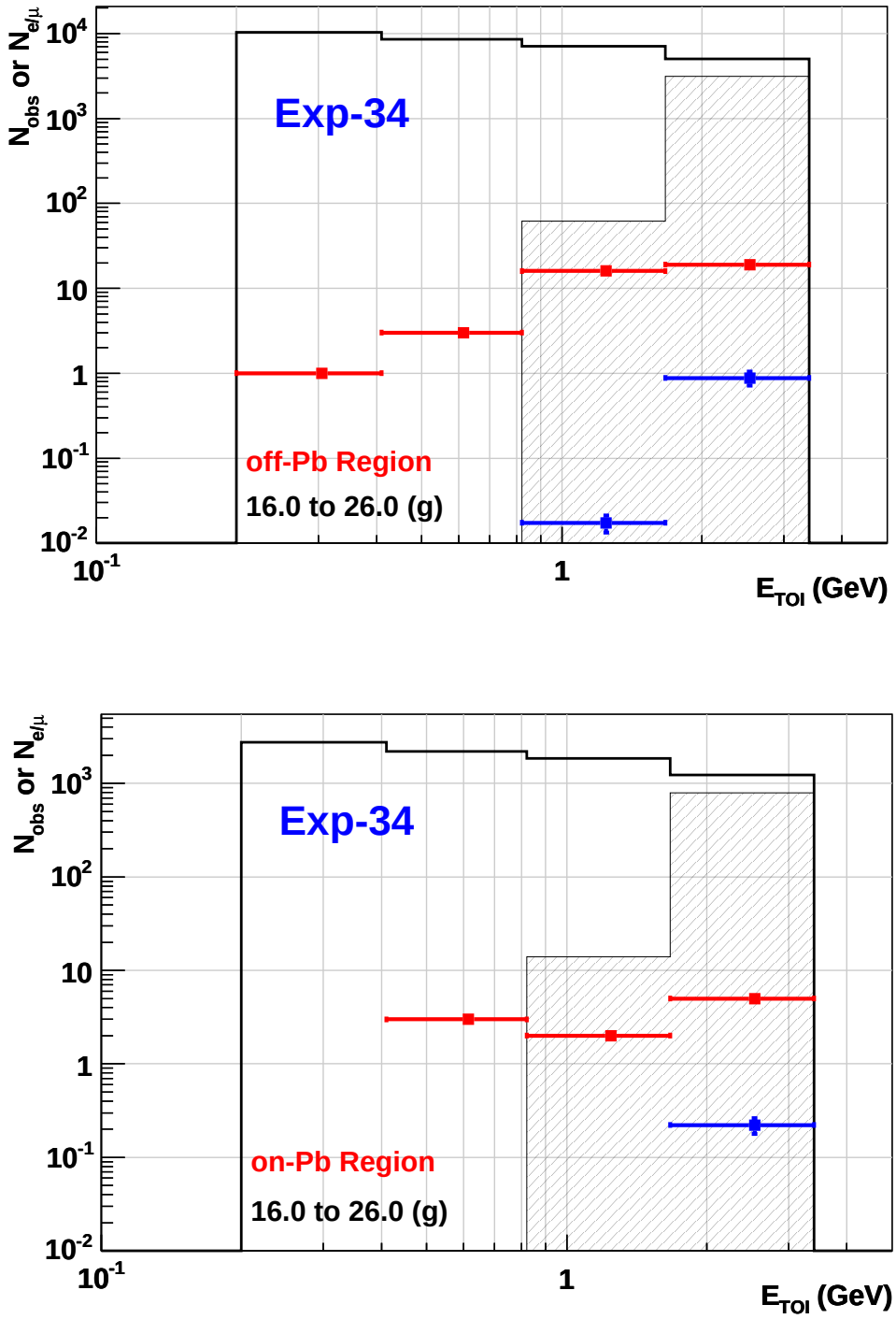

Figure 5.26: Background (blue points) for e and μ particles (hatched histogram) with $\overline{p}$ candidates (red points) in Exp-34 (16 to 26 g/cm^2). Open Histogram is total number of events with negative charge. Hatched Histogram is number of negative charged events in $\overline{p}$-band. Red points represent the number of antiproton candidates. Blue points represent the expected number of contaminated events.

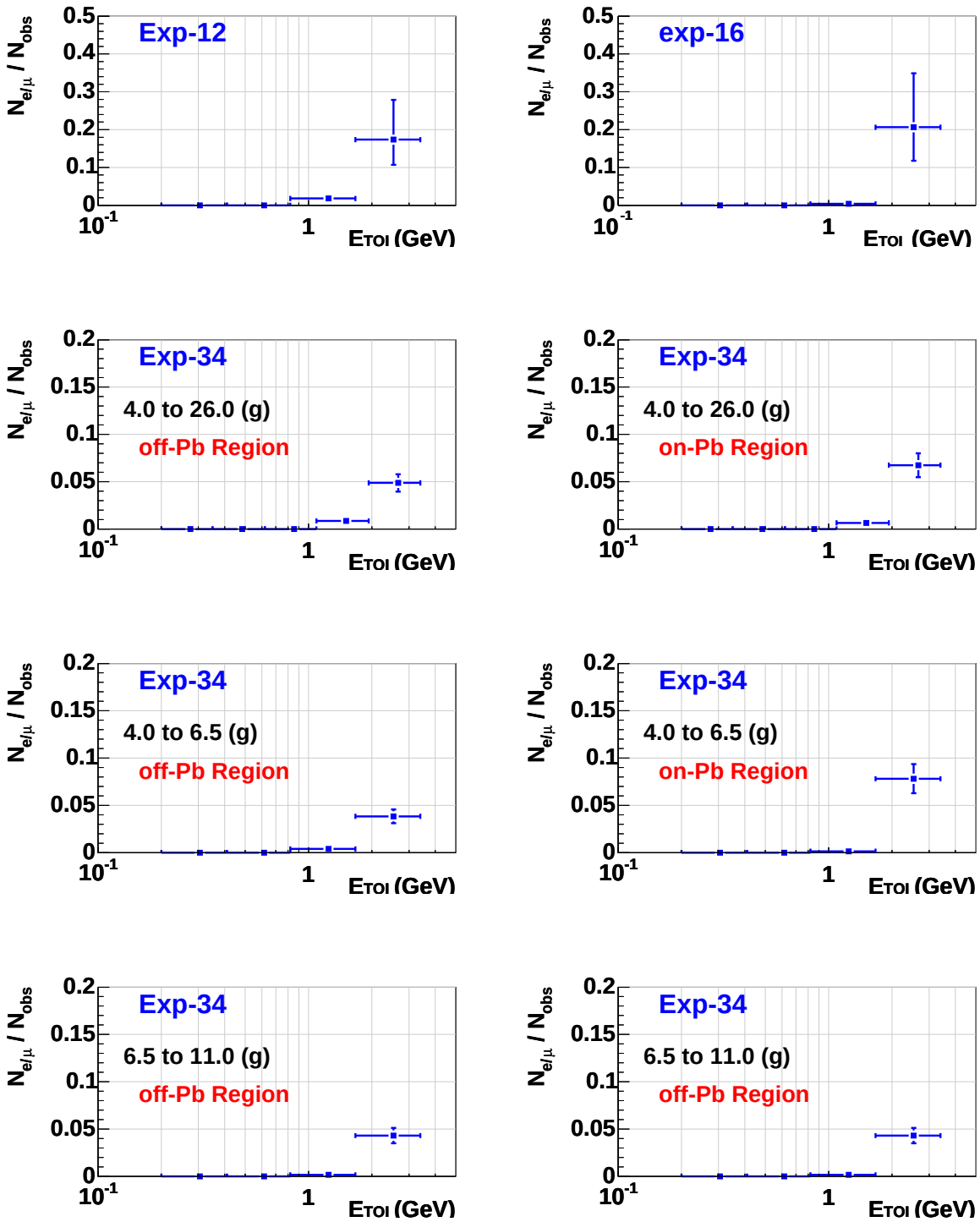

Figure 5.27: Contamination ratio of e and μ background on $\overline{p}$ candidates in each experiment and each atmospheric depth in Exp-34.

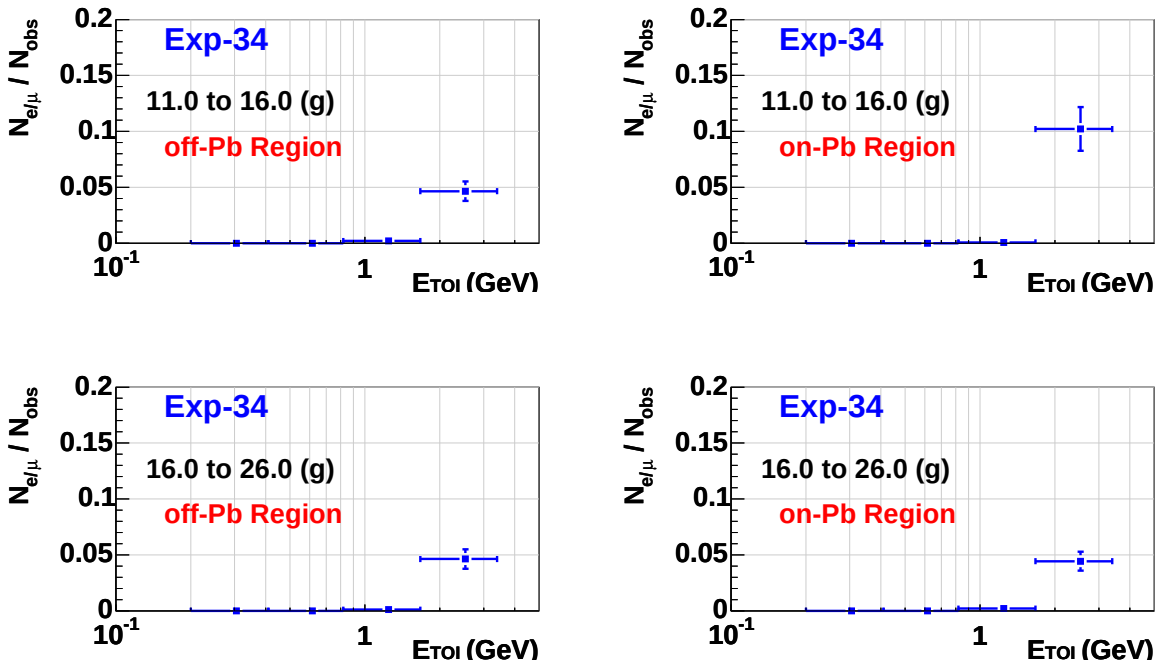

Figure 5.28: Contamination ratio of e and μ background on $\overline{p}$ candidates in each experiment and each atmospheric depth in Exp-34.

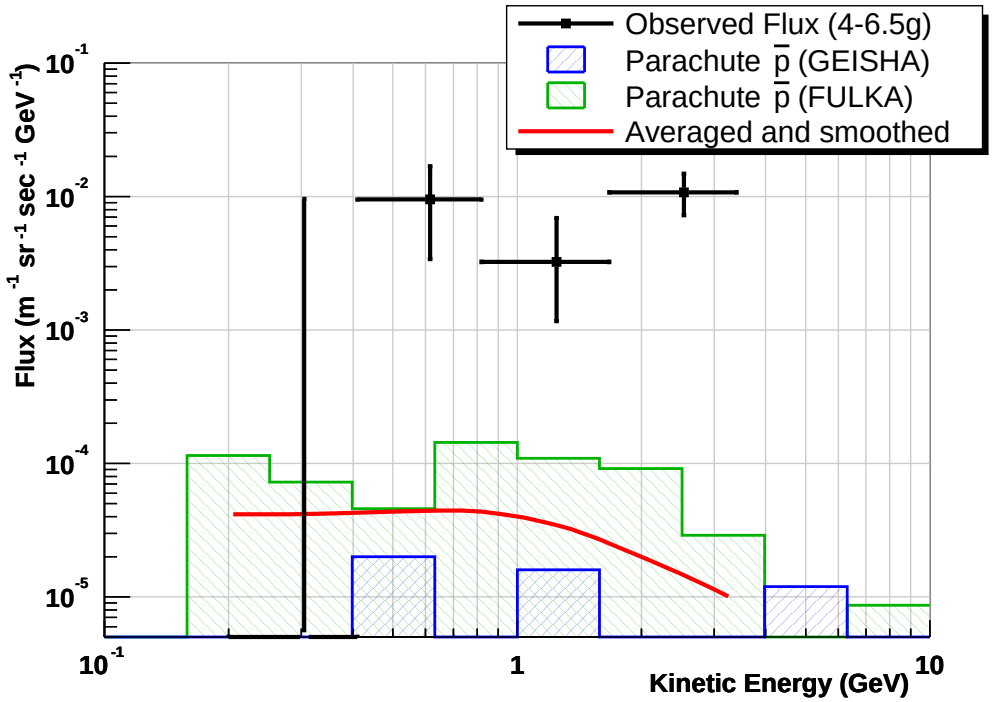

Figure 5.29: Observed most statistically poor $\overline{p}$ flux (black marker with error bar) and the simulated flux $\overline{p}$ flux (green and blue histograms) produced in the parachute.

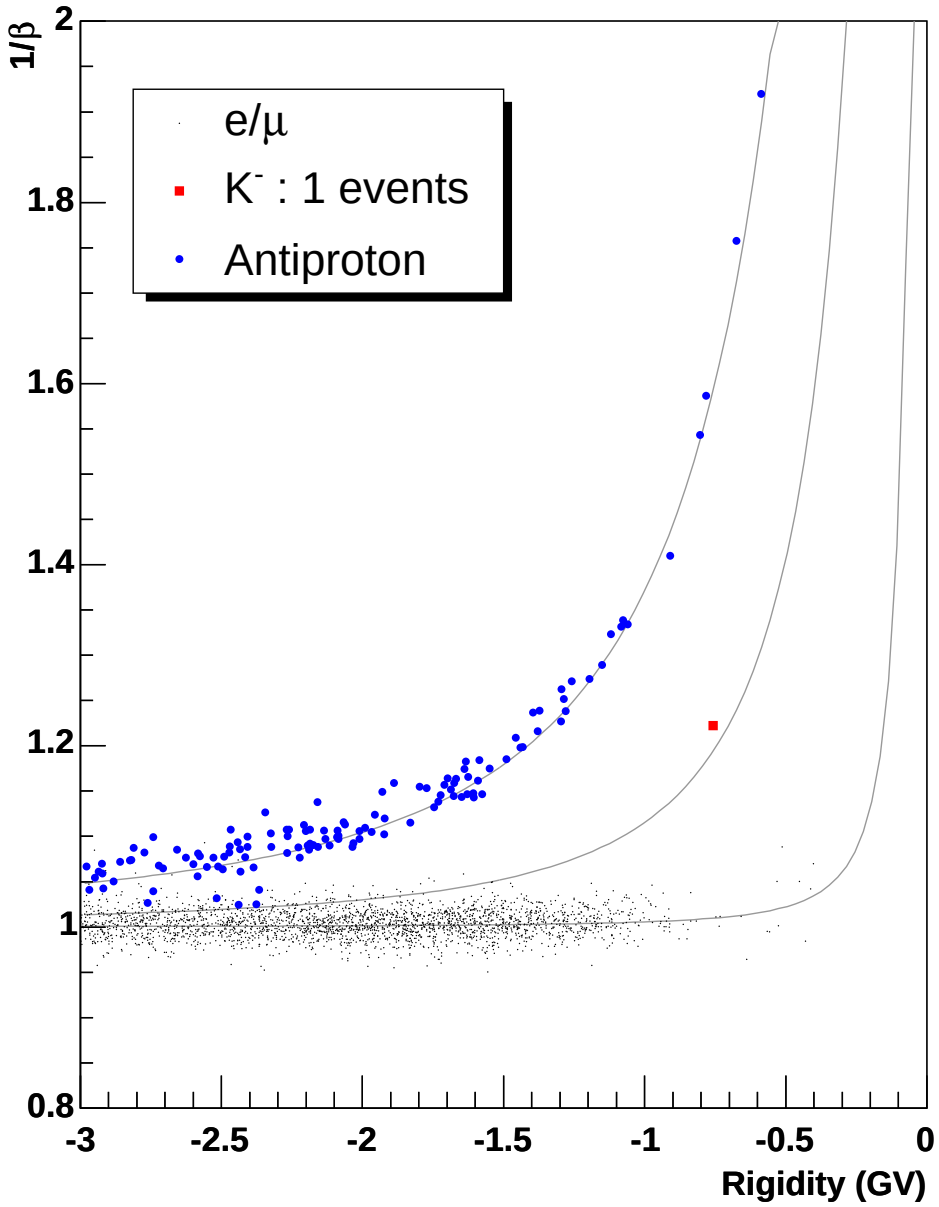

Figure 5.30: β^{-1} vs rigidity plot in which one K^- events are identified

5.4 Error Estimation

The following expression of the error of the $\overline{p}$ flux is derived from equation (5.1), assuming the variables are independent with each other:

$$\left|\frac{\Delta J}{J}\right|^2 = \left|\frac{\Delta N_{obs}}{N_{obs} - N_{BG}}\right|^2 + \left|\frac{\Delta N_{BG}}{N_{obs} - N_{BG}}\right|^2 + \left|\frac{\Delta(S\Omega)}{S\Omega}\right|^2 + \left|\frac{\Delta T_{live}}{T_{live}}\right|^2 + \left|\frac{\Delta\varepsilon}{\varepsilon}\right|^2 \tag{5.3}$$

5.4.1 Statistical Errors

In order to compute a 68.27% confidence interval which corresponds to 1σ for the Gaussian distribution, we adopted Feldman's "unified approach" [60] to Neyman's "confidence belts method" [61].

The confidence intervals are determined in following way: The probability distribution obtaining n events can be described by a Poisson distribution function as

$$P_\mu(n) = \exp(-(\mu + B))\,\frac{(\mu + B)^n}{n!}\ ,$$

where the background events B is assumed as a known value, and μ denotes true value. When the confidence interval is denoted as $[\mu_1,\mu_2]$, μ_1 and μ_2 are the minimum and the maximum value of μ satisfying a condition;

$$\sum_{n=n_1}^{n_2} P_\mu(n) \leq 68.27\%$$

The interval $[n_1,n_2]$ is chosen using the *ordering principle* [60], which is based on likelihood ratios, which has better properties than the previously used method (*central confidence interval*) when number of observed events are very small or zero. This method is used to obtain ΔN_{obs} and to treat statistics when number of the the data is small.

5.4.2 Systematic Errors

The systematic errors were estimated using the BESS MC simulation and real data sample. In the following, each term of systematic errors in Eq.(5.3) will be discussed.

- **Errors in muon contamination**
  It is not simple to estimate precise rejection factor of Aerogel Čerenkov counter, because of the difficulty in obtaining the pure sample of $\beta^{-1} \approx 1$ particles with enough statistics. Figure 5.31 illustrates the efficiencies for rejection of background particle which estimated by two different ways in Exp-34. The black points are obtained from high energy proton samples in the flight time. While the blue points are obtained on the ground in few weeks before the flight. The error bars in the figure are taken into account for statistical only. The number of ground data is small to study background rejection efficiency at low ADC threshold. Since the observed

negative particles are almost μ^- on the ground, we can consider all negative particles as background particles. Therefore, ground data can be trusted. However, flight data may contain some contamination of low-energy particles of $\beta^{-1} \approx 1$ samples. Although we required $R > 28$ GV to select $\beta^{-1} \approx 1$ samples, the tail of $\Delta(1/R)$ distribution may be suffered by the tail of the distribution. The agreement of the absolute value of these two data are not bad. However, in ADC Threshold ¡ 20, it seems flight data is a little bit greater than the ground data. Thus we put systematic errors to cover ground data as the red line shown in Figure 5.31.

For Exp-12, 16, we did not put systematic error of rejection factor, because it is smaller than the statistical error of rejection factors itslef.

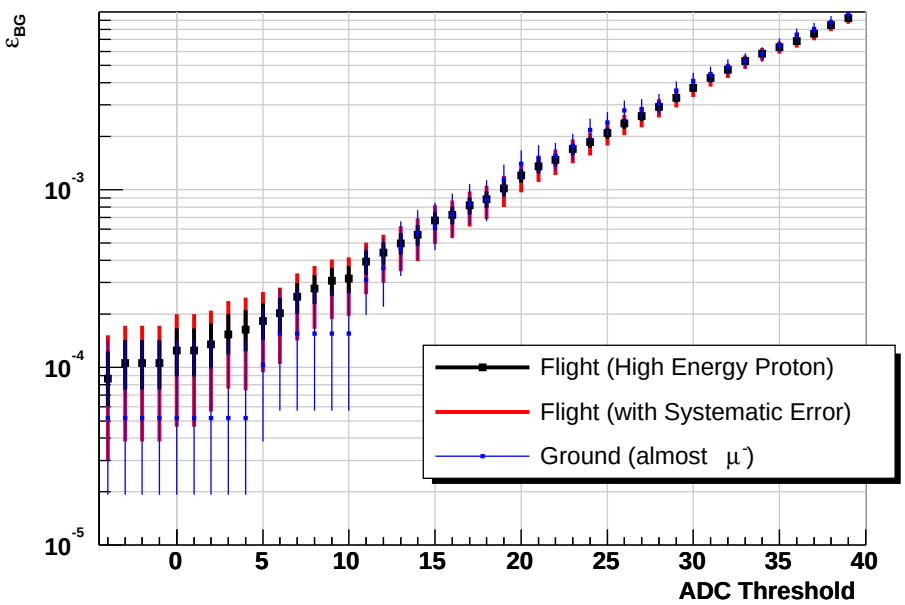

Figure 5.31: The Background Efficiency

- **Geometrical Acceptance**

  This systematic errors were estimated using the BESS MC simulation. In following, each term of systematic errors in Eq. (5.3) will be discussed.

  The geometrical acceptance was obtained from the Monte Carlo simulation without including the interaction and energy-loss. The geometrical acceptance is prescribed by "fiducial volume" cut, namely by N_{expect}, N_{TOF_U}, N_{TOF_L}, Z_{TK_U}, Z_{TK_L}, The error arises from the uncertainty of the detector alignment which is less than 1mm, and corresponds to about 0.3% systematic errors of the acceptance with upper and lower TOF hodoscope.

- **Live time**

  The live time was directly measured by the resolution of 10^{-6} sec. Thre dead-time fraction is small enough. Therefore, the error in the live time is negligibly small.

- **Detection efficiency**

  - **Detection efficiency measured directly by beam test**

    To investigate the accuracy of BESS MC, the beam experiment of the BESS detector has performed using low-energy $\overline{p}$ and proton beam at the KEK-PS K2 beam line [66]. From this experiment, a resultant systematic error in detection efficiency is:

$$\left(\frac{\Delta\varepsilon}{\varepsilon}\right) = \begin{cases} \pm 5\% & (\quad E_{TOI} < 0.3 \text{ GeV}) \\ \pm 2\% & (0.3 \text{ GeV} < E_{TOI} < 1.0 \text{ GeV}) \\ \pm 5\% & (1.0 \text{ GeV} < E_{TOI} \quad) \end{cases}$$

    Note that above values include a systematic errors due to the particle identification.

  - **Correction for Aerogel efficiency**

    Basic detector construction and a procedure for the analysis are very similar for the case of beam test and this analysis. Therefore, above detection efficiency is confident for this analysis.

    There is one different in Exp-34. It is a method of the estimation of the Aerogel efficiency for $\overline{p}$ identification described in section 5.2.3 which is obtained by subtracting e^+ and μ^+ contamination in the unbiased samples. Consequently, Aerogel efficiency contains errors originated from estimation of number of contaminating e^+/μ^+. In this estimation, we took $(e^+ + \mu^+)/(e^- + \mu^-) = 1.3 \pm 0.1$. The error bars in Figure 5.17 includes this error of $+/-$ ratio and statistical error of $(e^- + \mu^-)$. Thus, we consider that the error of each point in Figure 5.18 is the systematic error of Aerogel efficiency in addition to detection efficiency mentioned above. It is $\pm 2\%$ at maximum around $E_{TOI} = 2$ GeV. It can be neglected below 1.5 GeV and above 3 GeV, because the fraction of contamination is very small in such energy region.

5.5 Observed Results

We show the $\overline{p}$ flux at each altitude in Figures 5.32-5.36. The errors attached to the data in the figure was calculated by using Eq. 5.3. For non-observed bin, we put 68.27% as an upper limit. We also obtained the the upper by adopting Feldman's "unified approach" [60] to Neyman's "confidence belts method" [61].

In the ground experiments Exp-12 and Exp-16, the two flux are consistent within each error. We could not observe the $\overline{p}$ event in lowest bin (0.2-0.41 GeV) in each experiment due to the shortage of live time, although BESS detector can accept such energy of antiprotons. In other bins, number of observed events are less than 5. Consequently, statistical error is dominant in the final error.

For Exp-34 we also show the flux in on-Pb and off-Pb region at each atmospheric depth separately. Red markers and error bars represent the flux on off-Pb region, and blue markers and error bars represent the flux on-Pb region. These flux in the each atmospheric depth are consistent with each other. In this balloon experiment, there is also no event are observed in the lowest bin (0.2-0.4 GeV) except for atmospheric depth at 16-26g/cm^2.

Finally we show the combined flux at ground altitude in Figure 5.37, on-Pb and off-Pb region in Figures 5.38-5.42 with numerical data in Tables 5.1-5.6. In each atmospheric depth of Exp-34, we can see the shape which has the peak at $1 \sim 2$ GeV, although the total error is not small. A detailed discussion about these results is presented in the following chapter.

For the analysis of antiprotons fluxes observed at different altitudes, we first used following way to combine the flux:

$$J_{comb} = \frac{N_{comb} - BG_{comb}}{(S\Omega\, T_{live}\, \varepsilon)_{comb}} \ ,$$

where

$$N_{comb} = N_1 + N_2 \ ,$$

$$BG_{comb} = BG_1 + BG_2 \ ,$$

$$(S\Omega\, T_{live}\, \varepsilon)_{comb} = (S\Omega\, T_{live}\, \varepsilon)_1 + (S\Omega\, T_{live}\, \varepsilon)_2 \ ,$$

The index '1' and '2' indicate the each value at different altitude respectively. We treated their errors as following:

$$\left|\frac{\Delta J_{comb}}{J_{comb}}\right|^2 = \left|\frac{\Delta N_{comb}}{N_{comb} - BG_{comb}}\right|^2 + \left|\frac{\Delta BG_{comb}}{N_{comb} - BG_{comb}}\right|^2 + \left|\frac{\Delta(S\Omega\, T_{live}\, \varepsilon)_{comb}}{(S\Omega\, T_{live}\, \varepsilon)_{comb}}\right|^2$$

where ΔN_{comb} is calculated with BG_{comb} by confidence belts method described in section 5.4.1. The other errors are:

$$|\,\Delta BG_{comb}\,|^2 = |\,\Delta BG_1\,|^2 + |\,\Delta BG_2\,|^2$$

$$|\Delta(S\Omega\, T_{live}\, \varepsilon)_{comb}|^2 = |\Delta(S\Omega\, T_{live}\, \varepsilon)_1|^2 + |\Delta(S\Omega\, T_{libe}\, \varepsilon)_2|^2$$

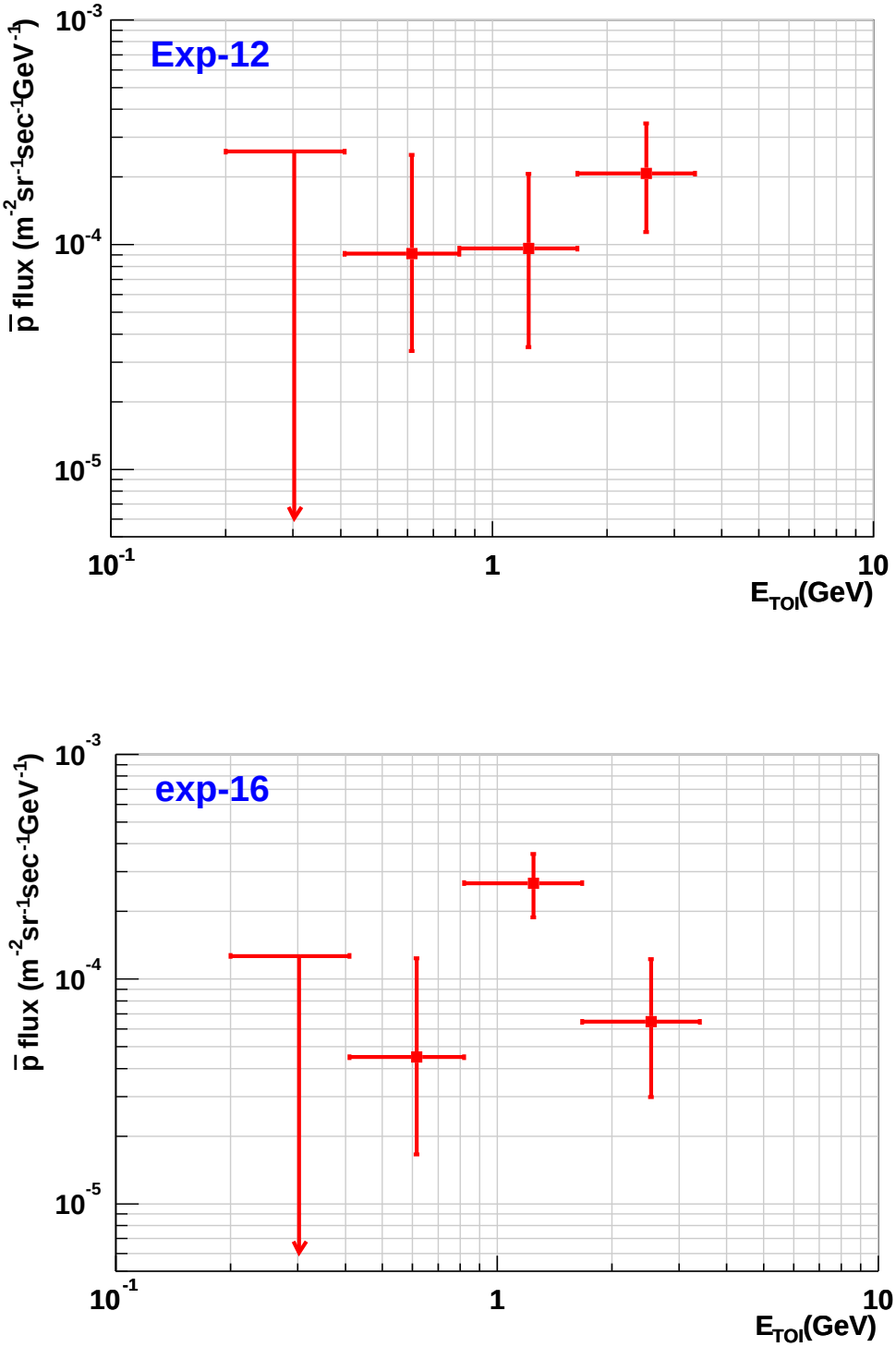

Figure 5.32: $\overline{p}$ flux measured by BESS in Exp-12 and Exp-16

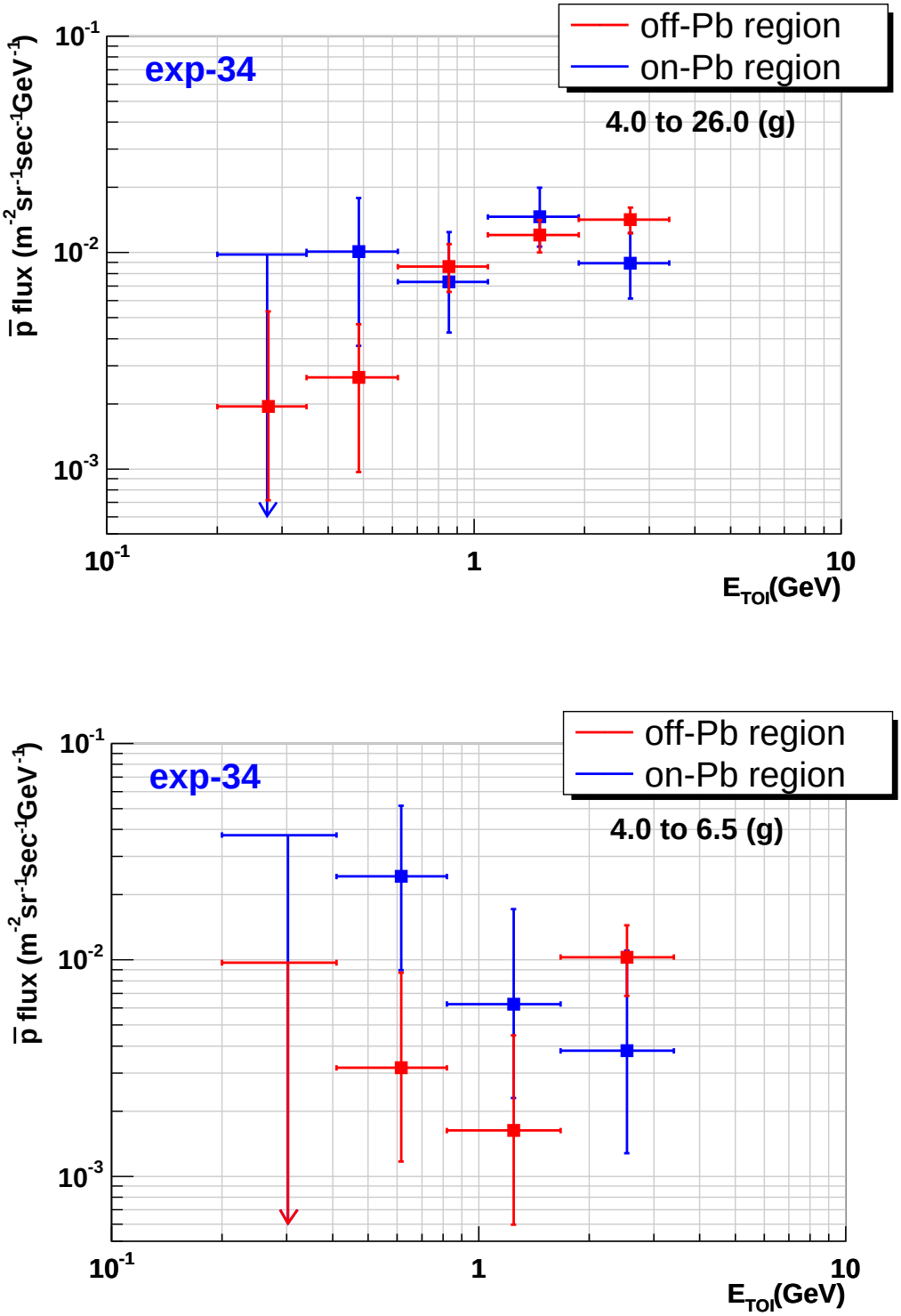

Figure 5.33: $\overline{p}$ flux measured by BESS in Exp-34 (I)

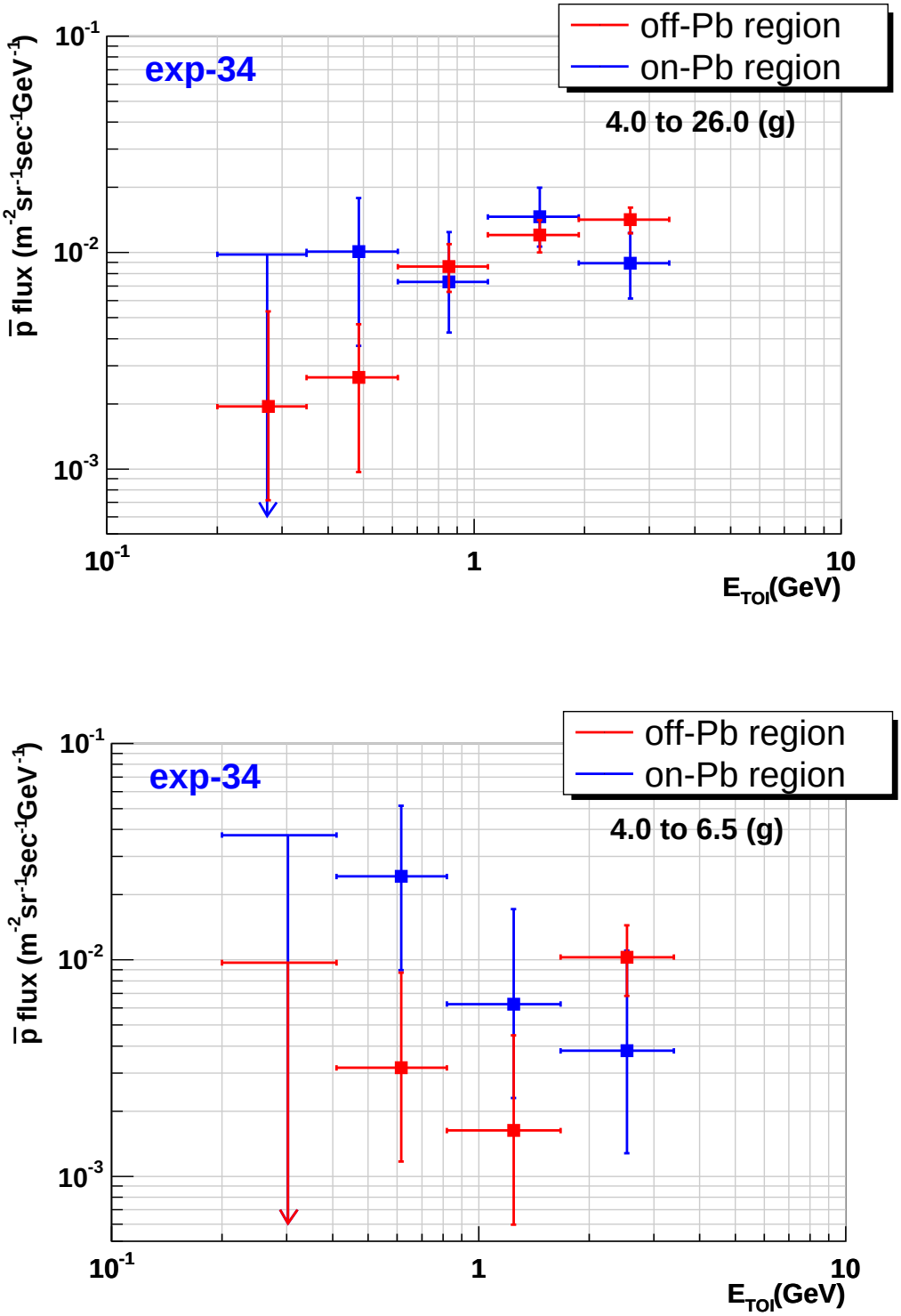

Figure 5.34: $\overline{p}$ flux measured by BESS in Exp-34 (I)

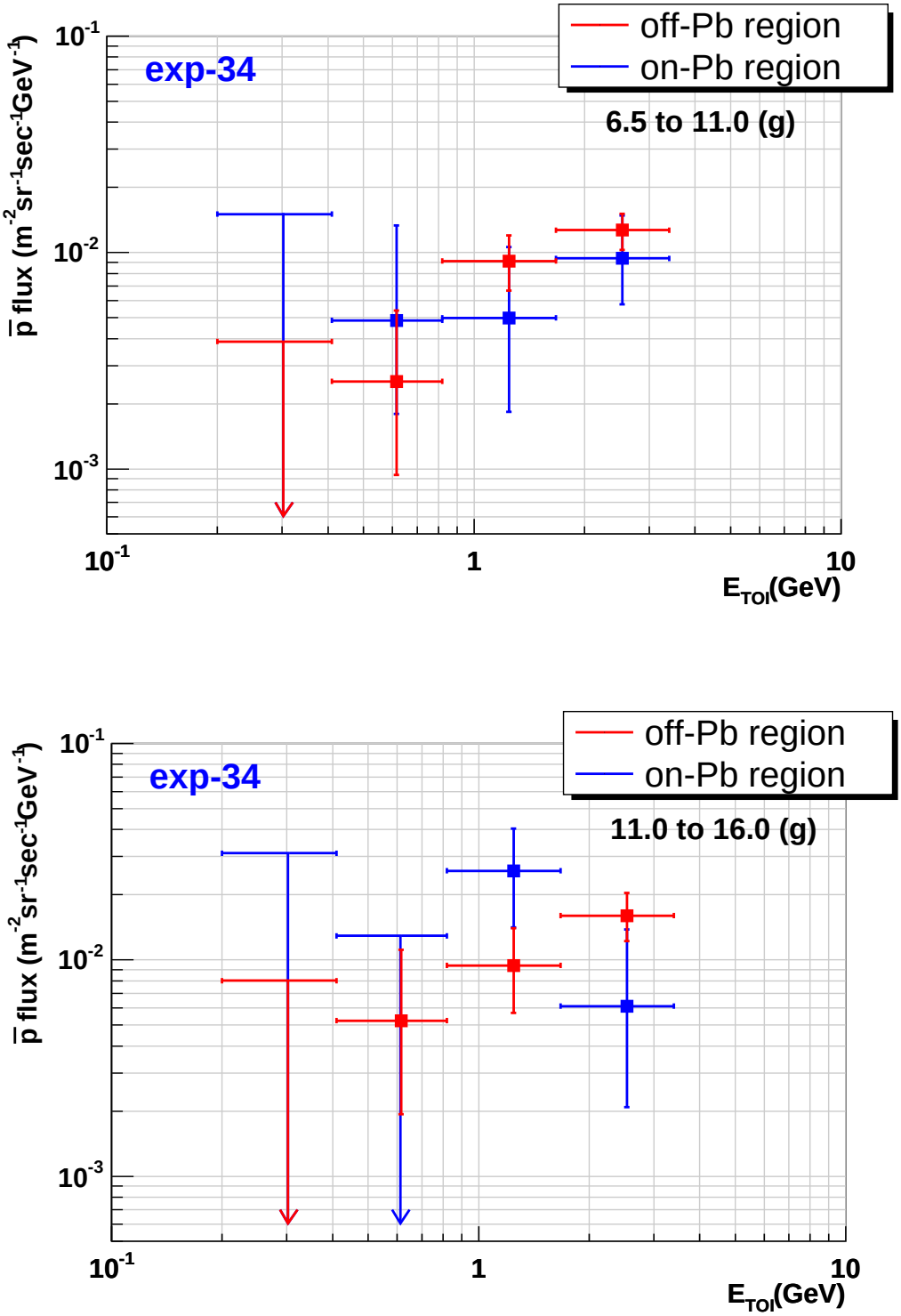

Figure 5.35: $\overline{p}$ flux measured by BESS in Exp-34 (II)

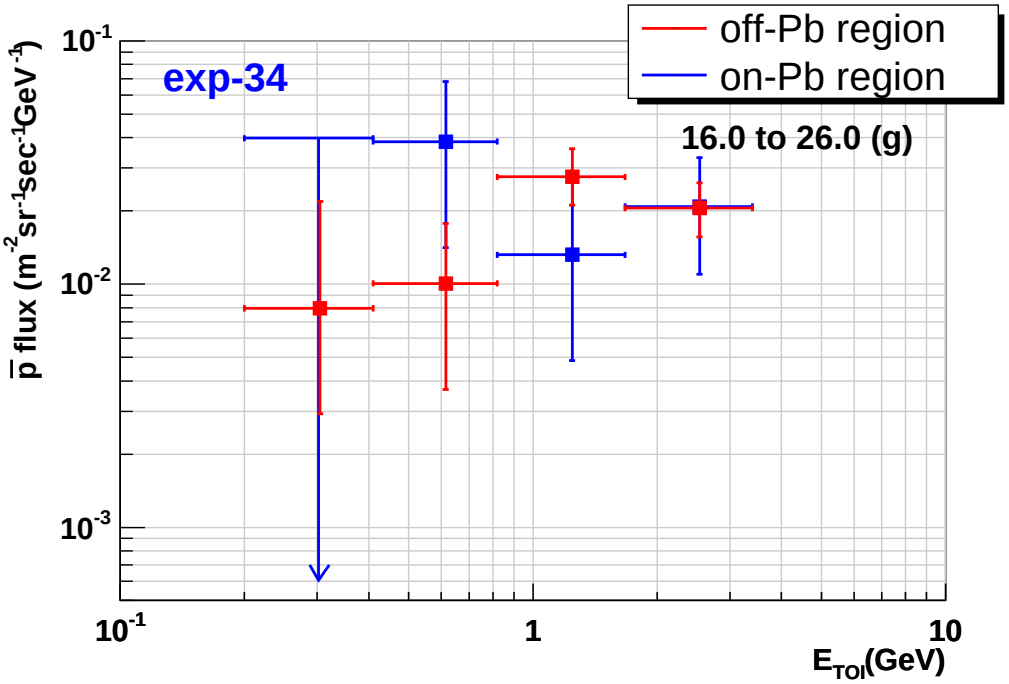

Figure 5.36: $\overline{p}$ flux measured by BESS in Exp-34 (III)

Table 5.1: Antiproton flux (in $\times 10^{-4}\mathrm{m}^{-2}\mathrm{s}^{-1}\mathrm{sr}^{-1}\mathrm{GeV}^{-1}$) on the ground (Exp-12 + Exp-16). T (in GeV) define the kinetic energy bins. $N_{\overline{p}}$ is the number of observed antiprotons.

T (GeV)	$N_{\overline{p}}$	N_{BG}	$\overline{p}$ flux	Statical Err.	Systematic Err.
0.20 - 0.41	000	$0.00^{+0.00}_{-0.00}$	U.L. 0.85 (68.27% C.L),		2.04 (95% C.L.)
0.41 - 0.82	002	$0.00^{+0.00}_{-0.00}$	0.60	$^{+0.68}_{-0.38}$	$^{+0.01}_{-0.01}$
0.82 - 1.67	013	$0.08^{+0.02}_{-0.01}$	2.10	$^{+0.70}_{-0.60}$	$^{+0.07}_{-0.07}$
1.67 - 3.40	010	$1.87^{+0.85}_{-0.53}$	1.11	$^{+0.52}_{-0.44}$	$^{+0.12}_{-0.08}$

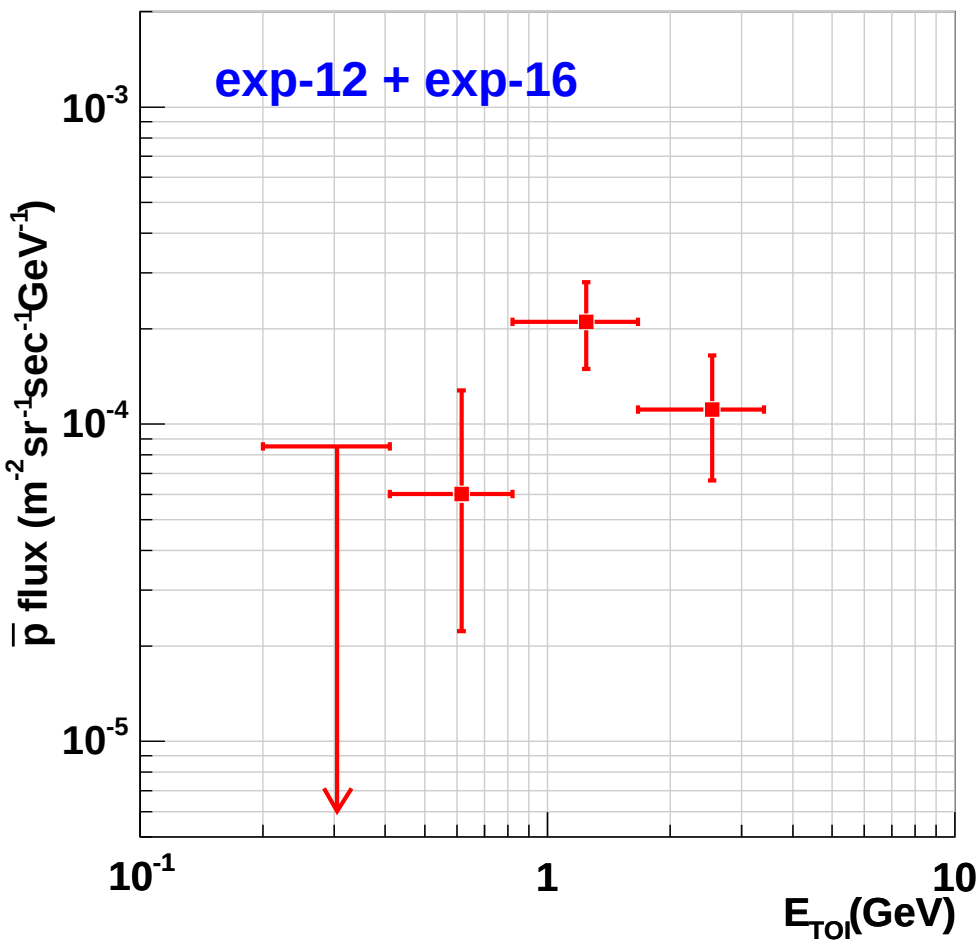

Figure 5.37: Combined $\overline{p}$ flux at ground altitude in KEK, Japan.

Table 5.2: Antiproton flux (in $\times 10^{-4} m^{-2} s^{-1} sr^{-1} GeV^{-1}$) at 4.5 - 26 g/cm^2. T (in GeV) define the kinetic energy bins. $N_{\overline{p}}$ is the number of observed antiprotons.

T (GeV)	$N_{\overline{p}}$	N_{BG}	$\overline{p}$ flux	Statical Err.	Systematic Err.
0.20 - 0.35	001	$0.00^{+0.00}_{-0.00}$	0.15	$^{+0.27}_{-0.10}$	$^{+0.01}_{-0.01}$
0.35 - 0.62	006	$0.00^{+0.00}_{-0.00}$	0.42	$^{+0.23}_{-0.15}$	$^{+0.00}_{-0.00}$
0.62 - 1.09	022	$0.00^{+0.00}_{-0.00}$	0.83	$^{+0.18}_{-0.18}$	$^{+0.02}_{-0.02}$
1.09 - 1.93	050	$0.37^{+0.06}_{-0.06}$	1.24	$^{+0.18}_{-0.18}$	$^{+0.05}_{-0.05}$
1.93 - 3.40	077	$3.86^{+0.61}_{-0.61}$	1.28	$^{+0.15}_{-0.15}$	$^{+0.05}_{-0.05}$

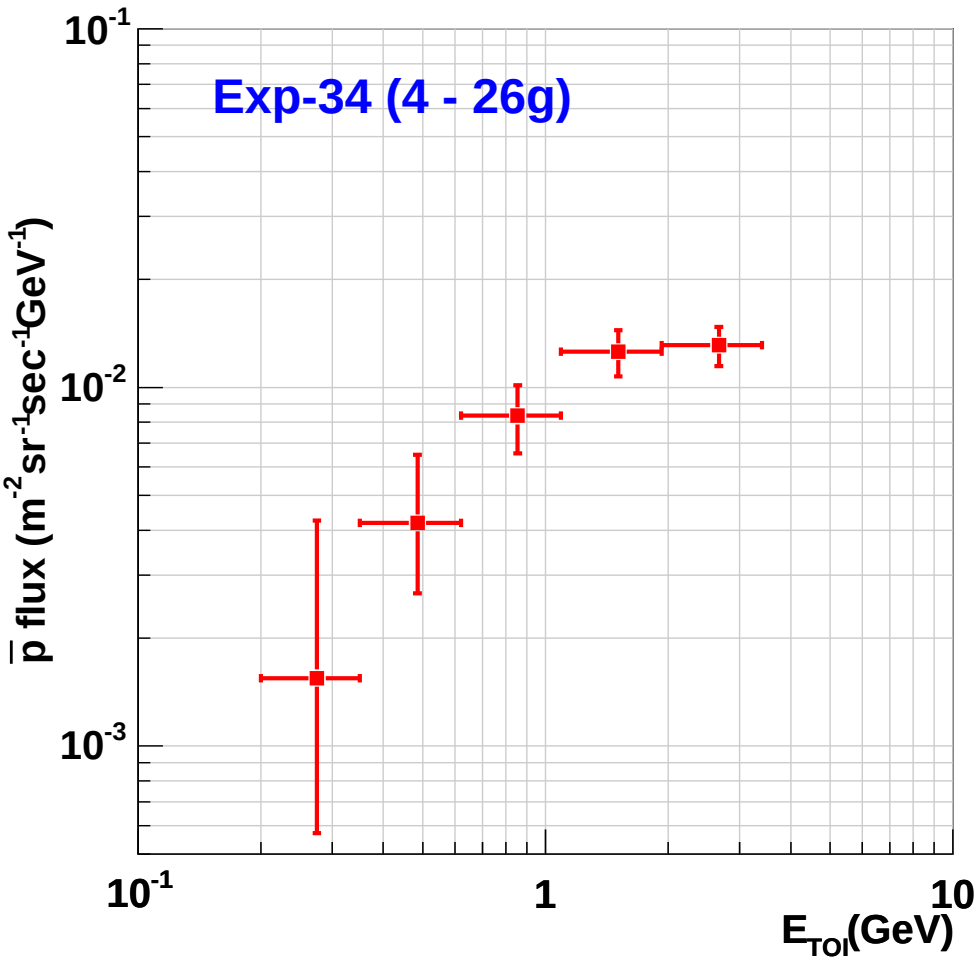

Figure 5.38: Combined $\overline{p}$ at atmospheric range of 4.5 to 26 g/cm^2

Table 5.3: Antiproton flux (in $\times 10^{-4}\mathrm{m}^{-2}\mathrm{s}^{-1}\mathrm{sr}^{-1}\mathrm{GeV}^{-1}$) at 4.5 - 6.5 g/cm^2. T (in GeV) define the kinetic energy bins. $N_{\overline{p}}$ is the number of observed antiprotons.

T (GeV)	$N_{\overline{p}}$	N_{BG}	$\overline{p}$ flux	Statical Err.	Systematic Err.
0.20 - 0.41	000	$0.00^{+0.00}_{-0.00}$	U.L. 0.77 (68.27% C.L),		1.85 (95% C.L.)
0.41 - 0.82	003	$0.00^{+0.00}_{-0.00}$	0.75	$^{+0.58}_{-0.48}$	$^{+0.01}_{-0.01}$
0.82 - 1.67	002	$0.00^{+0.00}_{-0.00}$	0.26	$^{+0.29}_{-0.16}$	$^{+0.01}_{-0.01}$
1.67 - 3.40	011	$0.45^{+0.07}_{-0.07}$	0.87	$^{+0.32}_{-0.26}$	$^{+0.04}_{-0.04}$

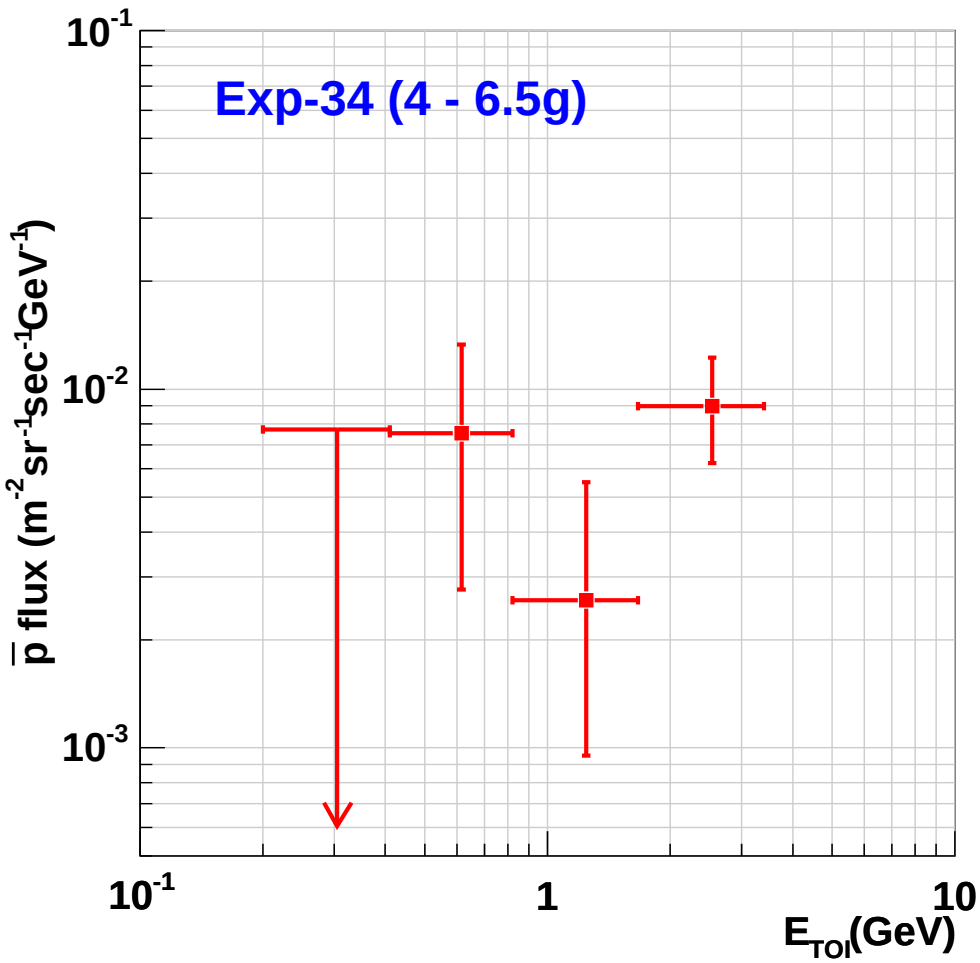

Figure 5.39: Combined $\overline{p}$ at atmospheric range of 4.5 to 6.5 g/cm^2

Table 5.4: Antiproton flux (in $\times 10^{-4}\mathrm{m}^{-2}\mathrm{s}^{-1}\mathrm{sr}^{-1}\mathrm{GeV}^{-1}$) at 6.5 - 11 g/cm^2. T (in GeV) define the kinetic energy bins. $N_{\overline{p}}$ is the number of observed antiprotons.

T (GeV)	$N_{\overline{p}}$	N_{BG}	$\overline{p}$ flux	Statical Err.	Systematic Err.
0.20 - 0.41	000	$0.00^{+0.00}_{-0.00}$	U.L. 0.31 (68.27% C.L),		0.74 (95% C.L.)
0.41 - 0.82	003	$0.00^{+0.00}_{-0.00}$	0.30	$^{+0.23}_{-0.19}$	$^{+0.01}_{-0.01}$
0.82 - 1.67	016	$0.02^{+0.00}_{-0.00}$	0.82	$^{+0.25}_{-0.19}$	$^{+0.03}_{-0.03}$
1.67 - 3.40	037	$1.59^{+0.25}_{-0.25}$	1.17	$^{+0.20}_{-0.20}$	$^{+0.05}_{-0.05}$

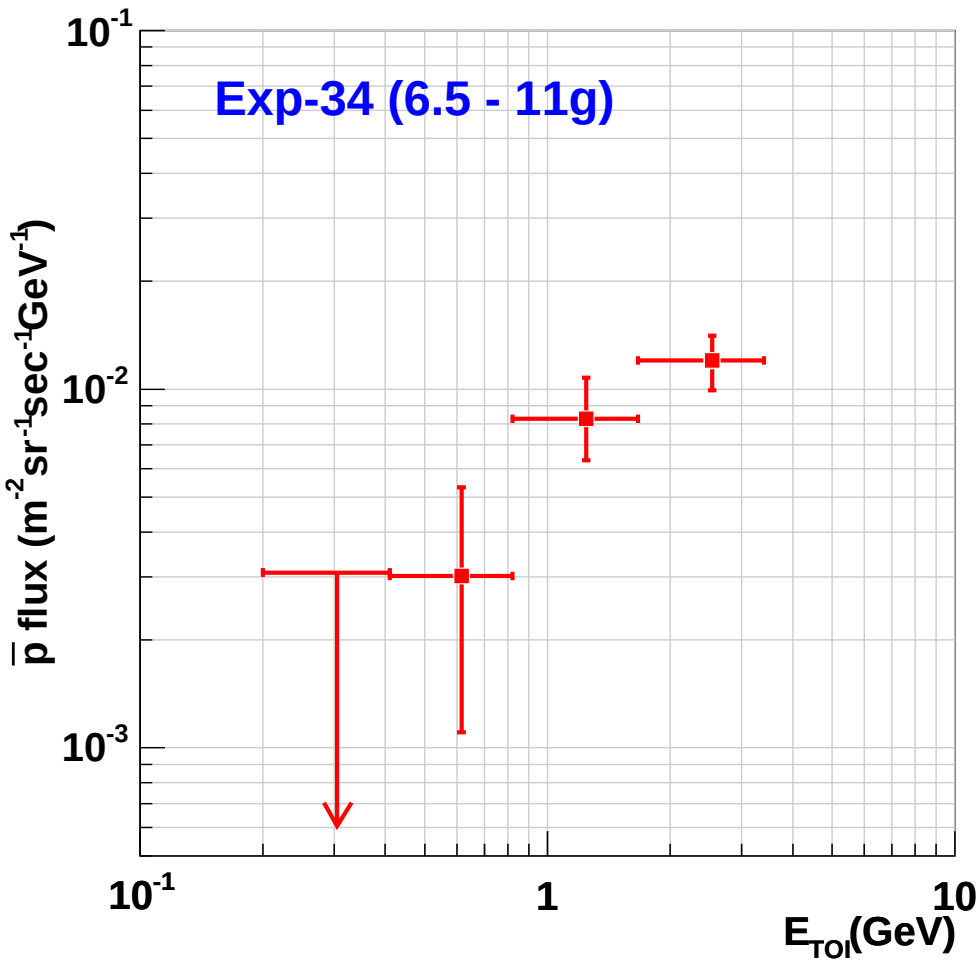

Figure 5.40: Combined $\overline{p}$ at atmospheric range of 6.5 to 11 g/cm^2

Table 5.5: Antiproton flux (in $\times 10^{-4}\mathrm{m}^{-2}\mathrm{s}^{-1}\mathrm{sr}^{-1}\mathrm{GeV}^{-1}$) at 11 - 16 g/cm^2. T (in GeV) define the kinetic energy bins. $N_{\overline{p}}$ is the number of observed antiprotons.

T (GeV)	$N_{\overline{p}}$	N_{BG}	$\overline{p}$ flux	Statical Err.	Systematic Err.
0.20 - 0.41	000	$0.00^{+0.00}_{-0.00}$	U.L. 0.64 (68.27% C.L),		1.53 (95% C.L.)
0.41 - 0.82	002	$0.00^{+0.00}_{-0.00}$	0.42	$^{+0.47}_{-0.26}$	$^{+0.01}_{-0.01}$
0.82 - 1.67	012	$0.02^{+0.00}_{-0.00}$	1.27	$^{+0.46}_{-0.34}$	$^{+0.05}_{-0.05}$
1.67 - 3.40	021	$1.06^{+0.17}_{-0.17}$	1.36	$^{+0.30}_{-0.30}$	$^{+0.06}_{-0.06}$

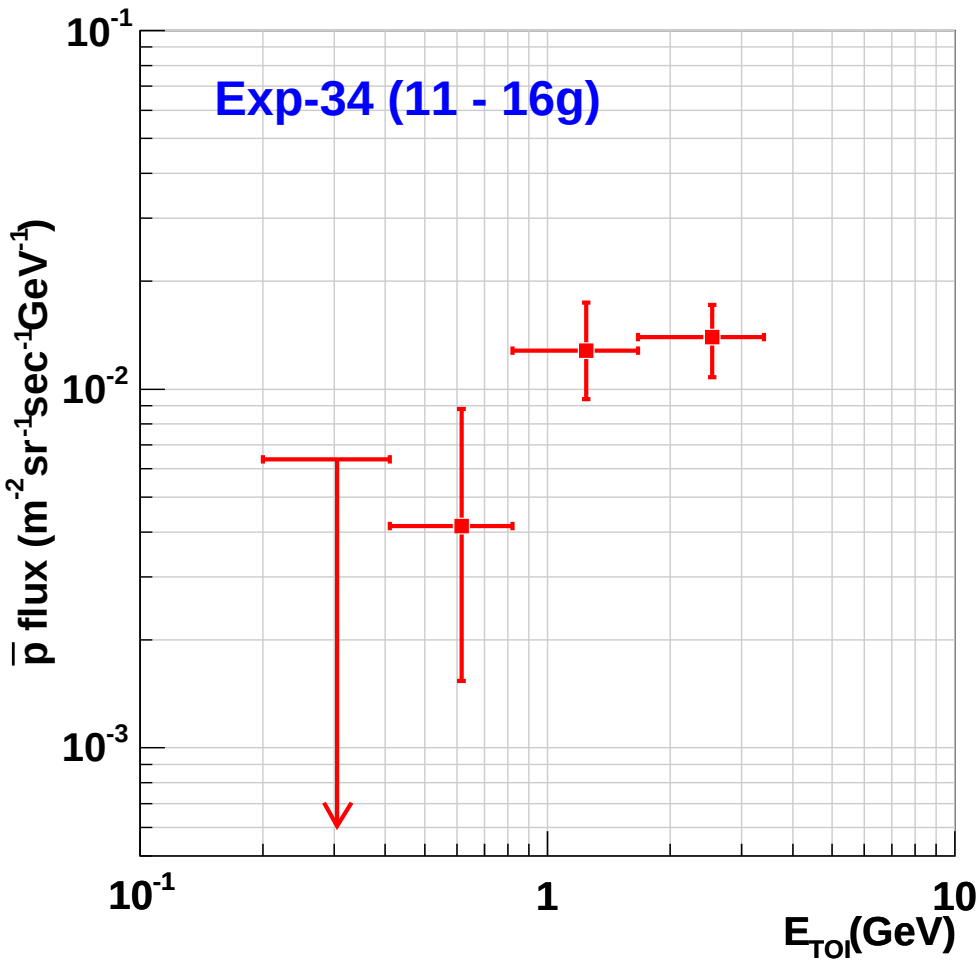

Figure 5.41: Combined $\overline{p}$ at atmospheric range of 11 to 16 g/cm^2

Table 5.6: Antiproton flux (in $\times 10^{-4}\mathrm{m}^{-2}\mathrm{s}^{-1}\mathrm{sr}^{-1}\mathrm{GeV}^{-1}$) at 16 - 26 g/cm^2. T (in GeV) define the kinetic energy bins. $N_{\overline{p}}$ is the number of observed antiprotons.

T (GeV)	$N_{\overline{p}}$	N_{BG}	$\overline{p}$ flux	Statical Err.	Systematic Err.
0.20 - 0.41	001	$0.00^{+0.00}_{-0.00}$	0.63	$^{+1.11}_{-0.40}$	$^{+0.02}_{-0.02}$
0.41 - 0.82	006	$0.00^{+0.00}_{-0.00}$	1.60	$^{+0.87}_{-0.58}$	$^{+0.03}_{-0.03}$
0.82 - 1.67	018	$0.02^{+0.00}_{-0.00}$	2.45	$^{+0.66}_{-0.57}$	$^{+0.09}_{-0.09}$
1.67 - 3.40	024	$1.07^{+0.17}_{-0.17}$	2.01	$^{+0.42}_{-0.42}$	$^{+0.09}_{-0.09}$

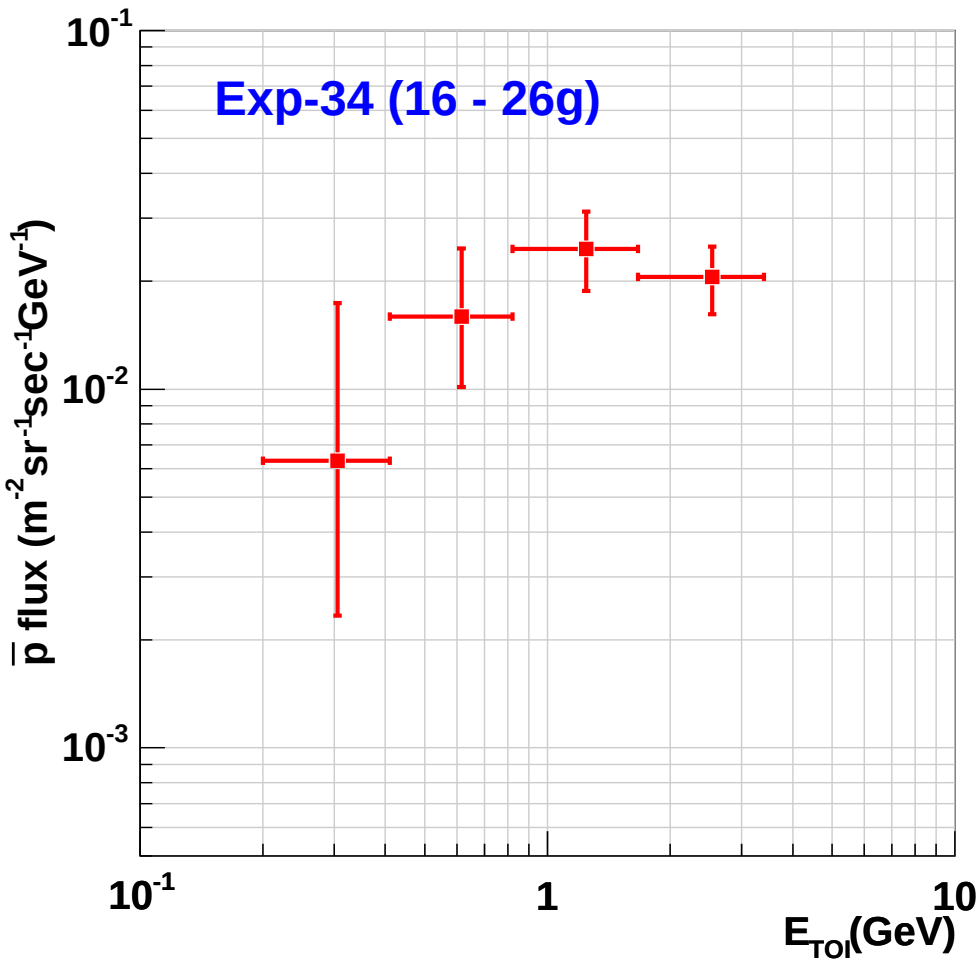

Figure 5.42: Combined $\overline{p}$ at atmospheric range of 16-26 g/cm^2

Chapter 6

Discussions

6.1 Transport of the Antiprotons inside the atmosphere

6.1.1 Transport equation

There have been reported some theoretical calculations for the atmospheric antiproton flux. The results are usually shown for the balloon altitude or at some fixed atmospheric depth. Our observation was carried out during the slow descending phase of the balloon and the altitude is lower than the typical balloon level altitude, and we can not compare the flux of antiproton with such calculations directly. Since we have been interested in the contribution of the process such as production, attenuation, tertiary production etc., we calculated the atmospheric antiproton flux incorporating to the models published so far.

A basic method of the calculation is to solve the Eq. (6.1) given by Stephens [16]. This transport equation is one-dimensional and it may be inaccurate compared with three-dimensional approach, but we can see the contribution of each process clearly. The equation is given by

$$\begin{aligned}\frac{\partial J_{\overline{p}}(E,x)}{\partial x} &= \sum_A Q_A(E_A,x,E) + \frac{\partial}{\partial E}\left[J_{\overline{p}}(E,x)\left\langle\frac{\mathrm{d}E}{\mathrm{d}x}\right\rangle\right] \\ &\quad - \frac{J_{\overline{p}}(E,x)}{\Lambda(E)} + \int_E^\infty \Phi(E')\left[\frac{J_{\overline{p}}(E',x)}{\lambda^{in}}(1-\alpha) + \frac{J_{\overline{n}}(E',x)}{\lambda^{in}}\,\alpha\right]\mathrm{d}E' \,,\end{aligned} \tag{6.1}$$

where $J_{\overline{p}}(E,x)$ is the differential antiproton flux at the atmospheric depth x g/cm^2. The first term of R.H.S. is an antiproton production term. Index A indicates the kind of incident particles (i.e. Proton, Neutron, Helium). $Q_A(E_A,x,E)$ is the production rate of antiproton with an energy E by an incident particle A of energy E_A. As the flux of incident particles depend on the atmospheric depth x, $Q_A(E_A,x,E)$ is also a function of x.

The second term represents the ionization energy loss. $\left\langle\frac{\mathrm{d}E}{\mathrm{d}x}\right\rangle$ is the mean of an ionization energy loss per g/cm^2 of antiproton with energy E.

Table 6.1: The definition of the calculation models.

Model	Production	Interaction	Tertiary	Comments
I	Stephens	Stephens	Stephens	Nearly Stephens' original
II	Stephens	Stephens	No	Stephens w/o Tertiary
III	Stephens	Huang	No	Huang w/ Stephens' production
IV	Huang	Stephens	Stephens	Stephens w/ Huang' production
V	Huang	Huang	No	Nearly Huang' original

The third term is the loss due to nuclear interaction including annihilation. $\Lambda(E)$ is the total inelastic interaction mean free path (mfp) of antiprotons passing through the atmosphere.
The fourth integral term represents the contribution of tertiary antiproton production by the inelastic interaction. $\Phi(E)$ is the energy distribution of the emitted antiproton after the inelastic interaction. λ^{in} is the inelastic interaction mfp not including the annihilation process. α is the charge exchange probability, which is taken to be 1/3. $J_{\overline{n}}(E', x)$ is the antineutron flux.
Other parameters and more detailed explanation are explained in the section 6.2. The transport equation of the antineutron flux $J_{\overline{n}}(E, x)$ can be written in a similar way to Eq. (6.1) as described in Appendix A. The the input flux of incoming cosmic rays (proton, neutron, and helium) used in this calculation are also shown in Appendix A.

6.1.2 A method to solve the equation

We compare the observed atmospheric antiproton flux with the solution of Eq. (6.1). Since the purpose of this comparision is to see the contribution of each process how the results well reproduce the observed antiproton flux, we then examine the solution of the equation with the different combinations of processes as shown in Table 6.1.
The equation was solved by taking 4th ordered Runge-Kutta method. In this process, we took each step of thickness as $\partial x = 0.01$. Energies are represented by 128 discrete points between 0.05 to 500 GeV dividing almost equally in logarithmic scale. The flux at lower and higher energy range (i.e. $E < 0.05$ GeV and $E > 500$ GeV) is set to zero.
The procedures of calculation are following: (i) Helium flux at any atmospheric depth is calculated by using the TOA flux of helium. (ii) Proton and neutron flux at any atmospheric depth are calculated by using TOA flux of proton and helium flux. These two transport equations are described in Appendix A. (iii) Then, using these proton, neutron, helium flux, antiproton and antineutron flux are calculated simultaneously, because Eq. (6.1) and (A.1) are coupled with each other.

6.2 Review of the various models

In this section, we mainly discuss on the model of Stephens [16, 21, 67] and Huang [25, 26], because only their calculations cover the flux at all atmospheric depth from balloon altitude to ground altitude.

6.2.1 Antiproton Production

Here we introduce two production cross sections adopted by Stephens and Huang. Each cross section is plotted in the Figure 6.1

Production cross-section used by Stephens [16]

The basic concept of Stephens is to scale the cross section of proton-proton to proton-Air nuclei in introducing the effect of Fermi momentum of the target nucleon as follows.

$$Q_A(E) = k \int_{E_{th}}^{\infty} \int_0^{P_F} \int_{-1}^{+1} \int_0^{2\pi} \int_0^{\theta_{max}} P^2 p_T \left(E \frac{\mathrm{d}^3\sigma}{\mathrm{d}p^3} \right) J_A(E_A, x, \theta)\, \mathrm{d}\theta\, \mathrm{d}\phi\, \mathrm{d}(\cos\alpha)\, \mathrm{d}P\, \mathrm{d}E_A \ , \tag{6.2}$$

$$\left(E \frac{\mathrm{d}^3\sigma}{\mathrm{d}p^3} \right) = \frac{A}{f(E_A)} \exp[-B(1 + 7/E_A)^{0.7} p_T](1 - \tilde{x})^q \ , \tag{6.3}$$

$$k = \frac{3\lambda_{\mathrm{p+P}}}{2m_p \lambda_{\mathrm{p+Air}} P_F^3} \ , \qquad P_F = \frac{h}{4r_0} \left(\frac{3}{\pi} \right)^{2/3} \sim 0.25 \ \ (\mathrm{GeV}) \ ,$$

$$\tilde{x} = \sqrt{x^{*2} + m_p^2 + p_T^2} \ , \qquad q = \frac{(C_1 - C_2\, p_T + C_3\, p_T^2)}{(1 + 12/E_A)} \ ,$$

$$f(E_A) = [1 + 5 \times 10^4 \exp(-0.8 E_A)](1 + 7/E_A)^{4.5} \ ,$$

First integral is carried out with respect to E_A that is the energy of an incident particle. Second and third integral is concerned with Fermi momentum of nucleon inside the nuclei. Fourth and fifth integral cover the all emission direction of the generated antiproton.
Here, E_{th} is a threshold energy of the antiproton production. θ_{max} is a maximum emission angle toward incident direction, which is $\tan^{-1}(p^*_{max}/p)$. p^*_{max} is the maximum momentum of the produced antiproton in the CMS. p is the momentum in the Lab. system at the emission angle θ. P is the Fermi momentum of the target nucleon. $p_T = p \sin\theta$. Eq. (6.3) is the invariant cross section. $J_A(E', x, \theta)$ is the flux of incident particle A at the atmospheric depth x g/cm^2. $\cos\alpha$ is a angle between the momentum of incident particle and the momentum of target nucleon. x^* is Feynman variable defined by p^*/p^*_{max}. The remaining parameters are $A = 3.5$, $B = 3.1$, $C_1 = 8.5$, $C_2 = 1.4$, $C_3 = 0.7$.

Table 6.2: Value of the parameter in the Eq. (6.4) and (6.5)

Parameter	C_1	C_2	C_3	C_4	C_5	C_6	μ	b_0	α
Value	0.042	5.92	0.96	2.19	84.3	10.5	1.1	0.12	2.24

Production cross-section used by Huang [26]

Huang developed a newly invariant cross section based on the Kalinovskiĭ, Mokhov and Nikitin (KMN) parametrization, which is

$$\left(E\frac{\mathrm{d}^3\sigma}{\mathrm{d}p^3}\right) = C_1 A^{b_0\cdot P_T}(1-x)^{C_2}\exp(-C_3 x)\,\Phi(p_T)\ , \tag{6.4}$$

$$\Phi(p_T) = \exp(-C_4\,p_T^2) + C_5\frac{\exp(-C_6 x_T)}{(p_T^2+\mu^2)^4}\exp(-\alpha\sqrt{s})\ , \tag{6.5}$$

where $x = E^*/E^*_{max}$ is the scaling variable, in which, E^* and E^*_{max} are the total energy of the inclusive particle and its maximum possible energy in the CMS. p_T is the transverse momentum of the inclusive particle. $x_T = 2p_T/\sqrt{s}$ is the transverse variable. The fitted parameters are summarized in Table 6.2.
In the Huang's original method [25], the antiprotons flux were calculated in his simulation program by tracing the incident particles with his cross section. While we define the Huang like production as Eq. (6.6) to compare with Stephens like production Eq. (6.2) and (6.3) through the transport equation Eq. (6.1).

$$Q_A(E) = \sigma_R\int_{E_{th}}^{\infty}\int_0^{2\pi}\int_0^{\theta_{max}} p_T\left(E\frac{\mathrm{d}^3\sigma}{\mathrm{d}p^3}\right)\,J_A(E_A,x,\phi)\,\mathrm{d}\theta\,\mathrm{d}\phi\,\mathrm{d}E_A\ , \tag{6.6}$$

$$\sigma_R = \sigma_0[1-0.62\exp(-E_A/200)\sin(10.9E_A^{-0.28})]\quad(\mathrm{mb})\ , \tag{6.7}$$

$$\sigma_0 = 45A^{0.7}[1+0.016\sin(5.3-2.63\ln A)]\ , \tag{6.8}$$

where σ_R (σ_0) represents the total $p+A$ ($p+p$) reaction cross section. Since air is the mixture of Nitrogen and Oxygen, we treat the production cross section for air as:

$$Q_{\mathrm{Air}}(E) = r_N\,Q_N(E) + r_O\,Q_O(E) \tag{6.9}$$

$$r_N = 0.785,\quad r_O = 0.215 \tag{6.10}$$

6.2.2 Ionization energy loss term

We used the Bethe-Block formula for the ionization energy loss, and give

$$-\frac{\mathrm{d}E}{\mathrm{d}x} = Dz^2\frac{Z}{A}\frac{1}{\beta^2}\left[\ln\left(\frac{2m_e\gamma^2\beta^2}{I}\right)-\beta^2\right]\ , \tag{6.11}$$

where

$$D = 4\pi N_A r_e^2 m_e^2 = 0.3071\quad(\mathrm{MeV\ cm^2/g}) \tag{6.12}$$

$$I \sim 16\,Z^{0.9}\quad(\mathrm{eV}) \tag{6.13}$$

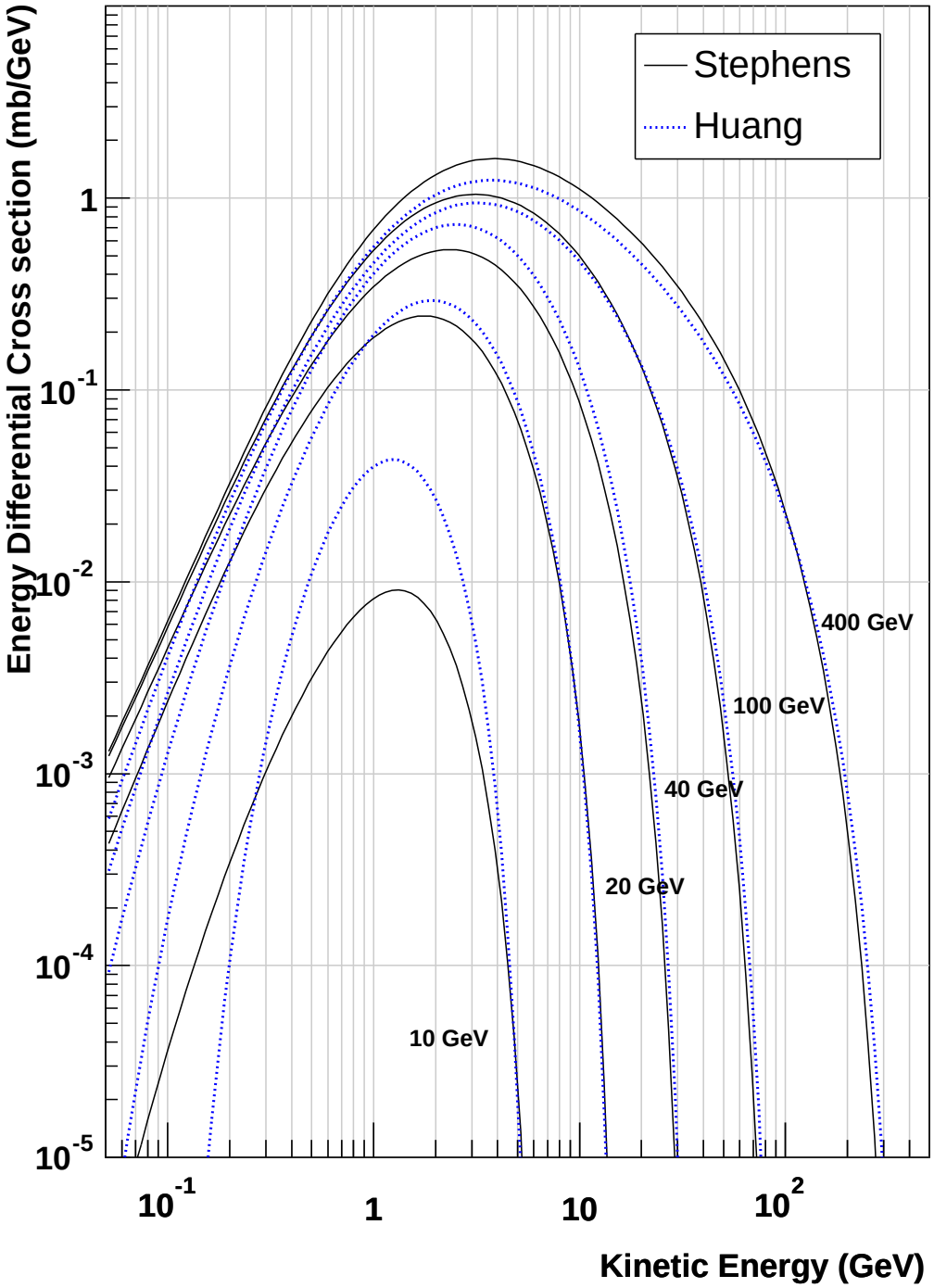

Figure 6.1: Differential cross section for production of antiprotons in the interactions of p + Air. This is defined by $\int\int p_T \left(E\frac{\mathrm{d}^3\sigma}{\mathrm{d}p^3}\right) \mathrm{d}\theta\, \mathrm{d}\phi$. x axis is the energy of generated antiproton. The printed energy in the figure represent the energy of an incident proton. Production cross section used by Huang is large where energy of incident protons ¡ ∼100 GeV s A condition that incident energy is below 100 GeV. However, cross section used by Stephens became large below a few hundred MeV. This is caused by the inclusion of Fermi momentum of target nucleons in his treatment.

6.2.3 Interaction loss

A precise estimate of interaction mfp of $\overline{p}$+Air is difficult, because it has not been measured directly by accelerator. Results of the following two estimations made by Stephens and Huang are quite different as shown in Figure 6.2.

Total inelastic mfp used in Stephens' model

Stephens takes the sum of the inelastic cross section of protons and the annihilation cross section as the total inelastic interaction cross section of antiprotons. He uses following relations

$$\Lambda = \left(\frac{1}{\lambda^{in}_{\mathrm{p+Air}}} + \frac{1}{\lambda^{ann}} \right)^{-1} \quad (\mathrm{g/cm^2}) \ , \tag{6.14}$$

$$\lambda^{in}_{\mathrm{p+Air}} = \frac{83.0\,[1.0 + 97.0\exp(-7.8E)]}{1.0 + 0.0273\,\omega + 0.01\omega^2\,\Theta(\omega)} \qquad \text{for } E > 0.7 \text{ GeV} \ , \tag{6.15}$$

$$= 4.39\,(E^{-4.8} + 21.0E^{-0.6}) \qquad \text{for } E \leq 0.7 \text{ GeV} \ , \tag{6.16}$$

$$\lambda^{ann} = \frac{70.5}{E^{-0.43} - 0.0476} \ , \tag{6.17}$$

where $\lambda^{in}_{\mathrm{p+Air}}$ is the interaction length of proton in the air. λ^{ann} is the annihilation interaction length of antiprotons in the air. $\omega = \ln(E/200.0)$ and $\Theta(\omega) = 1.0$ for $E > 200$ GeV or 0.0 for $E \leq 200$ GeV [68].

Total inelastic interaction mfp used in Huang's model

Huang newly parametrized the total inelastic cross section of antiprotons with atmospheric nuclei by using the accerelator data of $\overline{p} + \mathrm{C}$ collisions, and introduced a relation for $\overline{p}$+Air as

$$[\sigma_{\overline{p}+A}(E_{\overline{p}})]^{total}_{in} \approx 1000 \left(\frac{A}{46} \right)^{0.67} \left(0.68 + \frac{0.228}{p} \right) \quad (\mathrm{mb}) \ , \tag{6.18}$$

where p is the $\overline{p}$ incident momentum. A is a target mass number. This formula a gives better agreement with $\overline{p} + \mathrm{C}$ experiment data rather than the simple $A^{2/3}$ scaling. Thus we obtained a following total inelastic interaction mfp.

$$\Lambda = r_N \frac{M_N}{[\sigma_{\overline{p}+N}]^{total}_{in}} + r_O \frac{M_O}{[\sigma_{\overline{p}+O}]^{total}_{in}} \quad (\mathrm{g/cm^2}) \ , \tag{6.19}$$

where r_N and r_O are the fraction of Nitrogen and Oxygen of the air as given in Eq. (6.10). M_N and M_O are mass of Nitrogen and Oxygen in grams.

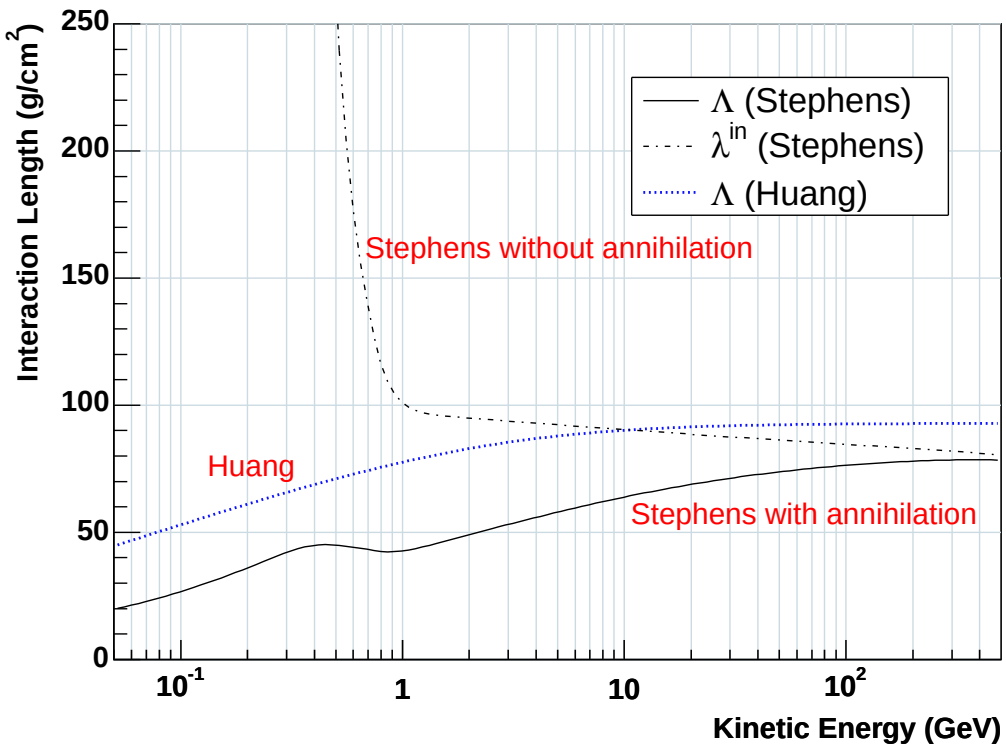

Figure 6.2: The interaction mean free path. The black (blue) solid line represents the Stephens (Huang) like total inelastic interaction length. The dot-dashed line represents the inelastic interaction length without annihilation which is identical to protons.

6.2.4 Tertiary production

In the tertiary production term (fourth term of Eq. (6.1)), λ^{in} is the interaction length which does not include annihilation, assuming that antiprotons behave as protons. λ^{in} is shown in Figure 6.2 together with the total interaction length. $\Phi(E)$ is the normalized inelasticity distribution, which is assumed to be constant in Stephens treatement.

6.3 Zenith angle dependence of the flux

Eq. (6.1) treats the vertically down-going flux. Since the acceptable zenith angle range of the BESS detector is about $0.8 \lesssim \cos\theta \leq 1$, our results shown in Chapter 5 includes particles with large zenith angle. Thus, we investigate the zenith angle dependence at small atmospheric depth by using the 3-dimensional Monte Carlo simulation.
Here, we use the Geant4 tool kit [69] as a Monte Carlo tool. Since antiproton production process is dominant at small atmospheric depth, the angular distribution of generated antiprotons is important. In this simulation, we use 'G4HEProtonInerastic' class as an antiproton generator. Figures 6.3-6.5 shows the production angle distribution of three models implemented in this simulation code. The three distributions are

generally consistent with each other at any combinations of incident and production energy. Therefore, we have a reason that zenith angle distribution of Monte Carlo simulation should indicate a similar tendency to the case of cross sections used Stephens and Huang.
Figure 6.6 shows the zenith angle distribution obtained by the Monte Carlo simulation. In this simulation, we assume only protons as the incident particles. We also assumed the energy spectrum reported by AMS and BESS-98 for the incident protons at the top of atmosphere [19, 20]. Cosmic-ray flux of alpha particles and other heavy components is set to zero.
We show the antiproton flux expected by the Monte Carlo simulation by black points at the atmospheric depth of 5 g/cm^2 in the simulator. We can see clearly that antiproton flux increase as with increasing the incident angle of θ. The blue points represent the $N_{\rm MC} \times \cos\theta$. This distribution is almost flat. That is, $J(\theta) \approx J(0)/\cos\theta$. Atmospheric antiproton flux should be proportional to the atmospheric depth at small depth (i.e. $J(kx) \approx k\,J(x)$). If the angular spread of secondary particles are small, and the following formula is a good approximation at small atmospheric depth.

$$J(x,\theta) \sim J_{\rm v}(x/\cos\theta)\ , \tag{6.20}$$

where, $J_{\rm v}$ is the vertically down-going flux, that is $J(\theta = 0)$.
We can understand this fact as follows. Since high energy incident particle is needed to create antiprotons, a Lorentz factor γ has large value of more than 10 in the most cases. Since angular spread of produced antiprotons is suppressed by Lorentz boost, passed length in the air is almost $x/\cos\theta$ at depth x g/cm^2,

6.4 Comparison with the calculated results

In order to observe antiproton events as much as possible, we used the almost full acceptance angle of the detector in the analysis. For these analysis, we need to consider the following points. One is that the geometrical acceptance of the BESS detector depend on the zenith angle, and the flux of atmospheric antiprotons also has the zenith angle dependence. $J_{\overline{p}}(E,x)$ in Eq. (6.1) represents vertical flux at atmospheric depth x g/cm^2. For the comparison with the observed data with calculated flux, we include the zenith angle dependence of the detector and the flux. We also take into consideration of the effective observation time at each different residual atmospheric depth. The weighted averaged flux observed during the depth x_1 and x_2 are calculated by Eq. (6.21), and we simply call this flux as averaged flux.

$$J^*_{x_1-x_2}(E) = \frac{1}{S\Omega(E)\,T_{x_1-x_2}} \int_0^{+1} \int_{x_1}^{x_2} J_{\overline{p}}(E, x/\cos\theta)\,\Delta S\Omega(E,\cos\theta)\,\Delta T(x)\ {\rm d}x\,{\rm d}(\cos\theta)\ , \tag{6.21}$$

where $S\Omega(E)$ is the geometrical acceptance used in the analysis and shown in Figure 5.2. $\Delta S\Omega(E,\cos\theta)$ is the partial acceptance at $\cos\theta$ and it is shown in Figure 6.7. $\Delta T(x)$ is the relation between live time and the atmospheric depth shown in Figure 5.3.

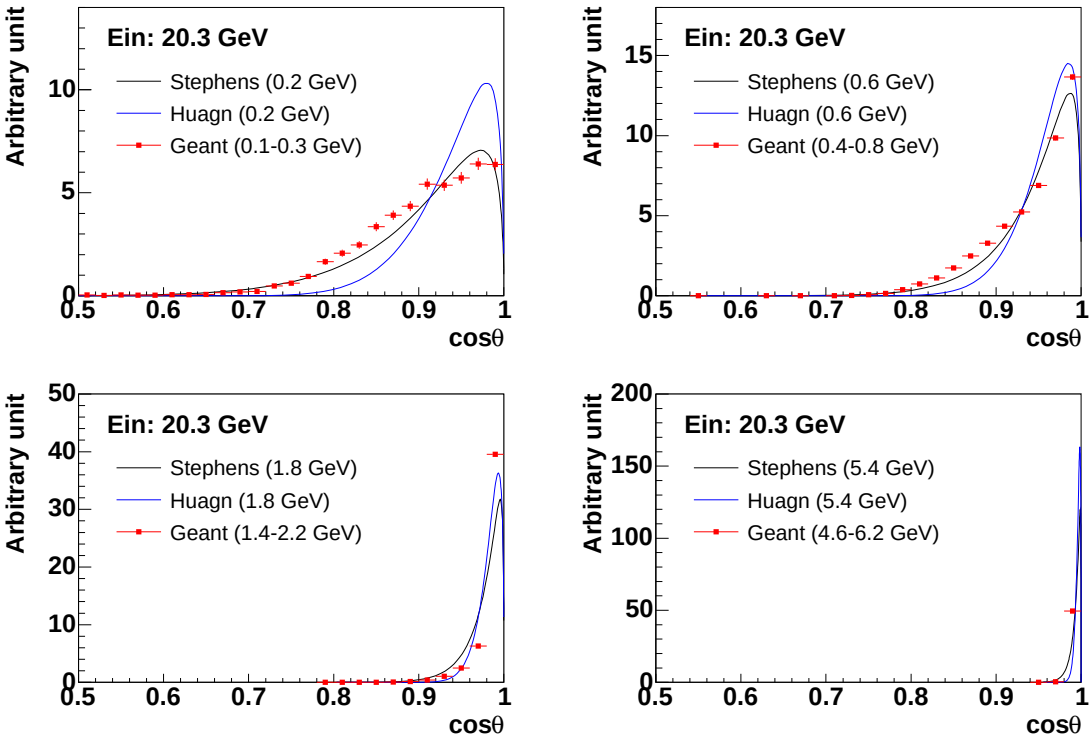

Figure 6.3: Production angle distribution (I). $E_{\rm in} = 20.3$ GeV

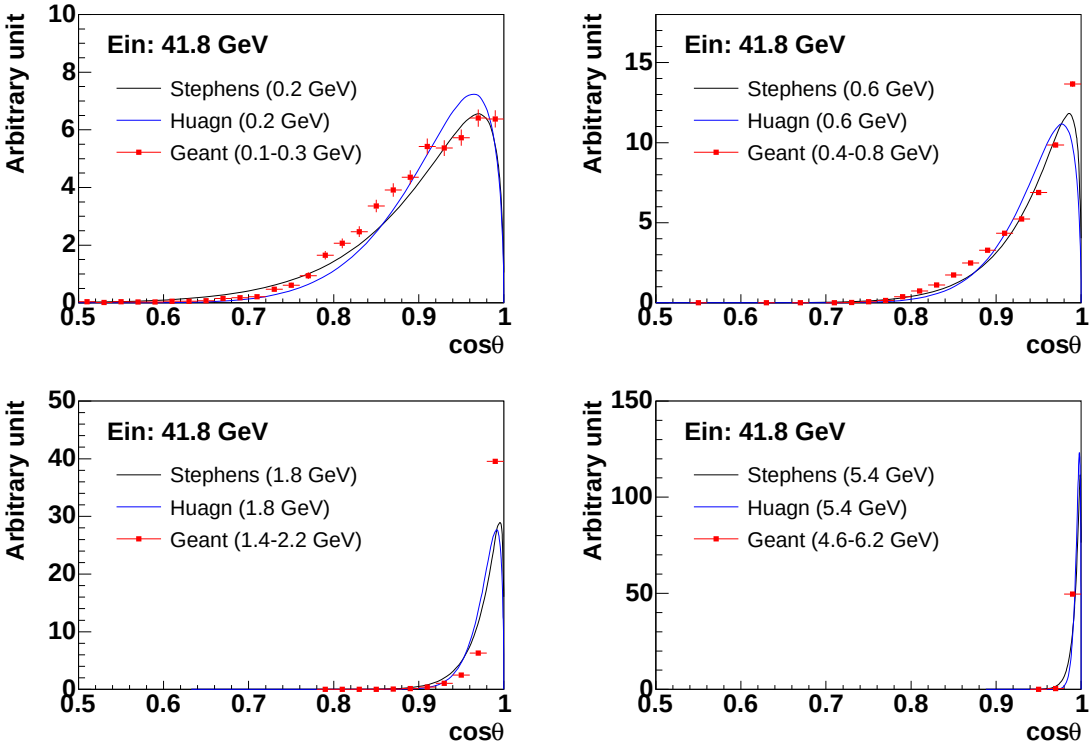

Figure 6.4: Production angle distribution (II). $E_{\rm in} = 41.8$ GeV

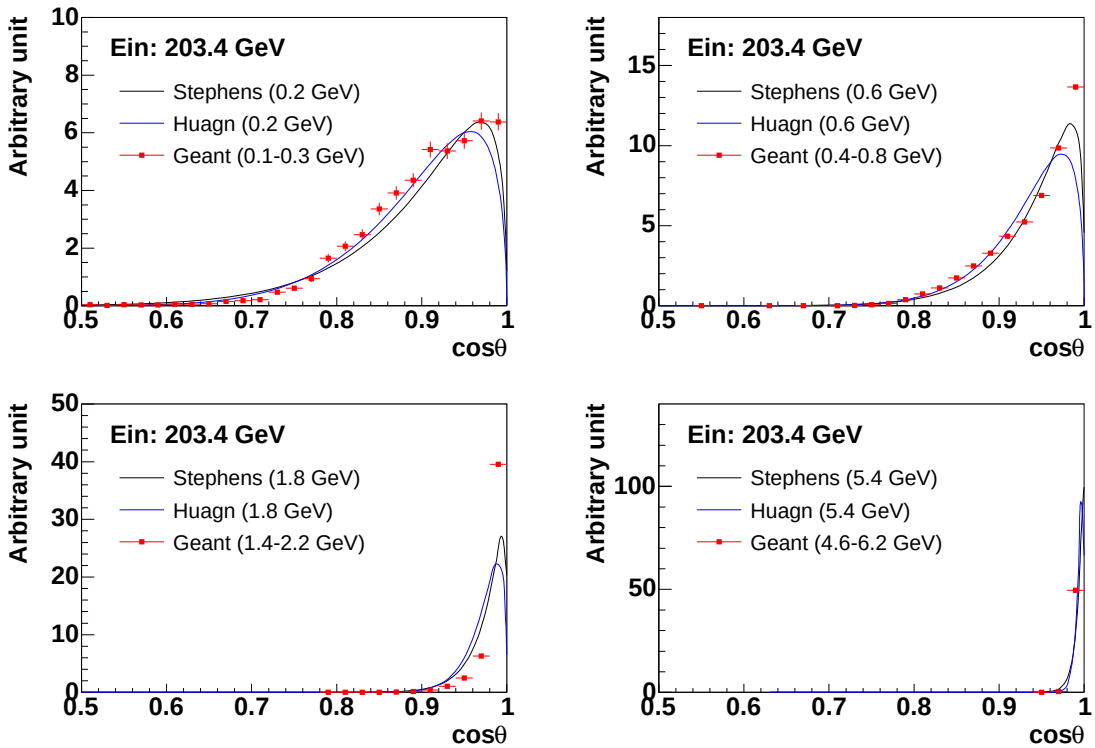

Figure 6.5: Production angle distribution (III). $E_{\rm in} = 203.4$ GeV

$T_{x_1-x_2}$ is defined by $\int_{x_1}^{x_2} \Delta T(x)\, dx$. While rationality of approximation $J(E, x, \cos\theta) \sim Jv(E, x/\cos\theta)$ is shown in Eq. (6.20).
The difference between two production models given by Stephens and Huang in the Table 6.1 is that the cross section used by Huang is a little larger as shown in Figure 6.1. Since the cross section used by Stephens take into account the Fermi motion of the nucleon inside the atmospheric nuclei, the expected flux of antiproton below 0.2 GeV is a little higher.
For the total inelastic interaction length, used by Stephens is shorter than that used by Huang as shown in Figure 6.2. Since this difference is not small, the results at large atmospheric depth will be different significantly. In the definition of the tertiary production in Eq. (6.1), Stephens assumed that an energy distribution of emitted antiprotons is flat after inelastic interaction at the parent proton with energy E (GeV). We call this treatment a Box Approximation for convenience. This distribution gives relatively large flux of low energy antiprotons below 1 GeV.

6.4.1 Antiproton flux at the small atmospheric depth

Figure 6.9 shows the calculated atmospheric antiproton flux at 5, 15, 45 g/cm^2. In the figure, the different color represent a Model defined in Table 6.1, and the line style

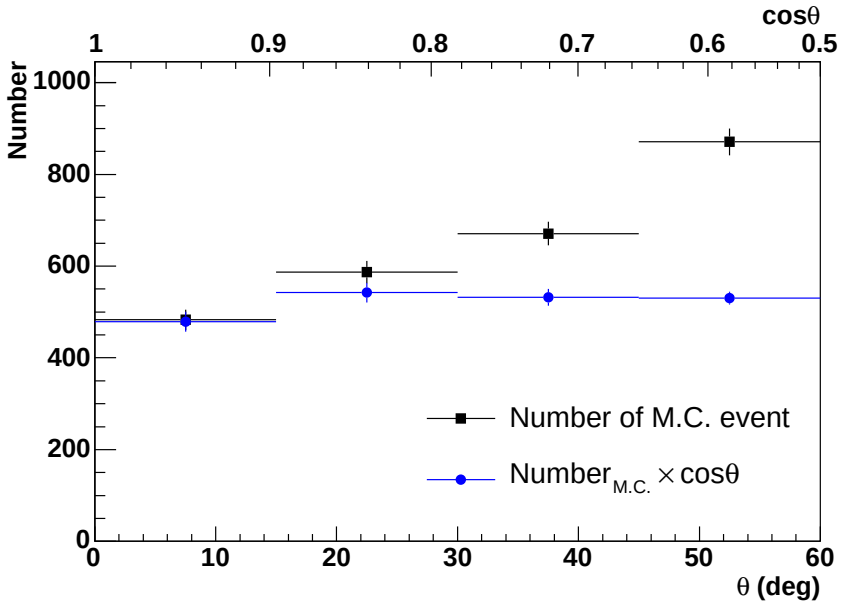

Figure 6.6: Zenith angle distribution of atmospheric antiprotons at 5 g/cm^2 by 3-dimensional Monte Carlo approach.

represent the atmospheric depth. Note that this results is the vertical down-going flux. In this calculation, we take into account the primary Galactic antiproton flux above the cut off rigidity, because the antiproton flux at hhigher energy region has a large contribution to the tertiary antiproton flux. Here, we use flux calculated by Mitsui ($\Phi = 1000$ MV) [15] for Galactic antiproton. In the figure, the flux has very sharp break around the cut off rigidity. This is mainly caused by following two reasons. One is that we do not consider the particles with large zenith angle which can enter the earth with energy below the vertical cut off energy. The other is that we take a little wide energy band to compute faster. Because of this reason, the figure can not display a smooth curvature around the cut off energy due to ionization energy loss, even at the place of deep atmospheric depth. However, the flux error arising from these approximations is estimated smaller than 10^{-4} (m^{-2} sr^{-1} s^{-1} GeV^{-1}) at 10 g/cm^2.
The calculated results of Model IV and V are based on the cross section fitted by Huang [26]. However, we made numerical calculations in a quite different way from his treatment. His original intension and procedure is to solve the three-dimensional equation of motion in the Earth's magnetic field. Therefore, there is no guarantee that our results agree with those he reported. In fact, at the peak of the flux, the results of Huang's original work [26] is about 10 % higher than that we calculated for Model V which assumed the same elementary processes except we made one dimensional calculation at 5 g/cm^2 with assumption of $J(x, \cos\theta) \sim Jv(x/\cos\theta)$.
Figure 6.10 shows the averaged flux by using overall observed data of 4-26 g/cm^2, and Figures 6.11-6.14 show the averaged flux at 4-6.5, 6.5-11, 11-16, 16-26 g/cm^2 respectively.

At small atmospheric depth, the contribution of the antiproton production term is the most dominant term, because the contribution by other process to the atmospheric antiprotons are small, as the intensity of antiproton is not yet high. Therefore, we can concentrate the comparison with the production term and the cross-section model.
The overall absolute value and the shape of the calculated flux is basically agree with the observed flux. In particular, around the flux peak ($1 \sim 3$GeV), the observed flux by using overall atmospheric depth (i.e. Figure 6.10) agree well with results obtained by Model I, II, and III based on the production term of Eq. (6.2). The Model IV and V based on the production term of Eq. (6.6) give a little higher flux. Since Huang's original result is higher than our calculation at small atmospheric depth, the cross-section Eq. (6.4) may be a little bit larger around 2 GeV.
In the low energy region below 1 GeV, the results can be classified into two groups. One is Model I and IV which include the tertiary antiproton production. The other is Model II, III, and V which do not include it. The calculated results shows the difference of the two group clearly as seen in Figure 6.10. The observed flux agree well without tertiary production model.

6.4.2 Antiproton flux at the large atmospheric depth

Since we carried out the observation on the ground, the flux was calculated using the Eq. (6.1) down to the depth of the ground level. In this calculation, we take into account the cut off rigidity for proton and Helium spectra at the top of the atmosphere. Because the threshold of antiproton production is about 5 GeV in kinetic energy with Fermi momentum of a target nucleon, the input flux below the cut off rigidity should be treated appropriately, since the cut off of Mt. Norikura and KEK (Tsukuba) is about 11 GV. Figures 6.15 and 6.16 show the effect of the cut off for the spectrum calculated for proton, neutron, and helium with various altitudes. This flux is calculated using Eq. (A.2) - (A.4). In this calculation, AMS, BESS-98 results were used as primary proton, and helium fluxes, and we set primary flux to zero below 11 GV at TOA.
Figure 6.17 shows observed results and the calculated averaged flux with the input flux in Figures 6.15 and 6.16. The Model I, III, V give almost the same flux around 2 GeV. However, Model I gives quite higher than Model III, V at low energy around a few hundred MeV. This is because of an existence of tertiary production cross section assumed by Stephens. The tertiary antiprotons based on Box Approximation have a broad energy spectrum, in contrast to the production spectrum by the collision of high energy cosmic rays and the air nuclei. The shape of observed flux is similar to the results of Model III and V. Therefore this indicates that the tertiary production should be small in the corresponding energy region, in order to make good agreement with observed data at low energy region.
The production cross section used by Stephens is smaller than that of Huang, and the total inelastic interaction cross section of the model II is the same as assumed by Stephens in Eq. (6.14), which is smaller than that assumed by Huang shown in Figure 6.2. In addition, Model II has no tertiary process. Therefore, the absolute value of Model II became quite lower than the observed flux, and this combination of process is

rejected.
The calculated result of Model IV is very higher compared with the observed flux in contrast. The Model IV takes in a combination which produce maximum value, and this model is also rejected.
Figure 6.18 shows calculated vertical flux and the ground data. In addition, the observed flux at the Mt. Norikura (2770m, 742 g/cm^2) by the BESS detector in 1999 is also illustrated. These two data were observed by almost the same detector configuration, and analysis tools and the procedure are performed in a similar way.
In both figures, The Model III and V have similar shape, but the absolute value around the peak flux is a little different. This is due to the difference of production model. As shown in Figure 6.1, production model used by Huang is greater and gives higher flux below the incident energy of 100 GeV. This difference of the production model is clear at this altitude.
The agreement of the absolute value between the calculated vertical flux and the observed flux on the ground is better than the averaged flux shown in Figure 6.17. If we apply the effect of the zenith angle distribution in the same way as Eq. (6.21) to the vertical flux at the mountain altitude, the averaged flux will be $1/1.5 \sim 1/2$ times smaller compared with the vertical flux. Hence we think that the approximation $J(x, \cos\theta) \sim Jv(x/\cos\theta)$ in Eq. (6.21) is not good in the large atmospheric depth. Perhaps, the zenith angle dependence is smeared and become less steep at the large atmospheric depth.
For the spectral shape, Model III and V also agree with the observed flux at the mountain altitude. Our conclusion obtained by the observed data at ground altitude that the contribution of the tertiary production is small is also consistent in the mountain altitude.

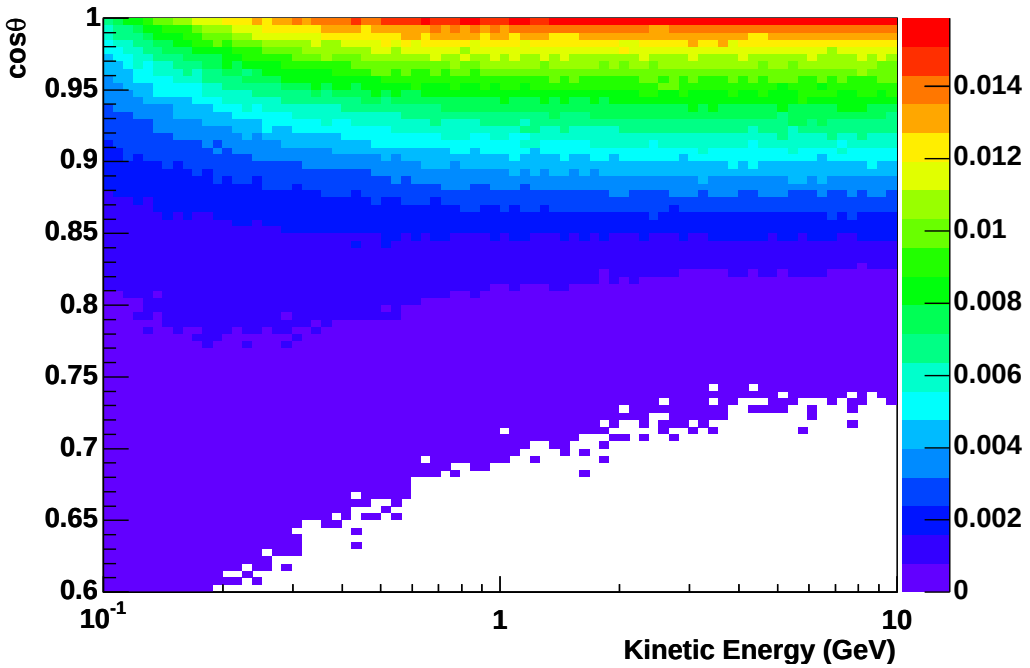

Figure 6.7: $\Delta S\Omega(E, \cos\theta)\,\mathrm{d}(\cos\theta)$ in Exp-34, The colors represent the values of $\Delta S\Omega\, d(\cos\theta)$ at the point. In this plots, $\mathrm{d}(\cos\theta) = 0.005$. No sensitivity in the white region.

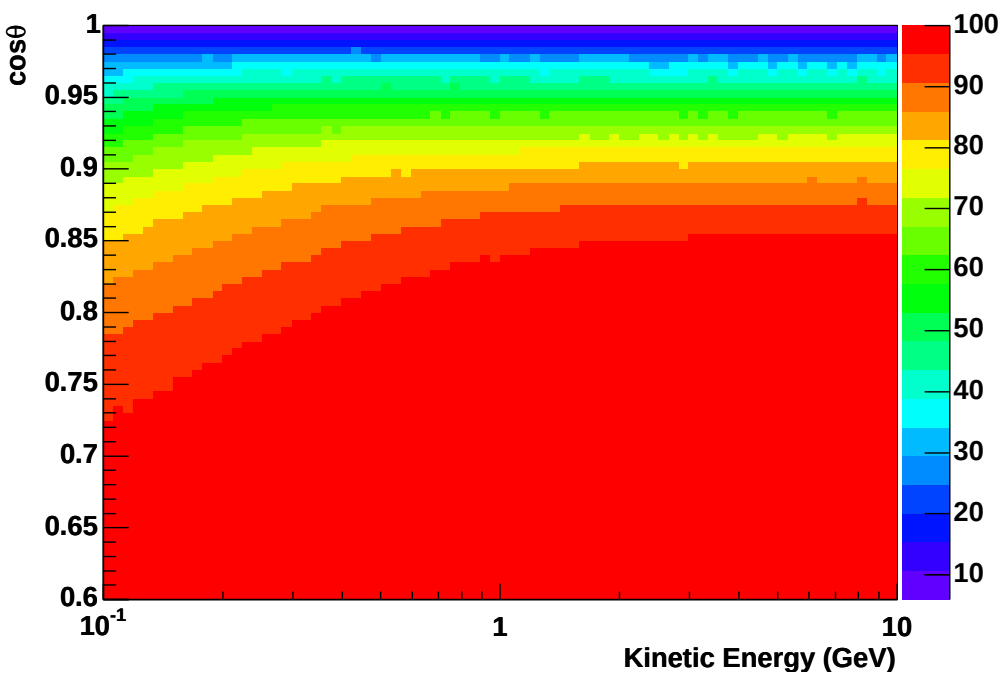

Figure 6.8: A percentage of the coverage as function of E and $\cos\theta$. This is defined by $\int_{\cos\theta}^{+1} \Delta S\Omega(E, \cos\theta')\,\mathrm{d}(\cos\theta')$. Colors represent percentage of coverage from $\cos\theta = 1$ to the point. We can see that an almost acceptable region is locating in $\cos\theta > 0.85$ in Exp-34.

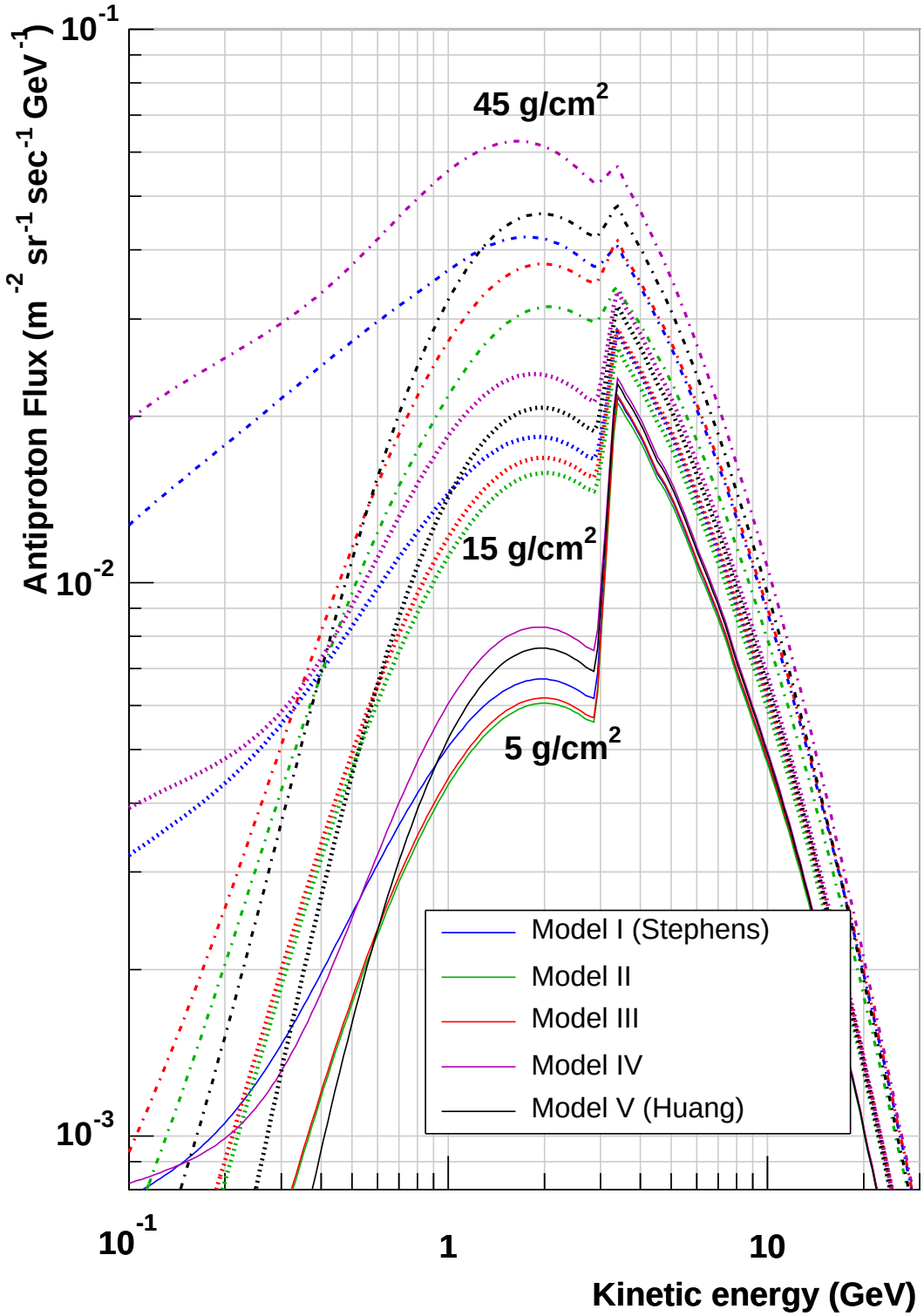

Figure 6.9: Calculated vertical atmospheric antiproton flux at small atmospheric depth. In this calculation, we take into account of the primary antiprotons above cutoff rigidity. The curves indicate the calculated flux at 5, 15, 45 g/cm^2. The solid lines represent the flux at 5 g/cm^2. The dot lines represent the flux at 15 g/cm^2 and the dot-dash lines represent the flux at 45 g/cm^2. The details of each 'Model's are summarized in Table 6.1.

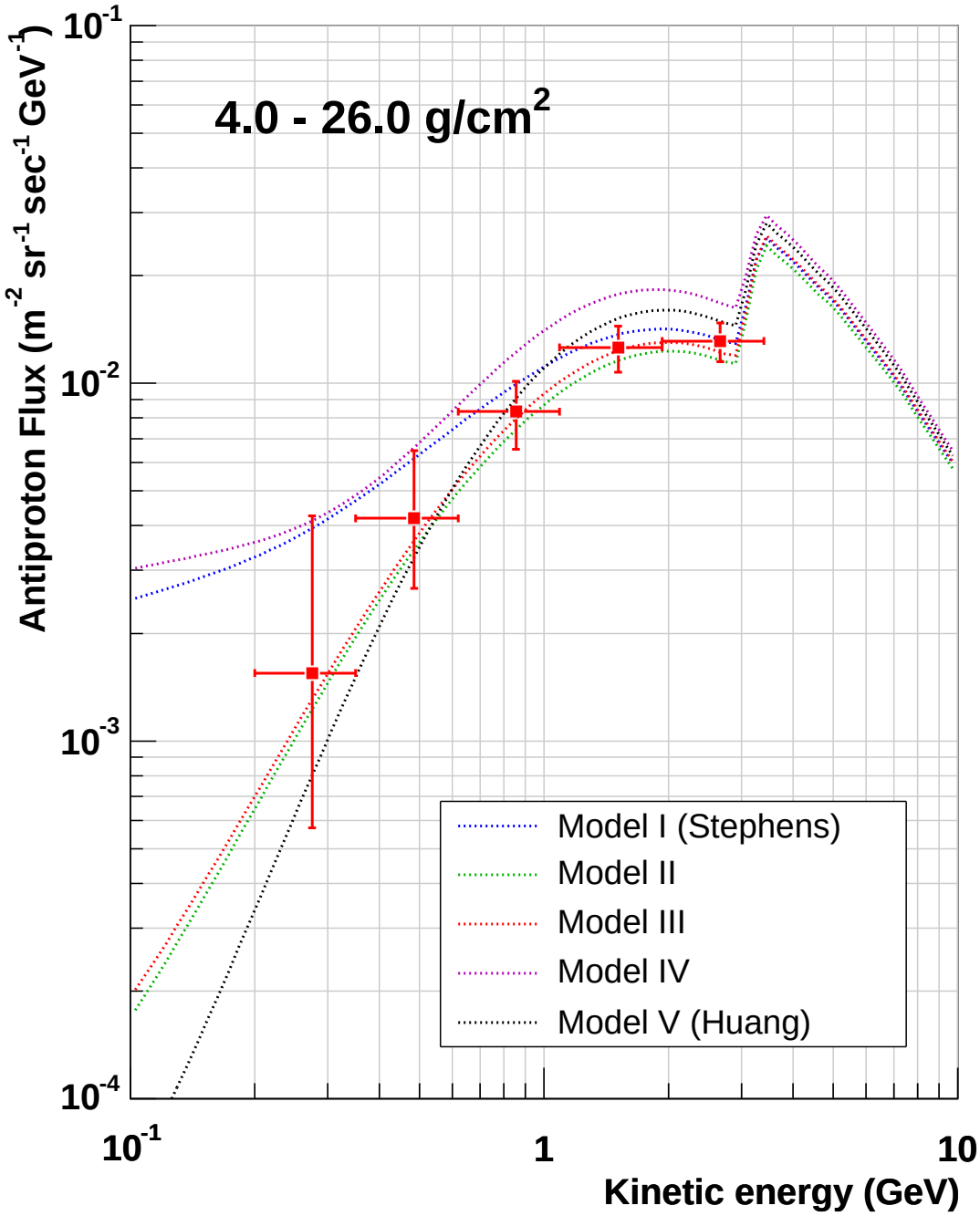

Figure 6.10: The averaged flux (lines) and observation flux (points) at atmospheric depth of 4 - 26 g/cm^2

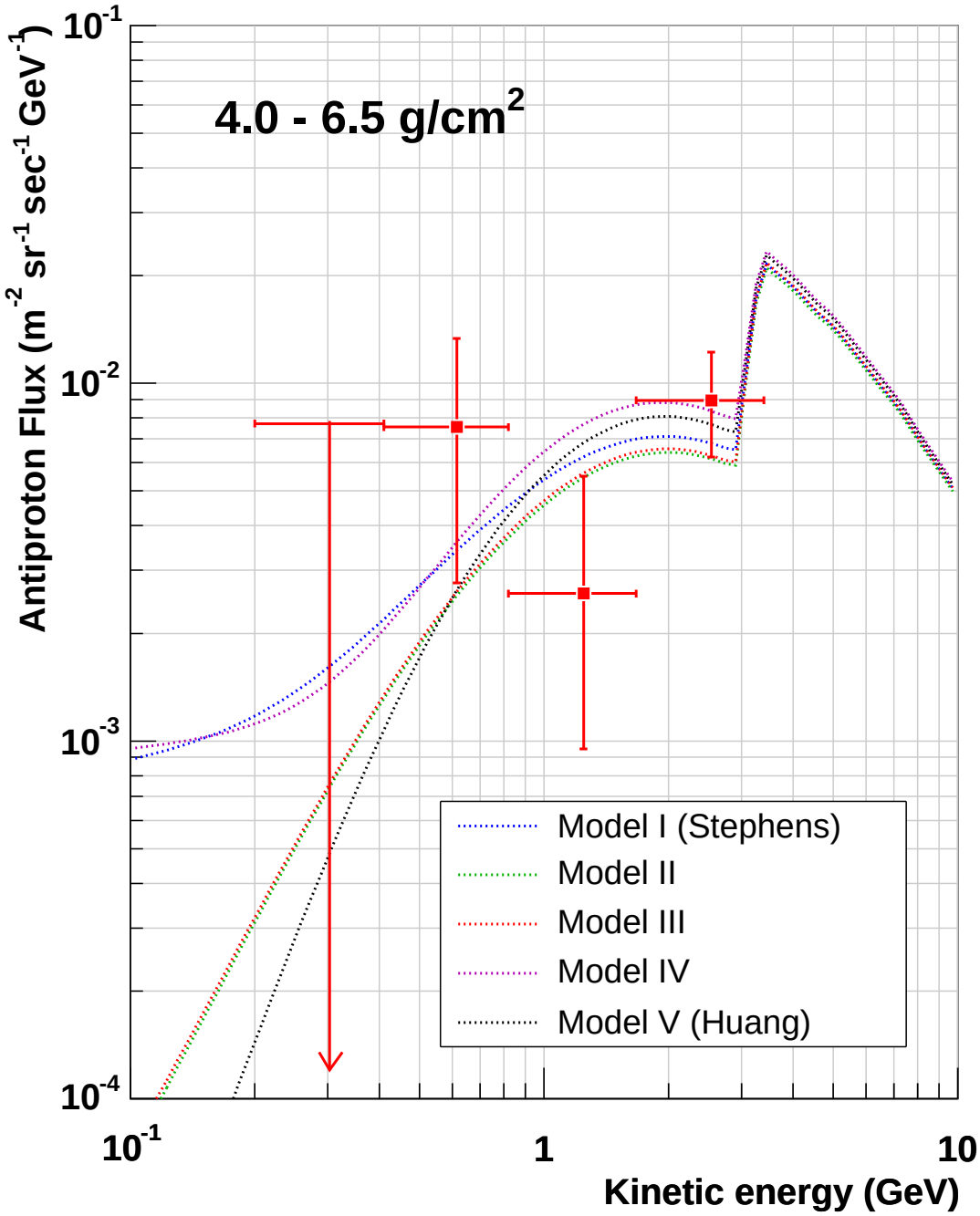

Figure 6.11: The averaged flux (lines) and observation flux (points) at atmospheric depth of 4.5 - 6.5 g/cm^2

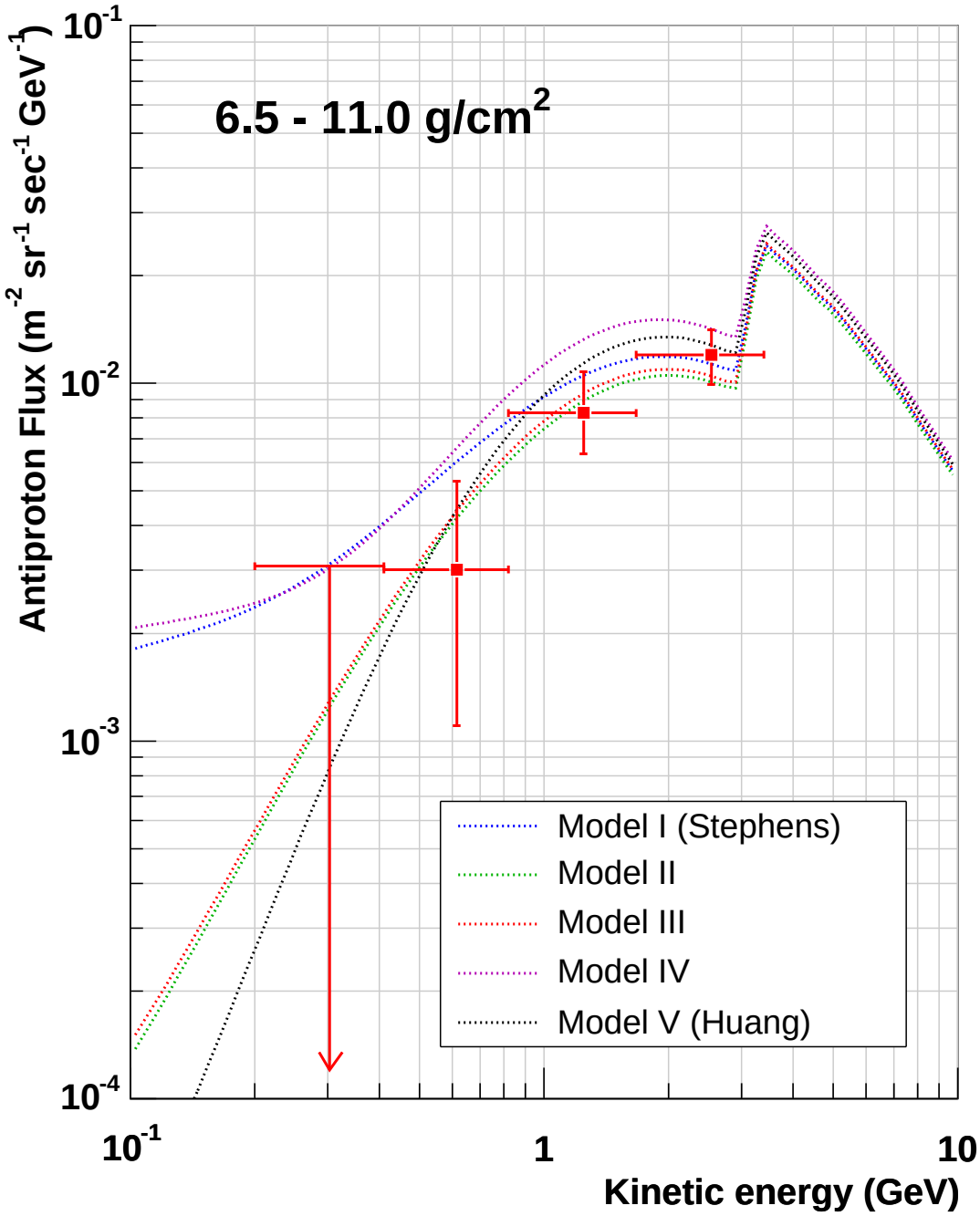

Figure 6.12: The averaged flux (lines) and observation flux (points) at atmospheric depth of 6.5 - 11 g/cm^2

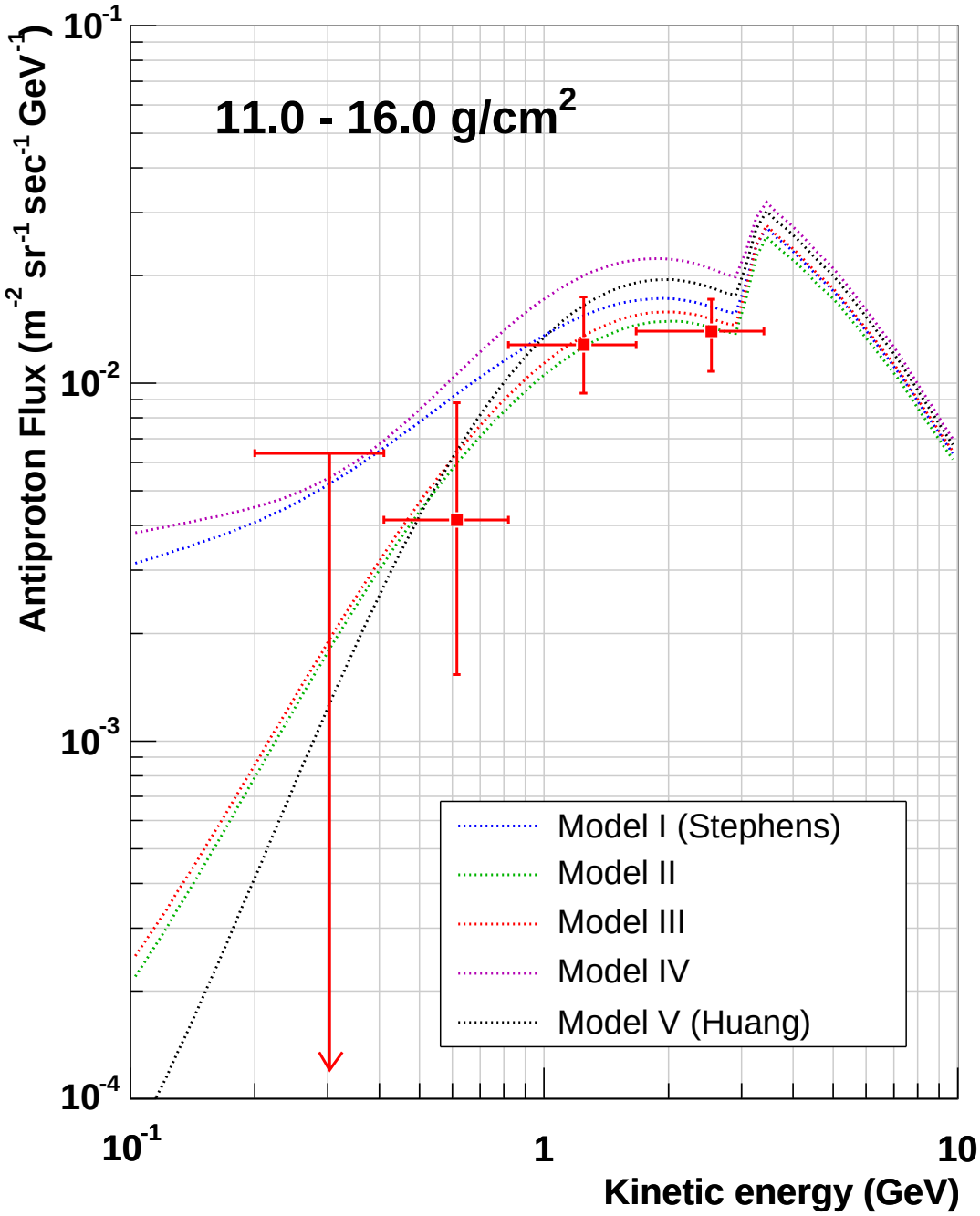

Figure 6.13: The averaged flux (lines) and observation flux (points) at atmospheric depth of 11 - 16 g/cm^2

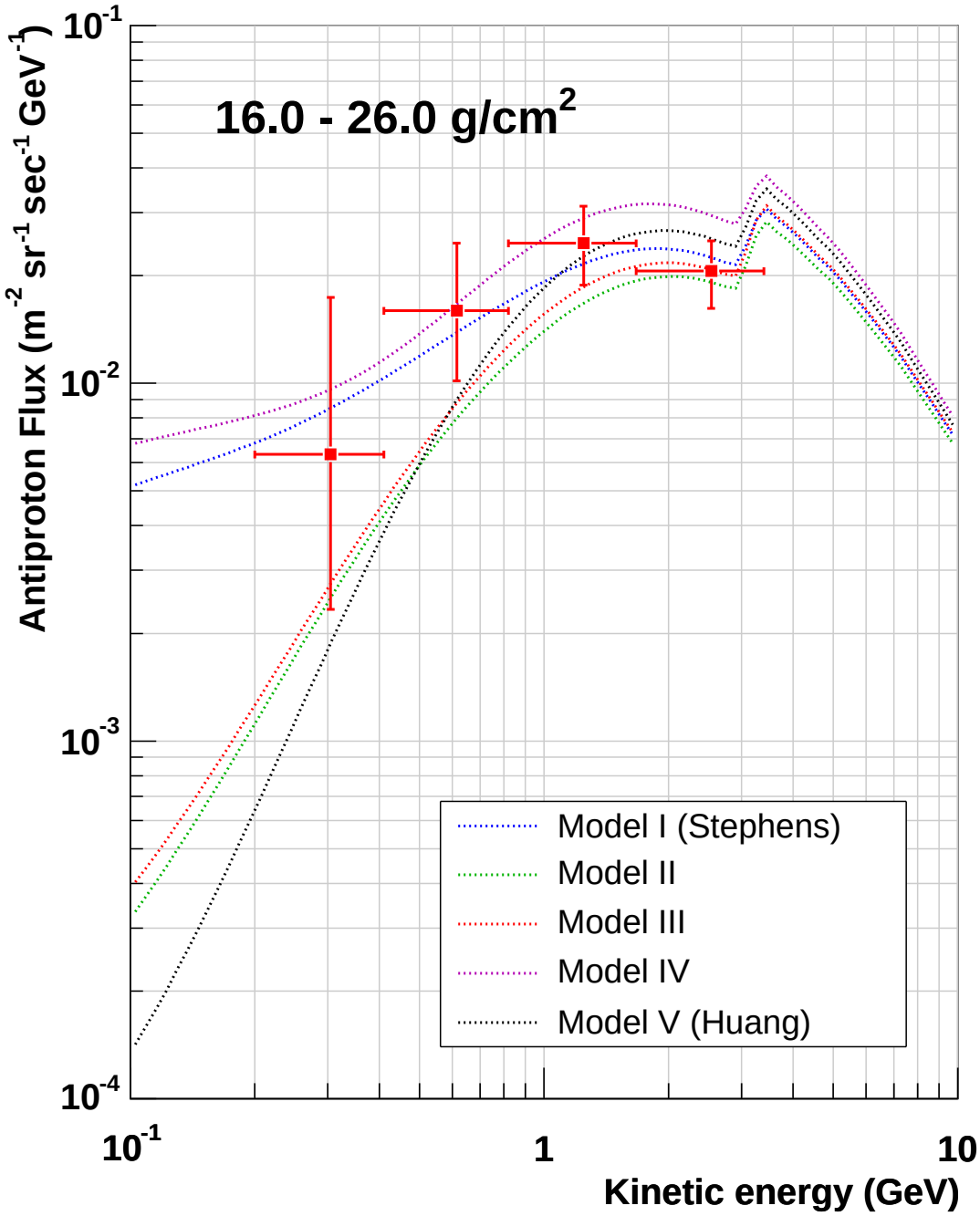

Figure 6.14: The averaged flux (lines) and observation flux (points) at atmospheric depth of 16 - 26 g/cm^2

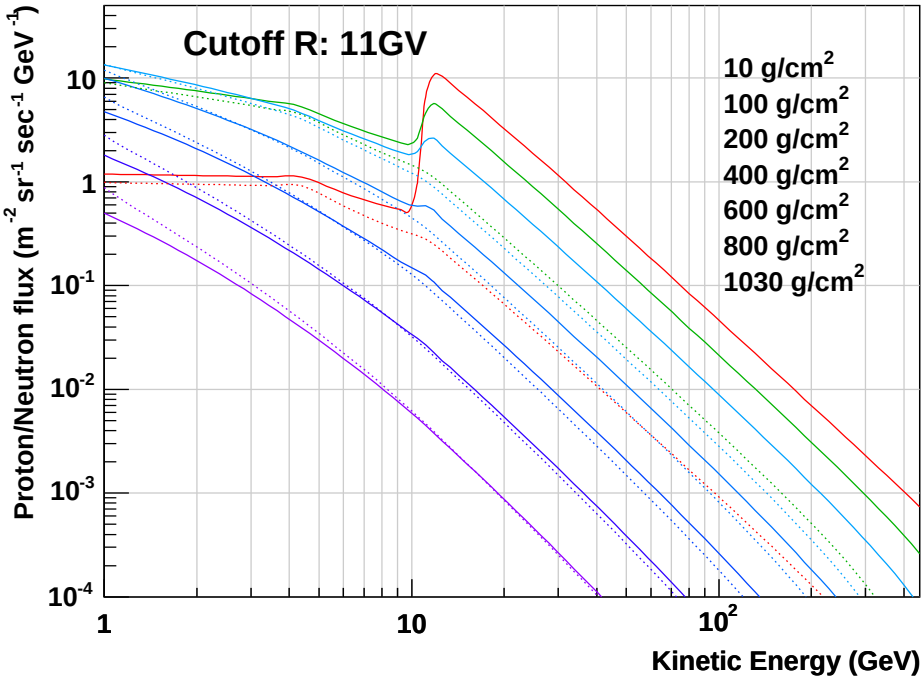

Figure 6.15: The calculated Proton and Neutron flux including cut off Rigidity 11 GV. The solid lines represent proton flux and dotted lines represent neutron flux.

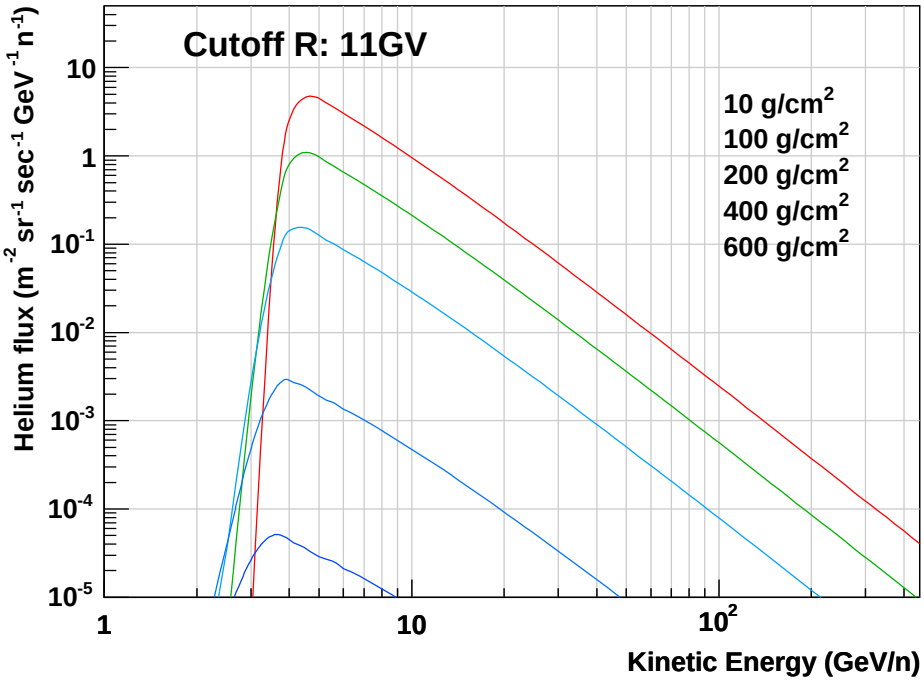

Figure 6.16: The calculated Helium flux including cut off Rigidity 11 GV.

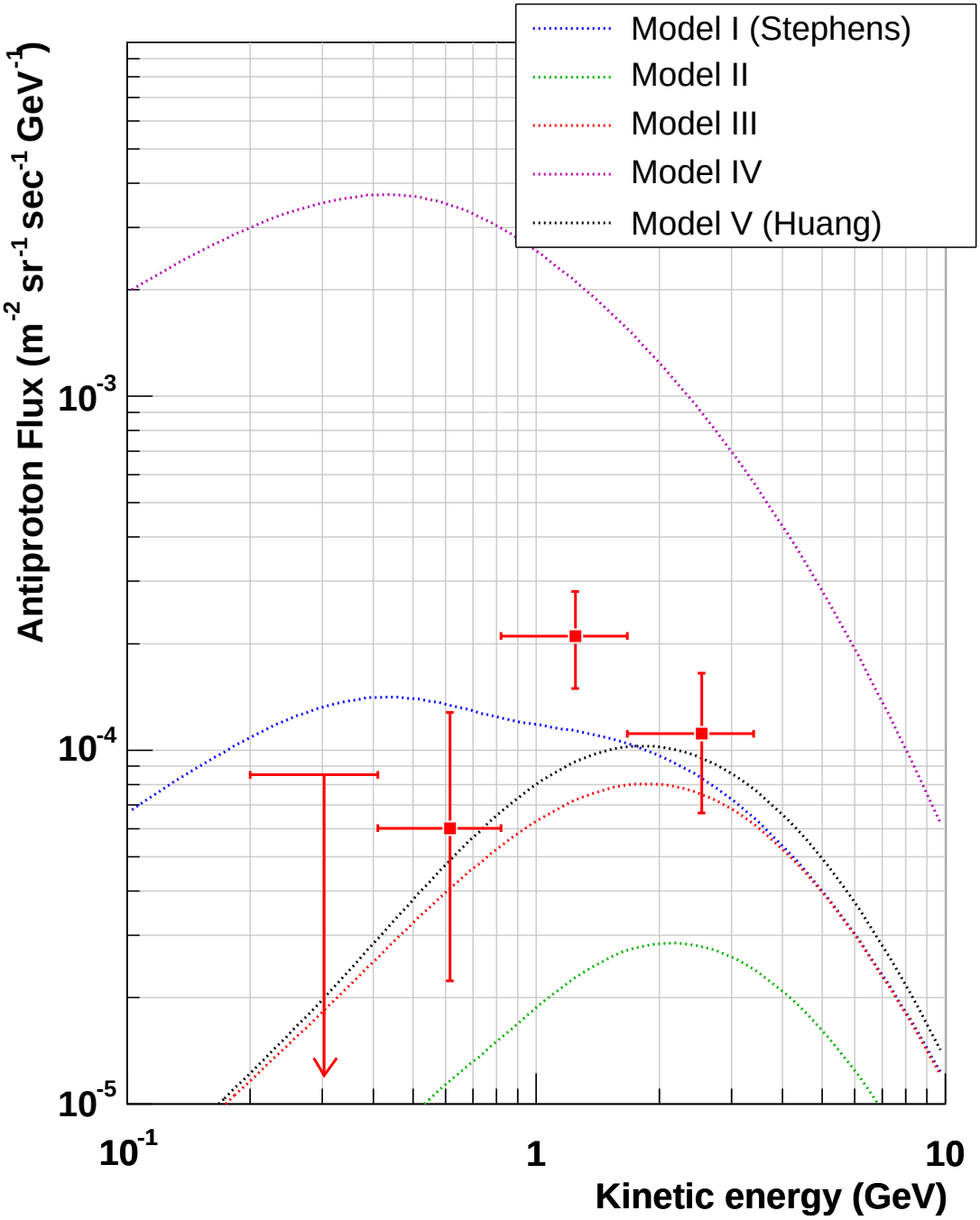

Figure 6.17: The averaged flux (lines) and observation flux (points) on the ground. The Model 'II' and 'IV' can not rejected by comparing with observed data. The agreement with the calculated using other models are moderate, but it gives a little bit lower flux.

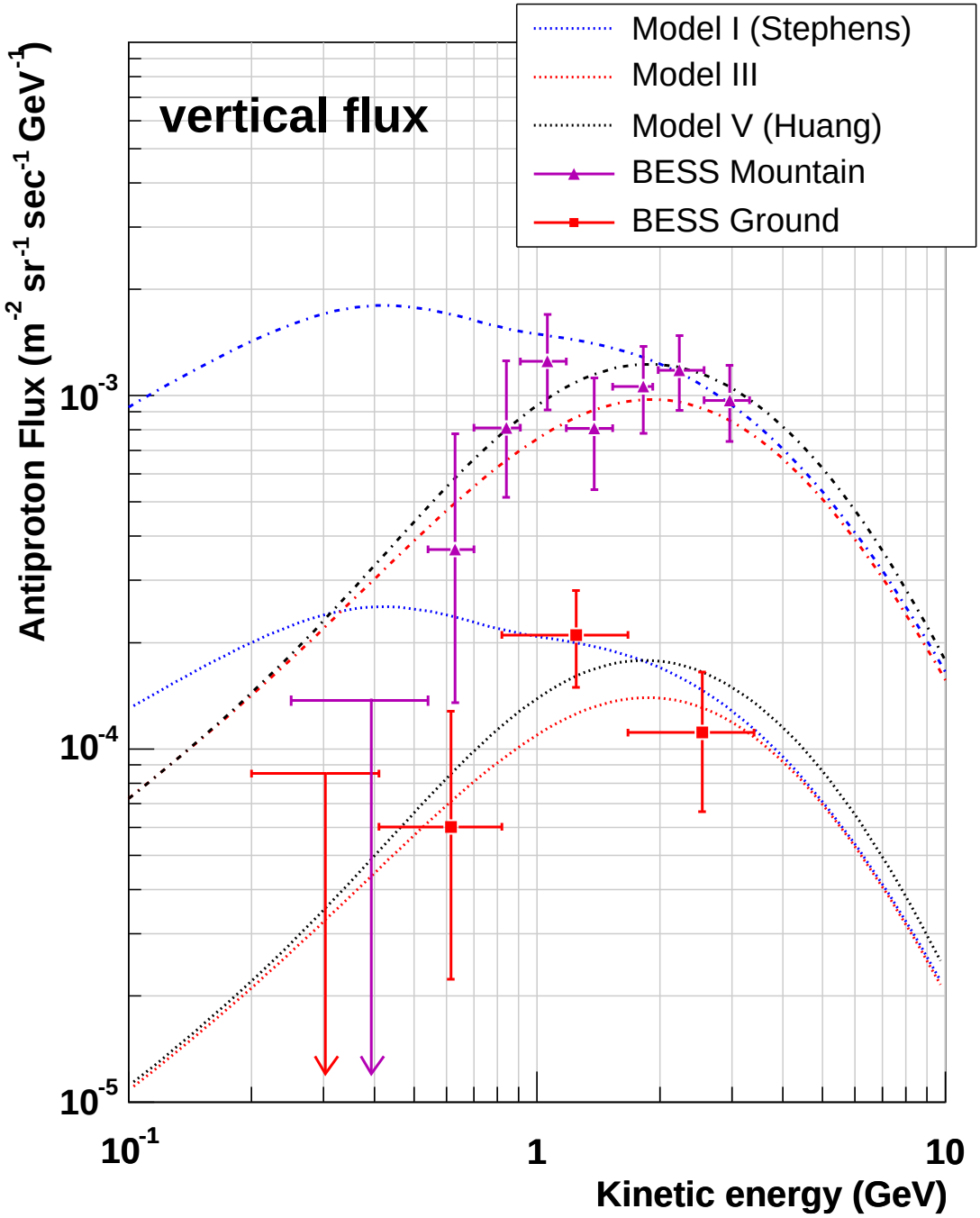

Figure 6.18: The vertical flux (lines) and observation flux (points) on the ground and the mountain altitudes. It seems that the agreement is better than averaged (lines in Figure 6.17).

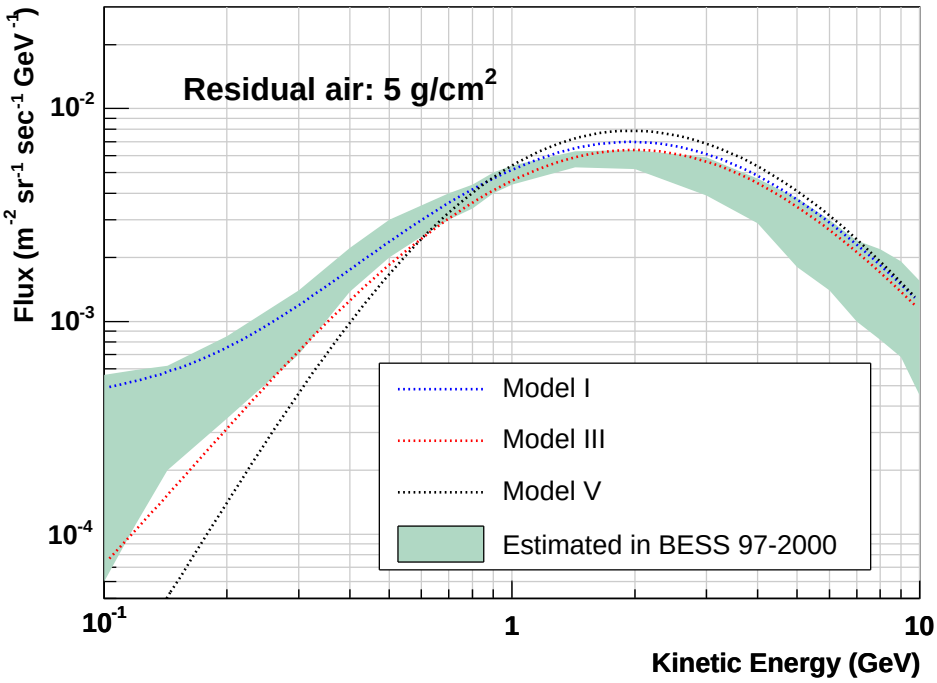

Figure 6.19: The estimation of atmospheric antiproton flux used in the analysis of BESS 97 - 2000 and the calculated averaged flux.

6.5 Consistency with the previous analysis

Figure 6.19 shows the calculated atmospheric antiproton flux at the atmospheric depth of 5 g/cm^2 using the flux of Model I, III, and V, and the estimated region of atmospheric antiproton flux used in the analysis of BESS 97 - 2000. In the analysis, the maximum difference of three calculations (Mitusi [15], Stephens [16], Pfeifer [17]) was regarded as systematic error of the estimation.
Model III agree best with observed data as discussed in previous sections, and the estimation in BESS 97 - 2000. The estimation of peak flux around 2 GeV may be a little lower by about 10 %. However, since this is within systematic errors, it can be justified to state that a subtraction of atmospheric antiproton flux in the previous BESS experiment was accurate enough.

6.6 Future prospects

We confirmed that the tertiary production may be smaller than the Stephens' model and other models assuming the similar tertiary contributions [16, 17]. To discuss quantitatively, we need to measure the detailed shape of the spectrum at the 0.1 - 1 GeV at the deep atmosphere, and wee need to observe for 2 or 3 years to get 10 events in the energy band between 0.1 to 0.2 GeV with the detector having ~ 0.1 (m^{-1} sr^{-1}

sec^{-1} GeV^{-1}).
Such results will give important information not only for the antiproton propagation in the atmosphere, but also the propagation in the Galaxy. Because details of propagation behavior of the antiproton inside the galaxy or atmospheric nuclei are not quite well known yet.
The BESS-Polar experiment is prepared for a long-duration flight at Antarctica with flight duration of 10 days or so [71, 72]. The flight duration is expected to be about 1∼2 weeks. To realize long duration observations, we need to resolve many problems, to establish the successful observation. A long duration atmospheric antiproton observation at the ground is also very suitable for this purpose, and I suggest it strongly.

Chapter 7

Conclusion

We succeeded in measuring in the atmospheric antiprotons at 4 - 26 g/cm^2 in kinetic energy range of 0.2 - 3.3 GeV for the first time. The flight was carried out at Ft. Sumner, New Mexico, U.S. in 2001, and the 243 antiproton candidates were identified. From this analysis, we confirm that the production cross section of Eq. (6.2) used by Stephens gives the consistent results with observed data. Although the statistical error is large, data points agree well with the calculated results, which do not include the tertiary antiprotons.
We also measured the atmospheric antiproton on the ground. In this experiment, we obtained total of 25 antiproton candidates in kinetic energy range of 0.4 - 3.3 GeV during the live time of 171 hours. The shape of observed flux is also similar to that calculated without tertiary production. For the absolute value around the peak, our calculation is about half compared with observed value. We can interpret this situation by the fact that the zenith angle distribution at large atmospheric depth is smeared by the angular spreads, and become less steep than that calculated by the one dimensional treatment. To confirmed this, the spectrum with much better statistics by the long duration observation on the ground or at Mountain altitude will resolve this problem.

Appendix A

Calculations of the input flux for the antiprotons

A.1 Atmospheric antineutrons

$J_{\overline{n}}(E,x)$ is differential antineutron flux, which can denote a similar to antiprotons as:

$$\begin{aligned}\frac{\partial J_{\overline{n}}(E,x)}{\partial x} &= \sum_A Q_A(E_A,x,E) + \frac{J_{\overline{n}}(E,x)}{\Lambda(E)} \\ &+ \int_E^\infty \Phi(E')\left[\frac{J_{\overline{n}}(E',x)}{\lambda^{in}}(1-\alpha) + \frac{J_{\overline{p}}(E',x)}{\lambda^{in}}\,\alpha\right]\mathrm{d}E'\end{aligned} \tag{A.1}$$

Note that this equation is identical to that of antiproton except that it does not have the term due to ionization loss. We have assumed that the annihilation cross section for antineutron is the same as that of antiproton, since the target nucleus has equal number of proton and neutron.

A.2 Proton/Neutron/Helium flux as an input

The transport equations describing the propagation of protons, neutrons, and helium nuclei in the atmosphere can be written for energies > 2 GeV/n from Papini et al. [70]

as,

$$\frac{\partial J_p(E,x)}{\partial x} = -\frac{J_p(E,x)}{\lambda_p(E)} \; + \; \frac{\partial}{\partial E}\left[J_p(E,x)\left\langle\frac{\mathrm{d}E}{\mathrm{d}x}\right\rangle\right] \; + \; 1.25 J_{He}(E,x)\left[\frac{1}{\lambda'_{He}(E)} - \frac{1}{\lambda_{He}(E)}\right]$$
$$+ \int_E^\infty dE'\Phi(E')\left[\frac{J_p(E',x)}{\lambda_p(E)}(1-\alpha) + \frac{J_n(E,x)}{\lambda_n(E')}\alpha + 1.25\frac{J_{He}(E',x)}{\lambda_{He}(E')}\right] \tag{A.2}$$

$$\frac{\partial J_n(E,x)}{\partial x} = -\frac{J_n(E,x)}{\lambda_n(E)} \; + \; 1.25 J_{He}(E,x)\left[\frac{1}{\lambda'_{He}(E)} - \frac{1}{\lambda_{He}(E)}\right]$$
$$+ \int_E^\infty dE'\Phi(E')\left[\frac{J_n(E',x)}{\lambda_n(E)}(1-\alpha) + \frac{J_n(E,x)}{\lambda_n(E')}\alpha + 1.25\frac{J_{He}(E',x)}{\lambda_{He}(E')}\right] \tag{A.3}$$

$$\frac{\partial J_{He}(E,x)}{\partial x} = -\left[1.0 - 0.5\exp\left(-\frac{x}{\lambda'_{He}}\right)\right]\frac{J_{He(E,x)}}{\lambda'_{He}(E)} \; + \; \frac{\partial}{\partial E}\left[J_{He}(E,x)\left\langle\frac{\mathrm{d}E}{\mathrm{d}x}\right\rangle\right] \tag{A.4}$$

where $J_p(E,x)$, $J_n(E,x)$, $(J_{He}(E,x)$ are the proton, neutron, and helium flux at atmospheric depth x g/cm^2 respectively. λ' is total inelastic interaction length, which includes both spallation and deep inelastic interactions. By scaling the measured cross section at high energies [18] for He Collisions with C target to air target, Stephens take $\lambda'_{He} = 50$ g/cm^2. For the deep inelastic interaction length,

$$\sigma_{CD} = 56.7\left[A_C^{1/3} + A_D^{1/3} - 1.25\right]^2 \quad \text{(mb)} \tag{A.5}$$

where σ_{CD} is the cross section for the interaction of nuclei C with D, having mass numbers A_C and A_D, respectively. λ_p and λ_n are same as λ^{in} in Eq. (6.15), (6.16). The calculated results are shown in Figures A.1 and A.2.

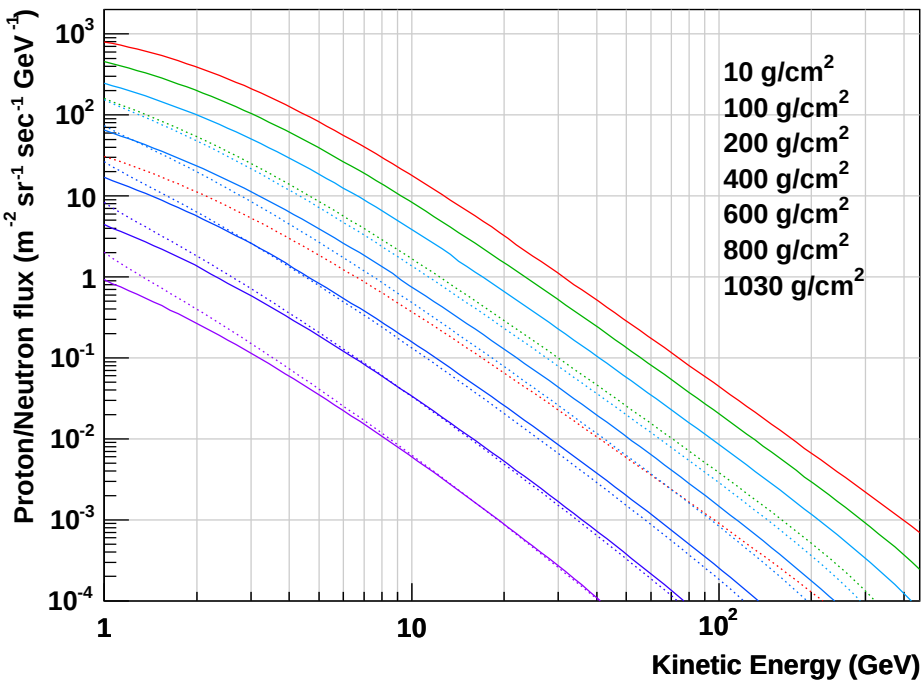

Figure A.1: The calculated Proton and Neutron flux. The solid lines represent proton flux and dotted lines represent neutron flux.

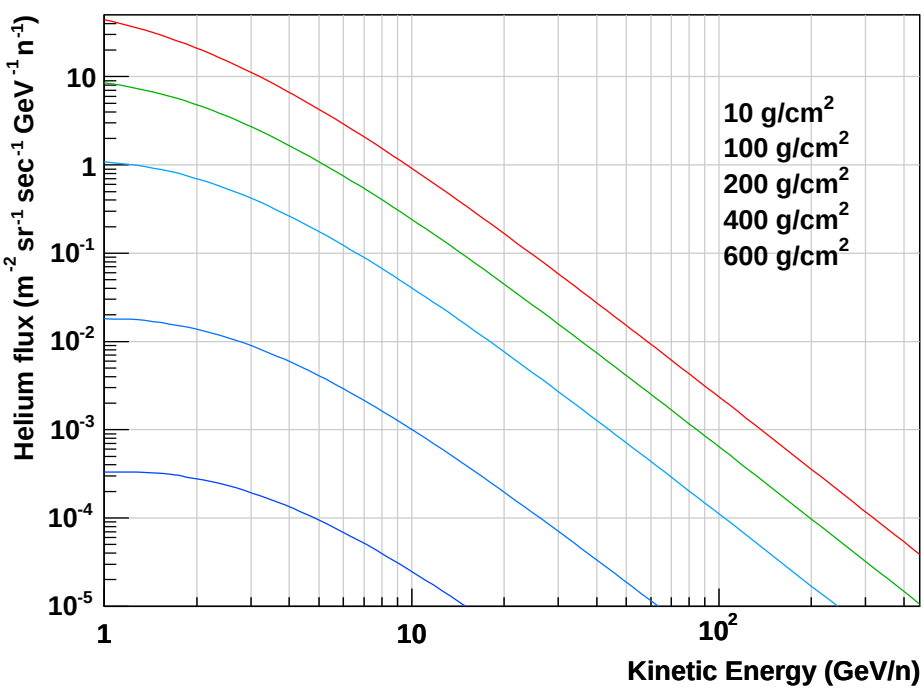

Figure A.2: The calculated Helium flux at various altitudes.

Acknowledgments

At the first I wish to express my special thanks to the late Professor S. Orito, who had led the BESS experiment and greatly motivated me to the research reported in this thesis. I pray for the repose of your soul.
I wish to express my sincere thanks to Professor M. Nozaki, and Professor A. Yamamoto, who have led the BESS experiment, for general guidance throughout my research reported in this thesis. I greatly appreciate helpful suggestion from Professor J. Nishimura, and discussions with him about the theoretical calculations. I also wish to gratefully appreciate Professor T. Yoshida, Professor K. Yoshimura, and Dr. T. Sanuki who have managed the campaign and lead it to a success. The calibration and analysis were done owing a lot to Dr. K. Abe, Dr. T. Sanuki, Dr T. Maeno. Y. Asaoka. I would like to acknowledge them for their suggestions and helpful discussion and assistance at the various stages of the analysis. I would like to thank Professor N. Yajima, Professor T. Yamagami, and all the other BESS-Japan colleagues for their effort to make a success of the experiment.
I would deeply appreciate Dr. J. Ormes, Dr. R. Streitmatter, Dr. J. Mitchell, Dr. A. Moiseev, and Dr. E. S. Seo, those who are the US collaborators of the experiment. Furthermore, I am greateful to Dr. V. Jones and all other people at NASA who suported BESS and to the balloon campaign team from the National Scientific Balloon Facility for their professional and skillful work in carrying out the BESS flights.
I greately acknowledge Professor O. Matsuo, Director General of ISAS, Professor H. Sugawara, Director General of KEKE, and Professor S. Iwata of KEK for their support and encouragement. Sincere thanks go to International Center of Elementary Particle Physics (ICEPP) of the University of Tokyo, and Professor K. Kawagoe in Kobe University for kindly allowing me to use their computing facilities.
The BESS experiment has been supported by Grant-in-Aid for Scientific Research on Priority Areas (12047227 and 12047206) from the Ministry of Education, Cluture, Sports Science and Technology (MEXT).

References

[1] R. L. Golden *et al.*, Phys. Rev. Lett. **43**, 1196 (1979).

[2] R. L. Golden and A. Stephens, Space Sci. rev. **43**, 87 (1986).

[3] T. K. Gaisser *et. al.,* Astrophys. J. **394** 174 (1992).

[4] J. W. Bieber *et. al.,* Phys. Rev. Lett. **83** 674 (1999).

[5] I. V. Moskalenko *et. al.,* astro-ph/0106567, Astrophys. J., in press.

[6] A. Bottino *et. al.,* Phys. Rev. D **58** 123503 (1998).

[7] L. Bergström *et. al.,* Astrophys. J. **526** 215 (1999).

[8] S. W. Hawking, Nature **248** 30 (1974); Commun. Math. Phys. **43** 199 (1975).

[9] K. Maki *et al.*, Phys. Rev. Lett. **76**, 3474 (1996).

[10] S. Orito *et al.*, Phys. Rev. Lett. **84**, 1078 (2000).

[11] T. Maeno *et al.*, Phys. Rev. Lett. **88**, 051101 (2002).

[12] J. W. Mitchell. *et al.*, Phys. Rev. Lett. **76**, 3057 (1996).

[13] M. Boezio *et al.*, Astrophys. J. **561**, 787 (2001).

[14] M. Hof. *et al.*, Astrophys. J. **476**, L33-L36 (1996).

[15] T. Mitsui, Ph. D. Thesis. The university of Tokyo (1996).

[16] S. A. Stephens, Astroparticle Phys. **6**, 229 (1997).

[17] Ch. Pfeifer *et at.*, Phys. Rev. C **54**, 882 (1996).

[18] W. R. Webber, J. C. Kish and D. A. Schrier, Phys. Rev. C **41** 520 (1990).

[19] T. Sanuki *et. al.*, Astrophys. J. **545** 1135 (2000).

[20] J. Alcaraz *et. al.*, Phys. Lett. B **472** 215 (2000).

[21] S. A. Stephens, Astrophys. Space Sci. **76**, 87 (1981).

[22] K. Nakamura *et al.* Phys. Rev. Lett. **52**, 731 (1984).

[23] V. F. Kuzichev, Yu. B. Lepikhin and V. A. Smirnitsky, Nucl. Phys. A **576**, 581 (1994).

[24] S. P. Denisov *et al.*, Nucl. Phys. B **113**, 1 (1976).

[25] C. Y. Huang. *et al.*, Phys. Rev. D **68**, 053008 (2003).

[26] C. Y. Huang. Ph. D. Thesis, Université Joseph Fourier.

[27] T. Sanuki, M. Fujikawa, *et al.*, Phys. Lett. B **541** 234 (2002).

[28] A. Buffington *et al.*, The Astrophys. J. **199**, 669 (1975).

[29] R. L. Golden *et al.*, Nucl. Instr. Method, **148**, 179 (1978).

[30] M. H. Salamon *et al.*, The Astrophys. J. **349**, 78 (1990).

[31] R. L. Golden *et al.*, Nucl. Instr. Method, **A306**, 336 (1991).

[32] S. W. Barwick*et al.*, Nucl. Instr. Method, **A400**, 34 (1997).

[33] A. Yamamoto *et al.*, Adv. Space Res., **14**, (2)75 (1994).

[34] A. Yamamoto *et al.*, IEEE Trans. Mag. **24**, 1421 (1988).

[35] Y. Makida *et al.*, Adv. Cryog. Eng,. **37**, 401 (1992).

[36] Y. Makida *et al.*, IEEE Trans. Applied Superconductiveity **5**, 658 (1995).

[37] EUROTOM reports, EUR-4100e (1972).

[38] R. J. Yarema *et al.*, FERMILAB-TM-1284 (1284).

[39] M. Imori *et al.*, IEEE Trans. Nucl. Sci. **39**, 987 (1992).

[40] R. Suda *et al.*, Nucl. Instr. and Meth. **A406**, 213 (1998).

[41] R. Enomoto *et al.*, Nucl. Instr. and Meth. and Method

[42] T. Massam, GUIDE7: a general program for evaluating the properties of scintillation and Čerenkov counter optical systems, CERN 76-21 (1976).

[43] H. Matsumoto *et al.*, IEEE Trans. Nucl. Sci., **43** 2195 (1996).

[44] K. Anraku, S. Inaba and M. Imori, IEEE Trans. Nucl. Sci., **40** 717 (1993).

[45] W. B. Atwood, Time of flight measurements, SLAC-PUB-2620, Octorber 1980.

[46] T. Tanimori *et al.*, Nucl. Instr. and Meth. **216** 57 (1983).

[47] E. Chen *et al.*, hep-ex/9606007.

[48] I. Adachi *et. al.*, Numcl. Instrum. Methods A **335**, 390 (1995).

[49] V. Karimaki, Comput. Phys. Commun., **69**, 133 (1992).

[50] T. Sumiyoshi, I. Adachi, R. Enomoto, T, Iijima, R. Suda, M. Yokoyama, "Silica aerogels in high energy physics", Journal of Non-Crystalline Solids **225**, 369-374 (1998).

[51] INMOS, Transputer Reference Manual, Prentice Hall (1998).

[52] G. Jones, and M. Goldsmith, Programming in Occam2, Prentice Hall (1998).

[53] T. Saeki, *et al.*, Nucl. Instrum. Methods A **355**, 506 (1995).

[54] LonWorks Technology Device Data, Rev. 5, Motorola Inc. USA.

[55] EIA Standard, EIA-709.1 "Control Network Protocol Specification" (1998).

[56] PhotoMOS Relay Specification, Matsushita Electric Works, Ltd., W5013.

[57] Product of Hawker Eternacell, Inc., Model G62/1.

[58] P. Papini *et al.*, Nuovo Cimento **19**, 367 (1996).

[59] R. Brun *et al.*, GEANT 3.21 CERN Program Library Long Write up W5013.

[60] G. J. Feldman *et al.*, Phys. Rev. D **57**, 3873 (1998).

[61] J. Neyman, *A selection of Early Statistical Papers on J. Neyman*, Univ. of California Press, Berkely (1967).

[62] H. C. Feselfeldt *et al.*, PITHA 85/02 Aschen, 1985.

[63] A. Fassò *et al.*, Proc. **IV** Int. Conf. on Calorimetry in High Energy Physics. (La Biodola (Italy)) 21-26 September 1993, Ed. A. Mezione and A. Scribano, World Scientific, 282 (1981).

[64] L. C. Tan *et al.*, J. Phys. G **9** 1289 (1983).

[65] K. Abe *et al.*, Phys. Lett. B **564** 8 (2003).

[66] Y. Asaoka *et al.*, Nucl. Instrum. Methods A **489**, 170 (2001).

[67] S. A. Stephens and R. L. Golden, Space Sci. Rev. **46**, 31 (1987).

[68] L. C. Tan and L. K. Ng, J. Phys. G **9** 227 (1983).

[69] S. Agostinelli, *et. al.*, Nucl. Instrum. Methods A **506**, 250 (2003).

[70] P. Papini, C. Grimani and S. A. Stephens, Nuovo Cimento **19C** 367 (1996).

[71] A. Yamamoto, *et. al.*, Adv. Space Res. **30(5)**, 1253 (2002).

[72] A. Yamamoto, *et. al.*, IEEE Trans. Applied Superconductivity **12**, 438 (2002).